Infrared hyperspectral imaging of 3D printing with prostate cancer cells for tissue engineering applications

A thesis submitted to The University of Manchester for the degree of Doctor of Philosophy

in the Faculty of Science and Engineering.

2021

Widad Al Rawahi

School of Engineering

Contents

Word Count: 35189

List of Tables

List of Figures

List of Abbreviations

AA   Arachidonic Acid

ATC   Anaplastic Thyroid Cancer

ATR   Attenuated Total Reflection

BPH   Benign Prostatic Hyperplasia

CAFs   Carcinoma-Associated Fibroblasts

CPD   Critical-Point Drying

CZ   Central Zone

DD   Dosing Distance

DRE   Digital Rectal Exam

DV   Deposition Velocity

ECM   Extracellular Matrix

EP   Extrusion Pressure

EPO-GEMM ElectroPoration-based Genetically Engineered Mouse Models

FA   Fatty Acid

FBA   Focal Plane Array

FDA   Food and Drug Administration

FDM   Fused Deposition Modelling

FTIR   Fourier-Transform Infrared

GEM   Genetically Engineered Mouse

H&E   Haematoxylin and Eosin

IHC   Immunohistochemistry

LDA   Linear Discriminant Analysis

MCT   Mercury Cadmium Telluride

PA   Palmitic Acid

PCa   Prostate Cancer

PCL   Polycaprolactone

PEG-DA Polyethylene Glycol Diacrylate

PEG-PLA Polyethylene Glycol–Polylactic Acid

PIN   Prostatic Intraepithelial Neoplasia

PSA   Prostate Specific Antigen

PZ   Peripheral Zone

QDA   Quadratic Discriminant Analysis

SLA   StereoLithogrAphy

SLS   Selective laser sintering

SMC   Smooth Muscle Cells

SMT   Somatic Mutation Theory

SNR   Signal to Noise Ratio

TE   tissue engineering

TOFT   Tissue Organization Field Theory

TZ   Transitional Zone

VOT   Valve Opening Time

Abstract

Prostate cancer is the most common cancer among men. Leading to approximately 10,000 deaths in the UK each year. Different models have been used to study this disease such as animal models, 2D and 3D *in vitro* models. These modelsall have their own limitations. The limitations of these models strongly compromise our understanding of important cellular mechanisms underpinning prostate cancer initiation and progression. This study uses tissue engineering approaches to design a 3D model capable of mimicking the tumour environment. Peptide hydrogels (alpha1, alpha2 and alpha2*) were used to engineer the ExtraCellular Matrix (ECM) in which prostate cancer cell lines (PC3, PNT2 and LNCaP) are encapsulated. The culture media were found to have a significant effect on the mechanical properties of the hydrogel; however, they have no impact on their viscosity. A number of biological tests are used to assess the encapsulated cells in which the viability of the cells and their ability to proliferate are assessed. The constructs built with alpha1 hydrogel were printed accurately, but the cells were not viable on it. Alpha2 was found to work as a better ECM for all the cell lines but accurate constructs shapes were impossible to be printed successfully. Alpha2*, on the other hand, was printed in more precise shapes than alpha2. The viability of PC3 and PNT2 cells was high on alpha2*; however, LNCaP cells shows a variation of their viability which confirmed by the metabolic activity test. The cell-laden constructs generated using alpha2* hydrogel were successfully embedded in paraffin and cut. The sections were stained with H&E, and five different antibodies were used to check the protein expression of the seeded and printed cells. Seeded and printed cells were found to express the same proteins. FTIR imaging is used to analyse the printed constructs. The hydrogel consists of amino acids, and hence it has the same absorption peaks as the cells which complicates the separation of the cells from the hydrogel. Multivariate Curve Resolution (MCR) was used to separate the signals of the cell, but further development of this methodology is required.

Declaration

No portion of the work referred to in the thesis has been submitted in support of an application for another degree or qualification of this or any other university or other institute of learning.

Copyright Statement

(i) The author of this thesis (including any appendices and/or schedules to this thesis) owns certain copyright or related rights in it (the "Copyright") and s/he has given The University of Manchester certain rights to use such Copyright, including for administrative purposes.

(ii) Copies of this thesis, either in full or in extracts and whether in hard or electronic copy, may be made only in accordance with the Copyright, Designs and Patents Act 1988 (as amended) and regulations issued under it or, where appropriate, in accordance with licensing agreements which the University has from time to time. This page must form part of any such copies made.

(iii) The ownership of certain Copyright, patents, designs, trademarks and other intellectual property (the "Intellectual Property") and any reproductions of copyright works in the thesis, for example graphs and tables ("Reproductions"), which may be described in this thesis, may not be owned by the author and may be owned by third parties. Such Intellectual Property and Reproductions cannot and must not be made available for use without the prior written permission of the owner(s) of the relevant Intellectual Property and/or Reproductions.

(iv) Further information on the conditions under which disclosure, publication and commercialisation of this thesis, the Copyright and any Intellectual Property and/or Reproductions described in it may take place is available in the University IP Policy (see `http://documents.manchester.ac.uk/DocuInfo.aspx?DocID=24420`), in any relevant Thesis restriction declarations deposited in the University Library, The University Library's regulations (see `http://www.library.manchester.ac.uk/about/regulations/`) and in The University's policy on Presentation of Theses.

Acknowledgement

Foremost, I would like to express my sincere gratitude to my supervisors Prof. Peter Gardner and Dr Marco Domingos for the continuous support of my PhD study and their patience, motivation, and immense knowledge. Their guidance helped me all the time of research and writing of this thesis.

Thanks to all members of Gardner's Group at the Manchester Institute of Biotechnology, particularly Dr Michael Pilling and Dr Nga-Tsing Tang for their vast help with the cell culturing and FTIR imaging, and Dr Alex Henderson and Dougal Ferguson who help with data processing and analysis.

Thanks to Tony Khalil who help with the 3D Discovery bio-printer and code generation for the printer and Hussein Mishbak who worked with me on the live/dead viability test data analysis.

Support for studies on various biological tests came from colleagues across the University of Manchester. Thanks to Vicki Workman from Manchester Institute of Biotechnology for the help with Live/dead viability test and Dr Louise Carney, from School of Materials for the support during the work in Sackville Street Building. Great thanks to Marie O'Brien from School of Materials for all her help and support with the histopathological tests. Also, the work with Immunohistochemistry won't be completed without the help of Bioimaging Facility and staff.

Great thanks to my father, Saif Al Rawahi and my mother Nasra Al Rawahi who never stop believing in me. Not to forget to thank my brothers ans sisters; Sulaiman, Maryam, Zainab, Zamzam, Abeer, Ahlam, Issa and Hiba for their love, prayer and continuous support.

My deepest gratitude to my caring, loving, and supportive husband, Dawood Al Rawahi. I appreciate your encouragement when the times got rough. It was a great comfort and relief to know that you are always there for me and always taking my back when I needed the time to complete my work. My heartfelt thanks to my lovely Kids; Elias, Alyassa and Ghena who without their desire endured my absence and the busy mood during this period.

Special thanks to my lovely friends who share with me the most wonderful moments in Manchester: Siham, Asma, Aysha. R, Kawther, Hafidha and Aysha. S.

Dedication

This thesis work is dedicated to my husband, Dawood and my lovely children, Elias, Alyassa and Ghena who deeply shared this part of my life with me. This work is also dedicated to my parents, Saif and Nasra, who encourage me to experience different adventures, especially this one.

1

Introduction

1.1 Project overview

Cancer is a disease caused by abnormal cell division in an uncontrolled manner. The change in cancer cells character causes the cells not to respond to or not to be affected by normal controls such as growth factors (Burnet, 1957). Prostate cancer is the most common cancer among men, with high death rates of 3.8% in 2018 (Rawla, 2019). Different models (*in-vivo* and *in-vitro*) are used for prostate cancer studies in which the biological process and structures are investigated and novel drug therapies are developed. Animal models such as dogs, primates, Genetically Engineered Mouse models (GEM), xenograft models and rats have been used to study prostate cancer (Ellem et al. (2014); Ittmann et al. (2013)). The limitations of these models arise from the high cost and long latency time in dogs, primates and GEM, while the lesions used in xenografts are from aggressive cancers and are not applicable to the early-stage ones. Additionally, the subcutaneous location of the cells in the host affects the tumour and it is subjected to change if the immune system is abnormal (Ittmann et al., 2013). The simplicity and reproducibility of 2D models mean that they are widely used; however, the absence of the microenvironment leads to the lack of cellular interactions between cancer cells and the surrounding cells (Ellem et al. (2014); Ittmann et al. (2013)). Co-culture models in which prostate cancer cells are cultured with stromal cells have been proposed to overcome the limitations of 2D cellular models, but their lack of basic heterogeneity and the tertiary structure of the prostate tumours still hinders their application in prostate cancer research (Azeem et al. (2017); Ellem et al. (2014)). Different 3D models, including spheroids and organoids, were created to mimic the tumour microenvironment and enable prostate cancer cellular interactions. These models, though, are time-consuming and have an uneven distribution of cells with the lack of prostate heterogeneity (Ellem et al., 2014). The benefits shown by Tissue Engineering (TE) strategies in generating reproducible tissue/organ

analogues for regeneration and disease modelling purposes has opened new avenues in prostate cancer research. Through the combination of automated manufacturing technologies (e.g. 3D bioprinting) with advanced biomaterials (e.g. hydrogels), it is now possible to generate highly accurate and reproducible 3D structures that can mimic the Extracellular Matrix (ECM) biomechanical environment and elicit specific cellular responses. Taking advantage of these recent developments, the present study investigates the 3D bioprinting of hydrogel-based constructs encapsulated with different prostate cancer cells to mimic the native tumour microenvironment. The aim is to produce a 3D model that mimics the structure and function of the prostate cancer microenvironment and propose FTIR imaging as a new tool to validate the printed constructs. FTIR imaging will be used to find the differences in the IR signals when the cancer cells are cultured in a 3D environment by themselves and the signals when cancer cells are cultured with other cells in the same 3D environment.

1.2 Aims of the study

The main aim of this study is to develop the foundations for building a 3D model for prostate cancer using hydrogels as extracellular matrix. The main vision comes from translating the prostate microenvironment into a 3D model, as shown in Figure 1.1.

Prostatic intraepithelial
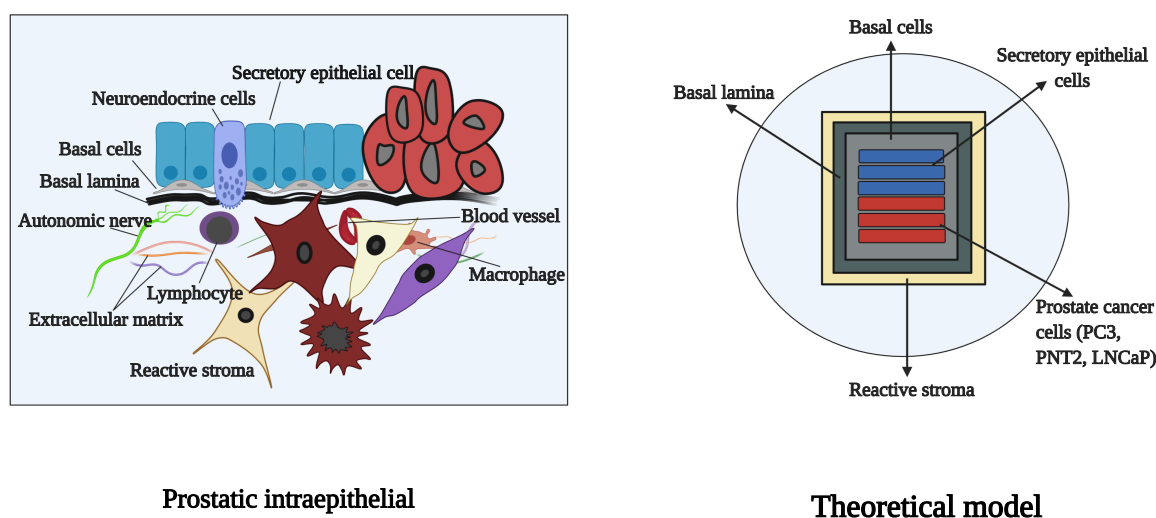
Theoretical model

Figure 1.1: The prostatic intraepithelial neoplasia that has been used to build a theoretical model for the prostate model.

Due to the complexity of the native microenvironment, a more basic model will initially be developed in order to validate the choice of materials and printing processes. As shown in Figure 1.2, this start-up model will encompass the printing of simple square-shaped constructs with high shape fidelity and cell viability. For that purpose, hydrogels encapsulated with prostate cancer cell lines alone will be printed and subsequently assessed for their ability to

19

support cellular viability, proliferation and function.
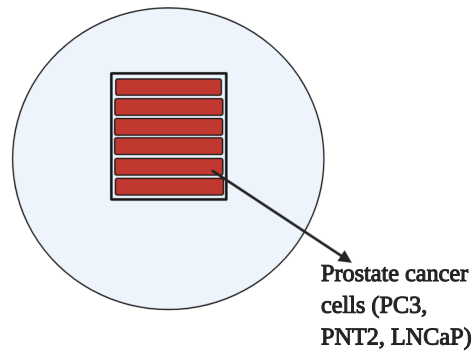
Figure 1.2: Prostate cancer start-up model used in this study.

Using the start-up model as a working platform, several objectives are set to reach the model overarching aim of this thesis as follows:

1. Design and production of 3D cell-laden constructs with well defined-geometry and dimensions.

2. To test the printability of the hydrogel (from Manchester BioGel) that can be used in building a prostate cancer model

3. To test the viability of the cells after encapsulating them on the hydrogel and printing them with a bio-printer.

4. To biologically assess the printed construct to evaluate the ability of using them as a cancer model.

5. To analyse of the printed constructs using FTIR imaging and developing of a new algorithm in MATLAB for enhanced spectra analysis

1.3   Thesis Structure

This thesis is divided into seven chapters added to this introductory chapter. Chapter 2 is the background and theory in which the most up to date literature on prostate cancer, tissue engineering and Fourier-Transform Infrared (FTIR) imaging technique is reviewed and discussed. The third chapter (chapter 3) is the methodology, where all the used experimental methods are discussed. The fourth chapter (chapter 4) is the first experimental chapter. The chapter discusses the mechanical properties of the different hydrogels used and the optimisation of the printing parameters for this project. The fifth chapter (chapter 5) has the start of the biological assessments of the printed constructs containing the hydrogel with cells encapsulated. These tests include live/dead viability test and a metabolic activity

test. The biological assessments continue in chapter 6 and it demonstrates the histological part, including Haematoxylin and Eosin (H&E) staining and phenotype expression using Immunohistochemistry (IHC). The seventh chapter (chapter 7) discusses the use of FTIR imaging on the analysis of the build constructs. The final chapter (chapter 8) contains the conclusion of the thesis and the suggested future work that can be done as a continuation of this study.

2

Background and Theory

2.1   Cancer

Cancer is a disease caused by abnormal cell division of newly formed cells in an uncontrolled way. It can be inherited through the carrier's germlines in which a faulty gene is inherited and the risk of the development of specific cancer is increasing. On the other hand, cancer can be caused by chemical, physical and biological agents in the environment called "sporadic" (Sonnenschein and Soto, 2008). The cause of cancer is the change in the character of the cells, which makes them not to respond or not to be affected by the normal controls such as growth capacity, which the normal cells have once the appropriate nutrients are provided to them. In addition, morphological and functional conditions in normal cells are appropriate to the organism's needs in a lifetime, while this is not happening with cancer cells (Burnet, 1957). It is estimated that globally about 18 million new cases of cancer were found in 2018, taking into account all cancers and all ages. Cancer is the second driving reason for death worldwide with 9.6 million estimated death in 2018, which means almost one in six death is because of cancer (WHO, 2018).

2.1.1   Theories of cancer origin

Different theories have been proposed to explain how cancer initiates in the human body. Some of the early proposed theories are: Hippocrates (humoral theory), which can be explained by the imbalance of the body hormones (body fluids), including blood, black bile, yellow pile and phlegm. Another theory is the lymph theory, which states that cancer is caused by lymph fermentation and degeneration (Sonnenschein and Soto, 2008). Blastema theory shows that cancer is caused by cells (that are not normal) instead of lymph. It was thought that these cells were creating budding element (blastemal) between normal tissues. With the development of science, each theory was disproved and new ones appeared. Different

theories were proposed in the 19th century explaining the cancer origin after the failure of the previous theories. The chronic irritation theory was presented by Rudolf Virchowstating, which suggested that cancer was caused by irritations in the tissue and trauma theory was given by Hugo Ribbert (Neubauer (1956) ; Sonnenschein and Soto (2008)). It states, as the name shows, cancer is caused by trauma, even though showing that injuries can cause cancer in animals was disproven. More recently, different scientists have shown that cancer is related to infections caused by protozoa, fungi, yeasts and bacteria. Trophoblast theory was proposed by John Beard after noticing that cancer cells have similar properties to placental cells. The theory shows that the trophoblastic cells in the placenta can turn into cancerous cells in case of any expression of them in the wrong place in the body and/or wrong time (Gurchot, 1975). Subsequent theories were established on the basis of genetic and epigenetic studies. The physio-mitotic theory states that cancer can develop under physiological conditions in systematically organised tissues. It involves the mitotic mechanisms of maturation and duplication. The limitation of this theory is the inability to explain the complicated nature of cancer at the cellular or tissue level (Soto and Sonnenschein (2004) ; Soto and Sonnenschein (2011). Two main theories were proposed to understand the forces that drive sporadic cancer and give a framework that helps to find new therapies: the Somatic Mutation Theory (SMT) and the Tissue Organization Field Theory (TOFT). The importance of these theories come from their ability to fit the biological data and bring forward new therapies (Soto and Sonnenschein, 2011). The somatic mutation theory has been the main theory in cancer during the 20th century. According to this theory, cancer takes place at the cellular and subcellular level due to multiple successive DNA mutations. The mutations take place in genes that are controlling the cell proliferation and cell cycle (Sonnenschein and Soto (2008) ;Soto and Sonnenschein (2004)). SMT also states that quiescence is the default state of cell proliferation (Soto and Sonnenschein, 2004). This means that the proliferation process has to be stimulated by "putative oncogenes, growth factors, or their receptors" (Sonnenschein and Soto, 2010) in order to occur. However, proliferation is known to be the default state of procaryotes, unicellular eucaryotes, and plant cells (Sonnenschein and Soto, 2010). Thus, to overcome the problems associated with the SMT, another theory was proposed; Tissue organization field theory. It states that proliferation is the default state of the cells (Sonnenschein and Soto (2008) ; Sonnenschein and Soto (2010) ; Soto and Sonnenschein (2004). However, cells will not proliferate if they are isolated unless they are exposed to a mitogen (Soto and Sonnenschein, 2011). The TOFT also states that cancer originates from changes in tissue architecture rather than mutations in genes (Sonnenschein and Soto (2008); Sonnenschein and Soto (2010); Soto and Sonnenschein (2004); Soto and Sonnenschein (2011)). This means that if any mutation is found in the DNA sequencing, then it should be random and not in all cancerous cells (Soto and Sonnenschein, 2011). Other theories that were proposed are extragenetic somatic

heredity in which a protooncogenic defect causes cancer, the modified classic theory of cancer, where cancer is caused by the DNA alteration that leads to changes in the structure of the proteins. Also, the aneuploidy and pananeuploidy theories in which cancer caused by the aneuploidy cells and the cancer stem cell theory where genetic alterations found in stem cells caused cancer. Additionally, the multistage manner of cancer development in which different mutation in the same population lead to the initiation of cancer (Paduch, 2015). Despite having common features, none of the proposed theories so far has been able to explain and answer every single point related to cancer initiation and progression. Therefore, the need to develop new models with greater physiological relevance for the in vitro study of cancer-associated mechanisms and therapy testing is more pressing than ever (Paduch, 2015).

2.2 Prostate Cancer

2.2.1 The prostate gland

The prostate gland is considered to be the largest male accessory in the reproductive system. It is a walnut-size and shape with about 3 cm long and 4 cm wide and 2 cm depth (Moore et al., 2014). It is located underneath the bladder and surrounds the upper part of the urethra (a small tube that transmits urine from the bladder to the penis) as shown in Figure 2.1. It contains different glandular and non-glandular regions surrounded by a fibrous capsule (Amin and Khalid (2011) ; Lee et al. (2011) ;Moore et al. (2014)). The glandular region is almost two-thirds of the prostate and one-third is fibromuscular (Moore et al., 2014).
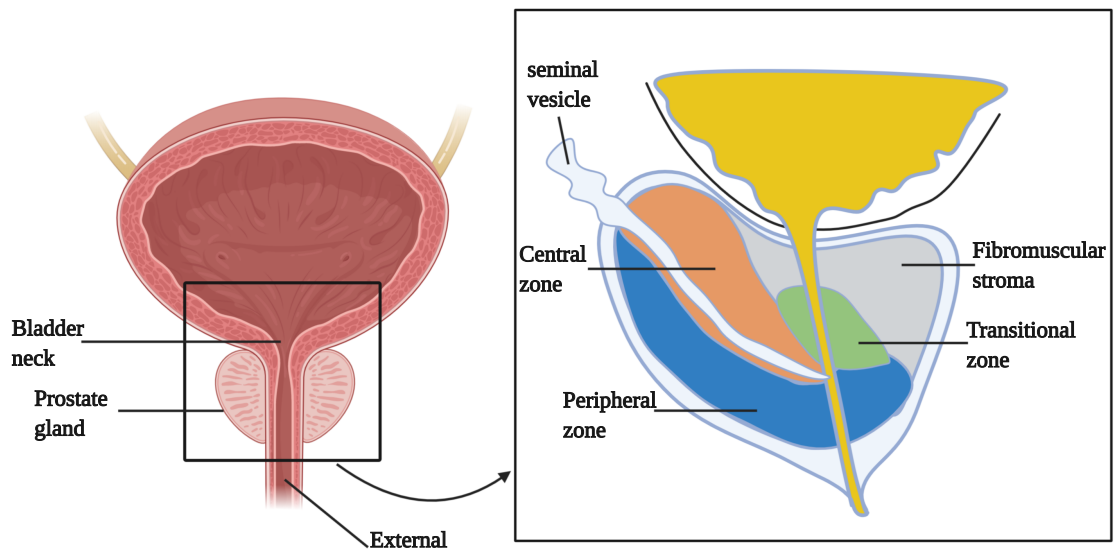
Figure 2.1: The location of the prostate gland underneath the bladder and the zonal anatomy of the prostate showing the fibromuscular stroma, central zone, peripheral zone, seminal vesicle, and transition zone. Adapted from (McLaughlin et al., 2005).

The prostate is divided into four different zones shown in Figure 2.1; the Peripheral Zone (PZ), the Central Zone (CZ), the Transitional Zone (TZ) and the periurethral zone or Fibromuscular stroma. Each zone has different histological and architectural features. The peripheral zone makes up 70% of the prostate glandular part. The wedge-shaped central zone is surrounded by the peripheral zone in its top part. It makes up to 25% of the prostate glandular part and surrounds the ejaculatory ducts. Studies show that this zone is quite resistant to some diseases such as carcinoma. The transitional zone consists of glandular tissue in a fibromuscular constituent of a periprostatic sphincter. Clinically, this zone is important since it grows with age and is a common site where prostatic benign hyperplasia starts. The last zone is the Periurethral zone and it is the only non-glandular zone among the four zones. It consists of small ducts and non-completely developed acini, which are spread along the proximal urethral segment. Fibromuscular stroma covers the front surface of the prostate and hides the surface of three glandular regions)Amin and Khalid (2011) ;McLaughlin et al. (2005)). In addition to the four zones, the anterior fibromuscular stroma is found within the prostate. It is a fibromuscular tissue located adjacent to both the bladder muscle and the external sphincter (McLaughlin et al., 2005). The main function of the prostate is to produce alkaline, thin milky fluid rich in enzymes and prostaglandins. This fluid, together with secretions produced by the testes, seminal glands, prostate, and bulbourethral glands makes up the semen (Moore et al., 2014).

2.2.1.1 Carcinoma of Prostate

Prostate cancer is the second most common cancer among men and it is the sixth cancer-causing death worldwide. In 2018, over 1.2 million new cases were estimated with more than 300,000 deaths (Culp et al. (2020);Schlag et al. (2013)). Different cases appear with this type of cancer; some men have the malignancy growing slowly with no progression resulting in no serious illness, while others progress with ageing and become aggressive forms of cancer (Schlag et al., 2013). Studies show that prostate cancer increases with age, with high incidence in men above 65 years, totalling 85% of the cases. However, men under 50 years have a low overall rate with less than 0.1% of the cases (Pienta and Esper, 1993). Other risk factors include race, environmental and genetic factors. Environmental factors such as smoking, alcohol consumption, ionizing radiation, ultraviolet light, low physical activity and dietary factors are found to be associated with the increased risk of prostate cancer. In addition, men with affected relatives are more likely to be at high risk of prostate cancer (Culp et al., 2020).

2.3 The Effect of Tumour Microenvironment in the Behaviour of Cancer Cells

2.3.0.1 Reactive Stroma in Carcinogenesis and cancer-associated fibroblasts

Epithelial and stromal compartments within a normal prostate tissue coexist in harmony. The epithelium consists of secretive epithelial cells with junctional composite, basal cells layer and neuroendocrine cells, each connected to the basal lamina. Opposite to the basal lamina, the fibromuscular stroma is found (Barron and Rowley, 2012). Different cell types are found in the stromal microenvironment such as fibroblasts, Smooth Muscle Cells (SMC), immune and inflammatory cells, lipocytes and endothelial cells (Beacham and Cukierman, 2005) (Figure 2.2).
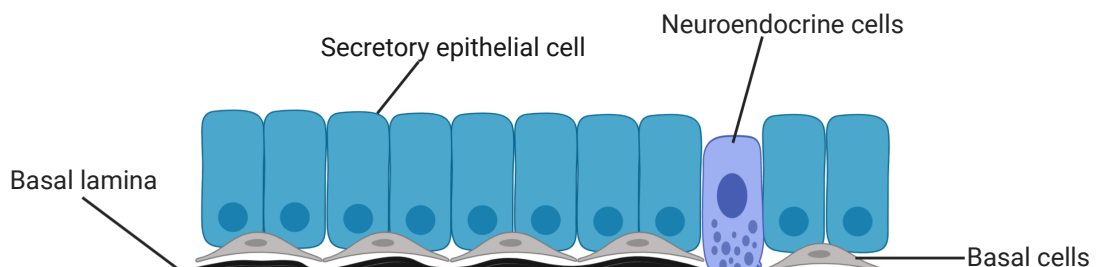
Figure 2.2: Cellular components of the human prostate gland. Adapted from (Barron and Rowley, 2012).

Comparing the normal stromal microenvironment with the one in human prostate cancer, it is possible to visualise that the stromal microenvironment in prostate cancer has the same features as in a wound repair stroma. These features include elevated stromal cell proliferation, altered expression of matrix components, neovascularisation, and expression of several common stromal markers, which are similar to the inflammatory conditions changes of the prostate (Barron and Rowley (2012); Rowley (1999)). The reactive stroma consists of myofibroblasts and fibroblasts, which produces extracellular matrix components rich in collagen fibres and are found between the acini. It appears that the reactive stroma is starting in Prostatic Intraepithelial Neoplasia (PIN) and grows as the cancer progress until the effective displacement of normal fibromuscular stroma Barron and Rowley (2012); San Francisco et al. (2004); Tuxhorn et al. (2002))(Figure 2.3). The reactive stroma causes prostate cancer to be androgen-sensitive and changes the prostate epithelial cell's phenotype to a tumorigenic phenotype (Morrissey and Vessella, 2007). The term "Carcinoma-Associated Fibroblasts" (CAFs) is used to describe prostatic tumour stromal cells. The appearance of CAFs is associated with progressive loss of smooth muscle cells (Cunha et al., 2003).
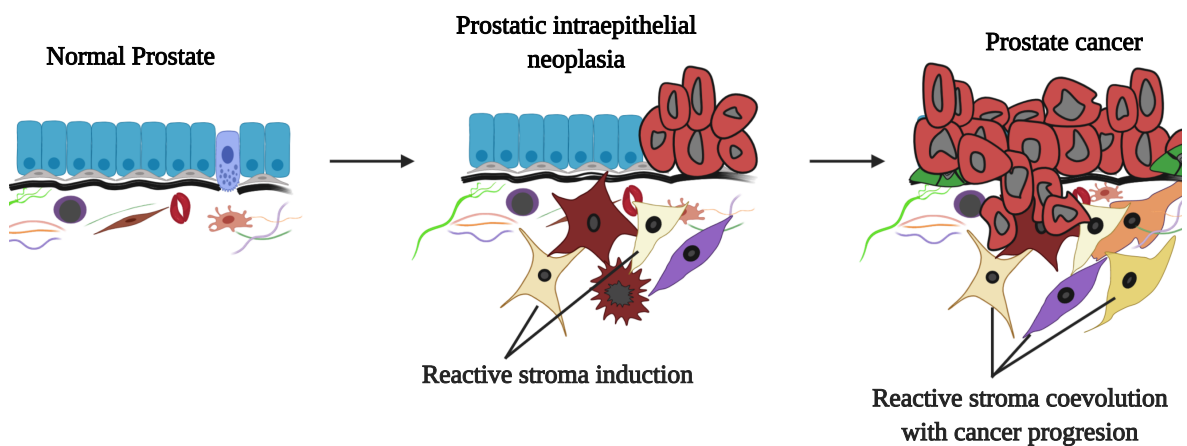
Figure 2.3: Normal Prostate gland and reactive stroma formation in cancer. Adapted from (Barron and Rowley, 2012).

2.3.0.2 Role of CAF in Cancer Initiation & Progression

Studies show that in prostate cancer, cells proliferation and prostatic epithelial cells initiation were found to be affected by CAFs. However, this effect was not seen with the normal fibroblasts. Additionally, at the metastatic site, myofibroblasts encourage the cancer cells proliferation, which looks the same as the tumour promoting behaviour in the main tumour

(Barron and Rowley, 2012). Additional studies show that the combination of non-tumorigenic prostate epithelial cells (from Benign Prostatic Hyperplasia (BPH)) with cancer-derived CAFs cause transformation of the epithelial cells and promote the formation of cancer (Barron and Rowley, 2012). Other studies have shown that in the tumour microenvironment, TGF-b signalling in stroma is lost and Wnt3a signalling is stimulated. This inductive nature causes the expression of the genes, which are regulated by TGF-b such as FGF2, CTGF, and SDF1 to be changed and so the gene expression of CAFs is different from the normal fibroblasts (Barron and Rowley (2012); Eriksson et al. (2006)). CAFs were found to simulate the progression of prostate tumour of initiated epithelial cells in both; in vivo tissue recombination and in vitro co-culture. The histology of the epithelial population is altered and its growth enhanced by CAFs. However, the growth of normal human prostatic epithelial cells was not affected by CAFs (Olumi et al., 1999). Barclay, Woodruff, Hall, & Cramer have used the tissue recombination method to compare stromal cells from the normal peripheral zone, benign prostatic hyperplasia (BPH-S) and cancer to induce the growth of a human prostatic epithelial cell line (BPH-1) in vivo. No visible grafts were found with stromal cells alone, BPH-1 epithelial cells alone and with the combination of stromal cells from the normal peripheral zone with BPH-1 cells. On the other hand, a well-organized and sharp small graft was seen when combining BPH-S with BPH-1, while combining cancer stromal cells with BPH-1 cells produced a graft that is very disorganized (Barclay et al., 2005).

2.3.1 Reactive Stroma in Cancer Diagnosis & Prognostication

According to the study performed by Davor Tomas and Bozo Kruslin, the reactive stroma can be used for prostate cancer diagnosis. The myofibroblasts and fibroblasts, which are the reactive stroma components, can be shown using Mallory trichrome method (Tomas and Krušlin, 2004). The Mallory trichrome method is a staining method that combines three different stains (acid fuchsine followed by a solution containing phosphotungstic PTA, orange G and aniline blue) and originates from the modification of Masson's trichrome stain. The study compared the adjacent peritumoral tissue and reactive stroma in prostatic hyperplasia (Stain (2012); Tomas and Krušlin (2004)). Reactive stroma was found to show an increase in the expression of vimentin protein and a decrease in the expression of desmin protein (Tomas and Krušlin, 2004). Other studies showed that the proliferation of cancer cells at the metastatic sites is promoted by the activated fibroblasts. A variant of CAFs might be presented by these metastasis-associated fibroblasts (Kalluri and Zeisberg, 2006). Additional studies show that the elements of the reactive stroma can be used as prognostic indicators of prostate cancer. The reactive stroma volume can be used as an important factor for the prediction of disease-free survival (Ayala et al., 2003). In addition, androgen receptor staining was found to have an inversely proportional relationship with Gleason score and metastasis,

and directly proportional relationship with the cancer-specific survival, staining in stromal smooth muscle cells and the density of smooth muscle cells in the tumour stroma (Wikström et al., 2009). Also, the expression of the marker of mesenchymal stem cells, CD90, is found to be higher in prostate cancer stroma compared to the normal tissue (Zhao and Peehl, 2009). Moreover, the response to chemotherapy and radiotherapy is affected by the presence of CAFs in cancerous tissue (Östman and Augsten, 2009).

2.3.2 Histopathological Assessment of Normal and Reactive Stroma

The most common method used in histopathology to distinguish between the normal and reactive stroma is the trichrome stain, such as Masson's and Mallory's trichrome staining (Tomas and Krušlin (2004); Tuxhorn et al. (2002)). Myofibroblasts and fibroblasts are the main components of the reactive stroma and were shown by Mallory trichrome method and confirmed by immunohistochemistry (Tomas and Krušlin, 2004). Immunohistochemistry technique used the interactions between the target antigens with specific antibodies to identify the reactive stroma components. The classification of fibroblast, myofibroblast and smooth muscle cell phenotypes is done according to the immunostaining of cells' differentiation markers. For example, the fibroblast phenotype can be indicated using vimentin expression when no smooth muscle markers are added. However, the myofibroblast phenotype is indicated by the co-expression of vimentin and sm α-actin with no calponin expression (Tuxhorn et al., 2002).

2.4 Diagnosis of prostate cancer

2.4.1 Presentation and Screening

Prostate carcinoma causes the appearance of metastases in different parts of the body, such as lymph nodes, bones, lung, and liver (Bubendorf et al., 2000). Most prostate carcinoma patients are diagnosed without the appearance of regular symptoms such as pain in the lower back, hematuria and urination difficulties. Screening is a test that helps to find out whether the person has cancer or not, especially for people who have no regular symptoms instead of waiting for the symptoms to appear. Early detection of cancer can help in extending life by treating it when it is still small and not yet spread. The prostate gland produces a protein called Prostate Specific Antigen (PSA) and the level of the antigen in the body is checked for prostate cancer. PSA can be found in the blood unbonded and called free PSA or binding to "serum protease inhibitor α1-antichymotrypsin (ACT)" and called complex PSA. Total PSA has been used as an indicator for the presence of cancer in the prostate gland. Most of the asymptomatic patients found to have irregular prostate specific antigen (PSA) levels (Bubendorf et al. (2000); Rong et al. (2019)). Healthy men have levels in the range of 2.5

— 4 ng/ mL in the blood. After the application of the PSA test, it has been found that the detected cases, which have prostate cancer in an advanced stage have become less with time (Berger et al. (2007); Bryant and Hamdy (2008); Michalski et al. (2016).

Several limitations are found on using the PSA test, such as unnecessary biopsies in cases where the risk of cancer is low. Additionally, The PSA is not only expressed by the cancer cells but also by the prostate that having other diseases than cancer, such as benign prostatic hyperplasia and prostatitis. Also, the patients' life quality is affected by the over-treatment and it is not possible to indicate the stage of cancer and whether it is slow or fast-growing using PSA test (Abrahamsson and Tinzl (2008); Miller et al. (2007) ; Rong et al. (2019); UK National Screening Committee (2015)). As per the UK National Screening Committee, the PSA test is poor and a test with better specificity and sensitivity is needed (UK National Screening Committee, 2015). In the United States, however the PSA test is one of the screening tests used for prostate cancer detection (Loeb and Catalona, 2007). The free PSA-to-total PSA ratio is known as per cent free PSA, Which has been used to help avoid taking unneeded biopsies in men with a high level of PSA. Nevertheless, more than half of those men are still undergoing needless biopsy test (Epstein et al., 2005). According to the ESMO Clinical Practice Guidelines for diagnosis, treatment and follow-up, the biopsy should not be taken if only the level of PSA is found to be higher than the normal. Other tests such as complex and %free PSA values, Digital Rectal Exam (DRE) test, ethnicity, age and history of the previous biopsy, should be taken into account before the decision of taking biopsy is made (Parker et al., 2015). Digital Rectal Exam (DRE) is a test where the doctor feels for any bumps or hard areas in the rectum using his fingers. This is not a precise test due to the lack of sensitivity and the results vary from one examiner to another regardless of the experience. It cannot be used to detect cancer in its early stage, so this test is not recommended to be done in routine cancer detection (Crawford et al. (1996); Michalski et al. (2016); Miller et al. (2007); Okotie et al. (2007)).

2.4.1.1 Histological Grading & Management

The Gleason grading system is a method used to evaluate the aggressiveness of prostate cancer. It was created in 1966 by Dr Donald F Gleason and members of the Veterans Administration Cooperative Urological Research Group. This system is based on the examination of the patient's biopsy under the microscope and the pattern of the organisation of the cells. Normal cells are highly organized, while cancer cells are disorganised. Pathologists used five grade patterns where grade 1 shows organised cells close to the normal cells and less aggressive cancer, while grade 5 shows highly disorganised cells and it is the most aggressive cancer, as shown in Figure 2.4.
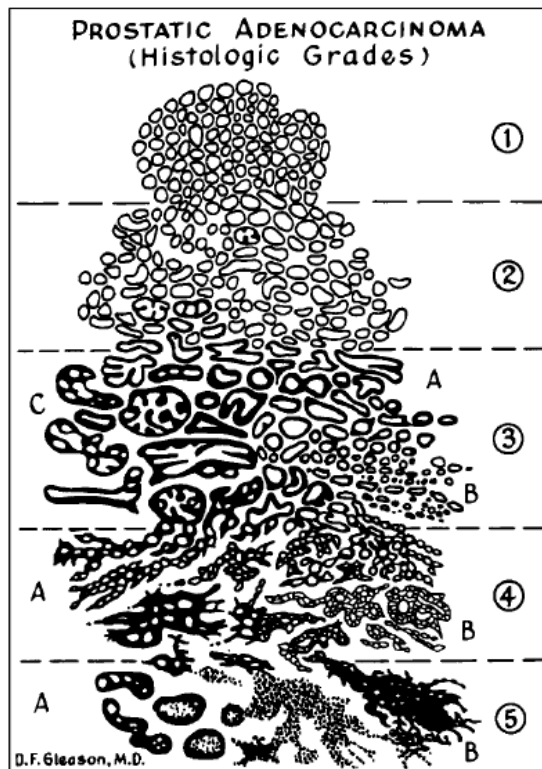
Figure 2.4: Gleason grades system showing the different grades from 1 — 5 in which 1 less aggressive and close to normal and 5 is highly aggressive cancer with no differentiation of the cells (Humphrey, 2004).

The grades are used to generate a Gleason score consisting of the sum of the grade of the two most common tissue patterns (Epstein et al. (2005); Humphrey (2004). Histopathological endpoints, such as tumour size, positive surgical margins, and pathological stage (including the risk of extraprostatic extension and metastasis) are directly related to the increase of Gleason grade. Gleason grade has to be combined with other factors such as serum total PSA, % free PSA, local clinical T stage (shown in table 2.1), and the amount of tumour in needle biopsy in order to get an accurate description of cancer in the patient (Epstein et al., 2005). Gleason grade shows a correlation between the aggressiveness of cancer, its volume and extent. Low Gleason grade < 5 is found to have the lowest aggressive behaviour, while high grades $8 - 10$ usually present high aggressive behaviour. The aggressiveness of the intermediate grades $5 - 7$ cannot be predicted and unfortunately, almost 76% of the tumours are in the intermediate grades. Thus it is difficult to predict how aggressive the cancer is using histology alone (Aihara M (1994); Isaacs (1997). Putting Gleason score into an application for several years shows the deficiencies that this system has. Gleason score 7 is classified as one score without differentiating between $3 + 4$ and $4 + 3$ although $4 + 3$ is a diagnosis for much worse than $3 + 4$. Also, the score 8 is combined with $9 - 10$ making them one high

grade. Additionally, Gleason scores range from 2 — 10; however, the lowest score assigned is 6, giving patients the false assumption that they are in the middle of the scale and they are in a very serious condition in which the treatment is needed (Epstein (2017); Epstein et al. (2016); Ham et al. (2017) ; Pierorazio et al. (2013)). A new grading system has been proposed by Jonathan Epstein and his colleagues from data gathered in Hopkins Hospital. The new system composed of five grades in which grade 1 is equivalent to Gleason score 6, grade 2 is equivalent to Gleason score $3 + 4 = 7$, grade 3 is equivalent to Gleason score $4 + 3 = 7$, grade 4 is equivalent to Gleason score 8 and grade 5 is equivalent to Gleason score 9 — 10. The new grading system is simpler and more accurate as it solves the problems associated with the Gleason grading system and has the potentials of reducing the fear, confusion and overtreatment of the low graded cases is high (Magi-galluzzi et al. (2015); Rong et al. (2019)). TNM classification (tumour size (T), number of lymph nodes involved (N), and metastasis (M)) is a management strategy used to stage the tumour and determine how far cancer has spread (Onoda et al. (2020); Parker et al. (2015)). The categories of Anaplastic Thyroid Cancer (ATC) are classified using this system. This classification is shown in Table 2.1.

Table 2.1: TNM Classification of prostate cancer. Adapted from (Parker et al., 2015).

TNM Classification	
stage	**definition**
T1	Tumour is very small. It cannot be seen on scans and is hard to find during the prostate examination. It might be found by needle biopsy, which has been done due to the increase in the PSA level.
T2	tumours are totally inside the prostate gland
	T2a : Only half of one lobe has a tumour
	T2b : More than half of one of the lobes has a tumour
	T2c : Both lobs have the tumour
3***T3**	Tumours have spread into the prostate gland capsule without spreading in the other organs.
	T3a : The tumour has spread into the prostate gland capsule
	T3b : The tumour reached the seminal vesicles
T4	Tumours have spread to the nearby organs such as the rectum bladder, muscles or the sides of the pelvic cavity
N	**Lymph nodes**
NX	It is not possible to check the lymph nodes
N0	No cancer close to the prostate in the lymph nodes.
N1	Cancer is present in lymph nodes
M	**metastases (cancer spread)**
M0	Cancer has not spread outside the pelvis
M1	M1a : There is cancer outside the pelvis
	M1b : Cancer has reached the bone
	M1c : Cancer spread to other places

Assessment of the general health and co-morbidities of the patient should be done. The general health of some patients might be poor and they are not suitable for the treatment. Thus the staging investigations are not required for them (Parker et al., 2015).

2.5 Prostate Cancer Models

2.5.1 Animal models

Different models are used for prostate cancer studies, including biology of the prostate or to test and develop cancer drugs ((Ellem et al., 2014). Different factors affect the choice of the animal, which can be used in cancer studies. Origin of the tumour and its latency time along

with the cost of those animals, are the most important factors. Dogs (Ellem et al. (2014); Ittmann et al. (2013); LeRoy and Northrup (2009)) and primates (Ellem et al., 2014) are the first animals used for prostate cancer studies. It has been found that the prostate gland has the same origin and structure (anatomic and micro anatomic) in both humans and dogs. Prostate cancer can be developed spontaneously, which is the case of high-grade tumours. Additionally, bone metastases are developed in dogs (similar to humans), which gives a great opportunity for studying the progression of cancer and testing therapies (Navone et al., 1999). However, the differentiation of the adenocarcinoma was poor in many studies and the carcinoma found to be indistinguishable. Dogs can still be used as models to study prostate cancer as they share the same environment with humans (Ittmann et al., 2013). In general, the use of both dogs and primates as models to study Prostate Cancer (PCa) is very limited due to the high costs and long latency time (Ellem et al. (2014); LeRoy and Northrup (2009). Rodents models have been developed experimentally to study the PCa mechanisms. Genetically engineered mouse models (GEM) are created to mimic the human PCa allowing the study of PCa initiation and progression mechanisms as well as testing and developing new therapies. GEM is created by targeted protein overexpression, loss of function mutations, compound transgenic and knock-out, and by targeted somatic mutations (Ittmann et al. (2013); Parisotto and Metzger (2013)). The tumour progression with a time scale from initiation to the invasivity of the disease has been studied through these models. On the other hand, the biological differences between those models and human PCa affect the phenotypes of the GEM models. In addition, GEM models have high costs and long latency time compared to the xenografts models (Ellem et al. (2014); Ittmann et al. (2013)). Xenograft models also use mice but as host for cancer cells rather than modifying them genetically. The cells are usually implanted in a nude or severe immunodeficient mouse. The xenografts are orthotopic models, tissue recombination models, models made from human prostate cancer tissues which are taken as xenografts and models made from mouse prostate cancer xenografts (mouse prostate cancer cell lines). Xenografts models are used in the evaluation of cancer biology and in testing and developing drugs as it is considered being fast and low cost. However, the cancer cells implanted in the host are derived from aggressive lesions that give no chance of studying the biology of less aggressive cancer. In addition, the tumour microenvironment is affected by the subcutaneous location of the cells in the host (or even in the capsule). Also, it can change if the immune system is abnormal (Ittmann et al., 2013). Rats are also used as models to study the PCa. Lobund-Wistar rats are found to develop PCa spontaneously, but bone metastasis has not been seen. These rates can be treated chemically with N-methyl-N-nitrosourea (MNU) or by adding hormones. After treatment, the development of PCa was fast and metastases were seen in the lung and lymph nodes, but not the bones. The effect of the chemicals and nutrition on cancer was studied through these models. The large size of the prostate in the rats compared to the mouse is one

of the advantages of using rats as a model to study PCa. However, they share the limitation of non-human origin causing great limitation on the applicability of the studies results on human PCa (Azeem et al. (2017); Ellem et al. (2014); Ittmann et al. (2013); Noble (1977); Pollard (1973); Pollard and Luckert (1986); Shain et al. (1975))

2.5.2 *In-vitro* Models

2.5.2.1 2D models

In 2D models, cells are grown in cell culture plates, dishes, flasks or tubes. This is used widely due to the simple cell culturing system. 2D models of prostate cancer are found to have advantages in getting reproducible results due to the consist response of prostate cancer cell lines. The availability and simplicity of the prostate cancer cell lines is another positive factor for these 2D models (Ellem et al., 2014). One of the greatest limitations of the 2D cell culturing is the absence of the microenvironment, leading to the lack of the cellular interactions of cancer cells with the cells surrounding them, such as fibroblasts, myofibroblasts, blood vessels, nerves, immune cells and extracellular matrix. In addition, the receptor expression signalling is absent so the data interpretation in these models is limited. Another difference is that the cells proliferation rate in vivo is much slower than the 2D culturing, which might be due to high serum, abnormal environment (flat hard surface) and the absence of any proliferation signals from the stromal components (Ellem et al. (2014); Ittmann et al. (2013)).

2.5.2.2 Co-culture systems

Scientists keep looking for systems were the tumour microenvironment or at least part of it, can be more accurately replicated and provided to cancer cells. This will potentially give a better idea of the influence that different cells surrounding the tumour have on the initiation and progression of the disease. On this basis, 2D co-culture (also called 2.5 D culture models) were created. In these models, the prostate cancer cells are co-cultured with stromal cells in either monolayer or double layers (Azeem et al. (2017); Ellem et al. (2014)). A study done by Ashlee K. Clark *et el*. reports the development of co-culture systems containing different cells such as stromal fibroblasts, stromal ECM and benign epithelium. The authors examined the mechanism by which epithelial cells transformed into turmeric cells in the presence of CAFs and indicated the difference in the phenotype expression when different types of cells are present. Additionally, they examined the influence of the stroma on epithelial transformation and tumourigenesis with CAFs, but not Normal Prostate Fibroblast NPFs, inducing discrete malignant changes in benign epithelial cells. The research of this study compared fibroblasts in different stages of cancer and showed that CAFs can change the proteins expressed by BPH-1 in different stages of cancer (Clark et al., 2013).

2.5.2.3   3D models

The lack of structural complexity and functional organization in 2D models has led to an increased research for alternative systems capable of mimicking the native PCa microenvironment. For that purpose, different 3D models have been proposed to overcome the limitations of the 2D models such as spheroids, organoids, purified ECM and hanging drops. Spheroids are multicellular aggregates growing in low adhesion conditions. Different studies took place where prostate cancer cell lines were used in spheroids models. A study performed by Takagi et al shows great differences between 2D models and spheroids. LNCaP cells were used and it was found the phenotype expression has changed due to the effect of the microenvironment, which is missing in 2D models, which gives this model the strength to be taken further for therapies testing (Takagi et al., 2007). Several studies were found culturing DU145 prostate cancer cell line as spheroids such as (Connor et al. (1997); O'Connor (1999); Wang et al. (2011)). The use of spheroids for prostate cancer shows a slower growth rate with stronger staining for cytoskeletal proteins (O'Connor, 1999). Alternatively, organoids, which are 3D structures derived from stem cells that develop to form a specific organ cell type with its genetic stability, can also be used as 3D systems. Drost *et al.* has designed a protocol to culture organoids for healthy prostate cells from mouse and human along with luminal and basal cells. Moreover, prostate cancer organoids were prepared to mimic the tumour histology. Successful organoids of prostate cancer were also developed by Gao *et al.* in which different conditions of genes mutations, fusions and loss with proteins overexpression were recapitulated (Gao et al., 2014). A purified ECM gel is another model used for the studies of prostate cancer. In this model, stem cells like are cultured in a purified ECM (e.g. matrigel and collagen) so that some of the in vivo processes are supported, including the cell-cell and cell-ECM interactions, phenotype expression and cell polarity. The differentiation of different types of cells was seen in these models, such as normal/benign prostate epithelial cells that differentiate into glandular epithelial cells and tumour cells that show disorganised and defective differentiation (Ellem et al., 2014). Hanging drop is a 3D model composed of cells placement in drops of culture media hanging in a plate. The assembly of these monodispersed cells uses gravity enforced microspheres. This found to be working well for different types of cells and used to assist the resistance of the chemotherapies in cancer models in addition to the assessment and analysis of the functionality in these models (Ellem et al. (2014); Kelm and Fussenegger (2004)). These 3D models were used to overcome the limitations found in 2D models. Each model has been used to mimic prostate cancer microenvironment by adding complexity in order to get a better image of tumour initiation and progression. The main limitations of all these models are the absence of the basic heterogeneity and the tertiary structure of the prostate tumours and the high variability and lack of reproducibility (Ellem

et al., 2014) Ellem *et al.* show a graph comparing the different layers that each of the models looks at (shown in Figure 2.5). The complexity of the models increase but still not has reached the same in the real prostate.
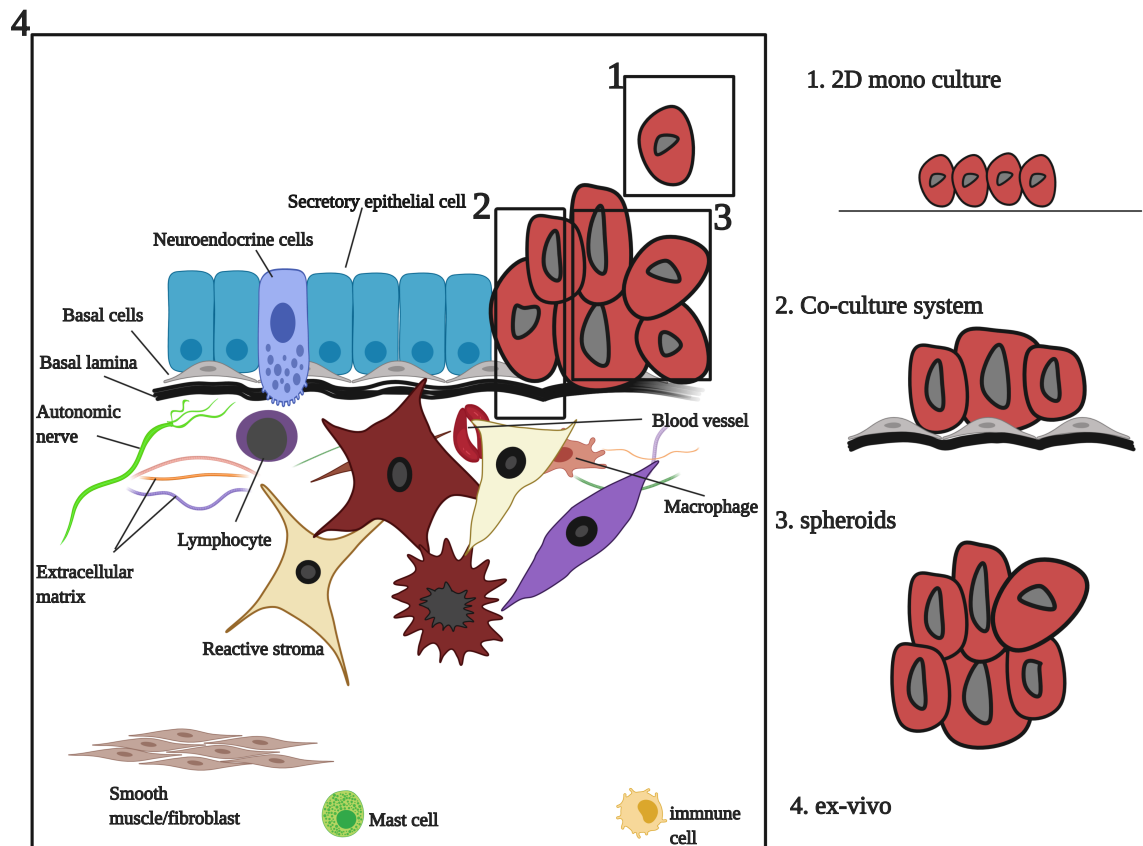
Figure 2.5: Comparison of the different layers taken in the current in prostate cancer models. 1. is for 2D monoculture where only cancer cells cultured in a plate, 2 is for the co-culture system in which cancer cells are cultured with other types of cells such as basal cells. 3 is the spheroids in which cells aggregates cultured in a sphere and 4 is the *ex-vivo* models containing the different layers and the complexity of the model even though it is limited as explained above. The bioengineering models are designed with the desire to reach the complexity of the *ex-vivo*. Although it has not been reached yet, the research on them is still going on. Adapted from (Ellem et al., 2014).

2.6 Tissue Engineering

The limitations of the current medical therapies (*i.e.* shortage of donors, biocompatible tissues, donor site morbidity, etc.) have promoted the emergence of Tissue Engineering as one of the most promising strategies to regenerate damaged tissues and/or organs (Meyer et al., 2009). TE can be defined as an interdisciplinary field of research where biological and physical sciences are combined to develop alternative medical therapies and restore the

essential repair mechanisms of the body (Naren and Yun, 2016). Depending on the tissue and size of the defect, different strategies can be adopted. However, the most common and successful strategy requires the combination of living cells with a scaffold or matrix (Fedorovich et al., 2008). In cancer research, advanced tissue engineering is used to design 3D models (*in vitro* or *in vivo*) with scaffold or matrix-based that mimics the tumour environment and used in the study of the tumour's pathogenesis (Dietmar W. Hutmacher, 2010). *In vivo* models were designed using animals such as mice, which were explained previously in the animal models used for prostate cancer, such as genetically engineered mice One of the recent studies that work on this type of tissue engineering is the study done by Leibold *et al.*. The researches have used ElectroPoration-based Genetically Engineered Mouse Models (EPO-GEMM) approach instead of the traditional germline approach. This method reduce the cose and time compared to the traditional one and it helps producing synchronized cohorts of mice that have bigger tumours in less time (Leibold et al., 2020). Tissue engineering is one of the popular methods in medical therapies that are used in order to overcome the drawbacks that are faced in artificial organs and organ transplantation. Artificial organs and organ transplantation were used when the organs are affected by severe disease or even lost because of cancer and in congenital abnormalities. Challenges appearing with those methods are the need for better biocompatibility and bio-functionality of the artificial organs and the shortage of organs which are donated and possible immune rejection in organ transplantation (Ikada, 2006). Despite still being in its infancy, TE has already demonstrated great potential in many medical areas through the development of novel therapies and products. The range of applications continues to broaden and exciting breakthroughs are being made in other areas such as cancer research and dementia (Ozbolat and Hospodiuk, 2016). For TE to be successful, future research will need to comprise the development of new biomaterials, better tissue analogues for the study of complex cellular interactions, advanced imaging methods for 3D constructs and advanced manufacturing techniques.

2.6.1 Tissue engineering components

Building a 3D tissue-engineered construct that can be used to regenerate the damaged tissue or design in vitro model relies on five key factors; cells, scaffold/matrix, biomaterials bioreactors and bioactive or growth factors (Chu et al. (2002); Nair et al. (2009); Norotte et al. (2009)). Cell Adhesion, proliferation and differentiation are affected by the physical and chemical properties of these factors (Chung and Burdick (2008); Oliveira et al. (2015)). For the purpose of this project, three main factors will be discussed; cells, scaffold/matrix and biomaterials.

2.6.1.1 Cells

Cells are considered the basic life units and are enclosed within a membrane that contains a concentrated aqueous chemical solution. They have the ability to divide, proliferate and differentiate into different types of tissues depending on specific biomechanical signalling (Bruce et al., 2013). Cells can be obtained from three different sources; from the patient (autologous), from another donor (allogeneic) or from animals (xenogeneic) (Pereira, 2013). Although autologous activity continues to be high after cell harvesting, there are still some limitations associated with this source, such as the low amount of cells that can be harvested. This can become an even higher limitation with increasing patient's age or associated diseases. Allogenic and xenogeneic are heterogeneous cells and the immune response needs to be suppressed partially or completely in order for the body to accept them. On the other side, in 3D models prostate cancer cell lines are used. With over 200 cell lines and sublines of prostate cancer that has been used in prostate cancer research,PC3, PNT2 and LNCaP cell lines are three of the most common cell lines used in 3D models.

2.6.1.2 Scaffold/matrix

Because most of the cell lines used in TE are anchorage-dependent, an artificial biomechanical templated (Scaffold) is required to support the initial cell adhesion and proliferation. Additionally, the scaffold or matrix must be bioactive and provide the required biomechanical and chemical signalling for the cells to differentiate and deposit their own Extracellular Matrix (ECM). In fact, the design and production of an optimal scaffold is a very complex process involving multiple factors and their mutability with time. Figure 2.6 illustrates the most important requirements for a TE scaffold (Billiet et al., 2012).
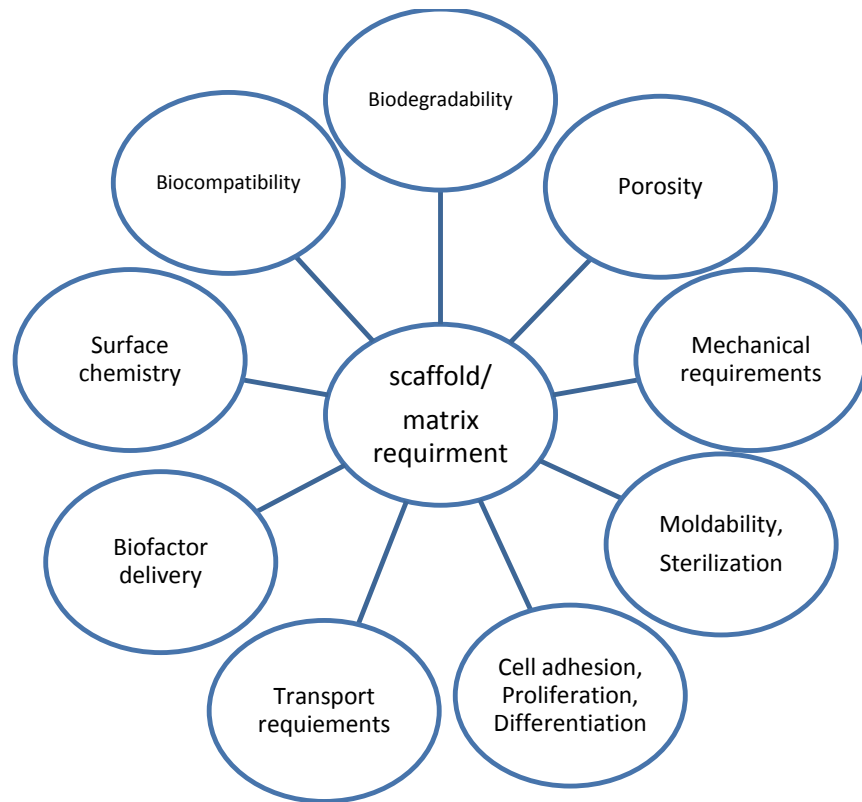
Figure 2.6: The requirements needed to build an ideal Scaffolds/matrix as described in (Billiet et al., 2012)

The above-mentioned scaffold's requirements can be divided into biological and mechanical depending on their nature:

Biological requirements: The scaffold/matrix should be biocompatible, avoiding any adverse cytotoxic effect on the cells/tissues. Also, the scaffold should be biodegradable with known degradation rate and time. The degradation rate and time can be controlled using enzymatic or non-enzymatic hydrolytic processes and it will be controlled according to the required properties for printed tissue type (Billiet et al. (2012); Chung and Burdick (2008); Ikada (2006); Lee and Mooney (2001a); Oliveira et al. (2015)).

Mechanical requirements: High porosity and proper pore size are required for vascularization and cell adhesion/proliferation. In addition, 100% interconnectivity of the pores will make ideal diffusion of the nutrient/waste. Adequate mechanical properties to match those of the native tissue. Proper surface topography to enable cell adhesion, proliferation and differentiation. Precise external geometry to enable a good biomechanical coupling with the native tissue. Easy to sterilize and fabricate (Billiet et al. (2012); Kim and Mooney (1998); Meyer et al. (2009); Wu et al. (2010)).

These requirements are extremely important at different levels of the TE process in order

to 1) Enhance the cell viability and allow the integration with native tissue; 2) Enhance the biomechanical coupling between implant and tissue at the site of implantation; 3) Promote a match between the degradation rate of the implant and regeneration of the tissue (Billiet et al. (2014); Chen et al. (2010); Chung and Burdick (2008); Freyman et al. (2001)).

2.6.1.3 Biomaterials

A biomaterial is a substance which can be connected to the biological system so it can be used for the evaluation, treatment and replacement of the body tissues or organs (O'Brien, 2011). Biomaterials are classified into different categories; polymers, ceramics, metals, composite and hydrogels (Eisenbarth (2007); Melchels et al. (2012)). **Polymers** can be classified (according to their origin) into natural and synthetics. **Natural polymers** including; alginate, gelatin, fibrin, collagen networks, chitosan, chondroitin sulfate, and hyaluronic acids (Eisenbarth (2007); Melchels et al. (2012). They use surface receptors to interface with the cells in addition to adjusting their function (Chung and Burdick (2008); Melchels et al. (2012)). Natural polymers have limited availability and differ between the batches. They also have low flexibility to design external ECM due to the limited mechanical strength (Kim and Mooney, 1998). **Synthetic polymers**, on the other hand, are probably the most used class of materials in TE and comprises poly (α-hydroxy esters), poly (NiPAAm), polyurethanes and poly (propylene fumarates) (Chung and Burdick, 2008). One of the main advantages of these materials is the possibility to precisely control their chemical, physical and biological properties hence inducing specific ECM environments (Chung and Burdick (2008); Melchels et al. (2012)). But, they are limited by the low recognition signals present in their structure hence reducing the bio-recognition (Chung and Burdick (2008); Kim and Mooney (1998)). **Ceramic materials** are another important class of material used in TE, in particular for orthopaedic applications, are ceramic materials. These include calcium phosphates, silica-based glasses and cement (Arcos and Vallet-Regí, 2013). Constructs of cells mixed with bio-ceramics have been used to mimic the bone structure and have demonstrated the ability to substitute the bone functions (Sangaj and Varghese, 2011). **Metals** were used as biomaterials due to their conductivity and mechanical properties. They are common scaffolds implanted in the body in the form of plates, wires or screw. They are used in different body parts such as the knee joints, shoulders, ankles or hips. In addition, these metals used in the dental field and cardiovascular and maxillofacial surgeries. Examples of the used metals are titanium and titanium alloys, cobalt-based alloys and stainless steel (Wilson, 2018). The other type of the biomaterial is **composites** which is by definition, are made by combining two or more biomaterials into a system with enhanced properties when compared to every single material alone. This is particularly useful in bone engineering, whereby combining polymers and ceramics, an enhanced scaffold with the formability and degradability of polymers, and

the bioactivity of ceramics can be produced (Rezwan et al. (2006); Wang (2003)).

The other biomaterial that is used is **hydrogels**, which has proven to have wide applications in this area. It will have a comprehensive explanation since it is the material used in the project. Hydrogels are a very important class of materials in TE, especially in terms of 3D cell encapsulation and Bioprinting. These are water-based networks (Figure 2.7) consisting of two parts; a long branched, solid part suspended in a liquid matrix (Chung and Burdick (2008); Meyer et al. (2009)).
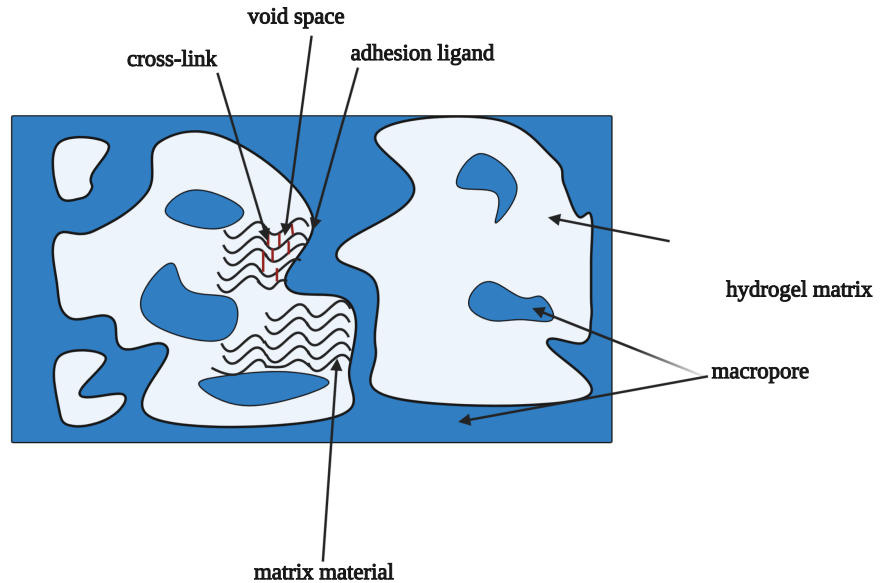
Figure 2.7: Diagram of the hydrogel components. Adapted from (Meyer et al., 2009).

They are considered to be one of the most bioactive materials and can be used to deliver cells (Chung and Burdick, 2008). Hydrogels can be from the natural or synthetic origin, where their chemical and physical properties can be distinguished according to their nature. Physical hydrogels are reversible networks crosslinked through molecular entanglements or through secondary forces such as ionic bonding and hydrophobic interactions. On the other hand, irreversible networks are known as chemical hydrogels crosslinked through covalent bonds (Billiet et al. (2012); Chung and Burdick (2008)). Natural hydrogels such as dextran and gelatin have properties that closely mimic the properties of ECM hence enhancing the support and growth of the cells. These have limited application in TE due to the differences in the batches, In contrast, synthetic hydrogels such as Polyethylene Glycol–Polylactic Acid (PEG-PLA) and Polyethylene Glycol Diacrylate (PEG-DA) overcome the problems associated with natural hydrogels. Hybrid gels (gels which have natural and synthetic parts) are used to combine the bioactivity of natural hydrogels with the tunable physicochemical properties of synthetic hydrogels (Drury and Mooney (2003); Minguell et al. (2001)). Hydrogels can be

injected in vivo or printed as a 3D structure in vitro. They can mimic the tissue by filling the defect and matching its shape and size after the injection (Chung and Burdick, 2008). The physicochemical properties of the hydrogel make it very attractive for the encapsulation of cells through 3D Bioprinting (Chia and Wu (2015); Lin and Anseth (2009)). This is particularly important as it allows a better cell distribution in 3D, homogeneous cell seeding, increased cell-cell and cell-matrix interaction and recreation of an adequate ECM microenvironment. However, the printability of hydrogels and the reproduction of complex tissue geometries remain as a paramount challenge for researchers (Billiet et al. (2012); Chung and Burdick (2008); Lee and Mooney (2001a)). This is mainly related to the conflicting requirements for printability and cell viability. On one side, highly viscous hydrogels are necessary to ensure the good structural integrity of the matrix after printing. On the other hand, low viscosity is ideal for promoting cell viability and proliferation inside the 3D network. Future work will certainly be needed to develop hydrogels or bio-inks with optimized properties for 3D bioprinting of cell-laden constructs with high cell viability.

2.6.2 Strategies of tissue engineering

Tissue engineering is the use of biomaterials to repair, restore or regenerate tissue. There are four main strategies used in tissue engineering; 1. The first strategy the use of cells only, in which the cells are extracted from the patient where then can be cultured in vitro. The cultured cells then transplanted in the body to regenerate the cells in the defect (Laurencin et al. (1999); Swieszkowski et al. (2007)). 2. In the second strategy, cells growth is stimulated by molecules or growth factors (Swieszkowski et al., 2007). 3. The third strategy is about the use of 3D scaffold to support tissue growth. The scaffold can be used alone or seeded with cells and it will degrade after the growth of the tissue (Laurencin et al. (1999); Swieszkowski et al. (2007)). 4. The fourth strategy is the use of matrix (such as hydrogel) with cells encapsulated in. constructs of it are built using a bio-printing technique, in which cells adherence, proliferation, and differentiation will take place (Drury and Mooney, 2003).

2.6.3 Approaches of tissue engineering

Three different approaches have been used in tissue engineering. Top-down tissue engineering (also called 'Scaffold-based tissue engineering') relies on the combination of a scaffold with cells and/or biomolecules in order to promote the tissue repair and regeneration processes (Hutmacher and Cool (2007); Pereira (2013)). This is probably the most used strategy in TE as it enables the manipulation of the produced biodegradable implant at different levels: the material of the scaffold, the fabrication technologies and the cells and biological molecules used. In top-down approaches, shown in Figure 2.8 (A), cells are seeded in a biocompatible and biodegradable scaffold, cultured in vitro and then implanted in the host

tissue environment. As the scaffold degrades at a controlled rate, cells will gradually deposit ECM and rebuild the new tissue hence restoring the biomechanical functions of the tissue (Lu et al., 2013). The scaffolds in this approach failed to distribute the cells homogeneously and mimicking the microenvironment of native ECM (Raphael et al., 2017). On the other hand, bottom-up tissue approach fabricates the tissue by assembling micro/nanoscopic building blocks to produce large scale structures and the 3D organization with different types of cells. This approach aims at mimicking the native biological microstructures with repeating functional units such as the sinusoid in the liver. It also gives a high chance of controlling the lengthy constructs (Khademhosseini and Langer (2007); Nichol and Khademhosseini (2009); Oliveira et al. (2015)). In the bottom-up approach, which shown in Figure 2.8 (B), there is a choice between different types of the building blocks such as cells, cell aggregates, hydrogels/cells encapsulated in hydrogels nano/microparticles, tubes and fibres (Nichol and Khademhosseini (2009); Oliveira et al. (2015)). Modules of biomimetic structures are built by one of the following fabrication techniques: self-assembled aggregation, cell-laden hydrogels microfabrication, and tissues direct printing. The module block is repeated and assembled to create a large construct (Nichol and Khademhosseini (2009); Oliveira et al. (2015)). Using the bottom up approach, different biomimetic constructs can be created. However, this approach still faces several challenges, mainly due to the limited mechanical properties of the printed blocks as well as the limited range of materials available for cell encapsulation. (Oliveira et al. (2015); Toh et al. (2011); Varghese et al. (2005)). One of the common materials used in the application of the bottom up approach is hydrogels (mainly synthetic). They are widespread because of their properties, such as they have a hydrated environment and controlled chemical and physical properties. In addition, they are biocompatible, biodegradable and they are close to the ECM (Lu et al. (2013); Raphael et al. (2017)).
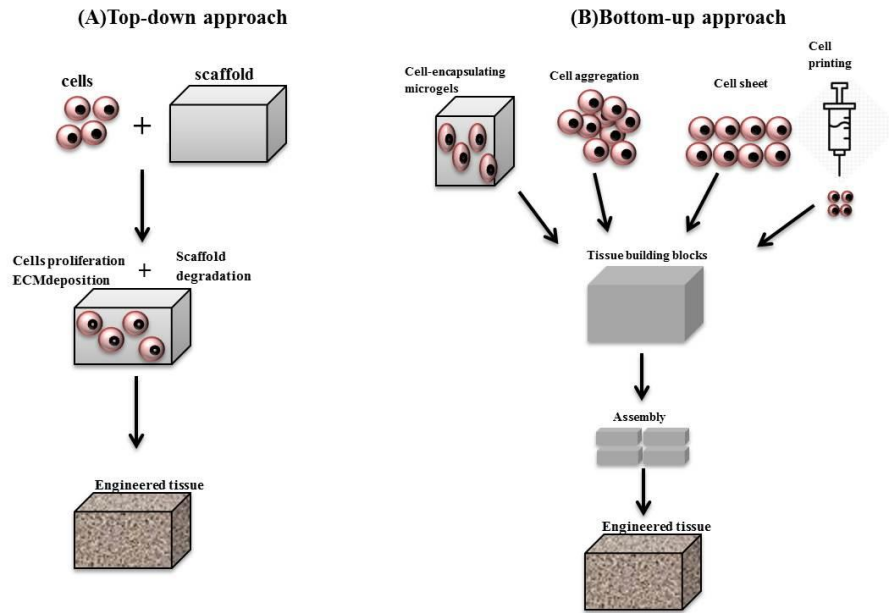
Figure 2.8: Schematic diagram for the top-down approach and bottom-up approach. Adapted from (Lu et al., 2013).

The third approach is the hybrid technique, which is a combination of scaffold-based and scaffold-free approaches. The tissue is generated by the use of a synthetic biopolymer as mould and hydrogel is deposited in the pores. This approach was used to overcome the limitations within the previous approaches, such as the need for sufficient strength of the printed model and the need to print tissues with the appropriate size and shape clinically. The hybrid approach improves the mechanical properties of the tissue construct and gives high cell viability (Park et al. (2016); Seol et al. (2014)).

2.6.4 Manufacturing Techniques

The fabrication techniques used in tissue engineering are classified into two categories; conventional techniques, such as freeze-drying, electrospinning and phase separation and non-conventional (bio-manufacturing techniques), which include powder bed fusion, vat photopolymerisation, binder jetting and material extrusion processes

2.6.4.1 Printing Techniques

Definition Bio-printing techniques are a group of automated layer by layer fabrication processes used to produce 3D structures from biological materials, bio-chemicals and living cells. This technology is used to fabricate scaffolds and tissue blocks in order to regenerate the tissue. A computer with a design model programme is used to ensure accurate positioning

of the material and control the shape and pore size (Ikada (2006); Seol et al. (2014)). Bio-manufacturing additive processes give the ability to produce a layer by layer 3D models very rapidly and allow the use of deferent raw materials (Bártolo et al., 2009). There are four main systems used in 3D printing: Vat Photopolymerization, Laser sintering, Binder jetting and Extrusion based processes

Vat Photopolymerisation

Stereolithography (SLA) is the most common and widely used Vat Photopolymerisation system for TE. This manufacturing process is based on the production of a multilayer 3D solid through the reaction between liquid photopolymers and the different radiation sources such as gamma rays, X-rays, UV, and visible light. The radiation provides the polymer with the required energy for the bonding of small molecules together and forms crosslinked polymer structures. Two different approaches were developed for photopolymerization processes in a vat: point-wise approach (Vector scan) and/or layer-wise approach (Mask projection) (ASTM International (2013); Gibbs et al. (2014), Pereira (2013)). Different materials can be used in this technique, such as polymers (Elomaa et al., 2011), ceramics (Chu et al., 2002) and composites (Melchels et al., 2009). In addition, it gives accurate and flexible printing. However, the fabrication time is long and the cells are normally distributed poorly in the polymer (Meijer et al., 2012).

Selective laser sintering (SLS)

Selective laser sintering (SLS) is a 3D manufacturing technique that uses a laser beam to heat a powder material to the melting point of the powder. The laser heats the powder according to the shape that it needs to be printed and the solid layer forms as it cools down very fast. Once the first layer is completed, another layer will be created on top of it. The heat of the laser is used to bond each layer to the previous layers. The model is supported by the loose powder that surrounds the part hence avoiding the use of support structures. Different powder materials can be used in SLS, including polymers, metals and ceramics (Bártolo et al. (2009); Kruth et al. (2005); Kumpaty et al. (2006)).

Binder Jetting In Binder-jetting processes, a partial cross-section is formed by printing a binder into a powder bed according to the shape of the layer. The excessive binder is then removed by placing the layer under an electrical infrared heater. Another layer is then printed on top of the previous one and the process is repeated until the part is completed (ASTM International (2013); Xu et al. (2015)). Some of the advantages of binder jetting are the ability to combine powder material with additives and the possibility to load slurries with a high content of particles which enables the production of metal parts and high-quality ceramic. Different materials can be used, including polymers, ceramics and hydrogels. One of the main advantages of Binder Jetting is the possibility to operate at low temperatures hence allowing the use of cells in the fabrication process.

Extrusion Based process

Extrusion based processes use a nozzle with diameters of $50 - 1000$ µm selectively dispense semi-molten materials on a building platform in a layer-by-layer fashion (Melchels et al. (2012); Pereira (2013)). Fused Deposition Modelling (FDM), shown in Figure 2.9, is an example of the extrusion-based processes. In this process, a thin filament is used to supply the nozzle with polymer or composite of polymer and ceramic. The semi-molten material is deposited on a translation building platform and the material is allowed to solidify prior to the deposition of the next layer. There are several parameters that control the printing process of materials using FDM, including the scanning speed, temperature, pressure, etc. and that have a direct influence on the quality of produced parts. One important aspect of FDM is the need to maintain the printed material at a relatively high temperature in order to ensure a good interlayer adhesion (Melchels et al., 2012). FDM has been widely used in TE and in particular in the regeneration of skeletal tissues such as osteochondral defects (Cao et al., 2003). Several biomaterials can be used for the production of TE scaffolds, including synthetic polymers and organic-inorganic composites. One of the most common materials used in FDM and approved by the Food and Drug Administration (FDA) for medical applications is Polycaprolactone (PCL). Several studies have reported the successful use of FDM to produce 3D scaffolds with good mechanical properties, high porosity and pore interconnectivity (Zein et al., 2002).
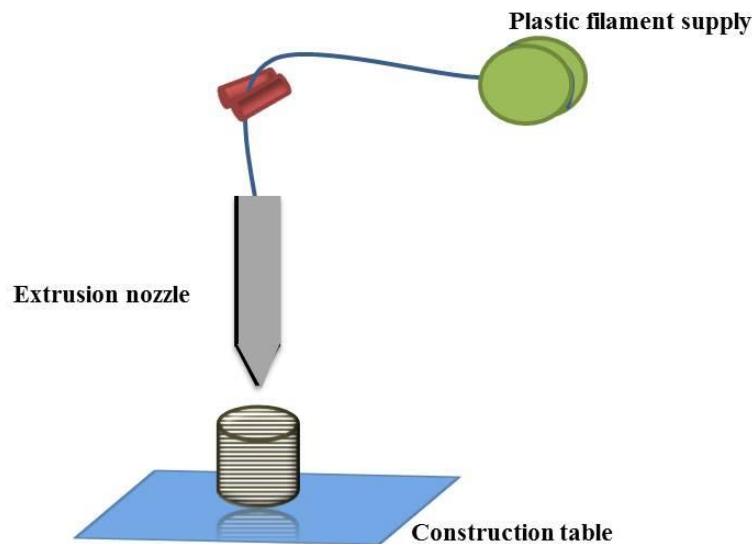
Figure 2.9: Fused deposition modelling relies on a plastic filament supply, extrusion nozzle and a construction table. Adapted from (Melchels et al., 2012).

Extrusion-based processes have evolved immensely over the past 10 years and it is now possible to thermosensitive materials, such as hydrogels, with encapsulated cells and biomolecules. This is done by the encapsulation of the cells in the hydrogel and placing it

in a cartridge connected to a nozzle. The material is then extruded by the application of compressed air hence reducing the amount of shear forces that can affect cell viability. After the completion of the printing process, culture media is added to the build construct (Censi et al. (2011); Melchels et al. (2012), Wüst et al. (2011)). Constructs with high accuracy, controlled porosity (to ensure the transfer of the nutrient and waste) and multiple materials can be easily printed using extrusion-based processes. Also, different cell lines can be printed in a single construct hence reproducing the functional gradients of the native tissues (Censi et al., 2011). However, the full potential of extrusion-based processes or Bioprinting is still hindered by some issues related with sterilisation, construction speed, software and standardisation of the process (Wüst et al., 2011). With cancer cells the extrusion based process, a study done by Khalil and Sun in which Rat heart endothelial cells were encapsulated in alginate to make a 3D scaffold. The research was used conducted to study the relationship between the nozzle velocity and the diameter of the alginate strands (Khalil and Sun, 2007).

2.6.5   Infrared Spectroscopy

2.6.5.1   Vibrational Spectroscopy

Spectroscopy is the study of the interactions between electromagnetic radiation and materials. The interactions might cause light to be absorbed, reflected or emitted as the energy and the wavelength varies. Mid Infrared Spectroscopy (which is one form of vibrational spectroscopy) deals with the spectral region $4000 — 400$ cm^{-1}, $2.5 — 25$ μm.

Covalent molecules (taking diatomic molecules as an example) undergo vibrations. The inter-nuclear distance between the two atoms is set so that the energy of the system is minimal and balance both repulsion and attraction forces. The repulsion forces are between the positive nuclei of the two atoms and negative clouds of the electrons of the two atoms, while the attraction forces are between the nucleus of one atom and electrons of the second atom (Banwell, 1983). When these molecules vibrate, their vibrational amplitude is a few nanometers only, but it increases when the molecule gains energy (Elmasry et al., 2012). The energy is expressed by the following equation:

$$E = h\nu = hc/\lambda \tag{2.1}$$

Where h is the Plank constant, c is the speed of light and λ is the electromagnetic radiation wavelength.

2.6.5.2   The Classical Mechanical Model for a diatomic molecule

The bond of the covalent molecule undergoes through compression and extension, which can be connected to a spring movement. Taking the assumption of a bond like a spring, it can be

said that it obeys Hooke's law. Hooke's law states that the energy needed for the compression and extension of a spring is proportional to the distance the spring moves and given by the following equation:

$$f = -k(d - d_eq) \tag{2.2}$$

Where f is the force, k is the force constant d is the inter-nuclear distance and d_eq is the distance at equilibrium. The harmonic oscillator vibrational frequency is:

$$\nu_o = 1/2\pi\sqrt{(k/m)} \tag{2.3}$$

$$m = (m_1 m_2)/(m_1 + m_2) \tag{2.4}$$

The diatomic molecular vibration is described by the simple harmonic oscillator in which the energy will be:

$$E = 1/2k(d - d_eq)^2) \tag{2.5}$$

The concept of vibrational energy can be understood by a simple harmonic oscillator which is shown in Figure 2.10 A. the figure shows the relationship between the energy (potential energy) and the inter-nuclear distance (interatomic distance). Simple harmonic oscillator though, failed to explain the real molecule's behaviour. Real molecules have a discrete energy system rather than continuous energy which is explained by Hooke's law (Banwell (1983); Elmasry et al. (2012); Wartewig et al. (2003)).
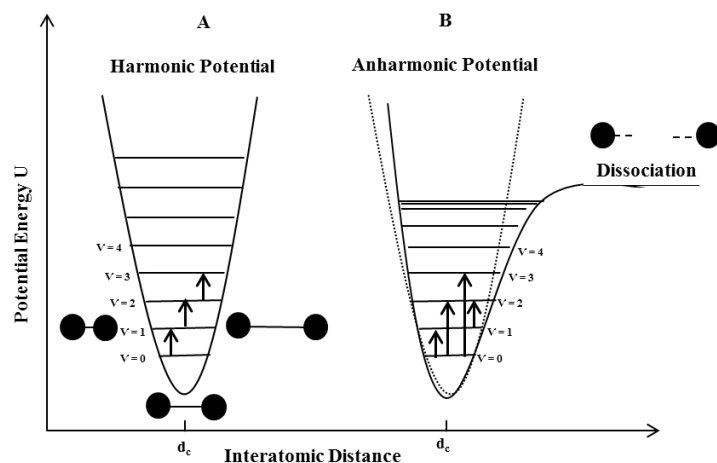
Figure 2.10: Schematic diagram of the simple harmonic oscillator system (A) and anharmonic oscillator system (B). Adapted from (Elmasry et al., 2012).
the long one for the document

The energy levels of real molecules are defined by quantum mechanics, with the following

equation:

$$E_\nu = (\nu + 1/2)h\nu \qquad (2.6)$$

In which ν is the vibrational quantum number, E_ν is the energy which is correlated to the νth quantum level and ν is the fundamental vibrational frequency.

The second limitation to the simple harmonic oscillator is that transitions in simple harmonic occur between adjacent levels ($\Delta\nu = \pm\ 1$) and the energy difference between those adjacent levels is always the same. While in an anharmonic oscillator system shown in Figure 2.10 B, the energy levels get closer together with increasing potential energy and the transitions occur when the amount of light absorbed is the same as the energy difference between any two levels if they are not adjacent levels.

In addition, the elasticity of the bonds in real molecules does not last forever, as the bonds are not fully homogeneous and so they won't obey Hooke's law. Stretching the bonds will cause dissociation at some point (Banwell (1983); Elmasry et al. (2012)).

2.6.5.3   Modes of vibration

Having a molecule with n number of atoms and the axis (x, y, and z) are used to specify the location of each atom. The molecule is said to have a 3N degree of freedom because of the independent specification of each coordinate and so the total number of coordinate will be 3N. Fixing the 3N coordinates will lead to the fixation of bond distances and angles. This allows the molecule to move freely in space with a fixed shape. The translational and rotational movements of a non-linear molecule require six degrees of freedom (3 for translational movement and 3 for rotational movements), which makes the molecule leaving 3N - 6 degrees of freedom (Banwell (1983); Hsu (1997); Stuart (2004)). In contrast, linear molecules have only two rotational movements occurring as there is no rotation around the bond axis e. This will leave 3N - 5 fundamental vibrations. Diatomic molecules always have one vibrational mode since N = 2 and they are linear (Banwell (1983); Hsu (1997); Stuart (2004)). Polyatomic molecules can be linear like CO_2 with four modes of vibration or non-linear like H_2O with three modes of vibration. The modes that have a net change in the dipole moment can be analysed by IR spectroscopy (IR active). The main molecular vibrations types are stretching and bending (Hsu, 1997). Figure 2.11 shows different types of vibrations for H_2O.
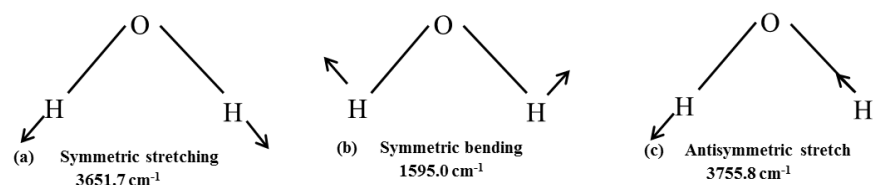
Figure 2.11: The main molecular vibrational modes for a nonlinear molecule H_2O. Adapted from (Banwell, 1983).

When the IR radiation is absorbed by the molecule, the energy is converted to vibrational motion, which is usually combined with rotational motions. Absorption bands rather than discrete lines (energy level transitions) are usually detected in mid of the IR region (Hsu, 1997).

2.6.5.4 Dispersive Spectrometers and Fourier Transform Spectrometers

Dispersive spectrometers were introduced in the 1940s. It has three main components: a source of infrared radiation, monochromator and detector, as shown in Figure 2.12. The common sources of radiation are Nernst glower, Globar and Nichrome coil. The radiation beam from the source is divided into two beams with the same intensity. One beam will go to the sample and the second one will go to the reference. The beams will then be directed to the monochromator which will disperse the light into different frequencies. The detector then determines the frequencies of light which have been absorbed by the sample and the unaffected one (Hsu (1997); Pavia et al. (2001); Thermo Nicolet Corporation (2002)).
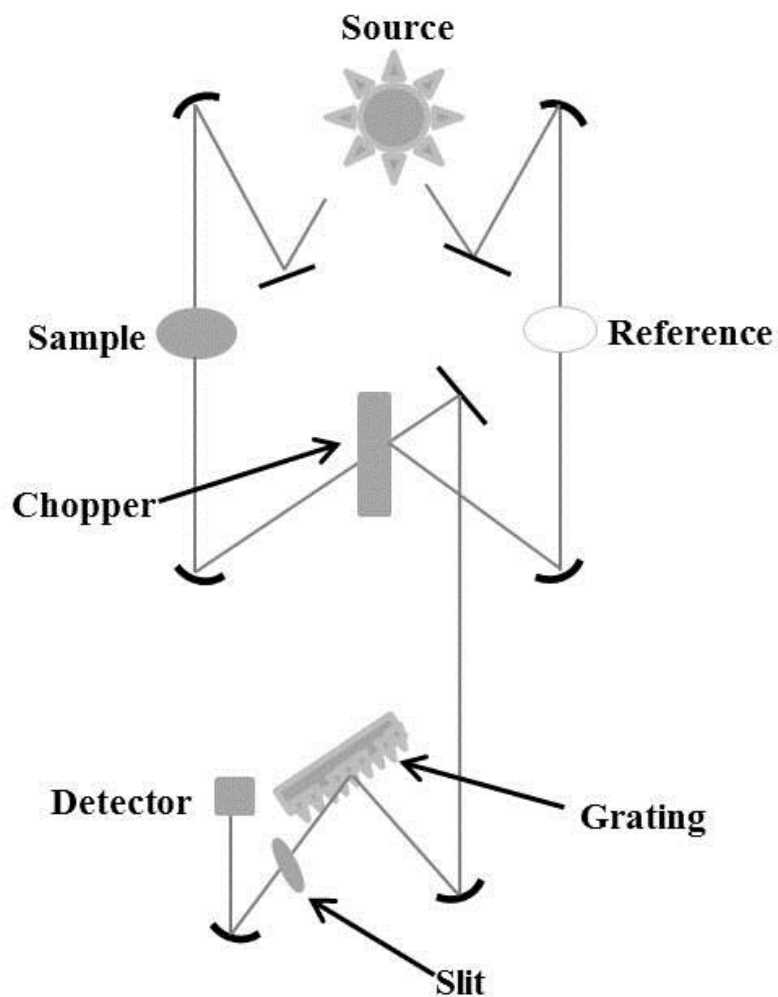
Figure 2.12: Dispersive spectrometer diagram. Adapted from (Thermo Nicolet Corporation, 2002).

The dispersive spectrometer has a slow scanning speed. In addition, the wavenumber range, which goes to the detector from the monochromator is limited due to the presence of the narrow slits at its entrance and exit. Those limitations can be overcome through a Fourier-transform infrared spectrometer (Stuart (2004); Thermo Nicolet Corporation (2002)). Fourier-transform infrared (FTIR) spectroscopy is based on the use of the interferometer system instead of the monochromator. The common interferometer used is a Michelson interferometer showed in Figure 2.13.
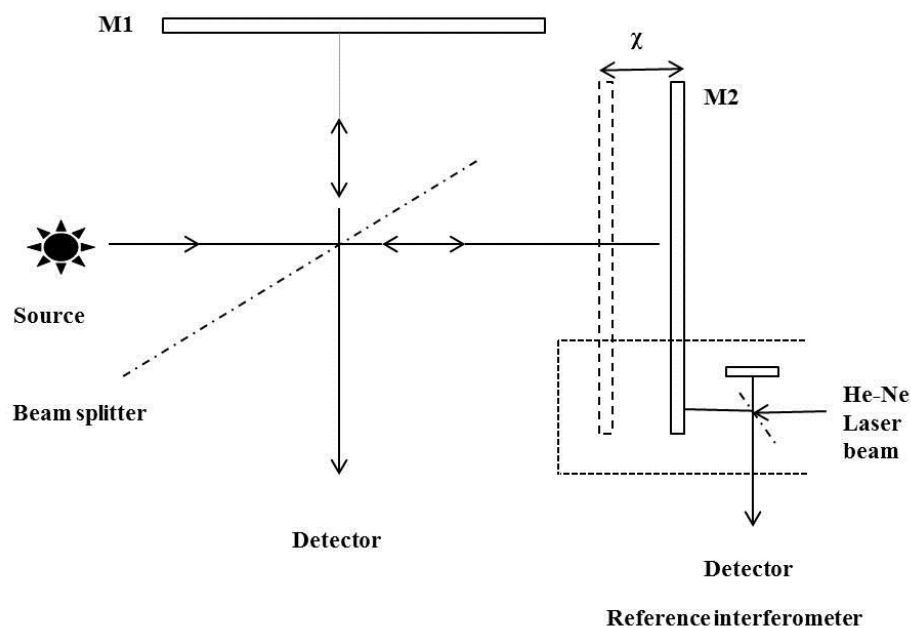
Figure 2.13: Diagram of a Michelson interferometer. Adapted from (Thermo Nicolet Corporation, 2002).

The interferometer contains a source of infrared radiation, beam-splitter, two mirrors, a laser and a detector. The radiation moves to the beam-splitter and it will split into two parts. One part will be transmitted through a moving mirror and a fixed mirror will reflect the second one. The two beams will be recombined at the beamsplitter and give an interference pattern which is called an interferogram. The interferogram then moves to the sample, where the energy is absorbed or transmitted. The transmitted part will reach the detector and the signal detected will go to the computer and it will be converted to a spectrum. The background is scanned by collecting the signal with no sample and the transmittance is produced by taking the ratio of the sample beam to the background (Hsu (1997); Pavia et al. (2001); Smith (2006); Wartewig et al. (2003); Thermo Nicolet Corporation (2002); Stuart (2004))

2.6.5.5 Hyperspectral imaging

Instrumentation Hyperspectral imaging which is known as chemical or spectroscopic imaging is a technique that combines conventional imaging and spectroscopy, so both spatial and spectral information of an object or molecule is obtained. This technique which was developed for remote sensing applications, is now used in different fields such as medicine, astronomy, pharmaceuticals and agriculture due to the acquiring of hyperspectral sensors (Gowen et al. (2007); Nair et al. (2016)). Intensity information is measured and collected from more than a hundred spectral bands within the electromagnetic spectrum. The sensor

of the Hyperspectral imaging produces data as a set of images. These images are normally in the form of a three-dimensional data cube, where the spatial coordinate of a pixel is represented by the first two coordinates and the wavelength of the spectral band is represented by the third coordinate (Nair et al., 2016). The hyperspectral imaging instrument is shown in Figure 2.14. It consists of three main components: an interferometer, an IR microscope, and an IR-sensitive multichannel detector. Within the FTIR microspectroscopy system, the interferometer interfaces with the IR microscope, which results in a specified spot size at the sample plane. The IR radiation is then applied to the sample and hits the detector. Generated data is then visualized in a combined computer (Levin and Bhargava, 2005).
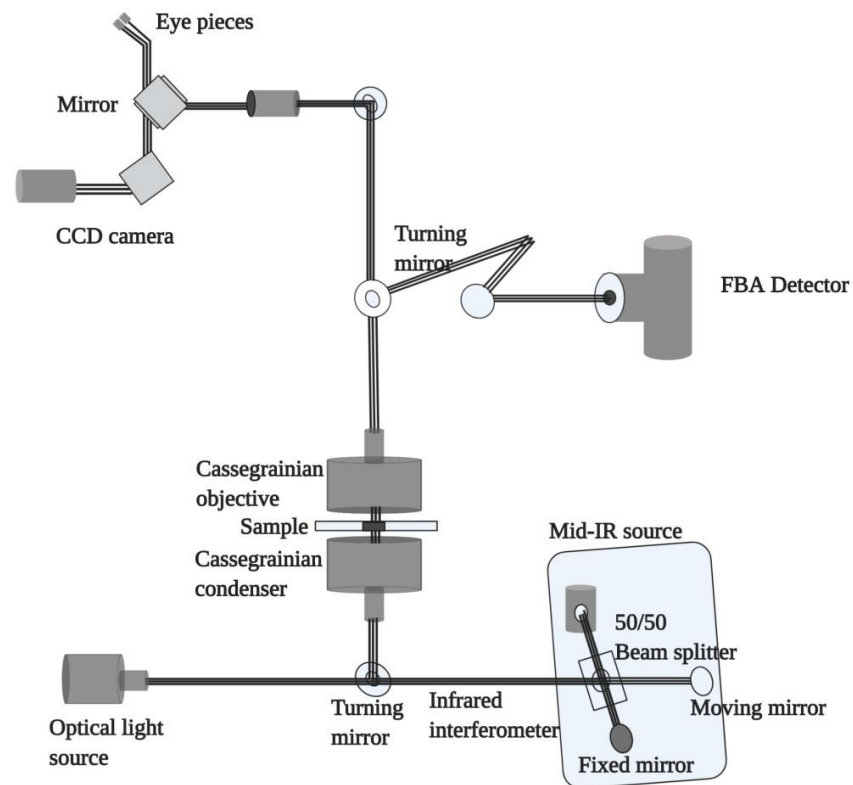
Figure 2.14: Hyperspectral imaging instrument consisting of an interferometer attached to a microscope and detector. Adapted from (Levin and Bhargava, 2005).

In microspectroscopy studies, usually,the Michelson interferometer is used (described above). The interferometer has two scanning modes based on the mirror movement. The first mode is the continuous scan interferometer, where the scanning speed of the mirror is constant and showed in Figure 2.15 A.
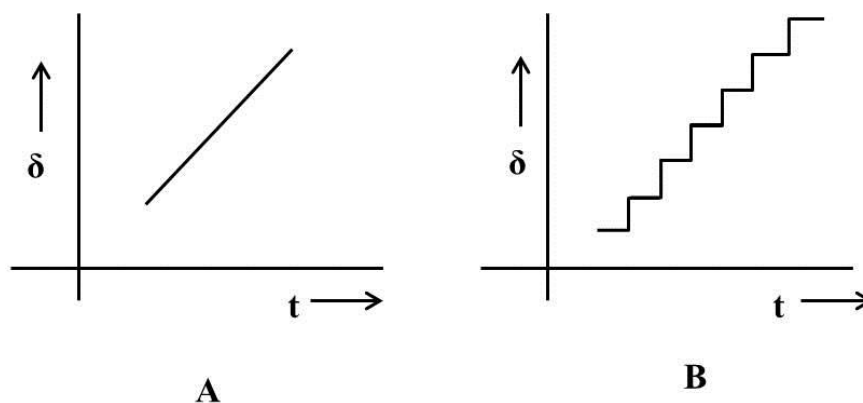
Figure 2.15: Modes of mirror scanning in interferometry: (a) continuous scan mode and (b) step-scan mode. Adapted from (Levin and Bhargava, 2005).

The second mode is step-scan interferometers showed in Figure 2.15 B. In this mode, the mirror radiation is changed to the obtained value and kept constant until the measurements are completed at this radiation. Then the interferometer is raised by one step to the second radiation and so on until the process is complete. The recorded signals are built point-by-point with discrete mirror delays instead of the time intervals. This mode is not preferred for routine spectroscopic analyses due to the time needed for the scan, the cost of the interferometer and its complexity (Levin and Bhargava, 2005).

The microscope used in IR is very much the same as the one used in visible light microscopes except for the glass refractive elements. These elements need to have an opaque glass to IR light with a wavelength higher than 5 μm. The spot size of the microscope can be increased using either a diffuser or diverging mirrors system. The beam is diverted from the spectrometer to the Focal Plane Array (FPA) detector using different mirrors. Optics such as Cassegrain used for the transmission mode shown in figure 2.15, are used to have a focused light on the sample. Different detectors are used in the FTIR imaging in which the choice of the detector will determine the data acquisition speed, quality, and chemical image quality. The most common detectors used are FPA detectors. FPA detectors give information about the compounds identity and concentration. Furthermore, these can provide information about the distribution of those compounds in the field, which is measured based on the simultaneous acquisition of thousands of spectra in minutes. In addition, n × n of resolved spectra are acquired simultaneously (n can be 16, 32, 64, or 128) in the detector

array (Agilent Technologies (2011); Levin and Bhargava (2005); Smith (2006)). An FPA detector that is used in imaging is liquid nitrogen-cooled Mercury Cadmium Telluride (MCT) detector. Its properties depend on the Hg: Cd ratio. Narrow-band MCT detectors are very sensitive (50 times more than 1×1 or 2×2 mm pyroelectric (either deuterated triglycine sulfate (DTGS), which is used in FTIR spectrometer) but they cut-off of about 750 cm^{-1} while mid-band MCT cut-off of about 600 cm^{-1} with sensitivity less by half than the narrow band MCT. Most samples have no useful bands below 700 cm^{-1} except few organic samples, so some FT-IR microscopes are equipped with narrow-band MCT detectors (Alzer and Siesler, 2009).

Hyperspectral imaging modes

FTIR imaging works with different modes such as transmission, Attenuated Total Reflection (ATR) and transflection. In Transmission Imaging, the amount of light absorbed by the sample is measured. The resultant spectra in this mode usually have a high Signal to Noise Ratio (SNR) due to the high intensity of infrared light received by the detector. A thin film is required to avoid the complete absorbance of light by the sample. Also, the thickness of the sample should be uniform in order to get a precise quantitative analysis (Kazarian and Chan, 2006). In ATR imaging, the IR light is passed from the ATR crystal (high refractive index material) to the sample (low refractive index material) at an angle higher than the critical one. The radiation is reflected internally at the interface. The sample for ATR FTIR imaging requires none or little preparation (Alzer and Siesler (2009); Kazarian and Chan (2006)). The Transflection mode is the measurement of reflection-absorption, where a highly reflecting substrate is used with the sample placed on top of it. When IR radiation is applied to the sample and substrate, the light will be transmitted through the sample and will be reflected from the substrate. The light then goes back through the sample one more time, causing the path-length to be doubled and the sensitivity will increase. One of the most commonly used substrates in transflection is Ag/SnO_2 coated glass slides as they are robust and cheap (Pilling et al., 2015).

Scattering effects

Scattering is one of the problems associated with FTIR imaging. It occurs due to the change in the refractive index in the sample. The sample particle's diameter is the same as the light wavelength which is interacting, causing distortion in the peak's intensities and difficulties in determining the baseline. The background will be broad and undulate. This scattering is known as Mie scattering. One of the major samples affected by Mie scattering is the tissue samples since the cells that make up the tissue are of similar size to the radiation wavelengths, between 2.5 and 12 mm. Different algorithms are available to correct the scattering effect and a pure absorbance is retrieved. Recent studies have recently demonstrated the potential of correction algorithms when applied to tissue samples (Bambery et al. (2012);

Goormaghtigh (2017); Pilling and Gardner (2016)).

Correction for water vapour contribution

The contribution of water vapour to the obtained spectra is very common due to its presence in the surrounding air. It can be minimized by using a box to surround the microscope parts and purging dry air inside it. With or without the minimization of the presence of water vapour by the box, its contribution still can be seen if not immediately, second derivatives will show it. Figure 2.16 shows the contribution of water vapour on a spectrum of epithelial cells. It can be seen at the wavenumbers 4 and 8 cm^{-1} and it is found at 16 cm^{-1} as well, but it cannot be differentiated. Using the second derivatives shows the one at 16 cm^{-1}.
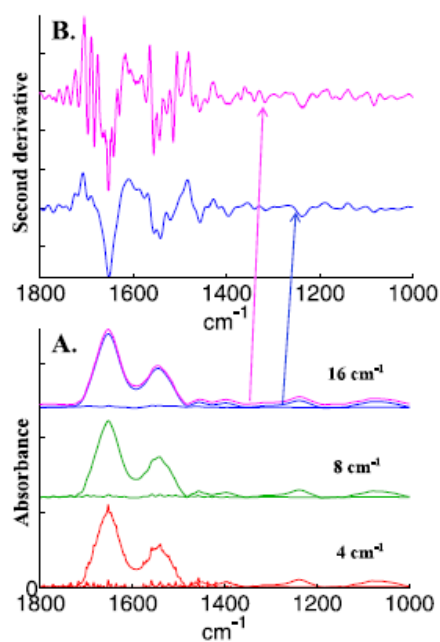
Figure 2.16: The contribution of water vapour as a function of spectral resolution in epithelial cells spectra. (A) Shows the spectra of the breast epithelial cells at 4 cm^{-1} and the water vapour spectrum have been added (bottom, red spectra). The decreased resolution by apodization of the interferogram by a Gaussian line shape to 8 cm^{-1} showed in the middle, green spectra and decreased more to 16 cm^{-1} showed in the top, magenta spectra. The original spectrum at 16 cm^{-1} is showed (with a small offset to make it clear) in blue. (B) shows the second derivative (Savitzky–Golay, 9 points, spectra encoded every 1 cm^{-1}) of the original spectrum at 16 cm^{-1} (blue) as well as the spectrum containing water vapour contribution in which the resolution was decreased (magenta). The correspondence between each spectrum and its second derivative is indicated by the arrows. The original cell spectrum appears in blue with a small offset for the sake of clarity. B, second derivative (Savitzky–Golay, 9 points, spectra encoded every 1 cm^{-1}) of the original cell spectrum (blue) and of the spectrum containing water vapour contribution whose resolution was decreased at 16 cm^{-1} (magenta). The arrows indicate the correspondence between each spectrum and its second derivative (Goormaghtigh, 2017).

The water vapour is scaled and subtracted from the spectra using different methods. It can be solved by image "noise" subtraction. In the case of scaling the subtraction coefficient on a single water vapour band, it is best to record the spectra at least at 8 cm^{-1} resolution (Goormaghtigh, 2017).

2.6.5.6   Biomedical applications of Hyperspectral imaging

IR methods are widely used in the biomedical field due to the presence of the IR active compound in most of the biological and clinical samples. IR spectroscopy gives a unique fingerprint for each sample without destroying the sample. The most common bands for the biological molecules in the area of $3,000 - 800$ cm^{-1} are shown in Figure 2.17. The figure shows a spectrum in the transmission mode for breast carcinoma. Basically, the spectroscopic analysis is associated with the presence of lipids, carbohydrate proteins, and conformational changes within the DNA (Baker et al. (2014); Siqueira and Lima (2016)).
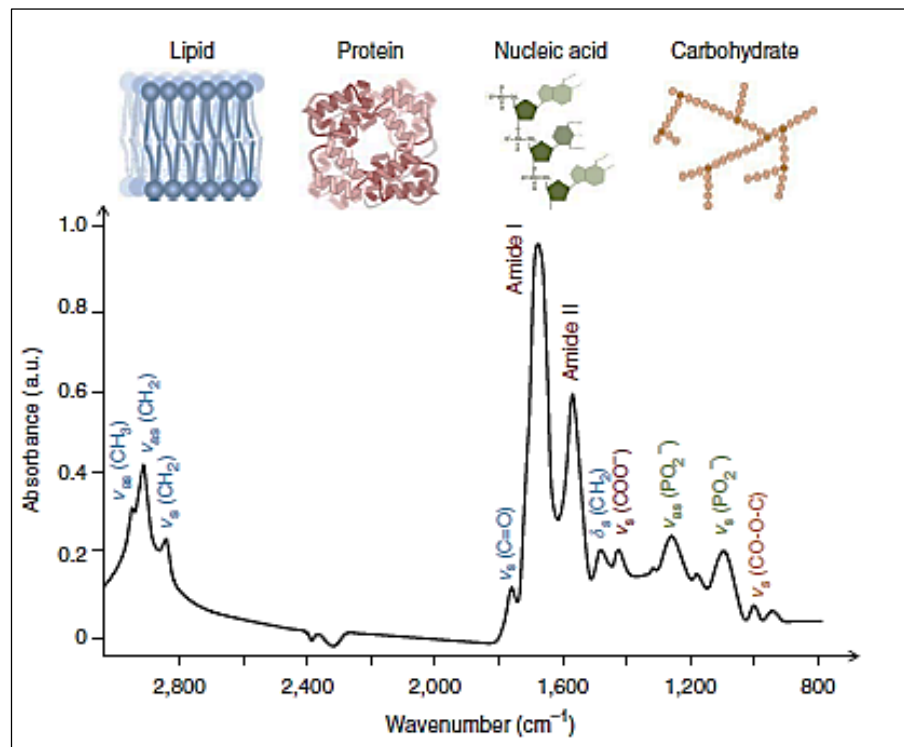
Figure 2.17: Biological spectrum showing biomolecular bands of some biological samples. Where ν is the stretching vibrations, δ is the bending vibrations, s is the symmetric vibrations and as is asymmetric vibrations (Baker et al., 2014).

For the analysis of biological or biomedical samples, there is a choice between the different modes (transmission, ATR and transflection) depending on, which one is more suitable for the sample. Dyes or labelling techniques are not required for IR analysis. In addition, fixed and live cells can be analysed or even tissues embedded in paraffin. Also, different cells types such as stem cells, transit-amplifying cells and terminally differentiated cells can be analysed by IR techniques (Baker et al. (2014); Kazarian and Chan (2006)). Different studies of the FTIR imaging in the biomedical field have been done and reported in the literature. Some

of the reported studies (arranged in the published years) will be demonstrated. Lasch, Boese and Diem have demonstrated spectral maps for tissue sections and used unsupervised and supervised algorithms to extract the information of the tissue which might be useful for the prescreen of the tissue sections (Lasch et al., 2001). Moreover, Haka, Kidder and Lewis were able to see the different tissue types by the biochemical composition and they were able to create different data sets for each region (Haka et al., 2002). In another study, Haka *et al.* demonstrated the spectral details of the cells showing the different components of the cells such as nucleus and cytoplasm. They were able to see the difference between active and dead cells since the dead cells show spectral information of the proteins and there is no spectral information of the nucleic acids and phospholipids which were seen in the active cells (Haka et al., 2002). In the work of Paluszkiewicz C and Kwiatek WM, the authors reported on the analysis of human cancer prostate tissues using FTIR microspectroscopy and SRIXE techniques (Paluszkiewicz and Kwiatek, 2001). In particular, they have studied the difference between cancer tissue and a non-cancer part of the prostate using FTIR microspectroscopy. In the area of 2800 to 3000 cm^{-1}, different band intensities were found when analysing cancer and the non-cancer part. In the spectrum of cancer tissue, the intensity of the band at 2930 cm^{-1} was found to be more than the band at 2960 cm^{-1}. The relative intensity ratios of bands in cancer and non-cancer spectra were calculated and found to be different, which indicates the disorder of the groups in the cancer tissue (Paluszkiewicz and Kwiatek, 2001). In another study by Gazi *et al.* (Gazi et al., 2003), the FTIR microspectroscopy was applied to different samples of prostate cancer including cell lines which are taken from different metastatic sites, Gleason-graded malignant prostate tissue and tissue from Benign prostatic hyperplasia (BPH). The authors suggest a potential method to distinguish benign cells from malignant cells based on the ratio of the peaks that correspond to glycogen at 1030 cm^{-1} and phosphate at 1080 cm^{-1}. The ratio associated with FTIR spectral imaging was used to provide an estimation of the malignant tissue areas in defined regions of a specimen (Gazi et al., 2003). In later studies, Lasch, Diem and Naumann were able to use multivariate cluster algorithms in the infrared spectra to build tissue structure maps and that gives more information than using chemical mapping technique (Lasch et al., 2004). Gazi *et al.* have published a study in which ToF-SIMS and synchrotron-based Fourier transform infrared (SR-FT-IR) microspectroscopy used to get information about the spatial distribution of the proteins and lipids in prostate cancer cells. Additionally, carbohydrate, phosphate and nucleic acid peaks were also analysed. The method can be used to study the variation in the phenotype expression, which might lead the demonstration of the specific ions associated with cancer progression (Gazi et al., 2004). In another study by Gazi *et al.* that have been published in 2005, the use of SR-FTIR microspectroscopy to generate a chemical map for PC-3 cells (prostate cancer cell line) was shown. The authors found that the basic biochemical processes of the cytokinetic cells

can be understood using the IR signals intensities of the amides and lipids (Gazi et al., 2005). A study to compare the architecture of tissue using Gleason grade and FTIR-LDA was performed by Gazi *et al.* FTIR-LDA is the use of Linear Discriminant Analysis (LDA) to the FTIR spectra, which has been done by the same group in a previous study. The results of the comparison show the availability of the correlation between the two and both found to predict the behaviour of the tumour metastatic in a similar way (Gazi et al., 2006). FTIR-PAS technique has been used to present a novel work by Harvey *et al.* on the analysis of cancerous cells. The different cell types were separated when using PCA in addition to the separation of BPH from PC3 and LNCaP cells (Harvey et al., 2007). Gazi *et al.* studied the direct evidence of lipid translocation between adipocytes and prostate cancer cells with imaging FTIR microspectroscopy (Gazi et al., 2007). In this study, the authors have shown the translocation of the lipids between adipocytes and prostate cancer cells. Additionally, a comparison between PC3 prostate cancer cells fixation methods through the IR spectrum was also reported. The fixation methods are formalin fixation and fixation by PF using OsO_4 post-fixation and Critical-Point Drying (CPD). The use of OsO_4 in the latter method, preserve the lipids without absorbing the radiation in the mid-IR region and (CPD) method keeps the 3D structure of the lipid, but the signal of the $\nu s(=C\text{-}H)$ that is found in the unsaturated hydrocarbons is lost. On the other hand, formalin fixation is found to be unsuitable of the adipocyte because of the presence of methanol that causes intracellular lipids extraction. However, it keeps the νs (C-H) signal present in the spectrum. Both fixation methods were found to make the resolution of the peaks to decrease, in particular the νas $(CH)_2$ and νas $(CH)_3$. Furthermore, the authors have also studied the location of subcellular in a single adipocyte containing isotopically labelled palmitic acid (D31-PA) using FTIR imaging. The percentage of adipocyte containing D31-PA was found to be high in large adipocytes. When PC3 cells co-cultured with D31-PA, and FTIR image was taken for the fixed PC3 the signal of D31-PA was seen in the spectrum showing translocation of the labelled Dietary fatty acids ((Gazi et al., 2007). A study that used FTIR technique to identify the aggressive prostate cancer was performed by M. J. Baker. The principal component-discriminant function analysis (PC-DFA) algorithm was used to analyse the spectra obtained by FTIR. The specificity and sensitivity of a three-band Gleason score criterion were improved, which gives an accurate diagnosis of prostate cancer (Baker et al., 2008). In order to find the relationship between dietary fat intake and prostate cancer, a study by Gazi *et al.* took place. Deuterated analogues were used in Fatty Acid (FA), Palmitic Acid (PA) and the unsaturated FA, Arachidonic Acid (AA) and then FTIR microscopy was used to measure them. The study results show that FTIR is a good technique to monitor the amount of AA in the cells. Also, the study shows that protein phosphorylation is occurring due to the metabolism of the lipids (Gazi et al., 2009) Baker *et al.* have investigated the use of FTIR based histopathology for prostate

cancer diagnosis. The researchers were able to differentiate the prostate confined cancer and extraprostatic cancer by the spectral analysis of FTIR using the amide and lipid region (Baker et al., 2009). Gasper et al. were able to find a fingerprint of the biochemical components such as DNA, RNA, proteins and lipids when treating prostate cancer cell lines with anticancer drugs. Moreover, the metabolic changes due to the application of the drug were identified accurately. The study also performed to check the effect of the antitumoral Cardiotonic Steroids (CS) on prostate cancer cell line PC3. Four CS were tested; ouabain, 19-hydroxy-2″ -oxovoruscharin, hellebrin and 19-hydroxy-hellebrin. Although the spectral signature for each CS used was unique, but the similarities with the signature of the control were very big. The authors suggested, based on the found results, that FTIR can be used to find the cellular pathways generated by the drugs (Gasper et al., 2010). A study of Multimodal microscopy for automated histologic analysis of prostate cancer has been published. The study addressed the use of FTIR imaging on the identification of the epithelial cells and the authors were able to extract information about cell type and morphology from stained images (the same images used in the clinics) (Kwak et al., 2011). Bassan et al. show in their study the ability to scan a whole organ with FTIR spectroscopy. The prostate was scanned using transmission mode and it took hours compared to days with transflection mode. The authors suggested the build of an automated model containing the chemical images and the histology of the different cell types within the organ. Other studies have to be combined with this study in order to get a better and comprehensive model (Bassan et al., 2013). Another study has used the FTIR to check the effect of the anticancer drugs on the cell cycle. The output of the study is that FTIR is not a good method to study the cell cycle since the spectrum was affected by Mie scattering and the use of RMies-EMSC algorithm still show the paclitaxel treatment, which dominates over the cells cycle effect. The FTIR was used to classify the cells in different phases of the cell cycle, but the classification was very poor (Derenne et al., 2013). The assessment of prostate biopsy with FTIR imaging was done by Bassan et al. in order to help the pathologist to get a more accurate and automated assessment of the tissue biopsies. The researchers have studied the use of FTIR imaging on embedded tissue without going through the processes of dewaxing and staining. The resulted spectra show the loss of the lipid signal because of the paraffin absorbance interference. The use of the other regions, though, provides a highly accurate classification with the benefits of the reduction of the scattering (associated with the dewaxed sample) and reduction of the need to used the signal processing methods (Bassan et al., 2014). Comparing between transmission and transflection modes in studying prostate tissue was done by Pilling M et al. (Pilling et al., 2015). The study shows a non-linear distortion in the spectra obtained in transflection mode as well as differences in the spectra measured in the same area. The benign and cancerous tissues were poorly distinguished in this mode. When the sample thickness is doubled in the transmission

mode, no difference was seen in the spectra, which suggests that the path length increment in the transflection was not the reason for the increase in the absorption band variability. Also, the study shows that the spectral biomarkers cannot be transferred from one mode to another (Pilling et al., 2015).

Kwak *et al.* had a study on the use of FTIR spectroscopy to predict the recurrence of prostate cancer without the use of stains and human interpretations. The authors have used a computational approach with FTIR imaging data. They have used the stromal features rather than epithelial once, which normally lead to a great distinction between recurrence cases and the non-recurrence controls (Kwak et al., 2015). The difference between High-Definition (HD) and normal magnification FTIR spectroscopy was studied and found that HD imaging has given more spatial information quality. This, according to the authors, will lead to a better assessment in the diagnosis of prostate cancer using IR spectroscopy (Wrobel et al., 2016). A study to compare two classification methods of the FTIR data was performed. The methods are Linear Discriminant Analysis (LDA) and Quadratic Discriminant Analysis (QDA). The comparison was based on prostate cancer database. The results show the ability to classify the low and high grades of prostate cancer by both methods with QDA method showing better classification. In addition, both models can be used for the identification of the structure of the proteins and the differences of the DNA/RNA. There is no recommendation given from the authors for the method to be used, a suggestion to find the best method by using data 'graphical exploration' with model quality performance calculations (Siqueira et al., 2017). Research to study the thermal effect on IR spectroscopic imaging by combining the IR spectroscopy with thermal emission imaging. The spectral differences between benign and malignant parts of prostate cancer tissue. The study shows the great contribution of the thermal effect with the reduction of acquisition time and the obtained chemical images were found to have similar to the spatial resolution with the one from FTIR. In addition, the study found that cancer surrounding the stoma has a spectral band that can be considered as a biomarker, which is the antisymmetric stretching band of the methylene group at 2921 cm^{-1} (Song et al., 2018). Cai Li Song and Kazarian have studied the effect of having a variable angel in the micro ATR-FTIR spectroscopic imaging. The team of the study were able to change the angel in the z-direction with about 2°. Very high-quality images were obtained at different depths. The importance of this work comes from the ability to apply the study on 3D models allows the study of different components within the model (Song and Kazarian, 2019). Recent study to compare HD-FTIR, Raman and atomic force microscopy infrared (AFMIR) techniques has been done by applying them to prostate cell line PC3. The result of the study shows that all three methods give high-quality chemical images of the cholesterol derivatives found in cancer cells. However, the AFM-IR technique found to show higher spectral heterogeneity than FTIR and Raman imaging, which had similar results. AFM-IR is

a powerful technique for the nanoscale imaging with improvements of some bands comparing to FTIR such as the lipid bands (Roman et al., 2020). These are some of the studies that have been done for the use of FTIR imaging for the study of prostate cancer. Different types of samples have been used, such as the use of biopsies from patients and cell lines. The studies aim to find more information about the initiation and progression as well as testing therapies. With all this research, there is still a lack of knowledge of cancer initiation and progression, and more studies are going on in the field.

2.7   Conclusion

Prostate cancer is the most common cancer among men with a high death rate. Studies show the effect of CAFs on prostate cancer cells proliferation. Different models have been used to study prostate cancer such as animal models (dogs and primates, genetically engineered mouse models, xenografts and rats), 2D models and 3D models (spheroids and organoids). All these models are limited and that causes the limitation of the knowledge of cellular mechanisms that lead to prostate cancer initiation and progression. Tissue engineering is used in 3D models design that mimics the tumour environment and it might be the right components needed to find the required knowledge on cancer initiation and progression as well as bringing the complicated models for drug testing. With the significant applications of FTIR imaging on the biomedical field, it is believed that it will be the best techniques for the analysis of the constructs that are built in the work of this project.

3

Methodology

3.1 Materials

F-12 Ham, RPMI-1640, PBS and Trypsin were purchased from Sigma Aldrich, UK. The hydrogels (Alpha 1, Alpha 2, and Alpha2*) were purchased from Manchester Biogel, UK. The LIVE/DEAD Viability /cytotoxicity kit was purchased from Thermo Fisher Scientific. Alamar Blue was purchased from Fisher Scientific UK Ltd. The antibodies N-Cadherin and E-Cadherin were obtained from New England Biolabs UK Limited, vimentin antibody was purchased from Proteintech Europe Ltd, pan Cytokeratin Ab was obtained from Bio Techne and HIF 1 alpha monoclonal antibody was purchased from Enzo Life Sciences (UK) Ltd.

3.2 Optimisation of bioprinting parameters

An extrusion-based printing system, called 3D Discovery (regenHU, Switzerland), was employed for the fabrication of cell-laden hydrogels. Several parameters control the extrusion process of materials with the 3D Discovery, including Valve Opening Time (VOT), Dosing Distance (DD), Deposition Velocity (DV) and the Extrusion Pressure (EP) that need to be optimised according to the materials used. In this study and due to the different rheological properties of the hydrogels (Alpha 1, 2 and 2*), an optimisation process was carried out in order to obtain 3D constructs with well-defined geometrical properties and high cell viability. The hydrogels which were used in this experiment were alpha1, alpha2 and alpha2*. They are ionic-complementary peptide hydrogels that are self-assembled into β-sheet-rich fibres. They are designed to produce a 3D structure in which its mechanical properties can be controlled.

3.2.1 Code generation for the 3D printing

The constructs were designed using BioCAD software (regenHU, Switzerland). Since the cell-laden constructs had to be directly printed into 6-well culture plates with and without

inserts, an optimised G-Code was written, taking into account the thickness of the disk and the geometry of the plate. All printed constructs were characterised by a Disc-shape geometry with an outer diameter of 14 mm, lay-down pattern of 0° for one layer and $0^o/90^o$ for four layers construct, Filament Distance (FD) of 550 μm (horizontal plane), layer thickness (LT) of 550 μm and height of 1 mm.

3.2.2   Optimisation 3D Discovery printing parameters

The polymeric solution or ink was prepared by adding 30 μL of the culture media (taking into account the cell density; 10 μL was added to the normal volume used of 20 μL) to the hydrogel and mixed homogeneously. Two different culture mediums were used (F-12 Hams and RPMI-1640). Then the mixture was placed in the printing cartridge, and optimisation took place. There are different processing parameters that control the low-temperature printing process of the 3D Discovery and that need to be optimised in order to achieve precise control over the dimensional/geometrical accuracy of printed constructs. Within the scope of this work, four parameters were studied and optimised, namely Deposition Velocity (DV), Extrusion Pressure (EP), Valve Opening Time (VOT) and Dosing Distance (DD). The DV is related with the movement of the printing head in X and Y directions. EP is the pressure applied to the piston of the cartridge. VOT specifies the period during which the micro-valve of the printing head is opened. DD determines the distance between the dispensed portions of the material. Through a series of trials, hydrogel constructs were printed using a nozzle of 330 μm and varying iteratively one parameter while maintaining constant the other three. This method was employed to ensure the generation of constructs with well-defined geometries and dimensions while ensuring good cell viability. To get the optimal parameters, VOT was varied between 1×10^{-4} s to 0.05 s, DD has a minimum distance of 5×10^{-6} m, and maximum distance $\times 10^{-3}$ m, Deposition Velocity (DV) ranges from 0.007 to 0.01 m/s, and the Extrusion Pressure (EP) varied between 1×10^5 Pa and 3×10^5 Pa (1-3 bar). Optimised processing parameters were then used to print 3D hydrogel-based constructs, encapsulated with different prostate cancer cell lines (PC3, PNT2 and LN CAP) directly onto a six-well cell culture plate. The optimised printing parameters were obtained in which the hydrogel filament extruded with the same diameter of the nozzle (internal) in the minimum amount of time possible.

3.2.3   Rheological properties measurements

The mechanical properties were measured for hydrogel samples (200 μL each) after they have been set on culture media for 24 hours. The three hydrogels (alpha1, alpha2 and alpha2*) were tested on two different culture media;F-12 Ham and RPMI-1640. The viscoelastic response of the hydrogels was measured using a Discovery HR-2 rheometer from TA Instruments.

The tests for all samples were conducted with 20 mm diameter parallel-plate at 25 ^oC with 50 μm gap. Dynamic oscillatory frequency sweep measurements were run at 0.05% strain amplitude and Storage (G′) and loss modulus (G″) were determined. The viscosity modulus was measured for a controlled frequency of 1Hz and a wide range of strain from 0.01% to 100%.

3.3 Cell encapsulation and viability assay

Since the one of the aims of this project is to print cell-laden constructs, the cells were encapsulated on the hydrogel and a series of biological assessments were conducted to ensure that the cells stay alive inside the hydrogel. Live /dead viability test was run to determine the amount of live and dead cells at each time point. Additionally, Alamar blue test was run to prove that the cells were metabolically active and to give more accurate methods to count the number of cells at each time point that counting them through live/dead test.

3.3.1 Cell Culturing

Three prostate cancer cell lines were used: PC3, PNT2 and LN CaP. The cell lines were cultured in F-12 Ham (used for PC3) and RPMI-1640 (used for PNT2 and LNCaP). Both culture media have 5% Fetal Bovine Serum (FBS), 250 μL insulin and 1% Penicillin/Streptomycin as supplements. 10 mL of the culture media was added to the defrost cells, and confluent cells were washed with PBS and centrifuged at 214 g for 5 minutes. Discarding the supernatant liquid and re-suspending the cell pellet in 10 mL of the culture media. The cells were then incubated at 37°C in 5% CO_2.

3.3.2 Cells Encapsulation

The cultured prostate cancer cells with a cell density of 2×10^6 cells per mL of the hydrogel were suspended in 20 μL of the media. The cells were mixed homogeneously with the hydrogel and plated into a six-well plate using two different methods:

1. Manual plating: Equal amounts of cell-laden hydrogels were manually dispensed into a six-well plate using a positive displacement pipette. Afterwards, cell culture media was added until complete submersion of the constructs was achieved and incubated at 37°C and 5% CO_2. At specific time points (1 hour, 2 hours, 1 day, 3 days, and 7 days), the viability of encapsulated cells was assessed using Live/dead viability test.

2. Bioprinting: The homogenous mixture of the hydrogel and cells was transferred to the printing cartridge, and the printing then took place immediately in 6-well culture plates. The resultant printed layer supplied with culture media. Incubation and viability test took place in the same as the manual printing.

3.3.3 Live/Dead Viability Test

Live/dead viability assay is a test used to evaluate the viability of cells and enables counting of both live and dead cells. The assay is based on the use of two fluorescent dyes; one for live cells and the other for dead cells. The dyes used in this research are calcein AM and Ethidium homodimer-1 (other dyes are available and have the same working principle). Calcine AM is a dye than can penetrate the cell membrane and dye the cytoplasm green. However, ethidium homodimer-1 has the ability to dye the nucleic acid with red colour. The number of live and dead cells can be counted using the images obtained from the fluorescent microscope (Invitrogen Molecular Probes (2005); Louis and Siegel (2011). The LIVE/DEAD Viability kit contains the reagent stock solutions Ethidium homodimer (EthD-1), and calcein AM. To 10 mL of sterile Dulbecco's phosphate-buffered saline (D-PBS), 15 μl of 2 mM EthD-1 and 5 μL of 4 mM calcein AM were added and mixed well. The culture media was removed from the well containing the construct, and it then washed with 2 mL of Dulbecco's phosphate-buffered saline (D-PBS). The amount needed of the stain (100 – 300 μL if 48 or 96 well plates was used and up to 1.5 mL if 6 - well plate was used) to cover the construct. Construct Incubation at room temperature then took place for 20-30 min. EVOS fluorescence microscope was used to view the labelled cells.

3.3.4 Cell Counting

The cells were counted using Fiji-image J software. After the counting, the area of each cell counted was divided by the area of the real cell (calculated assuming that the cells are round in shape) and the final number of cells was calculated. This is due to the inability of the software of separating the bulk cells aggregations and counting them as one cell instead. The area of the cells calculated using the average diameter found using the automatic cell counter and found to be: PC3 = PNT2: 143.14 μm^2 and LNCaP: 147.41 μm^2.

3.3.5 Metabolic activity test

Alamar blue solution was used to test the metabolic activity of the cells after encapsulating them in the hydrogel and printing them. Three different samples were prepared for the test: 1) Printed constructs: 100 μL of Alamar blue was add to the media in the top of the constructs and left in the incubator for 4 hours after covering the plate with aluminium foil to avoid any contact of the stain with light. After 4 hours, 3 — 6 samples (100 μL each) were placed in a 96 well plate, and the fluorescence intensity was determined by a fluorescent plate reader. The excitation wavelength that the plates were exposed to is 530 nm, while the emission wavelength is 590 nm. The average value was taken for each cell type. The same samples are tested the same in different time points (1, 3, 7 and 14 days); 2) Positive

control: the cells were seeded in the top of the hydrogel, and Alamar blue stain was added similar to printed constructs; 3) Negative control: Also, the test was done for the hydrogel itself without any cells to be used as a background (to be deducted from the values measured for the cell-containing gels for that time point). The same experiment was repeated with a different number of cells (2, 4, 6, 8 and 10 million) in 1 mL of the hydrogel and tested after 1 day. Beer-Lambert law was used to generate a straight line equation that helps to find the number of cells at each time point.

3.4 Histopathology

Histopathology is the microscopic study of the changes and the abnormalities found in the tissues caused by a disease. One of the common tests conducted in histopathology is examining haematoxylin and eosin (H&E) stained tissue sections. In this research, H&E stained sections will be focused on along with the phenotype expression test.

3.4.1 Embedding and cutting the constructs

The constructs, whether they are printed or placed manually in the plate, were embedded with paraffin. The fixed samples were processed using ethanol solution to ensure the removal of water. After dehydration, the samples are taken through the clearing process, in which xylene is used to remove the ethanol. The last step is infiltration, where the xylene is replaced with paraffin wax. The constructs were placed in a mould and filled with hot paraffin wax and then it is cooled down so the wax hardens and can be trimmed easily. The embedded construct's blocks were placed securely in a microtome and sectioned at 5 μm. The cut sections were allowed to float in a warm water bath and lifted using a microscope slide or calcium fluoride disk (in case they are used for FTIR imaging). The slides/CaF$_2$ discs were then left to dry.

3.4.2 Staining the constructs with H&E

The Haematoxylin and Eosin dyes give the nuclei a blue/purple colour and the rest of the tissue or hydrogel constructs varying shades of pink. The cut sections first were de-waxed in xylene for 5 minutes, and then they were taken through descending grades of ethanol (100% -70%) to water. The samples then stained with haematoxylin for 5 minutes and allowed to blue in running water for another 5 minutes. After that, they were stained with Eosin Y for 2 minutes and then transferred to 3 different containers of 95% ethanol (1 minute each). The sections then were taken into xylene (3 times) before they were coverslipped.

3.4.3   Immunohistochemistry

The embedded sections were dewaxed using xylene and graded alcohols. They were then placed into an endogenous block for 30 minutes. Antigen retrieval was performed next using Protease K for 10 minutes at 37°C. Slides were then allowed to cool for 10 minutes. The slides were then incubated with the primary antibodies overnight at 4°C. A HRP labelled secondary antibody and DAB substrate was used. The slides were then counterstained with nuclear fast red and coverslipped.

3.4.4   H&E and IHC data analysis

Semi-quantitative analysis was performed using Fiji image following the method used by Crowe and Yue (Crowe and Yue, 2019). The applied method used colour deconvolution and for H&E samples, (H&E) has been chosen, while for IHC samples H&E DAB was chosen. The same method as the reference then applied until the normalised stain intensity is calculated.

3.5   FTIR imaging

With the significant applications of FTIR described insubsubsectionBiomedical applications of Hyperspectral imaging, using FTIR imaging is giving great opportunities for the analysis of the printed constructs containing the hydrogel and the cells. The samples were scanned after embedding and cutting them.

3.5.1   FTIR imaging of the cross-sections

The FTIR imaging data collected by a Varian 670 IR infrared microscope coupled to liquid nitrogen cooled 128 x 128 MCT-FPA detector. The cut sections described on 3.4.1 were placed in CaF$_2$. The transmission mode was used with 128 x 128 scans were recorded with a magnification of x 15. The image size was 740 μm x 740 μm and the pixels 5.5 μm x 5.5 μm. Both the background and samples were done with 576 scans. Each IR image resulted in 16384 spectra with a spectral resolution of 5 cm^{-1} over the range 800 — 3800 wavenumbers. The hydrogel spectra were determined after placing a little of the hydrogel between two CaF$_2$ discs and scanned the same way.

3.5.2   Data processing

The data were processed through MATLAB software. All spectra were kept in the range 1000 — 3600. For the hydrogel and printed samples, a single mean spectrum of all spectra was extracted. The mean spectrum was denoised and the CO$_2$ signal was removed. For the seeded samples, the spectra in the hydrogel side processed as the hydrogel, while the cells side, the

cell finder algorithm was used to ensure having the cells spectra only. After that, the spectra were denoised and the CO_2 signal removed and finally, the mean spectrum was extracted.

Multivariate curve resolution(MCR): The second part of the processing is the use of MCR as following: The data of Printed constructs (Cells-in-hydrogel) was cropped to the range 1000 — 3800 wavenumbers. Then the minimum intensity was set to zero absorbance and After that, RMieS with one iteration was applied.

The data of the hydrogel was cropped to the range 1000 — 3800 wavenumbers. Then the minimum intensity was set to zero absorbance. The spectrum median spectrum then calculated.

The data the hydrogel spectrum appended to the printed construct data. The non-negativity constraint was set since the data was forced minimum of zero in an earlier step. Normalisation of the data then took place. Finally, the Set the number of components was set to two and the MCR was run.

4

Optimisation of printing parameters

Introduction

Peptide-based hydrogels are self-assembled peptides with 3D nanofiber networks that are prepared either using physical assembly or chemical and enzymatic cross-linking. They are biocompatible, biodegradable with microporous structure and a high content of water deriving from their building block consisting of amino acids. Additionally, they have the ability to mimic natural proteins (Liu et al. (2019); Yadav et al. (2019)). The optimisation of printing parameters was employed to ensure the generation of constructs with well-defined geometries and dimensions. Because the printing of hydrogels is directly related to their rheological properties, this optimisation study was conducted separately for all three types of hydrogels employed in this project, namely alpha1, alpha2 and alpha2*. Alpha1 is a neutral hydrogel that has a storage modulus of 5 KPa with pH range 3.1 — 3.8. Alpha2, on the other hand, is a charged hydrogel with storage modulus 10 KPa and pH range 3.1 — 4 and alpha2* is a bespoke hydrogel with pH 3.7 — 4 provided to overcome the limitation of alpha2, which will be described later on this chapter. It has the same chemistry as alpha2 with different amino acids concentration. This chapter will investigate the mechanical properties of these hydrogels, which includes the measurements of storage modulus, loss modulus and viscosity. Furthermore, the steps of the optimisation of the printing parameters are explained.

4.1 Mechanical properties of peptide hydrogels

Mechanical properties of the hydrogels are important criteria to measure since they can be used to judge the ability to use them for specific applications. An example of this is the use of the gel as an extracellular matrix in which the cells have to be within a certain stiffness range, that is important in regulating the cells' adhesion and phenotype expression (Engler et al. (2006); Haines-Butterick et al. (2007); Lee and Mooney (2001b); Yan and Pochan (2010)).

The mechanical properties of the hydrogels can be measured using the same instrument used to test the polymeric materials. The hydrogels, however, have a deformation that can be measured as a function of time as well as the mechanical behaviour. Therefore, the measurements of the mechanical properties are measured either in the time or frequency domain (Oyen, 2014). The elastic properties of the hydrogels were measured using a rheometer and applying Young's modulus. This model gives the relationship between the applied force to the hydrogel and its resultant deformation (Lee et al., 2019) The mechanical properties of these hydrogels were measured after hydrating them with the same amount of media used for cell encapsulation. The use of this amount of media will ensure that the measured properties are as close as possible to the real printing application (cell-laden hydrogels). Since the model will be built by encapsulating the cells in the hydrogel and printing them, and the culture medium will be added immediately after the printing. The medium then will ensure the cells are provided with the needed nutrition to survive and proliferate afterwards. Hence, there is no interest in measuring the mechanical properties of the dry hydrogels. Furthermore, due to the difference in the ion content of the media, the properties will differ, resulting in the test being conducted with the two media used for the cell lines used in the research (RPMI 1640 and F-12 Ham). Testing the mechanical properties of the hydrogels took place after leaving them in the media for 24 hours. The storage modulus (G') and the loss modulus (G'') were measured for the hydrogels: alpha 1, alpha 2 and two batches of alpha2*. The time difference between the purchase of the two different batches and conducting the test is eight months for the first batch and three months for the second. The test result is illustrated in Figures 4.1 and 4.2. Surprisingly, the difference between the two batches of alpha2* hydrogel is very significant, although the shelf life of the hydrogel is up to 18 months, according to the company. The storage modulus results as shown in figures 4.1 and 4.2 indicate that alpha2* has a higher ability to store the deformation energy compared to alpha1 and alpha2. Despite the decrease in the storage modulus of alpha2* with time, it is still the highest compared to the other two hydrogels used in this research.

Figure 4.1: Storage modulus and loss modulus as a function of oscillation strain (%) of the hydrogels alpha1, alpha2 and the two batches of alpha2* in RPMI-1640 medium.
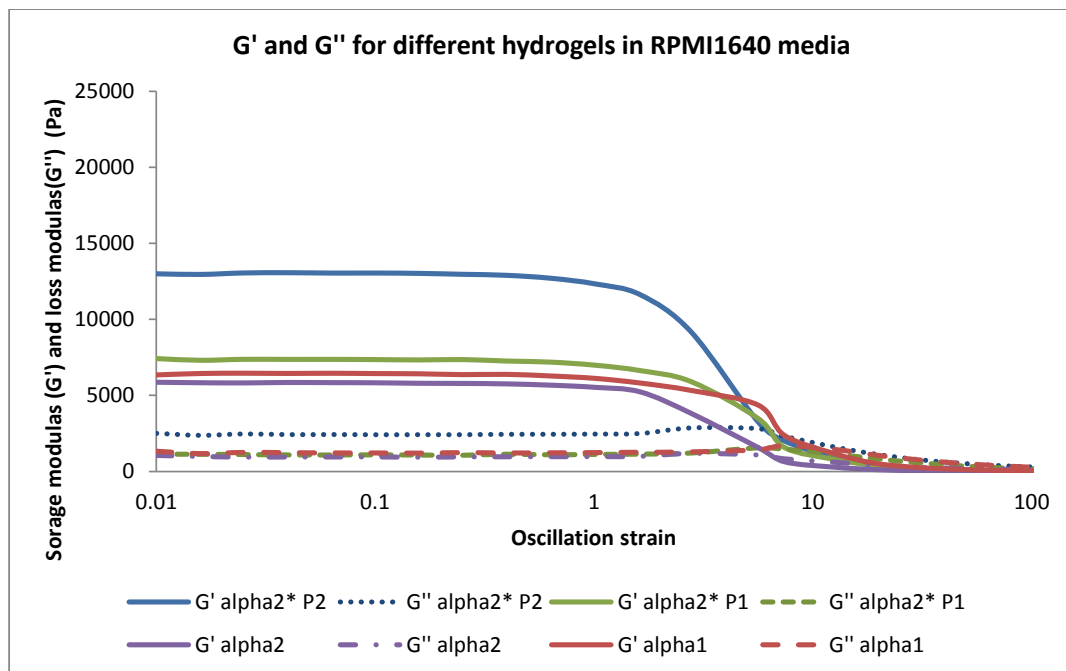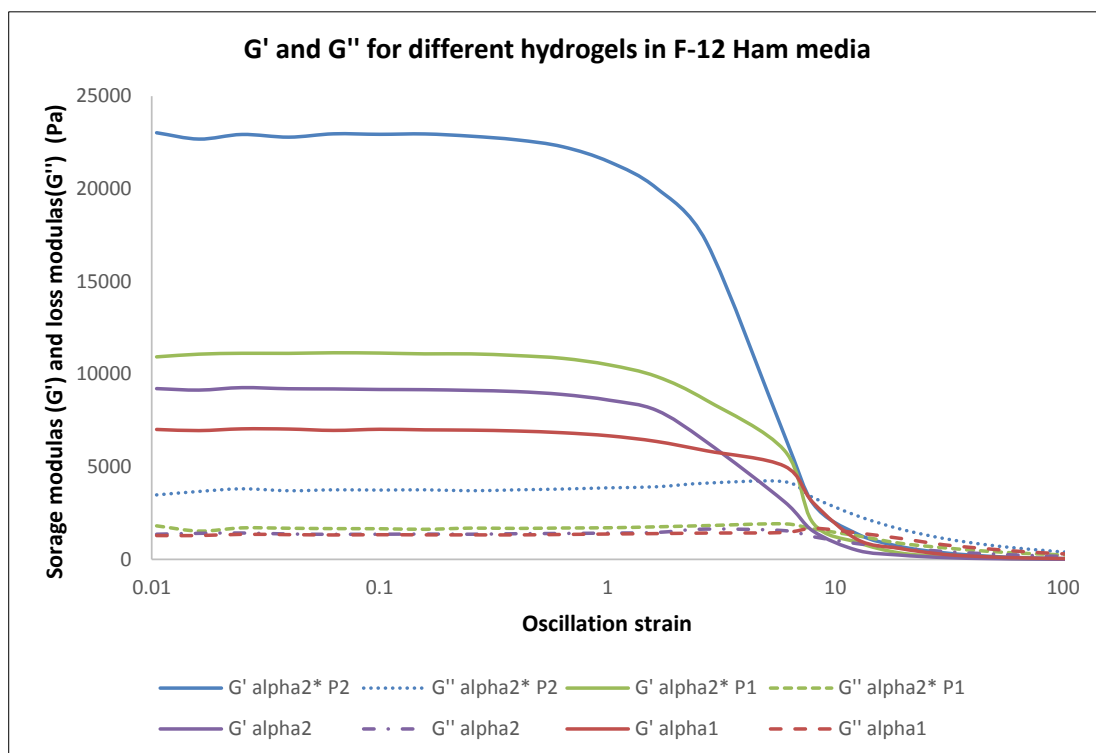

Figure 4.2: Storage modulus and loss modulus as a function of oscillation strain (%) of the hydrogels alpha1, alpha2 and the two batches of alpha2* in F-Ham 12 medium.

Storage modulus is a key indicator for the cross-linking and swelling degree of the

hydrogels. High storage modulus is caused by a high degree of cross-linking, which on the other hand, restricts the swelling of the hydrogel. in contrast, loss modulus (G″) measures the lost deformation energy or dissipated energy and shows the flow property of the material. Measuring the mechanical properties of the hydrogels after the hydration with media shows the significant effect of each media on those properties. As the content of the media differs, the ions will affect the hydrogel differently. The study made by (Koch et al., 2018) on the effect of buffer composition on the mechanical properties of peptide hydrogels shows that a significant increase in storage moduli is observed when divalent ions are used to prepare the buffer compared to when monovalent ions are used. This study concentrates on the effect of the media used for the cells, which were encapsulated on the hydrogel. Comparing the fact that storage modulus increases with the use of divalent ions on the buffer, with the use of different media (RPMI1640 and F-12 Ham), it has been found that the media with more divalent ions (F-12 Ham) has a higher effect on the storage modulus for all three hydrogels. Table 4.1 shows the storage and loss modulus for the hydrogels in the two media at oscillation strain 1 Hz and the difference factor between the two media. Both storage and loss modulus found to be higher when F-12 Ham used by the stated factor in the table below.

Table 4.1: The difference in storage modulus and loss modulus between the hydrogel with F-12 Ham and RPMI-1640 media.

	Alpha2* P2	Alpha2* P1	Alpha2	Alpha1
Storage modulus in F-12 Ham	21100.1	12537.3	13359.5	6926.93
Storage modulus in RPMI-1640	12352.1	7122.21	4875.99	4800.55
Factor of storage modulus	1.71	1.76	2.74	1.44
Loss modulus in F-12 Ham	3952.54	2168.5	2335.29	1320.51
Loss modulus in RPMI-1640	2374.35	1146.47	836.18	953.8
Factor of loss modulus	1.66	1.89	2.79	1.38

The curve of G′ and G″ starts as a flat line with G′ higher than G″, which indicates the elastic behaviour of the hydrogel. This flat line of the curve gives a constate ratio between G′ and G″ in an area that is called Linear-ViscoElastic Region (LVER). This region ends when the ratio starts to vary and become lower with higher shear stress; in other words, the material begins to flow (Bergström and Brown, 2005). The size of the LVER can indicate whether the

material is ductile or brittle since large LVER means the material can store the deformation and so it is ductile, while small LVER means the material has a lower ability to store the deformation and so it can be said it is brittle. Comparing the LVER of the used hydrogels, the difference in the size of the region is small, concluding that this region cannot be used for the elasticity prediction. The same effect was seen in both media. Another important value shown in the curve is the hydrogel breakpoint, which are the points where $G' = G''$. This is the transition point between elastic and liquid behaviours. The breakpoint for each hydrogel found to be higher with F-12 Ham than with RPMI-1640 except for alpha1, in which the media has a very limited effect. Table 4.2 shows the breakpoint values for the hydrogels in both media.

Table 4.2: The hydrogels G' and G'' at the breakpoint in RPMI-1640 and F-12 Ham media

	Alpha2* P2	Alpha2* P1	Alpha2	Alpha1
RPMI1640	2808.73	1566	826.80	1447.12
F-12 Ham	3336.13	1643.51	1226.09	1430.47

The viscosity of the hydrogels was measured as a function of shear rate. The obtained results are shown in Figures 4.3 and 4.4.
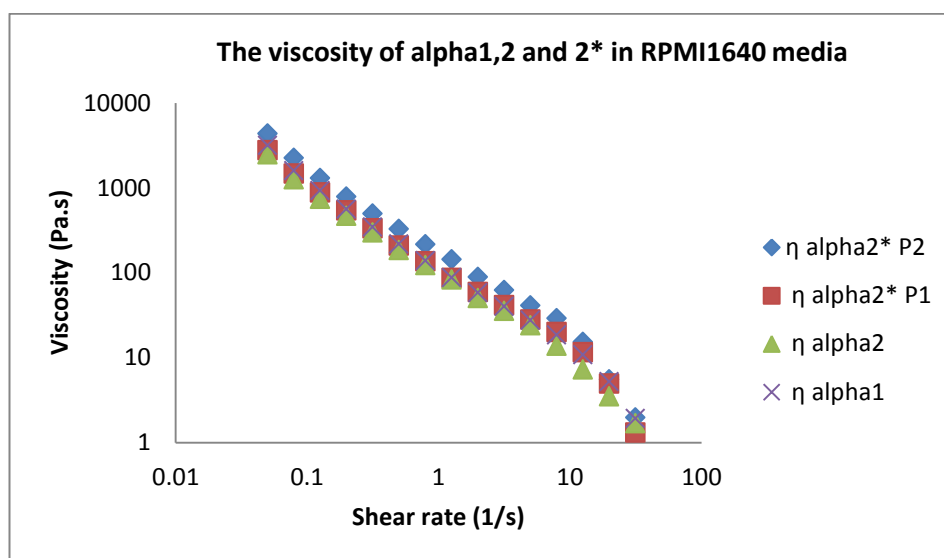
Figure 4.3: The viscosity of the hydrogels in RPMI-1640 media.
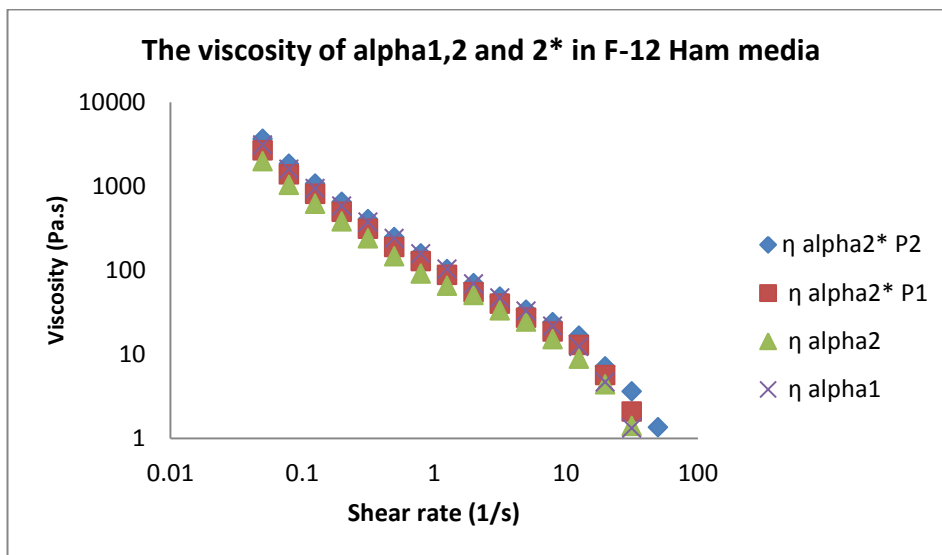
Figure 4.4: The viscosity of the hydrogels in F-12 Ham media.

The general trend of the hydrogels shows shear thinning behaviour. Alpaha2* P2 has the highest viscosity while alpha2 is the lowest for both media. Figure 4.5 shows a closer look at the effect of the media in each hydrogel. The difference in the viscosity of the hydrogels in different media was minimal.
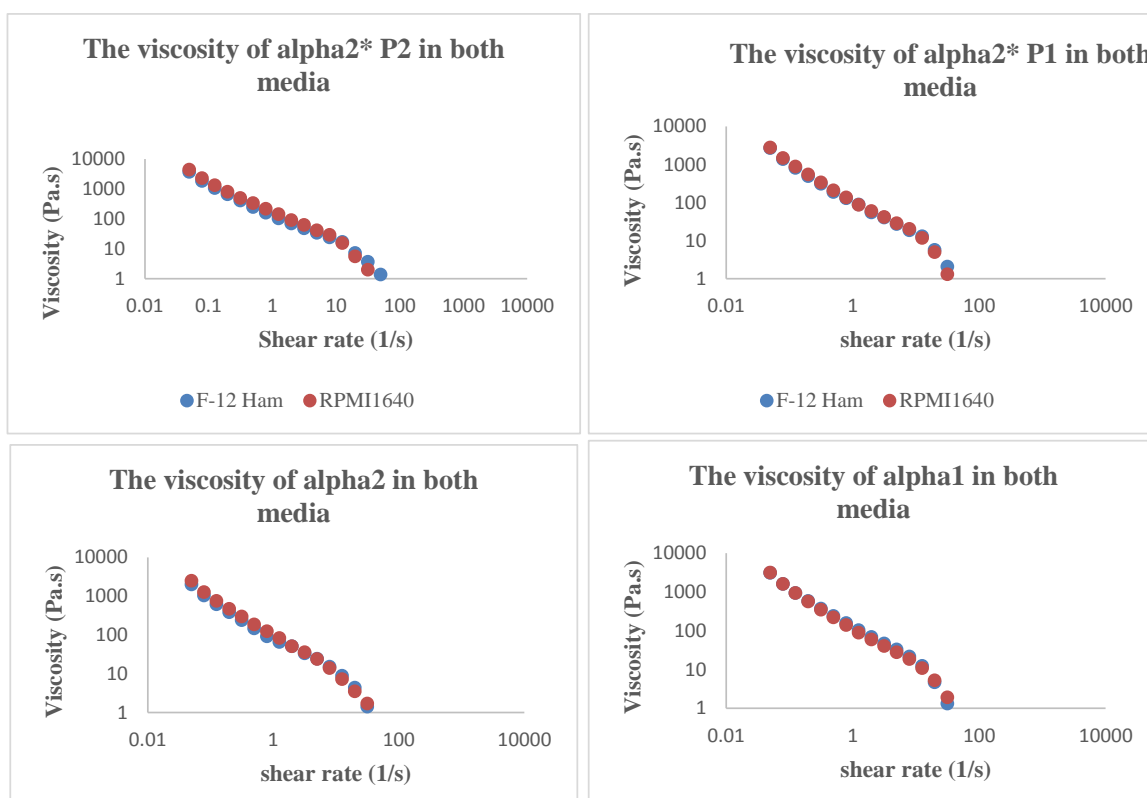
Figure 4.5: The effect of the media on the viscosity of the hydrogels.

4.2 Optimisation of 3D Discovery printing parameters

The printing process was performed using an Additive Manufacturing (AM) system called 3D Discovery bio-printer. The optimisation process aimed to investigate the influence of different process parameters and to determine the optimal printing conditions for the production of 3D cell-laden constructs with well-defined geometries and dimensions. The constructs were designed using BioCAD software. Initially, the constructs were designed as a disc-shape with a 500 μm layer thickness and 1 mm height. During the printing process, a 300 μm nozzle was used and the parameters: Extrusion Pressure (EP), Deposition Velocity (DV), Dosing Distance (DD) and Valve Opening Time (VOT) were modified in order to obtain the required constructs. The hydrogel used for the optimisation process was mixed with 2×10^{-5} (20 μL) of the media (the same amount used for encapsulating the cells on the hydrogel) to get constructs with the same conditions as printing them with the cells.

4.2.1 Optimisation of 3D Discovery parameters for PG alpha1

The following optimisation was done for the hydrogel alpha1 in order to get well-defined constructs.

4.2.1.1 Extrusion Pressure (EP)

The optimisation of the extrusion pressure is significant due to the need for maintaining the amount of extruded hydrogel that gives the required shape. Setting the parameters constant at DV = 0.01 m/s, VOT = 1×10^{-3} s, DD = $1 \times 10^{-4}$ m and varying the EP between 6×10^4 Pa and 2×10^5 Pa, different hydrogel-based constructs were obtained (Table 3). The obtained results demonstrate that by increasing the pressure, the volume of extruded material also increases hence affecting the diameter of printed hydrogels. The calculation of the filament diameter or Road Width (RW) and filament gap show whether or whether not having a reasonably good extrusion rate, which gives a well-defined construct. At low pressure, namely 6×10^4 Pa, the Road Width RW and pore size could not be measured due to the discontinuity of the deposited hydrogel. Increasing the pressure to 1×10^5 Pa the printed filament started to get the shape, but the volume of dispensed material was too much. As the pressure increased to 2×10^5 Pa, the printed filaments were continuous, but filament gab and diameter could not be measured due to the excessive amount of extruded material. Other values of pressure were tested but it was not possible to obtain well-defined constructs in a continuous process. Therefore, the rationale for the optimisation was to use the pressure (1×10^5 Pa) that allow for continuous printing and try to reduce the volume of material by controlling other parameters such as DV, VOT and DD.

Table 4.3: The calculated filament diameter or road width (RW) and filament gap at each pressure value along with the final comment on whether the filament continuous or not

EP (Pa)	RW	Filament gap	continuous	Construct image
2×10^5	2.75×10^{-3} m	0	Yes	
1×10^5	1.40×10^{-3} m	5.1×10^{-4} m	Yes	
6×10^4	Cannot be measured	Cannot be measured	No	

4.2.1.2 Deposition Velocity (DV)

Applying a constant pressure of EP $= 1 \times 10^5$ Pa, VOT $= 1.2 \times 10^{-3}$ s, DD $= 1 \times 10^{-4}$ m and changing the DV between 0.008 m/s and 0.015 m/s it was possible to determine the influence of DV on the dimensions and accuracy of printed constructs (Table 4.4).

By increasing the deposition velocity, it is possible to reduce the dimension of the filament diameter by reducing the volume of material per unit of length. Also, the stretching effect on the deposited material contributes to reducing the diameter of the filaments. From the obtained results, it is possible to observe that the best structures were obtained at high DV (0.015 m/s). However, the definition of the pores and filaments was still far from ideal as the volume of material was too high. Higher values of DV were tested, but the process became non-continuous.

Table 4.4: The calculated filament diameter or road width (RW) and filament gap at each deposition velocity value along with the final comment whether the filament continuous or not.

DV/(m/s)	RW	Filament gap	Continuous?	Construct image
0.008	Cannot be measured	Cannot be measured	Yes	
0.01	Cannot be measured	Cannot be measured	Yes	
0.015	2.13×10^{-3} m	0	Yes	

4.2.1.3 Dosing Distance (DD)

The effect of Dosing Distance (DD) on pore size and filament diameter was evaluated by keeping constant DV = 0.01 m/s, VOT = 9×10^{-4} s, EP = 24×10^{5} Pa and varying DD between 1.9×10^{-4} m and 2.7×10^{-4} m. Obtained results are illustrated in Table 4.5. Increasing the dosing distance is basically increasing the distance between the dispensed portions hence reducing the amount of printed material per unit of length. At DD = 1.9×10^{-4} m, the amount of dispensed material was too high and filament diameter and pore size calculations were unavailable. Increasing the DD to 2×10^{-4} m allowed less material to be printed and the shape was clearly better defined. However, the dimensions of both pore size and filament were still far from ideal pre-defined values. Increasing the DD up to 2.5×10^{-4} m and 2.7×10^{-4} m resulted in non-continuous filament deposition.

Table 4.5: The calculated filament diameter or road width (RW) and filament gap at each dosing distance value along with the final comment whether the filament continuous or not.
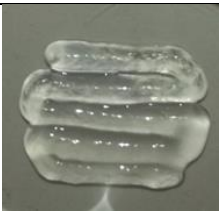
DD(m)	RW	Filament gap	Continuous?	Construct image
1.9×10^{-4}	2.73×10^{-3} m0	0	Yes	
2×10^{-4}	1.13×10^{-3} m	8.3×10^{-4} m	Yes	
2.5×10^{-4}	Cannot be measured	Cannot be measured	No	
2.7×10^{-4}	Cannot be measured	Cannot be measured	No	

4.2.1.4   Valve Opening Time (VOT)

The effect of VOT on the printing process was evaluated by keeping constant the DV = 0.01 m/s, DD = 1×10^{-4} s, EP = 2×10^{5} Pa and varying VOT between 5×10^{-4} s and 3×10^{-3} s. Obtained results are illustrated in Table 4.6.

Increasing the valve opening time means leaving the microvalve of the printing head opened for long periods hence allowing larger volumes of material to be dispensed. Going from 3×10^{-3} s to 1×10^{-3} s and then to 5×10^{-4} s shows this effect. The shape is not distinct at 3×10^{-3} s, but it became better at 1×10^{-3} s. At 5×10^{-4} s, the shape of the filament was very clear and the calculated values of filament diameter and pore size reflect a much better accuracy of the system.

Table 4.6: The calculated filament diameter or road width (RW) and filament gap at each dosing distance value along with the final comment whether the filament continuous or not.

VOT (s)	RW	Filament gap	Continuous?	Construct image
3×10^{-3}	Cannot be measured	Cannot be measured	Yes	
1×10^{-3}	2.11×10^{-3} m	4.6×10^{-4} m	Yes	
5×10^{-4}	8.8×10^{-4} m	1.17×10^{-3} m	Yes	

The optimisation process for the 3D printing of hydrogel constructs is indeed very challenging and the effect of different process parameters on the dimensions and geometries need to be studied carefully. During this process, other values were tested in order to obtain well-defined constructs with good geometrical and dimensional accuracy. The Optimal parameters for the 3D printing of cell-laden hydrogel constructs are in illustrated Table 4.7.

Table 4.7: The Optimal parameters for the 3D printing of cell-laden hydrogel constructs for alpha1.

Parameter	EP (Pa)	DV (m/s)	DD (m)	VOT (s)
Value	6×10^4	0.01	1×10^{-4}	1.5×10^{-4}

A study done by (Raphael et al., 2017) shows the optimal printing parameters for alpha1 using the same bioprinter (3D Discovery) as following:

Table 4.8: The Optimal parameters for the 3D printing of cell-laden hydrogel constructs for alpha1 (literature).

Parameter	EP (Pa)	DV (m/s)	DD (m)	VOT (s)
Value	1×10^5	0.01	1×10^{-4}	3×10^{-4}

The difference in the obtained parameters between Raphael *et al.*, and this study might be

due to the batch to batch variation, which was one of the problems faced when the company started to sell these types of hydrogels. Another reason is the period between the purchase of the hydrogel and the printing, which has been proven to affect the mechanical properties as shown above for alpha2* and so the printing parameters will change. Different media added to this hydrogel and did not affect the printing parameters and the parameters were found to the same with and without media.

4.2.2 Optimisation of 3D Discovery parameters for alpha2 and alpha2*

The parameters of both alpha2 and alpha2* were obtained based on Alpha 1. Since alpha2 has the lowest viscosity, as shown in Figures 3 and 4, it flows more and finding an excellent geometrical construct was challenging. Comparing to alpha1, adding culture medium makes a difference in the parameters, so the optimisation was done with the culture media on. Different culture media gives the same parameters. The same behaviour was seen with alpha2* as well except that the printed constructs have much better geometry that alpha2, which is due to the high viscosity of alpha2*. The optimal parameters were found to differ between alpha2*P1 and 2 and that might be due to the change in viscosity between the two. The optimal parameters obtained for alpha2, alpha2* P1 and alpha2* P2 with the photos of the printed constructs at the optimal parameters are shown in Table 4.9

Table 4.9: The Optimal parameters for the 3D printing of cell-laden hydrogel constructs for alpha2 and the two batches of alpha2*.

Parameter	EP (Pa)	DV (m/s)	DD (m)	VOT (s)	
Alpha2	6×10^{4}	0.01	8×10^{-5}	9.5×10^{-4}	
Alpha2* P1	6×10^{4}	0.01	1×10^{-4}	7×10^{-4}	
Alpha2* P2	6×10^{4}	0.005	1.3×10^{-4}	2×10^{-4}	

With the variations in the mechanical properties and the printing parameters of the different batches of alpha2* hydrogel, the cells encapsulation, printing and assessment all took place for hydrogel batches with almost up to three months period from the purchase time.

4.3   Conclusion

The study of the mechanical properties of the hydrogels and the optimisation of their printing parameters is crucial to investigate the ability to build a model that enables the study of prostate cancer. This chapter aims to examine the storage modulus, loss modulus and viscosity of the hydrogels (alpha1, alpha2 and alpha2*) with the use of the RPMI-1640 and F-12 Ham media. Moreover, the optimal printing parameters of these hydrogels are explored.

The use of media on the hydrogels was found to have a massive effect of their elasticity, yet does not affect their viscosity. To the best of our knowledge, this is the only study that studies the effect of different media on the mechanical properties of this type of hydrogels. This suggests that the composition of the media used in this research has a direct effect on

the hydrogels' elasticity. These findings require more investigations in order to confirm the effect of the media on the mechanical properties of the hydrogels.

During the optimisation process of the printing parameters of the hydrogels (alpha1, alpha2 and alpha2*), the hydrogel's viscosity found to affect the printing process in order to a well-defined geometrical construct. The study indicates that the least viscous hydrogel (alpha2) was the most challenging in obtaining the optimal printing parameters. Nevertheless, the viability of the cells in alpha2 was still examined to optimise the best environment for cells' survival. The viability test of the used hydrogels is described in chapter 5.

5

In Vitro Biological Assessment of Cell Viability and Metabolic Activity

Introduction

ExtraCellular Matrix(ECM) is a complex non-cellular network composed mainly of protein, glycosaminoglycan, and glycoconjugate (Fajardo et al. (2016); Frantz et al. (2010); Gough et al. (2012)). Manchester BioGel company hydrogels are made in order to mimic the ECM. No previous study has directly investigated the use of these peptide hydrogels as an ECM for prostate cancer cells. In this chapter, biological assessment of the use of these hydrogels (alpha1, alpha2 and alpha2*) as ECM for three prostate cancer cell lines, PC3, LNCaP and PNT2 are discussed. The key research question of this study was whether or not the cells are viable in the different hydrogels used and whether the cells are proliferating or not. The biological assessments that will be discussed in this chapter are the adhesion test, live/dead viability test and metabolic activity test.

5.1 Adhesion of Cells in the Hydrogel

Cells adhesion is their ability to stick to the extracellular matrix or other cells or even the well plate surface when cultured in a two dimensional (2D) system. The importance of cell adhesion comes from its significant role in the communication and signalling between the cells as well as the maintenance and the development of the tissues (Khalili and Ahmad, 2015). Cancer cells, on the other hand, are found to have abnormal cell adhesion, which affects the morphogens and the biological characteristics of the cells. The adhesiveness of cancer cells is much lower than it is in healthy cells and this allows them not to follow the regular signalling between the normal cells. The regular signalling of the cells maintains the social order of the cells and the case of cancer it is lost and so the histological structure found destroyed in the

malignant (Hirohashi and Kanai (2004); Khalili and Ahmad (2015). The adhesion of prostate cancer cells was studied by seeding the cells in the top of the hydrogels alpha1 and alpha2.

5.1.1 2D cell adhesion and viability

PC3 cells were directly seeded on top (2D) of the alpha1 hydrogel previously deposited on the bottom of 6-well culture plates and allowed to settle down for 24 hours. The microscopic images of the well containing the hydrogel and the cells are shown in Figure 5.1 (a & b). Interestingly, the cells were seen attaching exclusively on the well-plate and not on the hydrogel. In order to confirm this observation, a live/dead test was performed and the result is shown in Figure 5.1 (c). The live cells were surrounding the hydrogel and none of them was in the hydrogel. This test supports the idea that cells were adherent to the surface of the plate but not the hydrogel.
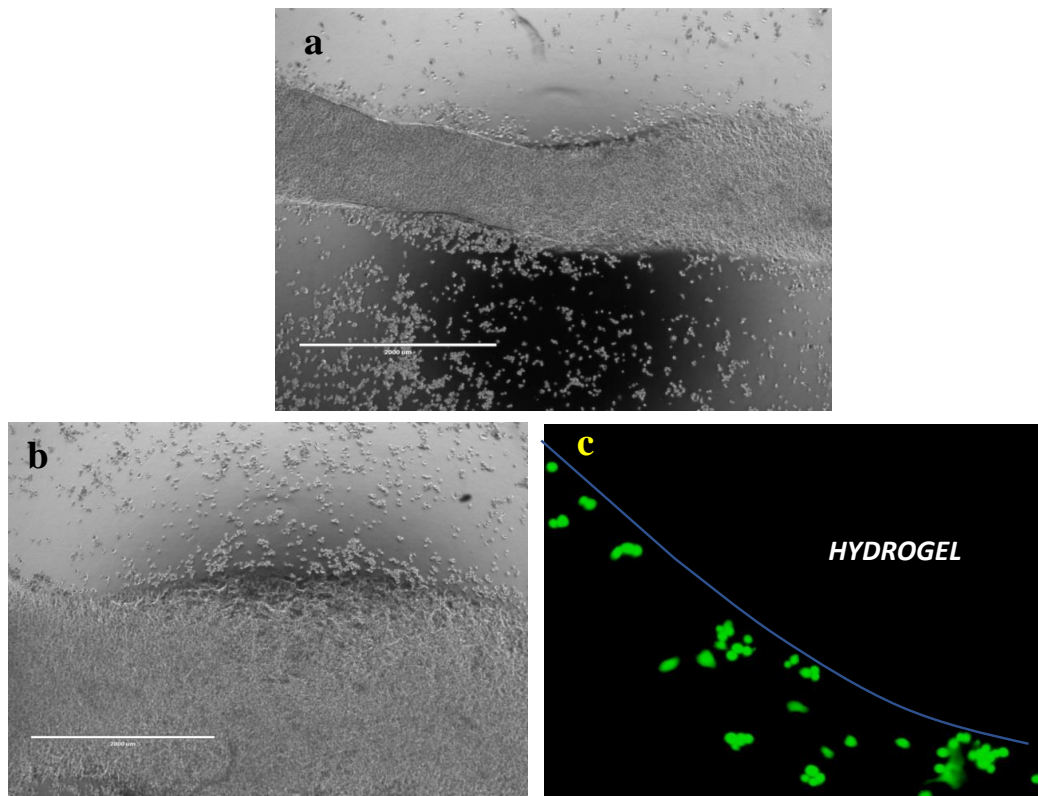
Figure 5.1: Microscopic image of the seeded cells in alpha1 hydrogel (a and b) where the cells are seen in the plate only. The viability test result (c) shows the cells stained in green for live cells with no sign for cells in the hydrogel, neither live (stained green) nor dead (stained red). The scale in the images is 2000 μm

Further investigation was carried out by forcing the cells to attach to the hydrogel. For that purpose, the wells were covered completely by the hydrogel and no spaces were left on

the bottom of the well plate for the cells. In this second experiment, three cell lines were used, namely PC3, PNT2 and LNCaP. An additional sample was prepared by culturing the cells in the well plate as a positive control with no hydrogel to allow the comparison of the different samples with the cells only and ensure live cells were used. The microscopic images of the seeded cells on top of the hydrogel and the cultured cells are shown in Figure 5.2. The difference between the cells only and cells on top of hydrogels can be seen clearly. The appearance of the cells on the surface of the plate shows that the cells were alive and adherent to the plate surface; however, they were not seen on the surface of the hydrogel. The hypothesis that will be tested is the influence of the hydrogel acidity on the low adhesion of the seeded cells. Since the hydrogel has a pH range of 3.1 — 3.8, it is suggested that it might have an effect on the cells adhesion.
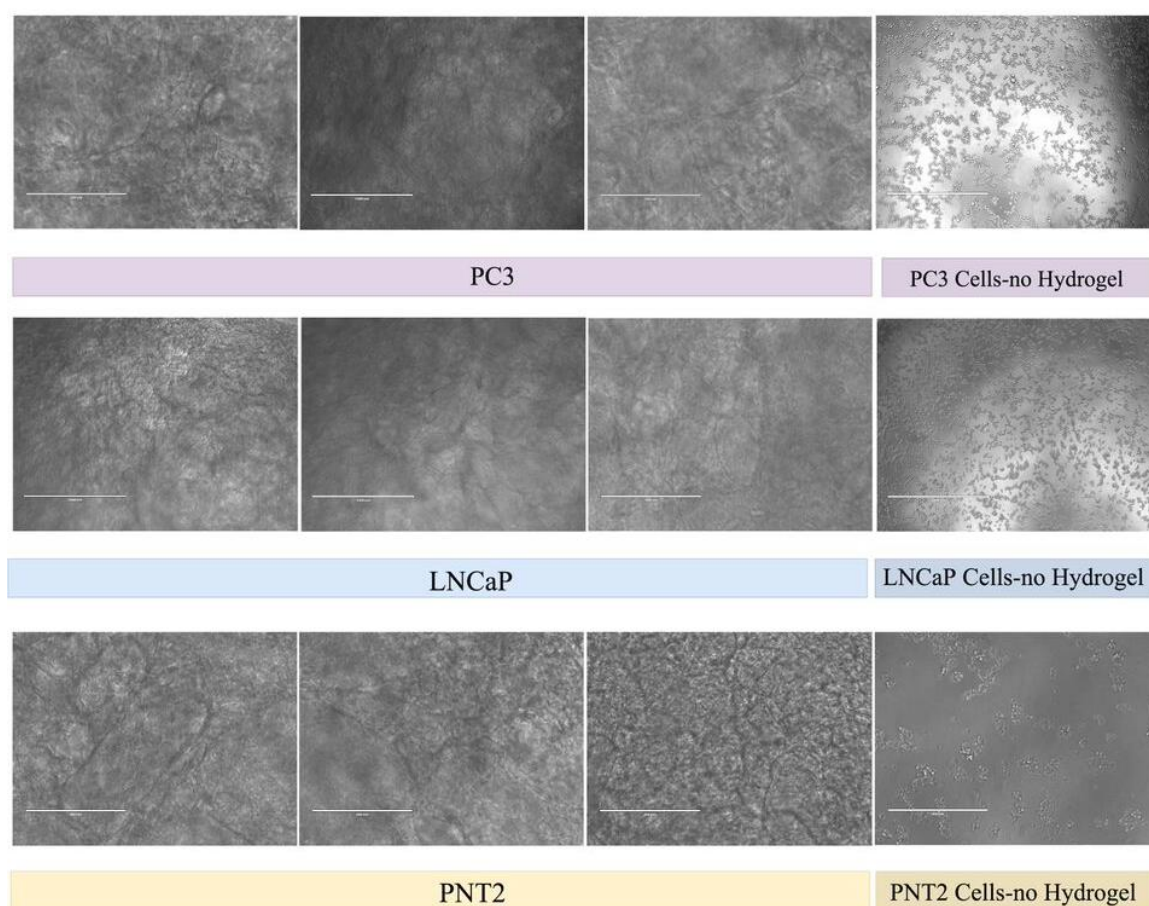
Figure 5.2: Microscopic images of the seeded cells in alpha1 and the one with no hydrogel.The images for each cell line are from replicated experiments.

Opportunities to investigate the effects of the hydrogel acidity on the adherent cells, the hydrogel was neutralised before seeding the cells. Alpha1 hydrogel was neutralised by adding culture media on top of the hydrogel and allowed to settle for 24 hours prior to cell seeding. No significant difference was seen on the microscopic images (Figure 5.3) of the neutralised

hydrogel seeded with prostate cancer cells. The cells also were not seen in the surface of the hydrogel. These results suggest that alpha1 hydrogel does not have the ligands (binding sites) that prostate cancer cells need to attach or bind to. Based on these results, alpha1 hydrogel was replaced by a more cell-adhesive hydrogel (alpha2) and the experiments repeated.
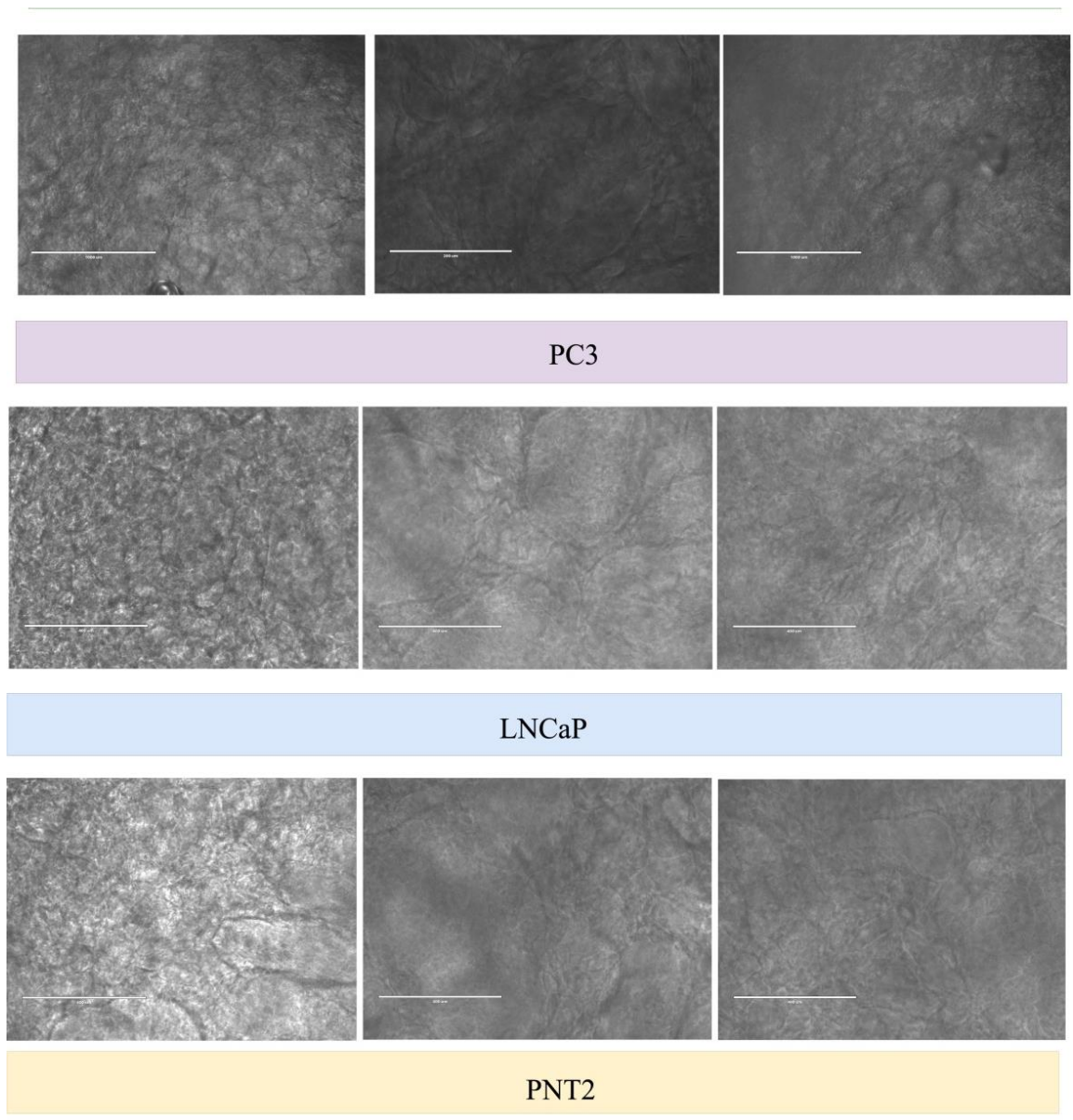
Figure 5.3: Microscopic images of the seeded cells in neutralised alpha1.The images for each cell line are from replicated experiments.

Prostate cancer cells were seeded on top of alpha2 hydrogel in a similar process to alpha1. The microscopic images of both normal (Figure 5.4) and neutralised (Figure 5.5) hydrogel show that the cells of all cell lines are adherent to the surface of the hydrogel.
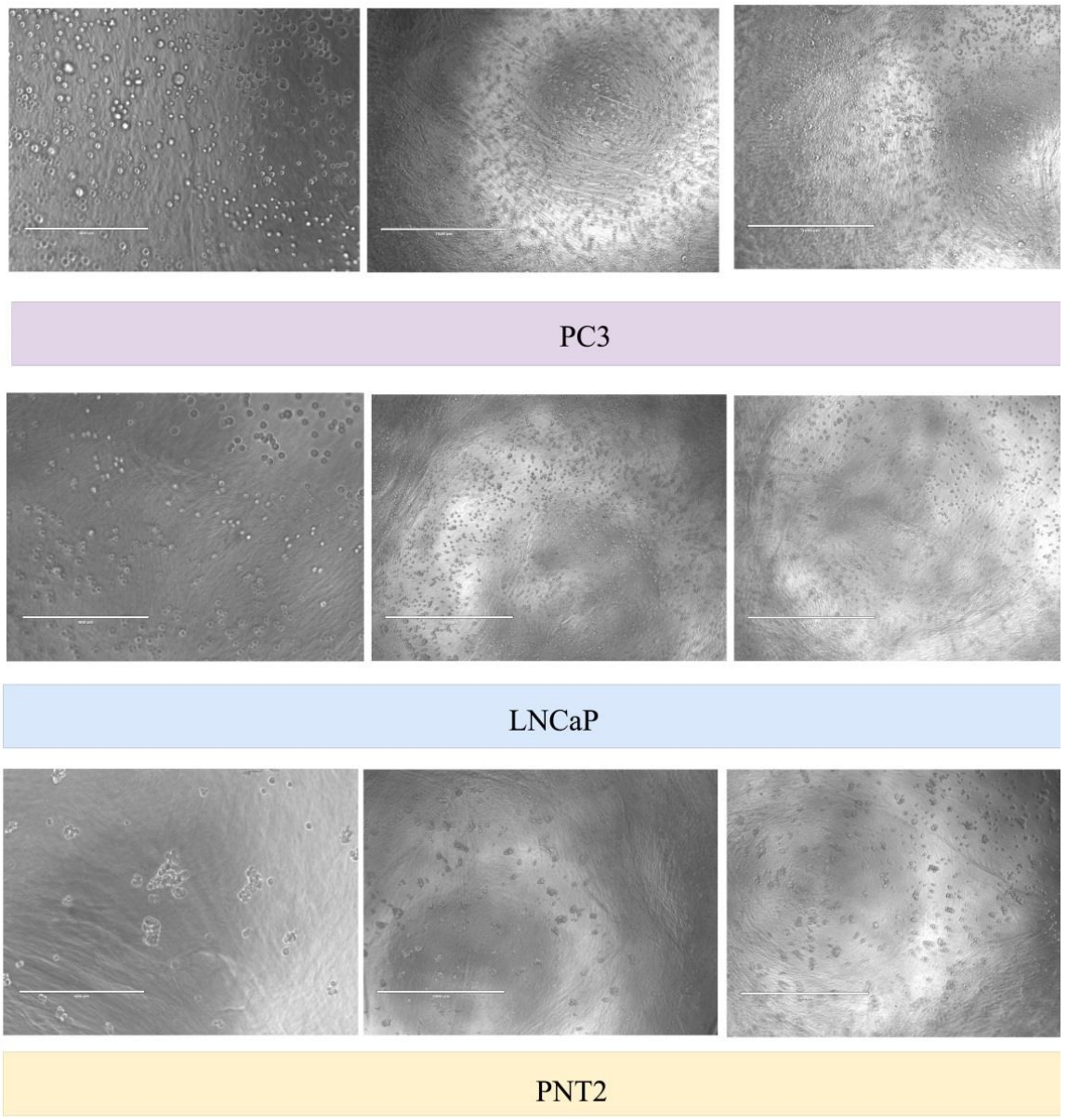
Figure 5.4: Microscopic images of the seeded cells in alpha2, showing the cells on top of the hydrogel. The scale bar is 1000 μm. The images for each cell line are from replicated experiments.
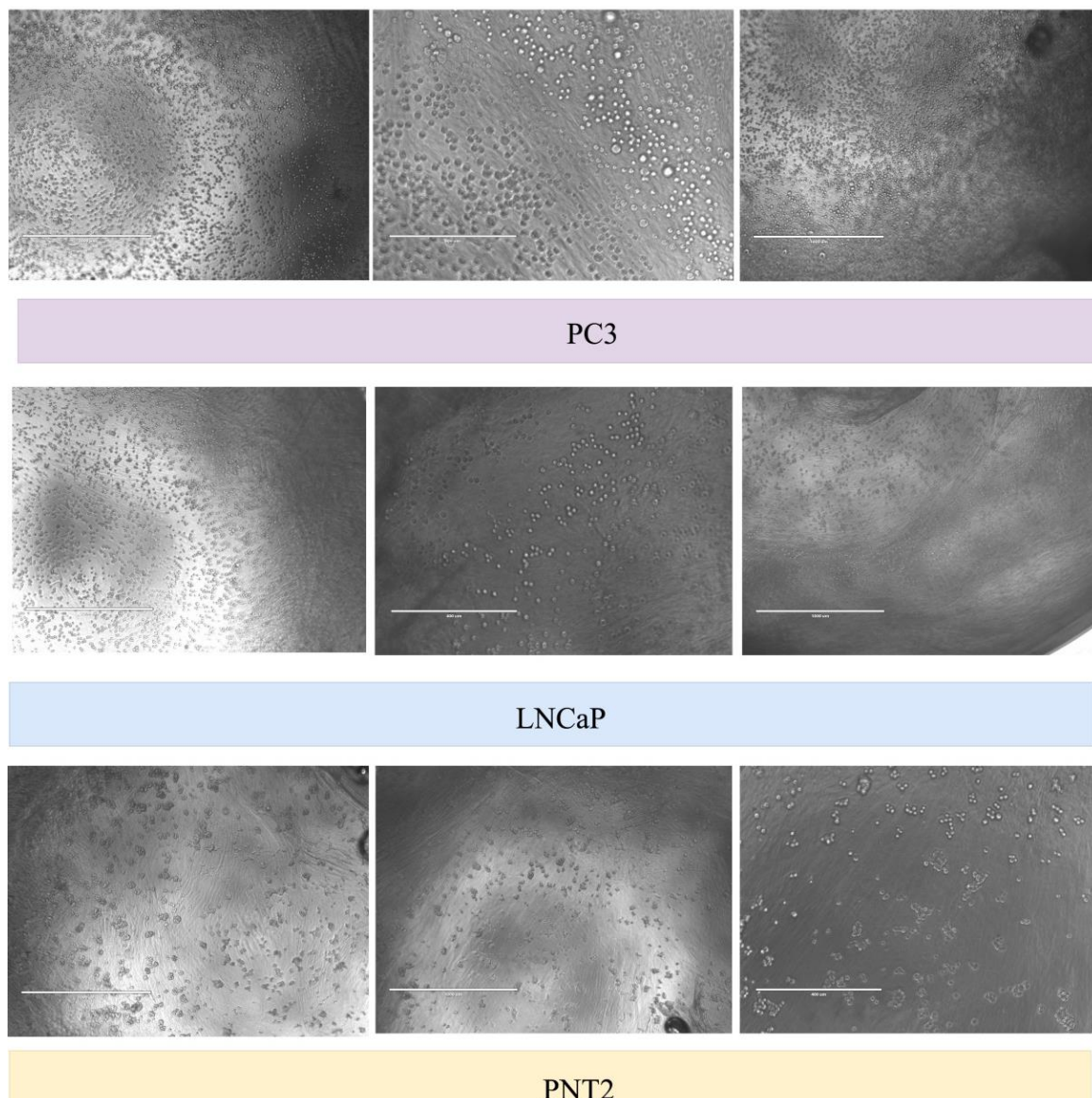
Figure 5.5: Microscopic images of the seeded cells in neutralised alpha2, showing the cells on top of the hydrogel. The scale bar is 1000 μm.The images for each cell line are from replicated experiments.

All prostate cancer cell lines used in this research (PC3, PNT2 and LNCaP) are found to be non-adherent to alpha1 and adherent to alpha2 regardless of the neutralisation of the hydrogels. Research on seeding cells on the hydrogels is limited, and none was found with prostate cancer cells. One of the studies that was successful in seeding cells in the top of the hydrogel is Faroni et al. Study. The study shows the viability of human adipose-derived stem cells (hADSCs) seeded on both alpha1 and alpha2. Their test shows that cells have different morphology in which rounded shape is seen for cells seeded in alpha1 while the cells seeded in alpha2 had spindle shape. The spindle shape, though was the shape of the cells when they were cultured in a plastic well plate. Additionally, the motility of cells was found to be higher when they are seeded in alpha1 rather than alpha2. The first suggested reason behind

the change in the effect of the two gels on the cells motility, proliferation and phenotype differentiation is the stiffness of the gels, and it has a marginal impact. The second reason is the charge, and it is found to lead to differences in the mechanical properties of the gel (Faroni et al., 2019).

5.2   3D cell viability

Cell viability can be defined as the count of the number of healthy cells within a specific sample. The proliferation, though, can be measured by repeating the test over different time points. There are various methods available to test the viability of cells, such as trypan blue, live/dead assay, Alamar blue and Raman microscopy. The choice of the right test usually depends on the cost and the speed of the test, along with the test complexity of the method and equipment and the aim of the analysis.

5.2.1   Live/Dead Viability Test

Live/dead viability assay is a test used to determine the viability of cells and enables counting both live and dead cells. The viability of the cells is determined based on the plasma membrane integrity and esterase activity of cells. The test differentiates the live from dead cells by indicating the intracellular esterase activity of the live cells, which will be stained green by calcein-AM to and indicating the loss of plasma membrane integrity in dead cells and stain them red with ethidium homodimer-1. The test was performed for cells in different conditions; manual encapsulation without printing to avoid the shear stress and the printed constructs. All the three cell lines (PC3, PNT2 and LNCaP) were tested in the three different hydrogels (alpha1, alpha2 and alpha2*). The various test results are discussed in the next subsections.

5.2.1.1   Cells Encapsulation with Manual Printing

Although the cells were found not to be adherent the surface of alpha1, it is still reasonable to encapsulate the cells in the hydrogel and investigate their viability. It is thought that cells might react differently when they are encapsulated in the hydrogel rather than seeded in the top of it. The cells encapsulation was done manually, as described in chapter 3.3.2. PC3 cells were encapsulated in alpha1 hydrogel and the live/dead test was performed after one hour of the encapsulation. The choice of one hour as the period for the test is to find the response of the cells after a short period of encapsulation. Also, to check whether the cells were able to adapt the new environment and can stay alive with the fact that they are not adherent to the surface of this gel. The resulted images are shown in Figure 5.6.
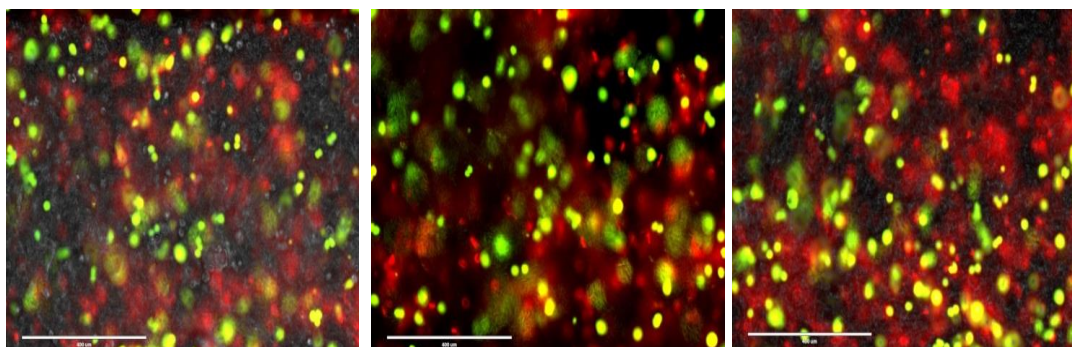
Figure 5.6: Live/dead viability test result (fluorescence images) for PC3 cells encapsulated in alpha1 and placed in the well plate manually.The scale in the images is 400 μm. The images were taken from replicated experiments.

Figure 5.6 shows the presence of both green (indicating live cells) and red (indicating dead cells) colours. Additionally, the yellow colour was noticed, which is believed that caused by the presence of live and dead cells on top of one another. In order to get a better sense of this finding, the estimated percentages of live and dead cells was calculated. Image J was used to calculate the number of live and dead cells after separating the green and red colours in each sample (see section 3.3.4. The percentages found through this part are not 100 % accurate since cells are growing in 3D and not all the layers can be seen through this microscope. The calculated percentages showed that the percentage of dead cells was high with 53 %, while the percentage of live cells was 47%. The significance of this result comes from the ability of the cells to live inside the hydrogel even if they are not adherent to its surface. This result is encouraging to go forward to the printing with a bio-printer. Further investigations were done with the printed samples since it is important for the cells not to be affected by the shear stress when they are printed and considering that cells will require more than 1 hour to adapt to a 3D environment. The printed (using a bio-printer) are far more important in order to get reproducible constructs with the same structure.

The same concept that has been followed in alpha1 hydrogel was followed for alpha2. With the fact that cells are adherent to the surface of alpha2 hydrogel, the test has been widened to include all three cell lines and the assessment of the viability of the cells was performed at different time points. PC3, LNCaP and PNT2 cells were encapsulated on the hydrogel, and live/dead viability test was performed after 1, 3, 7 and 14 days. Compared with PC3 cells in alpha2, the same cell line in alpha2 shows more viable cells. The estimated percentage of live

cells increases from 72% on day 1 to 94 % on day 14 (see Table 5.1). The microscopic images of PC3 cells in alpha2 at different time points are displayed in Figure 5.7. This indicates how PC3 cells were able to adapt the environment of alpha2 hydrogel.

Table 5.1: The estimated percentages of live and dead cells for PC3, LNCaP and PNT2 after 1, 3, 7 and 14 days.

	day 1		day 3		day 7		day 14	
	Live	**Dead**	**Live**	**Dead**	**Live**	**Dead**	**Live**	**Dead**
PC3	72	28	76	24	89	11	94	72
LNCaP	86	14	67	33	82	18	49	86
PNT2	93	7	76	24	94	6	87	93
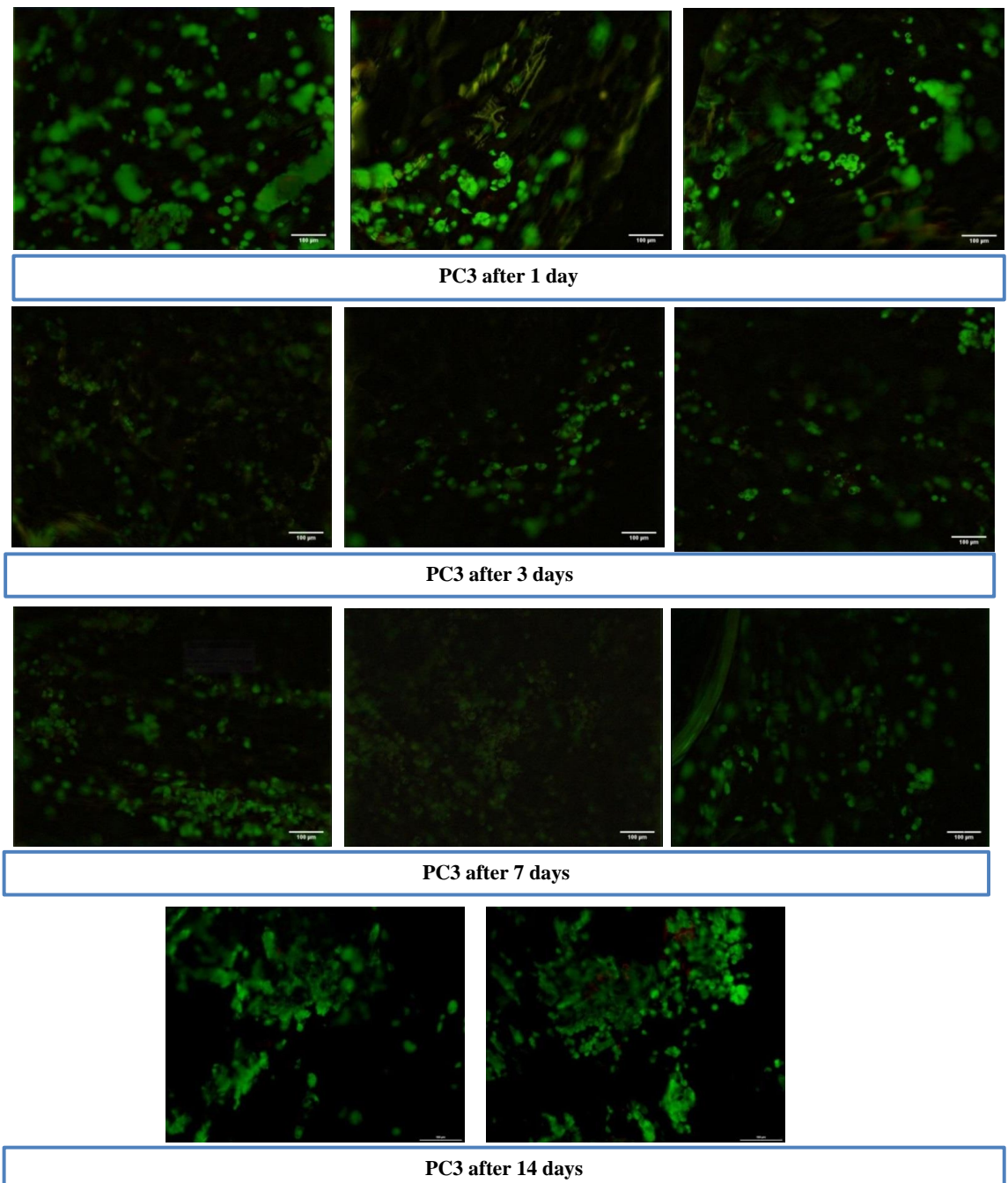
Figure 5.7: Live/dead viability test results (fluorescence images) for PC3 cells encapsulated in alpha2 at different time points.The scale in the images is 100 μm. The images for each time-point are from replicated experiments.

Interestingly, the LNCaP cells interact differently in which more dead cells were seen in the samples and the estimated percentages show that there was a fluctuation in the number of live and dead cell over time. The images resulted from the live/dead test can be seen in Figure 8 and the estimated percentages are illustrated in Table 5.1. On day 14 the percentage of dead cells found to be more than 50%. This fluctuation might be explained by the sensitive nature of LNCaP cells compared to the other cell lines. Further studies need to be done to

find the time needed for LNCaP cells to adapt this environment fully or they might collapse and die after some time. The third cell line PNT2, is found to adapt the hydrogel environment and the estimated percentage of live cells was higher than the dead cells in all tested time points. Cells were proliferating and reaching almost 87% by day 14. Figure 9 shows the images resulted from the live/dead test for PNT2 and the percentages of the live and dead cell can be seen in Table 5.1.
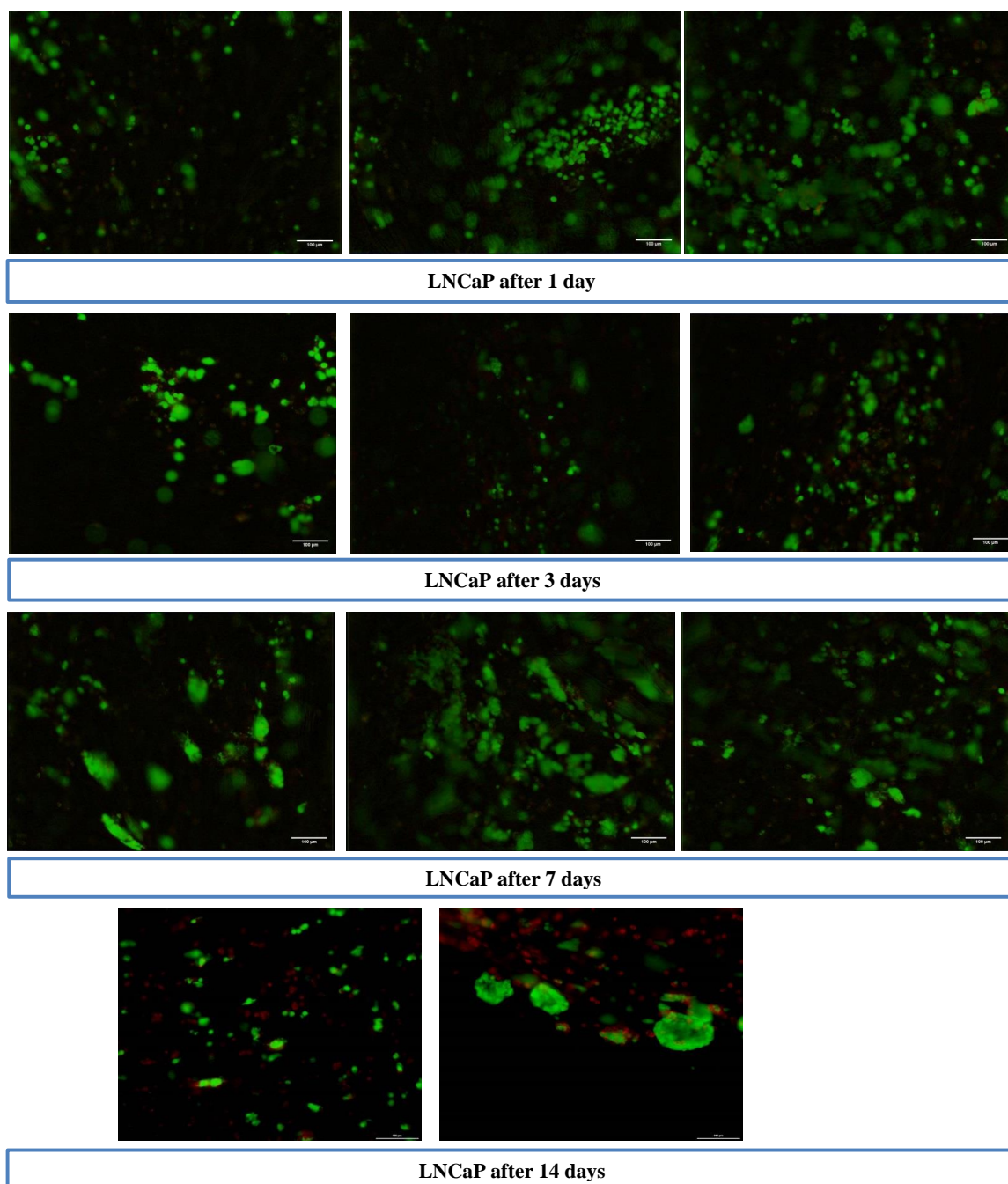
Figure 5.8: Live/dead viability test results (fluorescence images) for LNCaP cells encapsulated in alpha2 at different time points. The scale in the images is 100 μm. The images for each time-point are from replicated experiments.

Figure 5.9: Live/dead viability test results (fluorescence images) for PNT2 cells encapsulated in alpha2 at different time points. The scale in the images is 100 μm,The images for each time-point are from replicated experiments.

Overall, the results of encapsulating prostate cell line in alpha2 hydrogel indicate that this hydrogel can work better than alpha1 and the cells were able to survive for at least 14 days. The reader, though, should bear in mind that this test was done with manual printing. The effect of the hydrogel on cells proliferation might not be the same when the hydrogel printed by a bio-printer due to the other factors affecting the viability of the cells, such as shear stress.

A detailed analysis of Live/dead viability test results of the printed samples is given in the next section.

5.2.1.2   3D bio-printing and *in vitro* cell viability

The printing process was implemented using 3D Discovery bioprinter. 2 million cells were encapsulated in 1 mL of the hydrogel following Raphael *et al.* in their study (Raphael et al., 2017). With alpha1 hydrogel, both one layer and four layers constructs were printed and the viability of the cells was measured with the live/dead assay test. The printing process added shear stress to the equation, so it is expected to see some differences from the manual printing. The test firstly is done with PC3 cells and the viability test results after one hour, 2 hours and 1 day are shown in Figures 10, 11 and 12. Interestingly, the number of living cells after one hour was higher (Figure 5.10). The estimated number of live cells is 54%. Dead cells were mainly concentrated on the sides of the hydrogel.
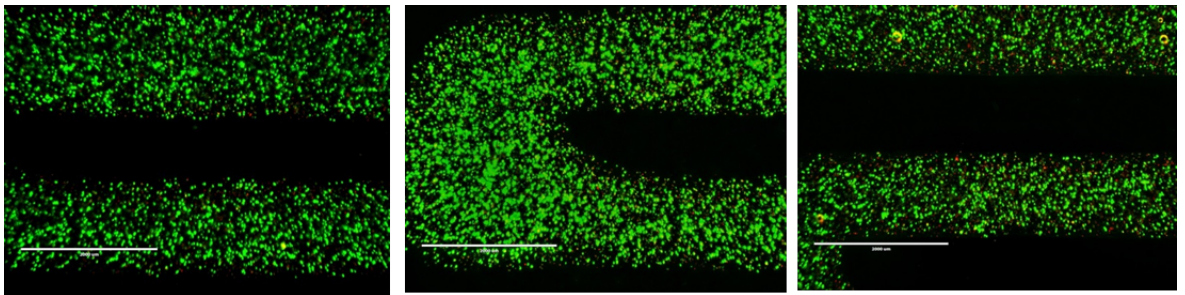
Figure 5.10: Live/dead viability test result (fluorescence images) for the printed construct of PC3 cells and alpha1after one hour of incubation. The scale in the images is 2000 μm. The images are from replicated experiments.

After 2 hours of incubation, more cells were found dead. In each sample, some areas contain only dead cells and others still have live cells with the domination of the dead cells (Figure 5.11). The estimated percentage of live cells drops to 35.57%. A possible explanation for this might be that the cells undergo apoptosis signalling and consequently cell death.
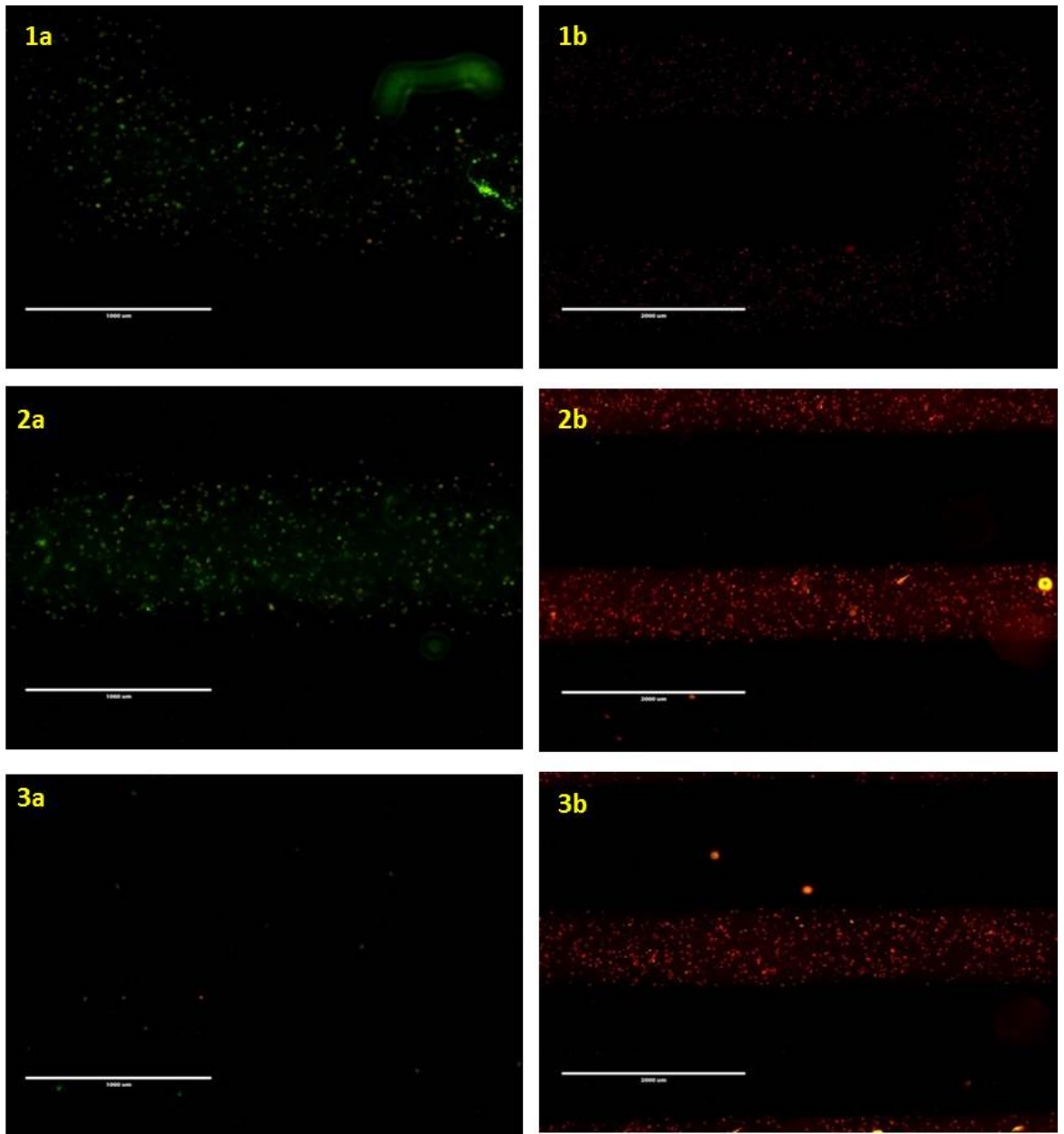
Figure 5.11: Live/dead viability test result (fluorescence images) for the printed construct of PC3 cells on alpha1 after two hours of incubation. (a) and (b) are different areas of the same sample. The scale in the images is 1000 µm for (a) images and 2000 µm for (b) images

The application of the viability test after one day of the incubation shows that a very high percentage of cells were dead and less than 3% of cells were alive (Figure 5.12). The Apoptosis signalling seems the most appropriate explanation for it
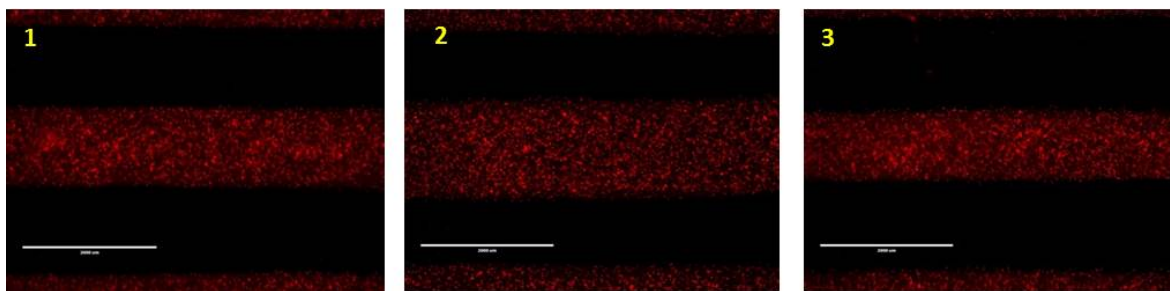
Figure 5.12: Live/dead viability test result (fluorescence images) for the printed construct of PC3 cells on alpha1 after one day of incubation for the three samples. The scale in the images is 2000 μm

A significant problem was found when printing the constructs with alpha1 is the loss of parts of these construct as they found floating in the culture media. The amount of these constructs left, though, was enough to go through the viability test and find the estimated number of live and dead cells. On the other hand, printing four-layer constructs using alpha1, showed the domination of dead cells as shown in Figure 5.13 with a percentage of 98. This might be due to the long time for the nutrients to reach all the cells within the layers of the hydrogel after longer printing time (compared to one layer printing). The printing time, starting from encapsulating the cells until the addition of the media to the construct after printing, for one layer is 2-5 min, while for four layers, it is 7-10 min.
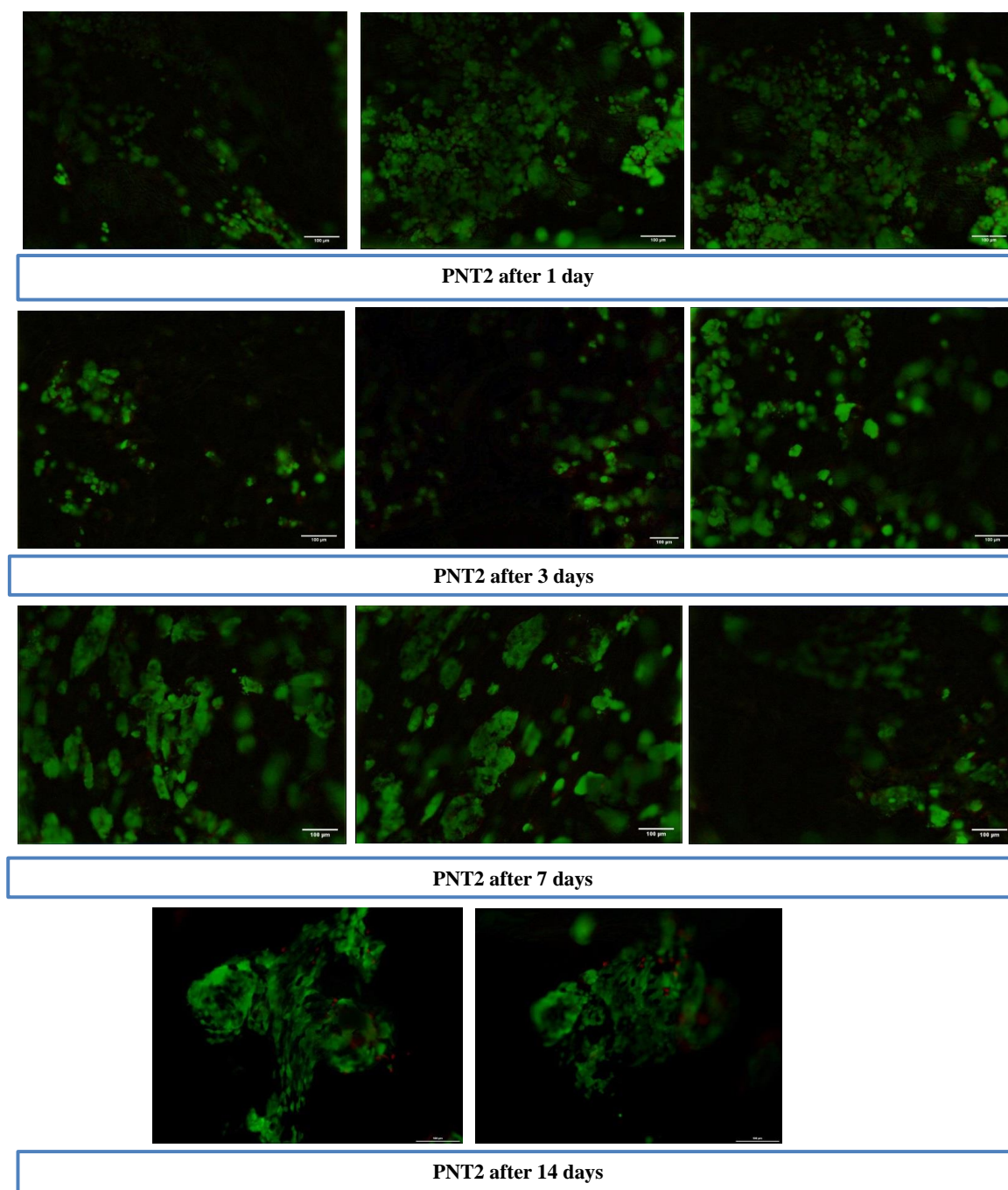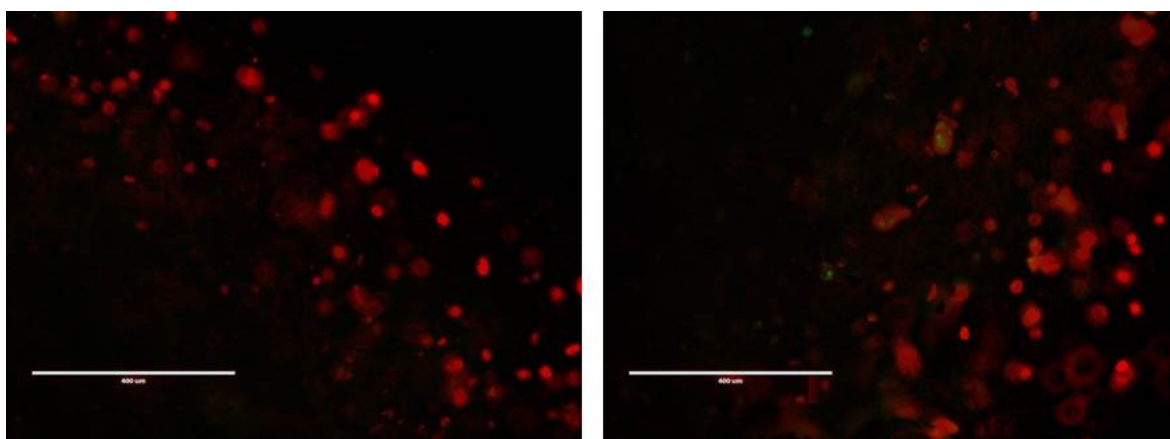

Figure 5.13: Live/dead viability test result (fluorescence images) for PC3 cells encapsulated in alpha1 and printed in 4 layers.The scale in the images is 400 μm. The images are from replicated experiments.

This result suggests the attention has to be drawn to the one layer construct to be optimised first and only then the four layers construct can be built and tested. Having the focus to be on the one layer construct The interaction of the three cell lines (PC3, LNCaP

and PNT2) in PG alpha1 was studied by printing them and testing their viability (PC3 was repeated along with LNCaP and PNT2). The same previous method and printing parameters were used. Live/dead test was done after one hour and one day of incubation. The estimated percentages of the live and dead cells are illustrated in Table 5.2. What stands out in this table is the dominance of dead cells. Figure 5.14 shows the images taken for the live/dead test for all three cell lines. Surprisingly, most of the PC3 cells were found dead even after one hour (less than 2% were alive). The difference in these results each time the test was repeated might be because of the variation from one batch to another. In all cases, though, the cells were not able to stay alive for 24 hours. The number of live cells for PNT2 and LNCaP was also small and did not exceed 6%.

Table 5.2: The percentage of live and dead cells for PC3, LNCaP and PNT2 after one hour and one day.

	% of cells after one hour		% of cells after one day	
	Live	Dead	Live	Dead
PC3	2	98	3	97
LNCaP	6	94	4	96
PNT2	4	96	5	95

Despite the repetition of the experiment, the estimated percentages of live cells of the three cell lines were very low.
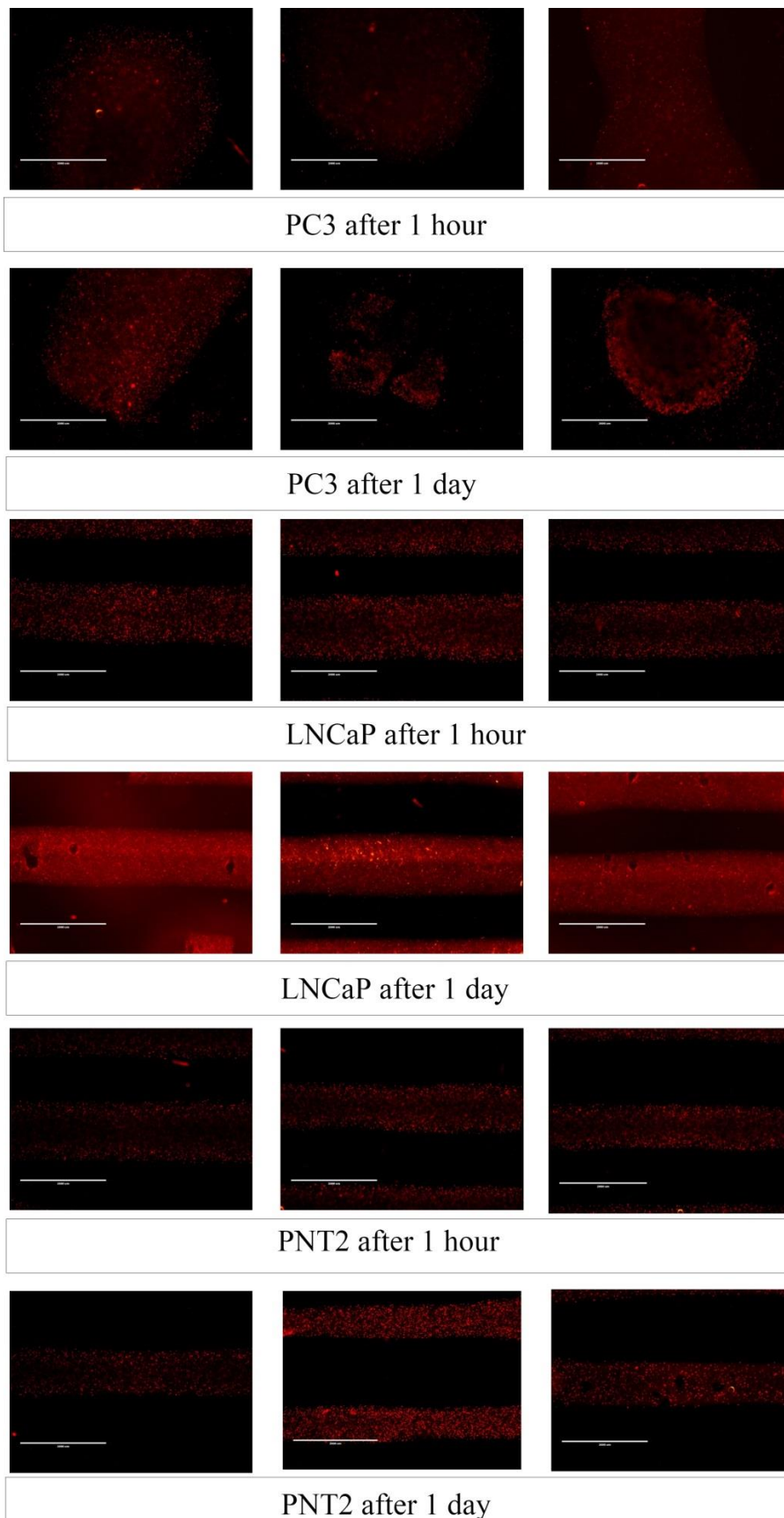
Figure 5.14: Live/dead viability test results (fluorescence images) for PC3, LNCaP and PNT2 cells encapsulated in PG alpha1 after1 hour and 1 day of incubation. The scale in the images is 2000 μm. The images for each time-point are from replicated experiments.

The experimental data suggested that alpha1 is not suitable for the growth of prostate cancer cells and cannot be used to build the model to study the effect of the microenvironment in tumour progression. However, different types of cells (other than prostate cancer cell) were found to be viable in alpha1, such as mammary epithelial cells, according to Raphael.et al in their study. They found the cells to have a high level of viability of cells and proliferation of cells was proved (Raphael et al., 2017).

Cells encapsulation in alpha2 with 3D Discovery printing

The three cell lines (PC3, LNCaP and PNT2) were printed after encapsulating them in alpha2 hydrogel using the optimised parameters showed in Table 4.9. Figures 5.15, 5.16 and 5.17 show the viability test result for PC3, LNCaP and PNT2, respectively. The figures indicate the time scale viability test result (1, 3, 7 and 14 days) for each cell line. Cells clusters are seen to increase with time, which gives an indication of the proliferation of the cells. Live cells were dominant with estimated percentages higher than 85% for all cell lines in all-time points (except PNT2 day 1), as shown in Table 5.3.

Table 5.3: The estimated percentage of live and dead cells for PC3, LNCaP and PNT2 printed with alpha2 hydrogel at each time point.

	day 1		day 3		day 7		day 9	
	Live	Dead	Live	Dead	Live	Dead	Live	Dead
PC3	87	13	93	7	95	5	90	10
LNCaP	87	13	90	10	89	11	89	11
PNT2	83	17	88	12	89	11	88	12
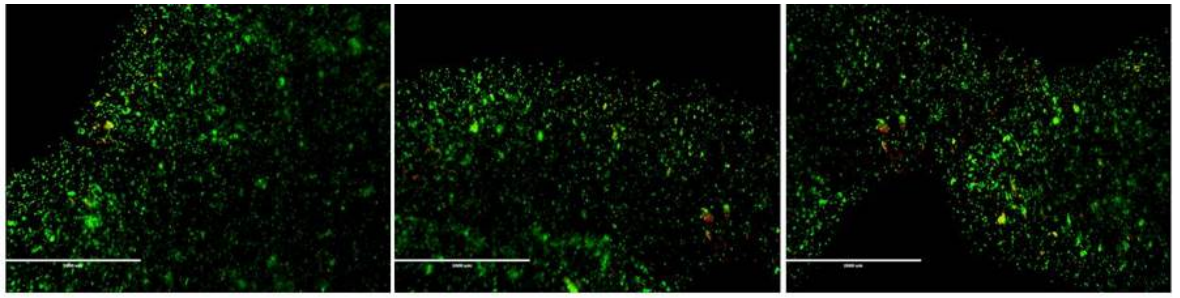
PC3 after 1 day
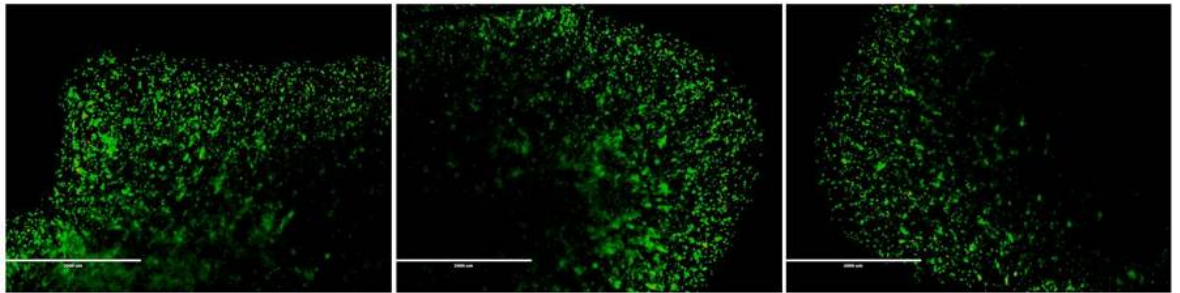
PC3 after 3 days
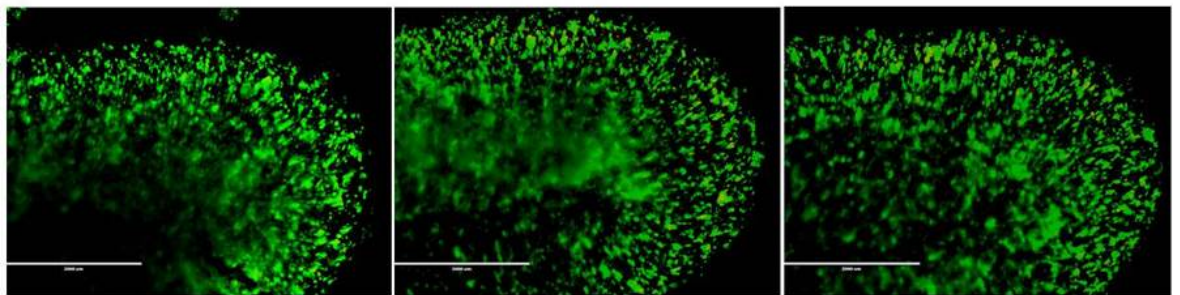
PC3 after 7 days
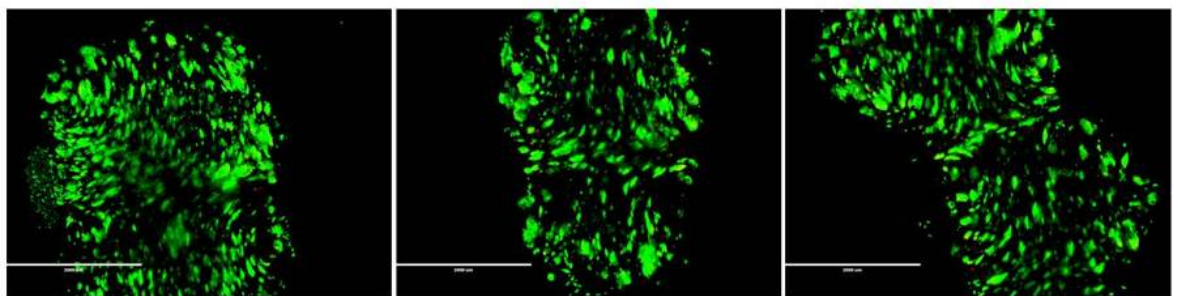
PC3 after 14 days

Figure 5.15: Live/dead viability test results (fluorescence images) for PC3 after 1, 3, 7 and 14 days of incubation. The scale in the images is 2000 μm. The images for each time-point are from replicated experiments.
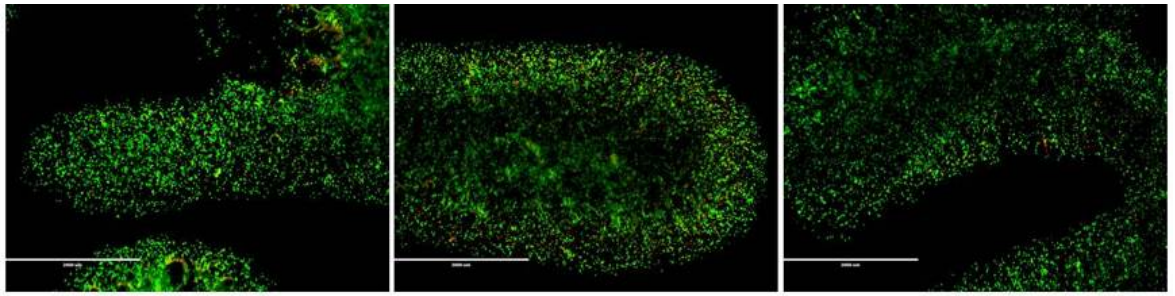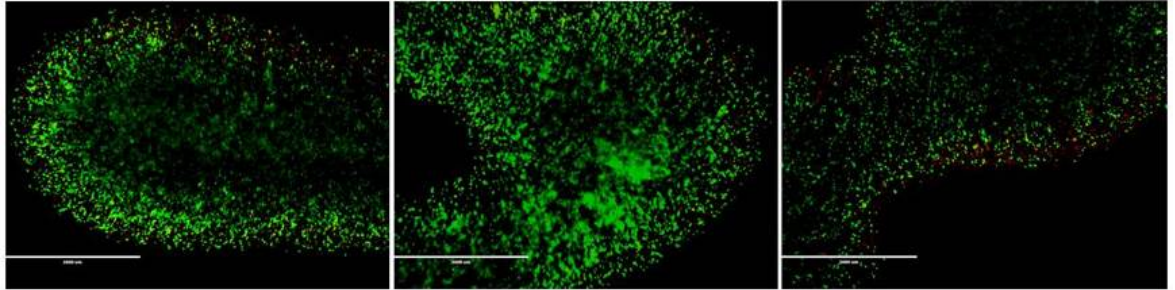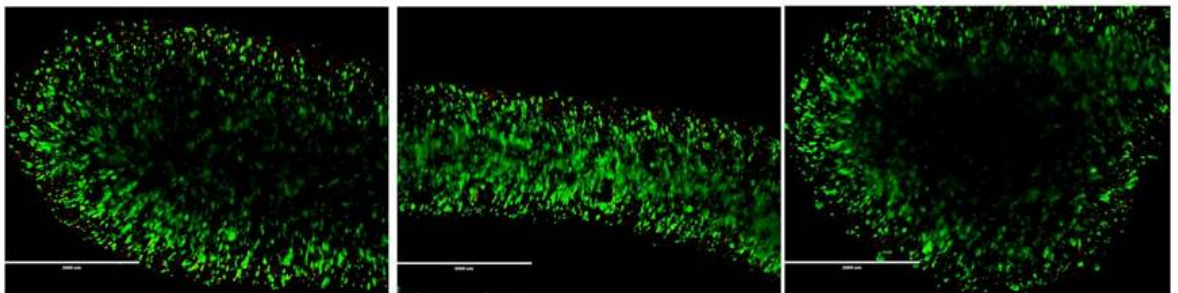
Figure 5.16: Live/dead viability test results (fluorescence images) for LNCaP after 1, 3, 7 and 14 days of incubation. The scale in the images is 2000 µm. The images for each time-point are from replicated experiments.
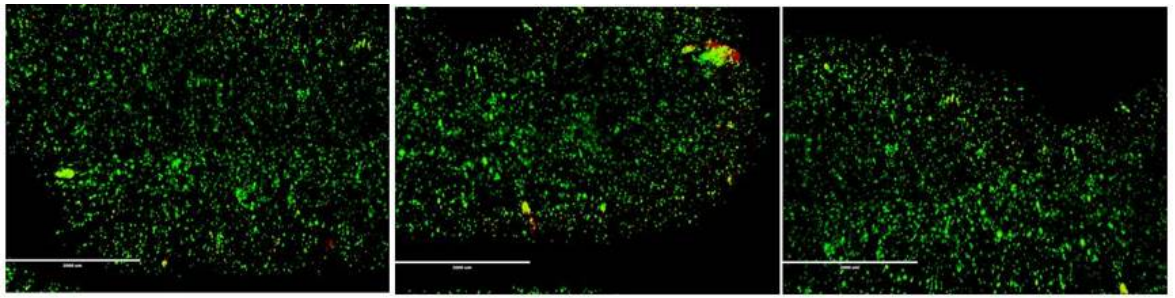
PNT2 after 1 day
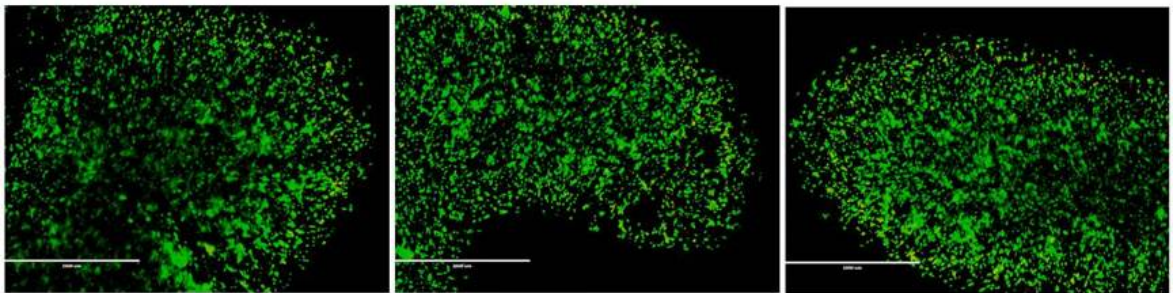
PNT2 after 3 days
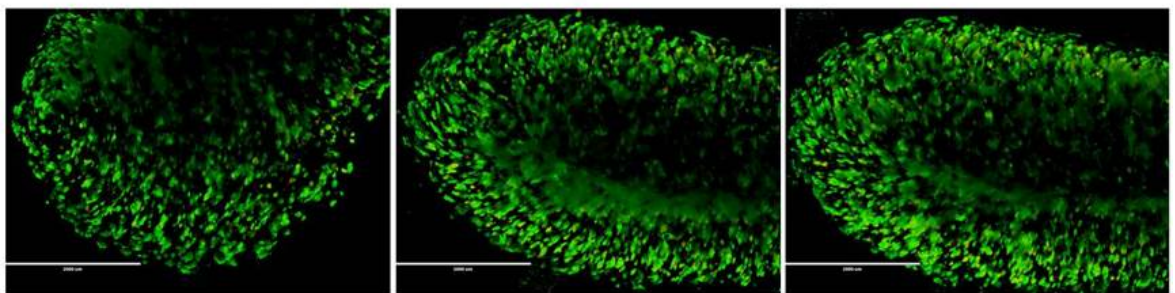
PNT2 after 7 days
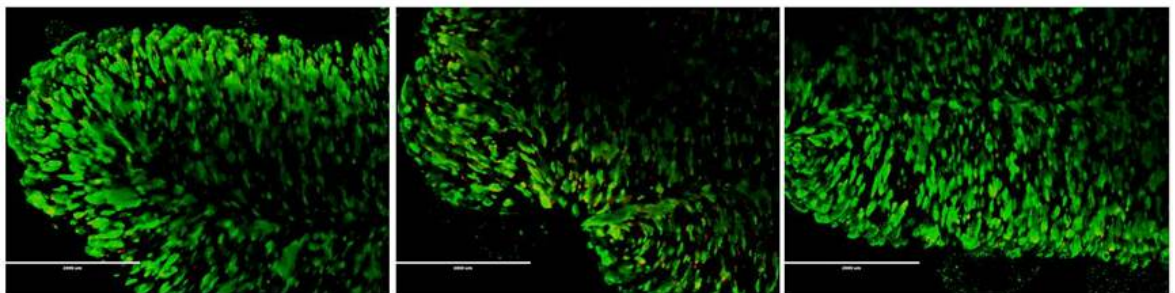
PNT2 after 14 days

Figure 5.17: Live/dead viability test results (fluorescence images) for PNT2 after 1, 3, 7 and 14 days of incubation. The scale in the images is 2000 μm. The images for each time-point are from replicated experiments.

Alpha2 hydrogel makes a good environment where prostate cancer cells (PC3, LNCaP and

PNT2) to survive and proliferate in. The most obvious finding to emerge from this study so far is that alpha2 is a more reliable hydrogel for the cells to work with. The only limitation to this hydrogel is the inability to control the printed construct in which a well-defined structure will be printed. The next section illustrates the viability test of the cells after their encapsulation in alpha2*, which has been found earlier to have the ability to print it with better shape fidelity.

Cells encapsulation in alpha2* with 3D Discovery printing

The investigation of how cells interact with alpha2* starts with PC3 cells and then it moves forward with LNCaP and PNT2. The constructs were printed with the optimal printing parameters (for alpha2* P1) shown in Table 4.9. The use of these parameters was due to the fact that the hydrogel was used almost within the first three months after the purchase. The live/dead test images are shown in Figures 5.18, 5.19 and 5.20 for PC3, LNCaP and PNT2, respectively. PC3 and PNT2 cells follow the same trend as with alpha2; however, LNCaP shows an interesting result with a fluctuation through the four time-points. This result can be seen in images since the green colour (which represent the live cells) is not showing the trend of PC3 and PNT2. The estimated percentage of live cells shows an increase to a very high percentage in day 3, followed by the lowest percentage at day 7 and then a small increase on day 14. LNCaP cells were known to be the most sensitive cell line among those used and it seems that the cells were fighting for their lives. The reason for this is not clear but it may have something to do with the sensitivity of these cells toward the environment of the hydrogel. Additionally, from these results, it can be said that LNCaP cells are the cell line most affected by the hydrogel stiffness since they are viable in softer hydrogel alpha2 and the viability does not have the same trend in stiff hydrogel alpha2*; they are fluctuating instead. Further work is required with LNCaP cells by giving the cells more time to adapt to this hydrogel environment and the test needed to consider more time points or use a hydrogel that is softer than alpha2* and stiffer than alpha2.

Table 5.4: The estimated percentages of live and dead cells for PC3, LNCaP and PNT2 cells in alpha2*.

	day 1		day 3		day7		day 14	
	Live	dead	Live	dead	Live	dead	Live	dead
PC3	86	14	94	6	76	24	93	7
LNCaP	87	13	92	8	76	24	64	36
PNT2	83	17	81	19	91	9	92	8
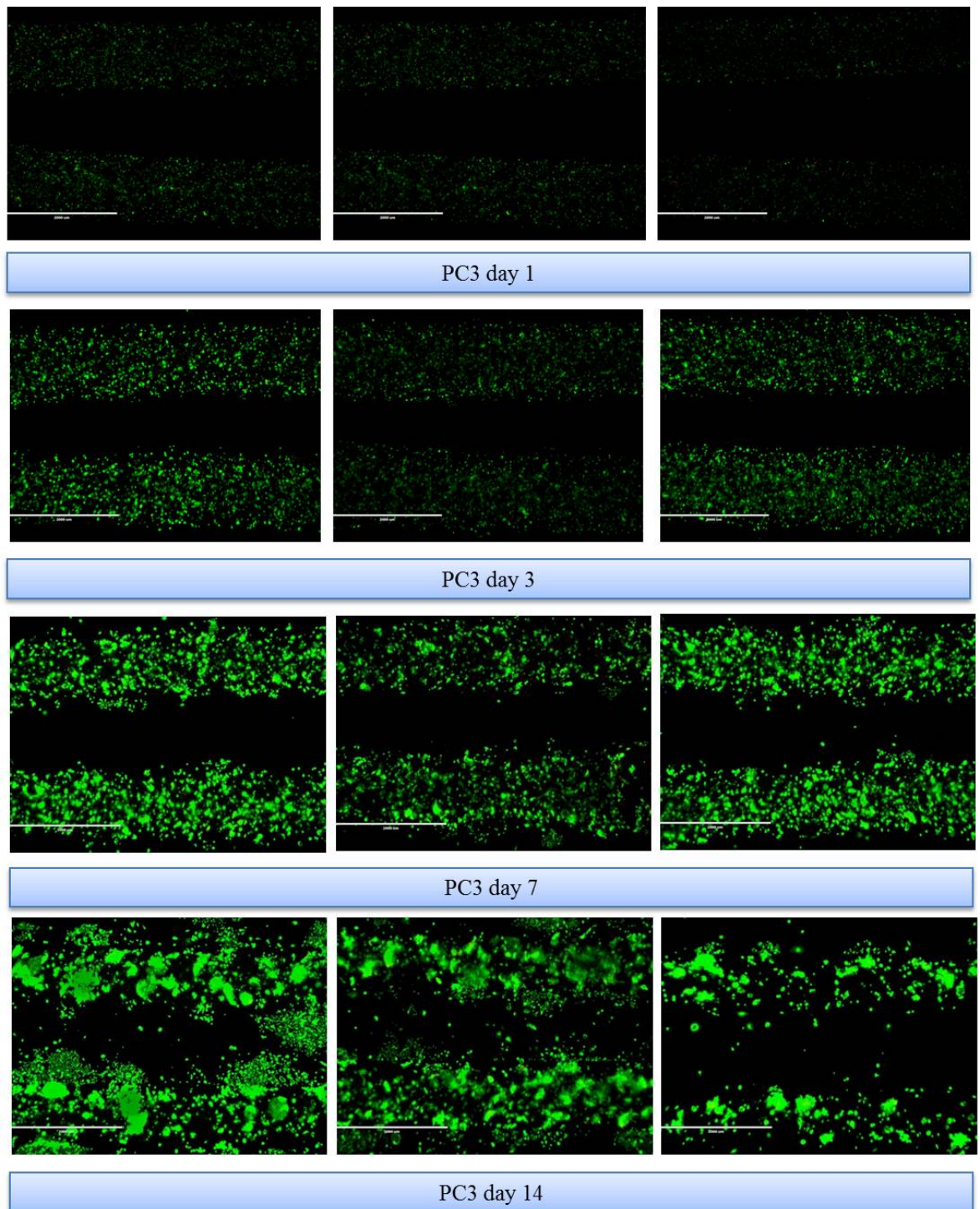
Figure 5.18: Live/dead viability test results (fluorescence images) for PC3 cells in alpha2* hydrogel after 1, 3, 7 and 14. The scale in the images is 2000 µm. The images for each time-point are from replicated experiments.
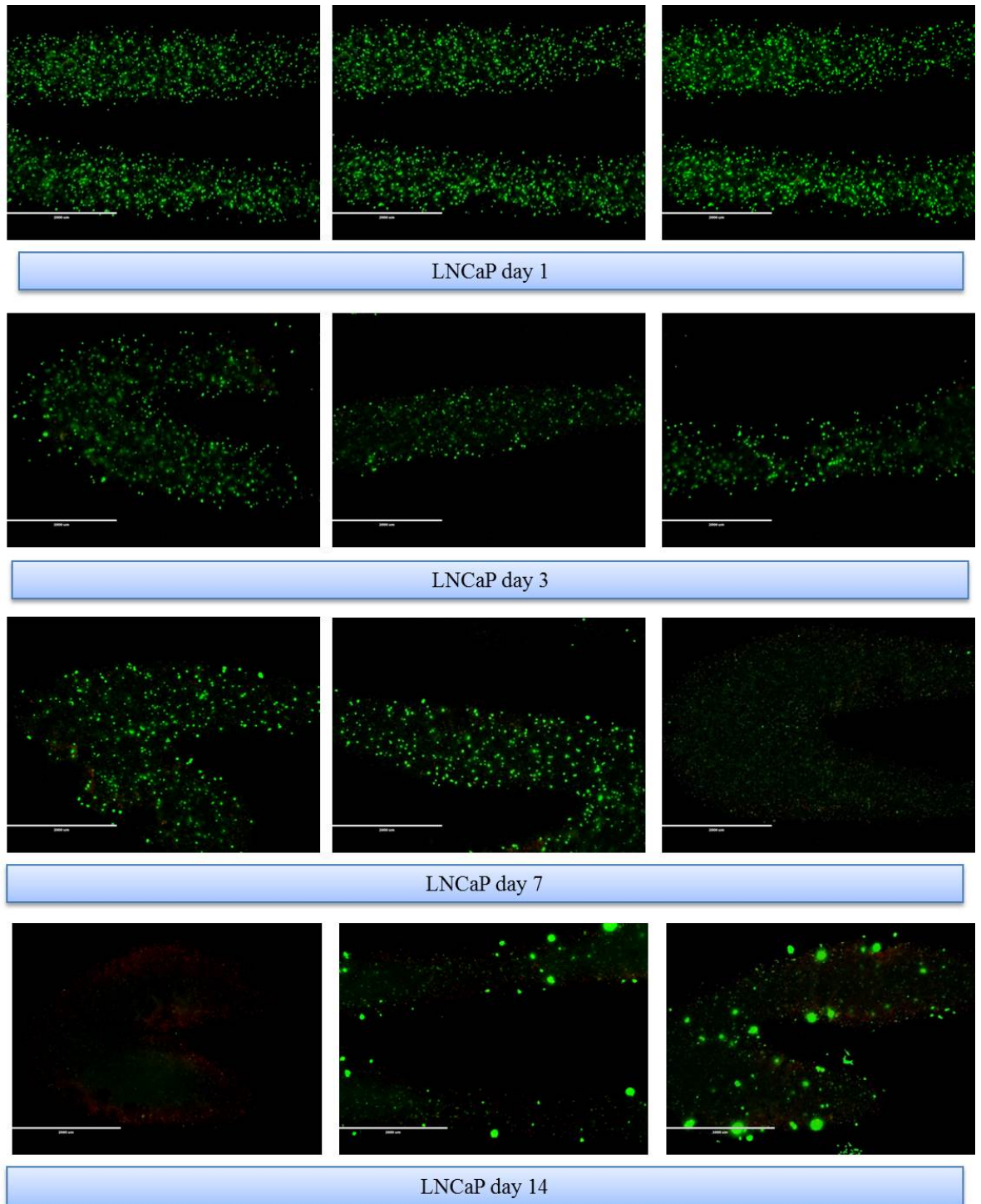
Figure 5.19: Live/dead viability test results (fluorescence images) for LNCaP cells in alpha2* hydrogel after 1, 3, 7 and 14. The scale in the images is 2000 μm. The images for each time-point are from replicated experiments.
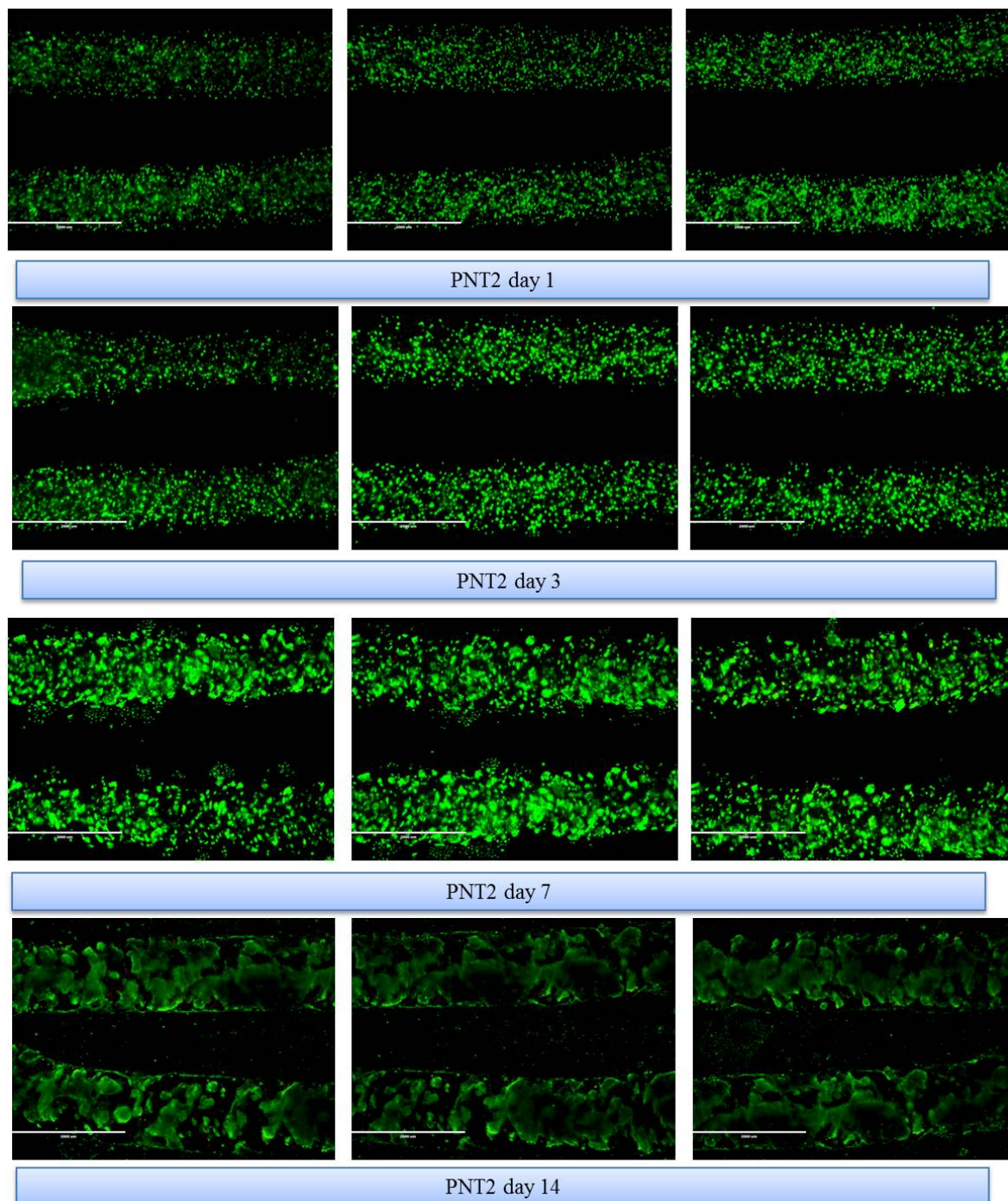
Figure 5.20: Live/dead viability test results (fluorescence images) for PNT2 cells in alpha2* hydrogel after 1, 3, 7 and 14. The scale in the images is 2000 μm. The images for each time-point are from replicated experiments.

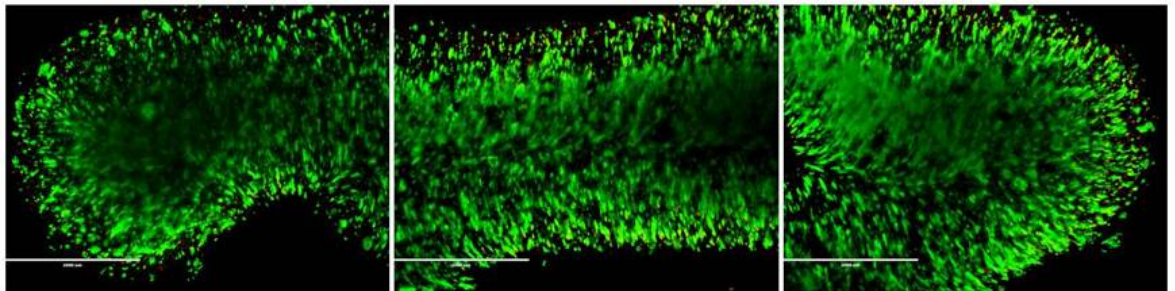With these findings, two main choices came out for which hydrogel should be used for building the model this study aimed for. First, the use of alpha2 with all the three cell lines highly viable in, but the printed construct is not well defined. Second, the use of alpha2*, which has a much better-printed shape than alpha2; however, one of the cell lines (LNCaP) has unpredictable viability in. Comparing the stiffness of the hydrogels; in F-12 Ham media,

according to the data of G' collected and discussed in chapter 4, alpha1 is the softer hydrogel. The stiffness is increasing, going from alpha2 to alpha2*. This gives the conclusion that PC3 cells (the only cells cultured in F-12 Ham medium) are viable in stiffer hydrogels (alpha2 and alpha2*). Keeping in mind that stiffness is not the only factor that affects the viability of the cells. Alpha1 has a different chemistry than alpha2 and alpha2* with a different charge. The effect of the stiffness of the hydrogels on the viability of LNCaP and PNT2 is different from PC3 since in RPMI-1640, alpha2 found to the softest hydrogel and yet the cells are highly viable on it. Alpha1 is stiffer than alpha2 and softer than alpha2*. With the inability of the cells to survive in this hydrogel, the chemistry of the hydrogel is probably the vital factor in studying the viability of the cells. Whereas, since alpha2 and alpha2* have the same chemistry, the viability test results suggest that only LNCaP cells are affected by the stiffness of the hydrogels. According to the obtained results, alpha2* has a high probability to be used in the build of the model of using alpha2* for the build of the model. Since the model has to printed with high accuracy, the control of the printability of the hydrogel has high priority. The two cell lines PC3 and PNT2 can be used to start with. Further studies are needed to investigate the best conditions in which LNCaP can survive in this hydrogel. However, further investigation was taken to confirm this result. Alamar blue test was used to check the metabolic activity of the cells when they are encapsulated in the hydrogel. The test was performed for alpha2*

5.3 Metabolic activity of cells

One of the tests that allow testing the metabolic activity of the cells and measure their concentration is Alamar blue test. Alamar blue is a quantitative test used for the measurement of the proliferation of different types of cells, such as mammalian cell line, fungi and bacteria. The dye used in the test is stable, soluble in water and has no toxicity to the cells. This allows monitoring the cells in the same sample at different time points. The working principle of Alamar blue is an oxidation-reduction reaction that leads to fluorescent active material. During the metabolism process in the cell, a reducing environment is produced and spectrophotometric methods can be used to measure it. Alamar blue consists of a weakly fluorescent material; resazurin sodium salt, which can be reduced to highly fluorescent material; resorufin sodium salt, as shown in Figure 5.21.
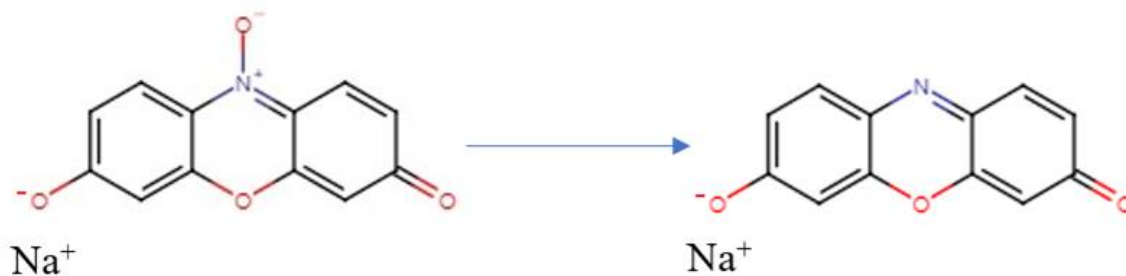
Figure 5.21: Alamar blue equation in which resazurin sodium salt reduced to highly fluorescent resorufin sodium salt.

For the test of metabolic activity, negative, positive and printed samples were analysed using Alamar blue. The samples are then printed constructs (hydrogel and cells encapsulated) with media while the negative control is the hydrogel with media (no cells). The positive control, on the other hand, was the seeded cells at the top of the hydrogel. The negative control used a background in which they have been subtracted from all the samples. Alamar blue used to measure the intensity of resorufin sodium salt in the sample, which resulted from the reduction of the resazurin sodium salt by the cells environment. The fluorescent intensity does not show the exact number of cells and high fluorescent intensity does not necessarily mean that the cells are proliferating, but it might mean that they are metabolically active. Figure 5.22 shows the results of the Alamar blue test of the printed and seeded cells (PC3, LNCaP and PNT2) after the background subtraction. The printed samples show the same trend that seen in live/dead test; in which PC3 and PNT2 cells numbers are increasing with time (or maybe their metabolic activity increase with time) while LNCaP fluctuated going from one time-point to another. The seeded samples, on the other hand, are used as a positive control and shows the increase of the fluorescence intensity except for day 14 in which the confluence status has been reached.
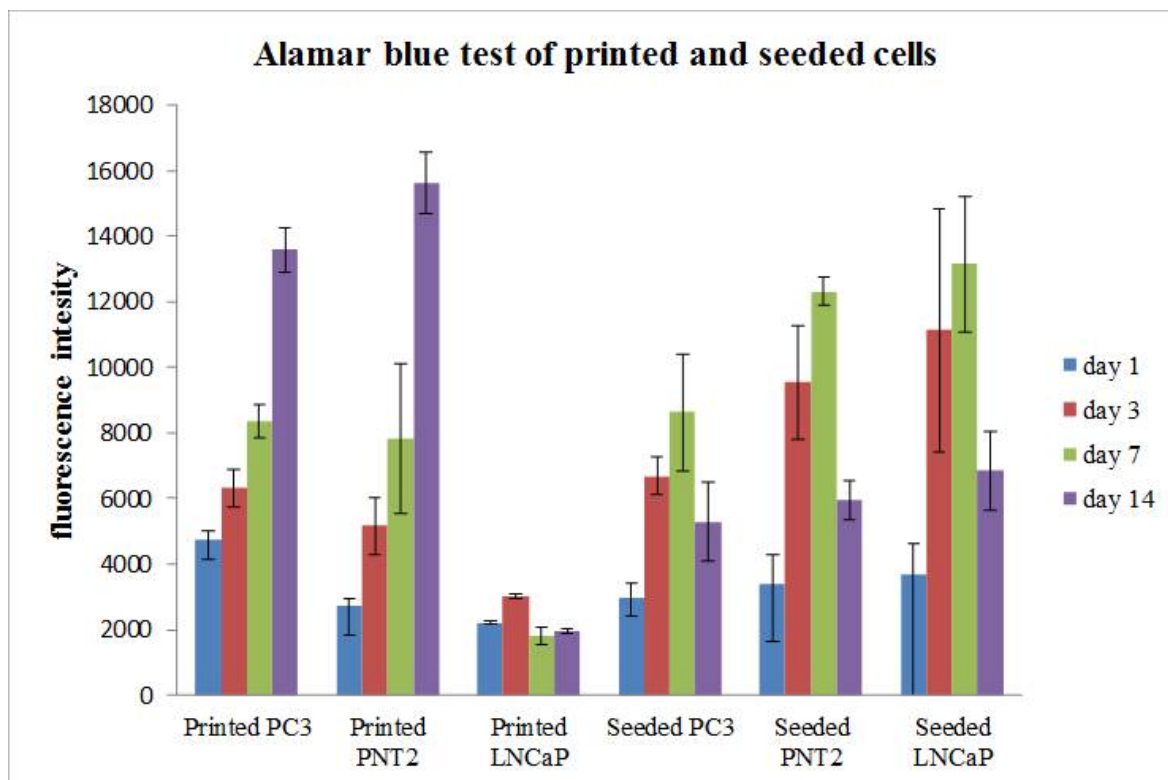
Figure 5.22: Alamar blue test results of the printed and seeded cells (PC3, LNCaP and PNT2) with standard deviation bars, which do not necessary means high error. It shows that at some time point the deviation of the data from the mean is higher. All data were taken as mean of six samples. The deviation was found to be very high in the seeded cells compared to the printed one. Also it found to increase with time for the printed samples.

To correlate the fluorescent intensity and the number of cells, the test was run with a different number of cells (2, 4, 6, 8 and 10 million cells per 1 mL of the hydrogel). Beer Lambert Law then applied to draw a straight line and with the use of the equation, the number of cells at each time point has been calculated. Figure 5.23 presents the graphs showing the number of cells used in the associated with the fluorescent intensity for PC3, LNCaP and PNT2. The equations of the straight lines are illustrated in the figure and they have been used to calculate the number of cells present at each time point. Additionally, the figure shows the graph presenting the number of cells calculated from the results in Figure 5.22, from day 1 to day 14. Due to the significant differences in the number of PC3 and PNT2 cells compared to LNCaP cells, LNCaP cells numbers were barely seen. Hence, a logarithmic scale was used. There is a significant positive correlation between these results with the obtained from live dead test explained in the previous section. Both show the same trend for all three cell lines, even the fluctuation of LNCaP cells.
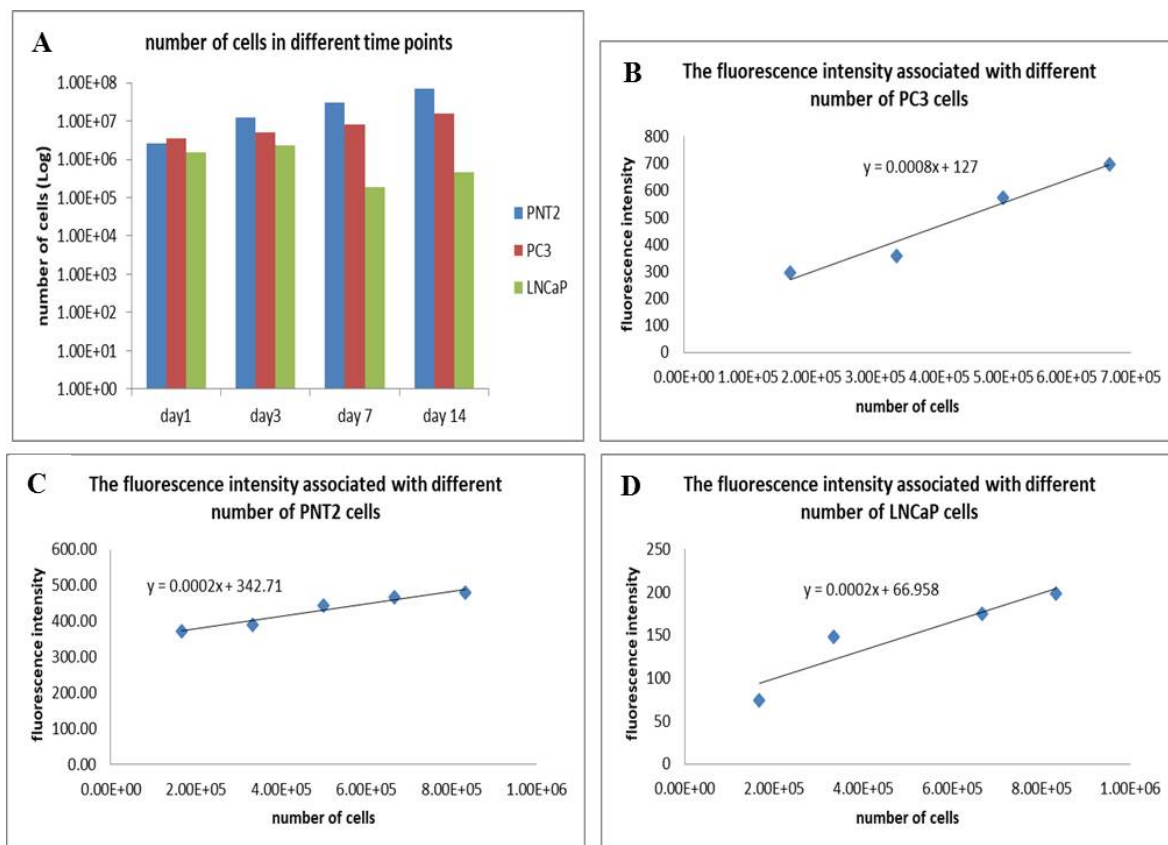
Figure 5.23: A: the number of cells used in the associated with the fluorescent intensity for PC3, LNCaP and PNT2 with the straight-line equation. B, C and D: the resulted number of cells for PC3, PNT2 and LNCaP respectively from day 1 to day 14 in logarithm scale for better illustration due to the skewness of the data.

The above results that prostate cancer cells (PC3, LNCaP and PNT2) are viable in alpha2* hydrogel for up to 14 days. Regardless of the need for further investigation in order to maintain the viability of LNCaP Cells in alpha2*, alpha2* is found to the best option for building the model for prostate cancer. Since alpha2* is a bespoke hydrogel, no studies were found published using this hydrogel.

5.4 Conclusion

The assessment of alpha1, alpha2 and alpha2* as ECM for three prostate cancer cell lines, PC3, LNCaP and PNT2 has been studied. In this chapter, the investigation of the ability of prostate cancer cells to live in 3D environment of the hydrogels was carried out. Although alpha1 can be used to print accurate constructs, the cells are not viable on it as the results of the live/dead test show. Some variation has been seen in different batches, but the overall results conclude that these cell lines cannot survive in alpha1. The suggested reasons behind cells behaviour on this hydrogel is the neutrality of the hydrogel compared to the charged

alpah2 and alpha2*. The viscosity of alpha1 is found to in the middle between alpha2 and alpha2* (both have viable cells), which remove the viscosity from the equation when talking about alpha1. Alpha2, on the other hand, works as a better ECM for all the cell line. High viability of all the three cell lines was found in this hydrogel. The issue that emerged for this hydrogel is the inability to print accurate constructs shape, which will limit the potentials to print the required model later on. Alpha2* shows better printing shape accuracy than alpha2. The viability of PC3 and PNT2 cells was high, while variation on the viability of LNCaP cells was seen. These results confirmed by Alamar blue test. Further research is needed for a better understanding of the behaviour of LNCaP cells in alpha2* hydrogel. The difference between the viability of cells in alpha2 and alpha2* can be related to the change in the concentrations of the amino acids between the hydrogels and the difference in their viscosities, which has been shown in chapter 4. The next section of the thesis is concerned with a more biological assessment (histological assessment) for alpha2* hydrogel since it can be controlled in the printing process more than alpha2 and the cells are viable on it regarding the fluctuation of LNCaP cells.

<center>6</center>

In Vitro Histopathological Assessment of the printed constructs

Introduction

Traditionally a diagnosis of prostate cancer is a multi-step process. Normally there will be a digital rectal examination and a PSA blood test, which if lumps are found or the PSA level is above a specified level (typically 4 ng/ml), a biopsy is required. The biopsy is a small piece of tissue removed from the prostate. This tissue is then fixed and stained with haematoxylin and eosin (H&E) and subsequently examined by a trained pathologist under an optical microscope. Detailed examination of these tissues means that we have excellent knowledge of the prostate tissue architecture and changes in tissue architecture as a function of disease progression. We, therefore, have an abundance of clinical examples of each Gleason grade that can be related to the aggressiveness of prostate cancer. Additionally, different methods are used to check the phenotype expression of the tissue sections, such as polymerase chain reaction (PCR) (Birnie et al., 2008), Immunofluorescence (Chang et al., 2013) and immunohistochemistry (Humphrey, 2017). This chapter will go through the experimental part of the use of H&E, Immunofluorescence and immunohistochemistry in the printed and seeded sections of the constructs.

6.1   Embedding and cutting

The constructs of the different cell lines (PC3, PNT2 and LNCaP) in alpha2* hydrogel have been embedded with paraffin using the same protocol as that used for biopsy tissue. The seeded constructs were easy to embed since the layer of the hydrogel was thick and could be removed easily from the well of the plate. These constructs were cut vertically, allowing cells to be present in all the sections cut. It appears from these constructs that some of the cells

have lost contact with the hydrogel during or after the fixation process and they were held in place during the embedding process. This seen by having a gap between the hydrogel and these cells in cut constructs. On the other hand, the printed constructs were very thin and they were often stuck on the plate and scratching them was the way to remove them from the plate for the embedding process. The best solution found for this issue was to print on a small insert inside the well plate. The insert with the printed hydrogel could all be embedded with paraffin and then the construct was cut horizontally.

6.2   Staining with H&E

Staining the sections of samples with H&E is a fundamental method used for the clinical assessment of the cancerous and non-cancerous cells in the tissue. Moreover, different types of cells can be seen in the stained samples, such as epithelial cells, stroma and lumen cells (Fogarasi et al., 2011). Different studies show the analysis of prostate cancer tissue with H&E staining in which the different types of cells are distinguished, such as the research by Khan *et al.* and researchers have also been studying the use of computational programs for this classification (Khan et al. (2017); Avenel et al. (2019)). Since each printed constructs has only one cell line, distinguishing the different types of cells was not applicable. In future work experiments, the addition of different types of cells is vital and that will lead to better histological assessment when H&E stain used. The cells in printed constructs of the three cell lines were found to adopt a round shape, which is different from their shape when they cultured in well plates. Seeded cells, on the other hand, show differences in their shapes since some of the cells were seen elongated while others were round. Although round shape might be an indication of cells not being in good condition, the different environment the cells were exposed to has to be considered. The H&E images of the cells also show signs of cells proliferation with cells fixed in the division process. Also, dead cells were recognised by the spread of the purple colour outside the cell. One of the features that can be seen in prostate cancer tissue and the printed constructs is the presence of large nuclei that contain prominent nucleoli (single or multiple). Figures 6.1, 6.2 and 6.3 show the scanned images for the H&E stained of PC3, LNCaP and PNT2, respectively. The figures illustrated zoomed parts of the images for day 1 and 14, in which the multiple nucleoli are noticed. This feature, though, was seen in all the three cell lines on different days printed and seeded.
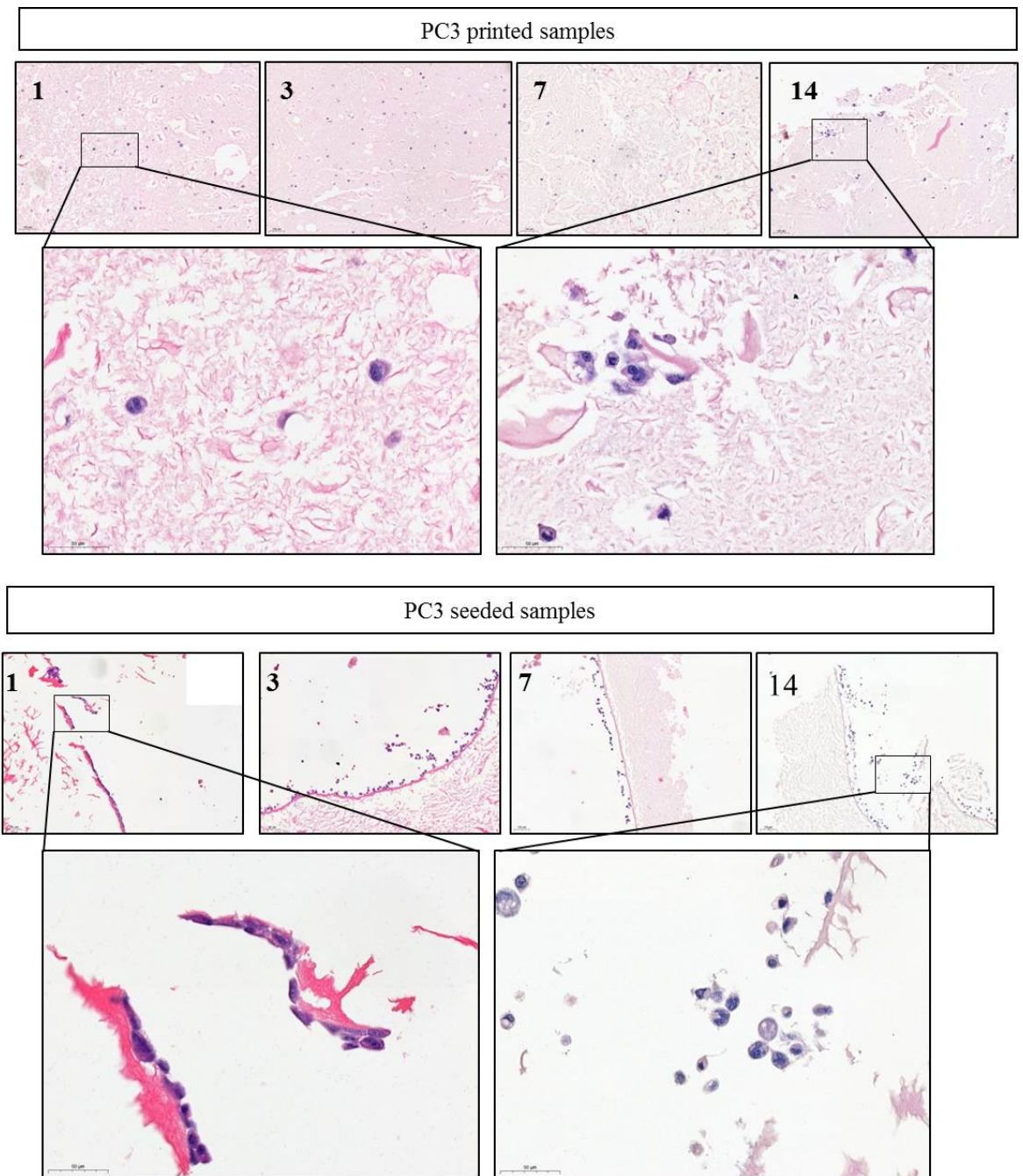
Figure 6.1: H&E stained samples for PC3 printed and seeded constructs, where the numbers 1, 3, 7 and 14 indicate the fixation day of each sample.
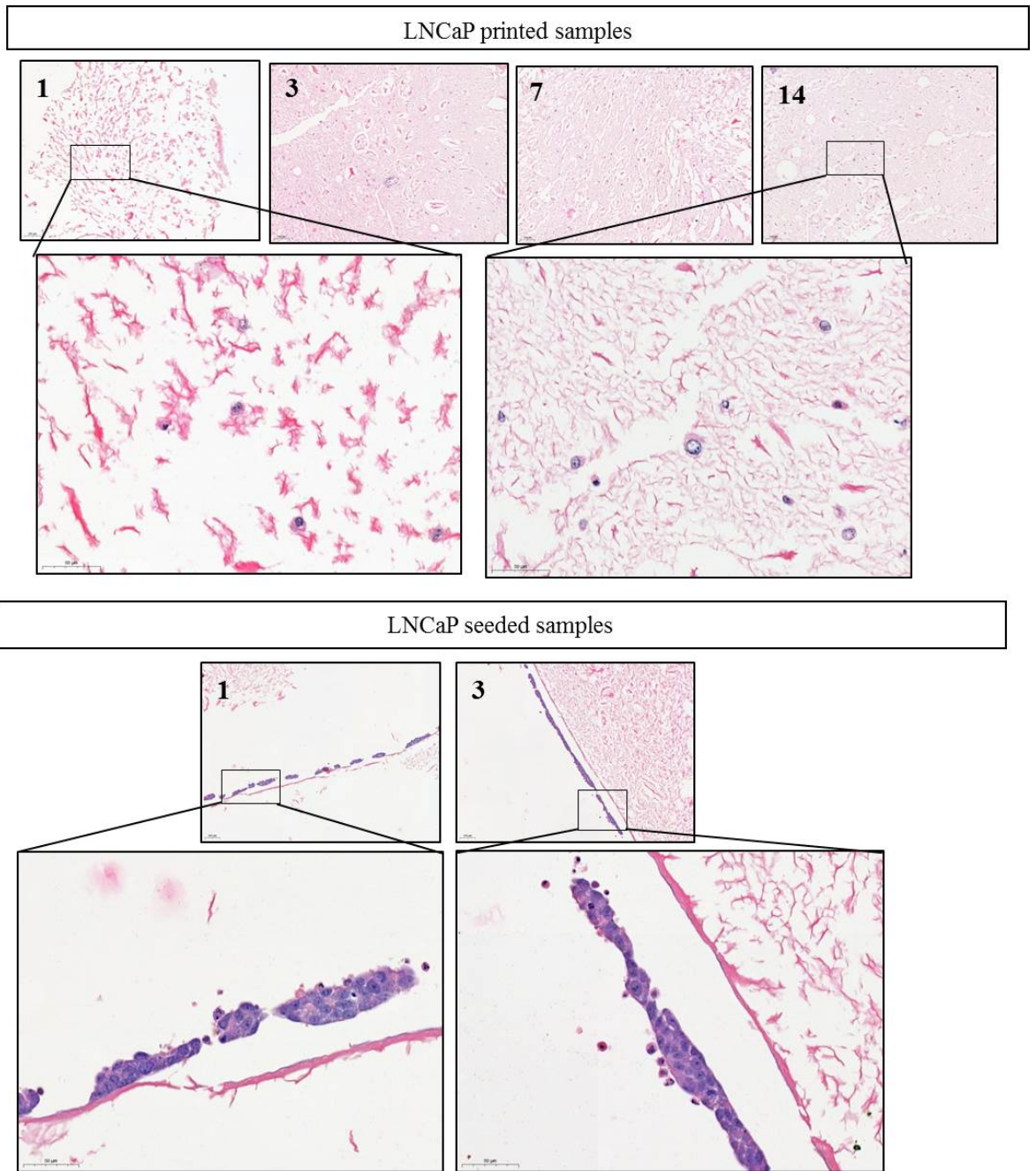
Figure 6.2: H&E stained samples for LNCaP printed and seeded constructs, where the numbers 1, 3, 7 and 14 indicate the fixation day of each sample.
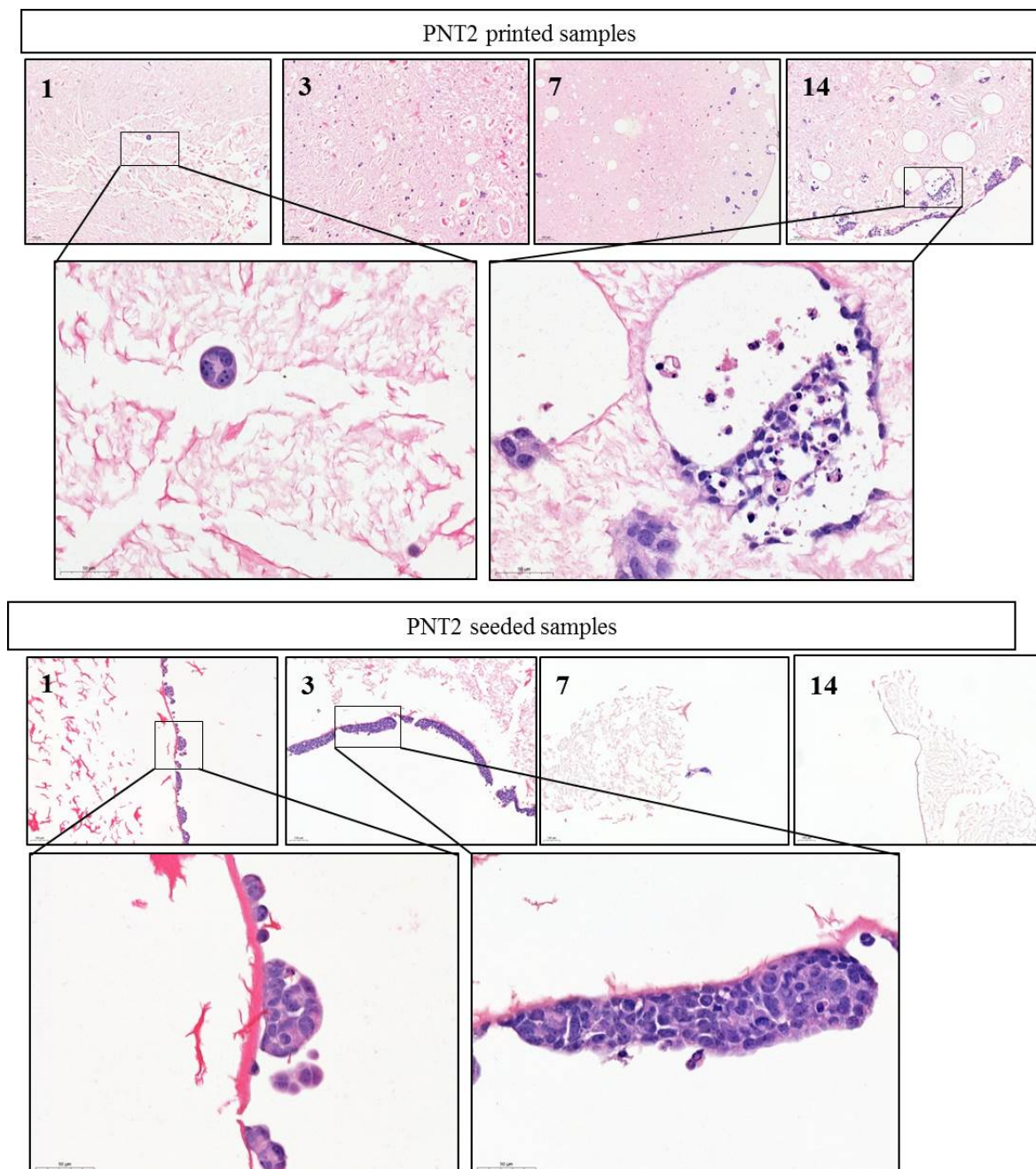
Figure 6.3: H&E stained samples for PNT2 printed and seeded constructs, where the numbers 1, 3, 7 and 14 indicate the fixation day of each sample.

It should be known that that missing images (LNCaP seeded days 7 and 14) are not available due to errors in scanning the slides. The scanned slides were found to be scanned upside down. Unfortunately, due to the current circumstances of the university closure due to the COVID-19 pandemic, it was not possible to repeat this part of the experiment. Following the qualitative analysis of the stained samples, a semi-quantitative analysis was performed using Fiji image J through image deconvolution. It aims to compare the normalised staining intensity at different time points. This approach was employed for the available images by calculating the staining intensity normalised by the nucleus. Normalisation is dividing

data sets (stained intensity in this case) by a common variable (number of nuclei), which allows controlling the variation in the number of cells in used images. Azevedo Tosta. *et al.* studied the colour normalisation of the H&E stained samples. The study goes into making an algorithm for computational normalisation in which the different factors, such as staining time, solution's concentration and pH are considered ((Azevedo Tosta et al., 2019). Although the aim of the normalisation in this study is different, both are going through the normalisation to overcome a variation that affects the analysis of the stained images. Figure 6.4 illustrates the normalised intensities of different cell lines printed and seeded constructs. The normalised intensities for the printed cells of PC3 and PNT2 decrease with time. This indicates that the number of cells increases with time. The printed cells of LNCaP, on the other hand, shows fluctuation as the intensities decrease day 3 and increase day 7 then decrease again day 14. Interestingly, the fluctuation was also seen in the PC3 seeded cells. Due to the lack of data for seeded cells of LNCaP cells, the results cannot be compared to the other cell line or interpreted. The seeded constructs of PNT2 of day 7 and 14 were found not be appropriately cut to show the right amount of cells present, and so the images show a lower number of cells. A repeat of the seeded experiment has to be done to ensure the obtained data is reliable, so the trend in Figure 4 might differ, and so it cannot be relied on.
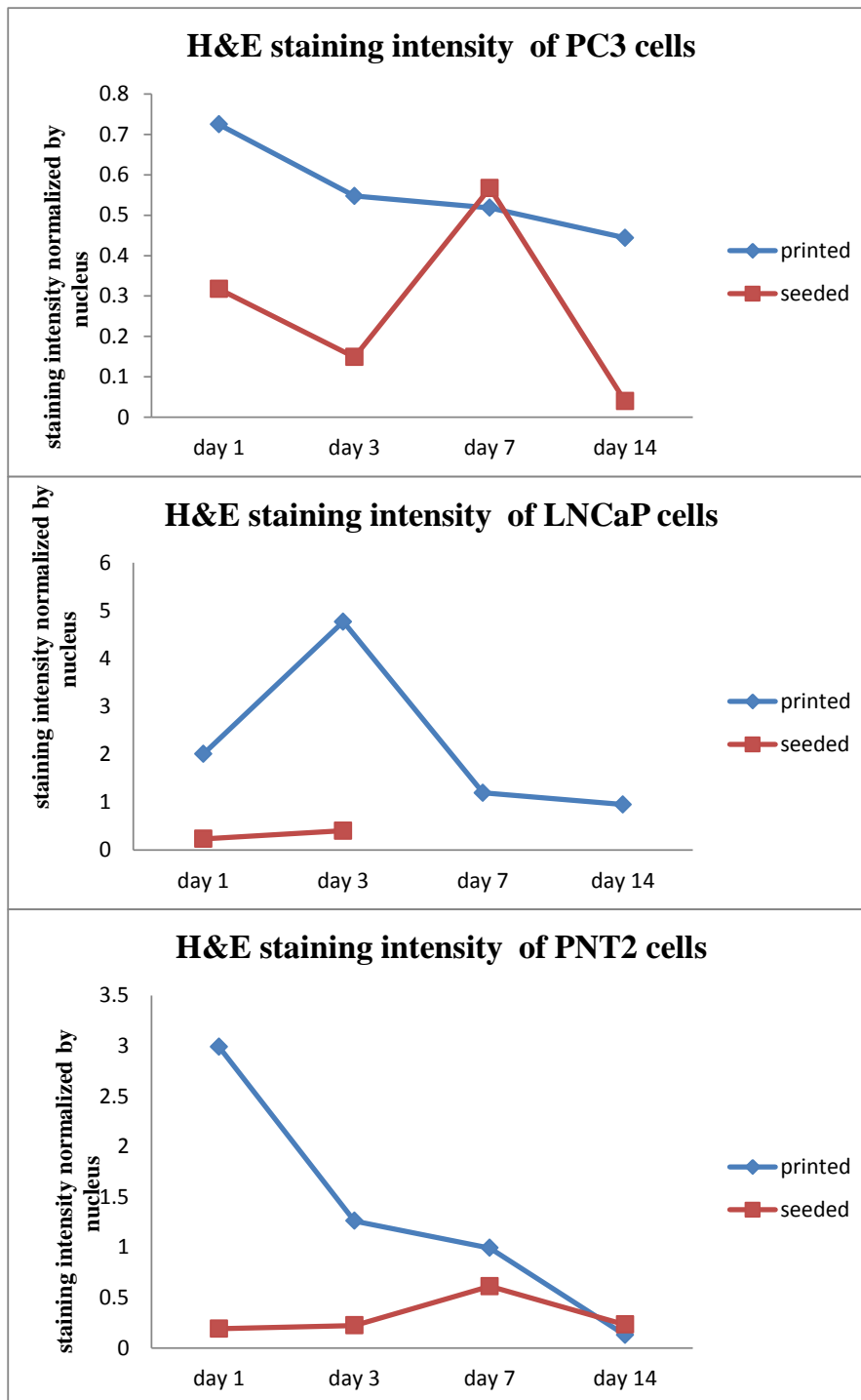
Figure 6.4: H&E stained samples for PNT2 printed and seeded constructs, where the numbers 1, 3, 7 and 14 indicate the fixation day of each sample.

6.3 Phenotype expression

The different interactions between the organism's genes and the surrounding environment lead to different phenotype expression. The phenotype expression changes because of the development and growth of the organs and the change occurring due to the difference in

the environment (Tester and Jorgensen, 2014). This study aims to check the changes in the phenotype expression when the cells are cultured in a 3D environment by encapsulating them in the hydrogel. The cells were printed after the encapsulation in alpha2* hydrogel and tested for specific proteins after 1, 3, 7 and 14 days. The analysed proteins are Vimentin, Pan Cytokeratin, N Cadherin, E cadherin and HIF1. Vimentin is an intermediate fibroblast filament that found in different types of cells, such as fibroblast, endothelial cells, lymphocytes and melanocytes. Vimentin found in the in-vitro cultured cells (which is not the case in normal epithelial cells). It also shows positive expression in the tumour cells that have an epithelial origin. In the tumour, vimentin is used as a marker for the epithelial-to-mesenchymal transition (EMT) in which the epithelial cells convert into a mesenchymal phenotype by several factors, including activating the transcription factors, expressing cytoskeletal proteins and producing ECM-degrading enzymes (Kalluri and Weinberg (2009); Robinson-bennett and Han (2006); Roche (2018)). Cytokeratins are organ- and tissue-specific expressed proteins found in epithelial cells with subtypes classified with numbers from 1 to 20. Pancytokeratin is the most common type of cytokeratin that is found in almost all epithelial cells (Painter et al., 2012). Cadherins are cell-cell junction proteins that mediated cell adhesion. The expression of E cadherin is found to be by normal epithelial tissues and it is lost in cancer cells with an epithelial origin. N cadherin, however, is found to be expressed by the epithelium-derived cancer cells (Loh et al. (2019); Wheelock et al. (2008)). Hypoxia-inducible factors (HIFs) are factors that cause the transcription of different genes allowing cells to adapt to hypoxic environments. HIF-1 is a protein that consists of O2-regulated HIF-1α and HIF-1β. Under hypoxia, HIF-1α is accumulated, enabling the cells to survive by changing the metabolism mechanism from glucose to glycolytic phenotype (Jun et al. (2018); Meijer et al. (2012)). These different proteins were tested using immunofluorescent and immunohistochemistry.

6.3.1 Immunofluorescence

Immunofluorescence is a technique in which a fluorescent dye for a specific antibody is applied to the tissue section. The assessment of the resulting image shows the location (if present) of the antibody. Different studies used the immunofluorescence technique while investigating the expression of different proteins by prostate cancer. An example of these studies is the study performed by Singh et al., which examined the expression of Vimentin by LNCaP cells using immunofluorescence. They found that vimentin is overexpressed by LNCaP cells and it increases with the invasiveness of cancer (Singh et al., 2003). This technique has been tested for this study to check the expression of the different phenotypes, such as vimentin, Pan cytokeratin, E-cadherin and N-cadherin. Unfortunately, due to the highly fluorescent hydrogel, it was very hard to notice the effect of the dye in the cells. The next available choice to do the test is the use of immunohistochemistry, which will be explained in section

6.3.2 Immunohistochemistry

As the samples stained with the antibodies, they were scanned and subjected to qualitative analysis by comparing the stain colour in the positive and negative slides. Additionally, semi-quantitative immunohistochemical analysis for the positive samples was performed using Fiji image J (the same process done in H&E samples). One of the issues that have been noticed during this experiment is the interference of the hydrogel on the obtained results as it gets stained as well with the antibody. This basically means further optimisation of the stain needs to take place. No more optimisation was able to be carried out due to the closure of the university because of the COVID-19 pandemic. Comparison of the hydrogel slides for each antibody with the samples containing cells will be made in each stage of the analysis. The staining of the hydrogel with **vimentin** shows a high intensity of brown colour. A closer look at the slides stained with vimentin, in all the three cell lines, a dark brown stain is found to surround the cells, separating them from the hydrogel, which was stained brown even when there are no cells on it. The seeded cells show a clear coating of this dark brown colour and with the fact they are seeded on top of the hydrogel gives them some separation from the rest of the hydrogel. Hence, it can be said that all the three cell lines (PC3, PNT2 and LNCaP) are expressing vimentin for both seeded and printed cells. The stained cells for the PC3, LNcaP and PNT2 are shown in Figures 6.5, 6.6 and 6.7 respectively. The images of the Alpha2* Hydrogel only, i.e without cells in figures 6.5, 6.6 and 6.7 gives a clear indication of how much the hydrogel can interfere with the result of the staining. The figures also the images at different time points with a zoomed image of the printed construct at day 14 to show the differences.

Figure 6.5: The images taken for the hydrogel, PC3 printed and seeded constructs after staining with vimentin, whereas P indicates printed constructs and S indicates seeded constructs. The dark brown stain surrounding the cells indicates the positive expression of the protein. In contrast, the only blue cells (with the absence of the dark brown surrounding them) indicates the negative expression of the protein. The stained hydrogel slide and the negatively stained slide of the printed construct are shown to compare the colour of the stain constructs.

Figure 6.6: The images taken for the hydrogel, LNCaP printed and seeded constructs after staining with vimentin, whereas P indicates printed constructs and S indicates seeded constructs. The dark brown stain surrounding the cells indicates the positive expression of the protein. In contrast, the only blue cells (with the absence of the dark brown surrounding them) indicates the negative expression of the protein. The stained hydrogel slide and the negatively stained slide of the printed construct are shown to compare the colour of the stain constructs.

Figure 6.7: The images taken for the hydrogel, PNT2 printed and seeded constructs after staining with vimentin, whereas P indicates printed constructs and S indicates seeded constructs. The dark brown stain surrounding the cells indicates the positive expression of the protein. In contrast, the only blue cells (with the absence of the dark brown surrounding them) indicates the negative expression of the protein. The stained hydrogel slide and the negatively* stained slide of the printed construct are shown to compare the colour of the stain constructs.

Figure 6.8 represents the calculated intensity of the stain normalised by the nucleus. The normalised intensity is the ratio of the mean stained area and the number of nuclei. For each sample, three different images were analysed. The measured normalised intensity was found to differ in each cell line. Figure 6.8 provides the different charts of the measured normalised intensities of PC3, LNCaP and PNT2 cells stained with different antibodies (the positive expression proteins are shown). PC3 cells show an increase in the normalised intensity on day 3 and then it decreases for both day 7 and 14. From chapter 5, it has been seen that the number of PC3 cells increases with time. The increase in the intensity on day 3 indicates that the expression of the proteins was higher than the rest time points since the trend seems to be normal at other time points. The normalise intensities of the LNCaP, are fluctuating at different time points. It has been noticed that the increase in the number of cells caused the normalised intensity to drop and vice versa. According to the live/dead test and metabolic activity test results explained in chapter 5, there is fluctuation in the number of cells at different time points. This fluctuation is consistent with the previous results found in this test. The number of cells is high on day 1 and 14, and so, the normalised intensity is lower at the same time points. With PNT2 cells, the same conclusion as LNCaP was drawn. The increase in the number of cells causes the normalised intensity to drop. The live/dead test and metabolic activity test results show that PNT2 cells number increases with time and so the normalised intensity if found to decrease with time. On the other hand, it can be noticed that the vimentin intensity of the printed cells is lower than the seeded cells for all the three cell lines, which probably indicates that the number of cells in the printed constructs is higher. This can be explained by the amazing adaptation of these cells the hydrogel environment when they encapsulated on it. Or it might be due to the loss of some cells during the fixation and embedding (cells found to lose the attachment to the hydrogel at these points).
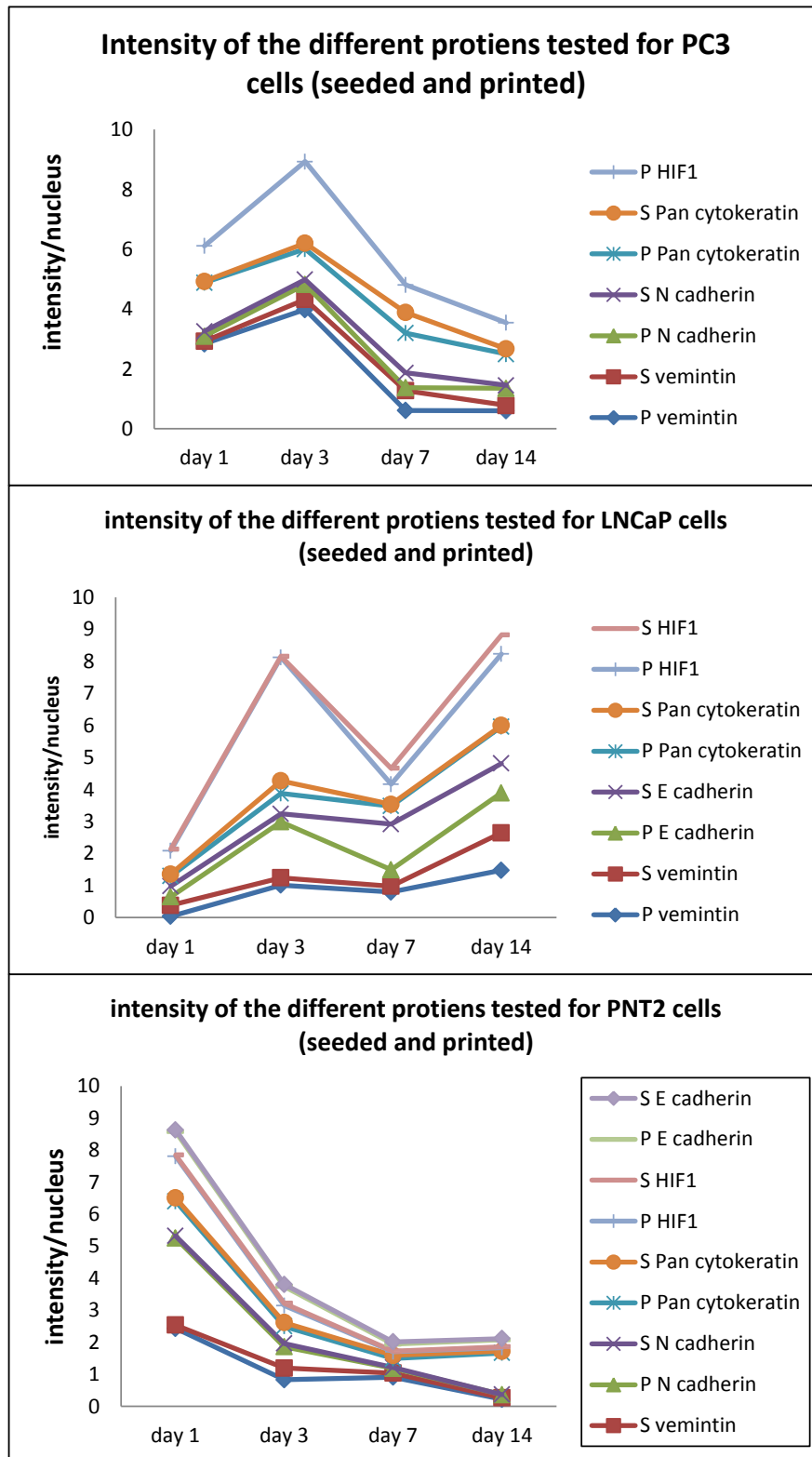
Figure 6.8: The normalised intensity of the proteins (vimentin, N and E cadherin, Pan Cytokeratin and HIF1) where S is for seeded and P is for printed.

Different studies have found that the expression of vimentin is high in poorly differentiated cancers. It was seen in cell lines, such as PC3, PNT1a and P4E6, and only mitotic cells of

LNCaP have expressed it (Lang et al. (2002); Singh et al. (2003)). Staining the slides for **N cadherin** and **E cadherin** show significant differences between the three cell lines. For PC3 cells, staining with N cadherin shows dark brown stained found around the cells for both printed and seeded cells, as shown in Figure 6.9. The measured normalised intensity for N cadherins shown in Figure 6.8. The seeded cells have a higher intensity than the printed ones, but the same trend as vimentin was seen for both seeded and printed constructs. The cells stained with E cadherin, on the other hand, shows that no difference between the negatively stained slides and the positive one regardless of the brown colour caused by the hydrogel for E cadherin. Both shows cells stained blue and no signs of any brown colour surrounding them. This result indicates that the PC3 cells did not express E cadherin in both seeded and printed constructs at all time points, which also can be seen in Figure 6.9. This dark brown stained is seen in both printed and seeded cells. PC3 found to express N cadherin in both seeded and printed constructs, however, it did not express E cadherin, as shown in Figure 6.9. LNCaP cells, on the other hand, are expressing E cadherin in both printed and seeded cells. Although the number of cells in seeded cells at day 7 and 14 is very low, the dark brown stain surrounding the cells still seen, as it can be seen in Figure 6.10. On the contrary, LNCaP cells did not express N cadherin, which illustrated in Figure 6.10 as well. The normalised intensity of the E cadherin stain in the samples at different time points; summarised in Figure 6.8. The same trend as vimentin was noticed. The seeded cells have higher normalised intensity than the printed ones. This is an expected result since the cross-section was cut vertically for the seeded cells to ensure getting cells in each section. The number of cells in the vertically cut section is much lower than the horizontally cut one (as the printed constructs). As discussed with the vimentin antibody, the number of cells affect the staining intensity. PNT2 cell line is the only cell line found to express both N cadherin and E cadherin in printed and seeded cells, as shown in Figure 6.11. Although N cadherin was found expressed by PNT2, the dark brown stain for the N cadherin was not seen surrounding all the cells (Only some of the cells found to express N cadherin). The normalised intensities shown in Figure 6.8, found to be higher for E cadherin than N cadherin and in the seeded is higher than the printed for both proteins and they have the same general trend in the different time points.
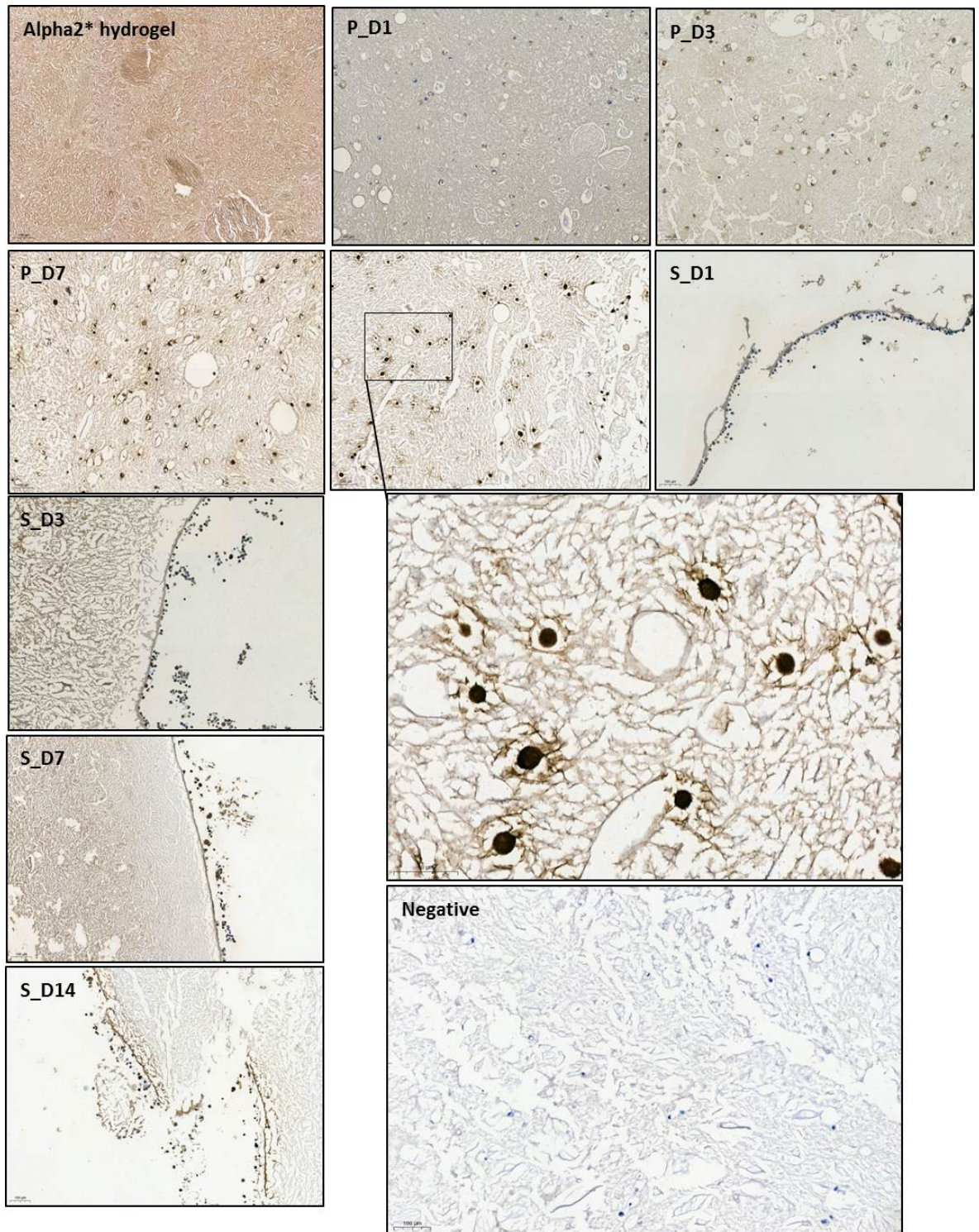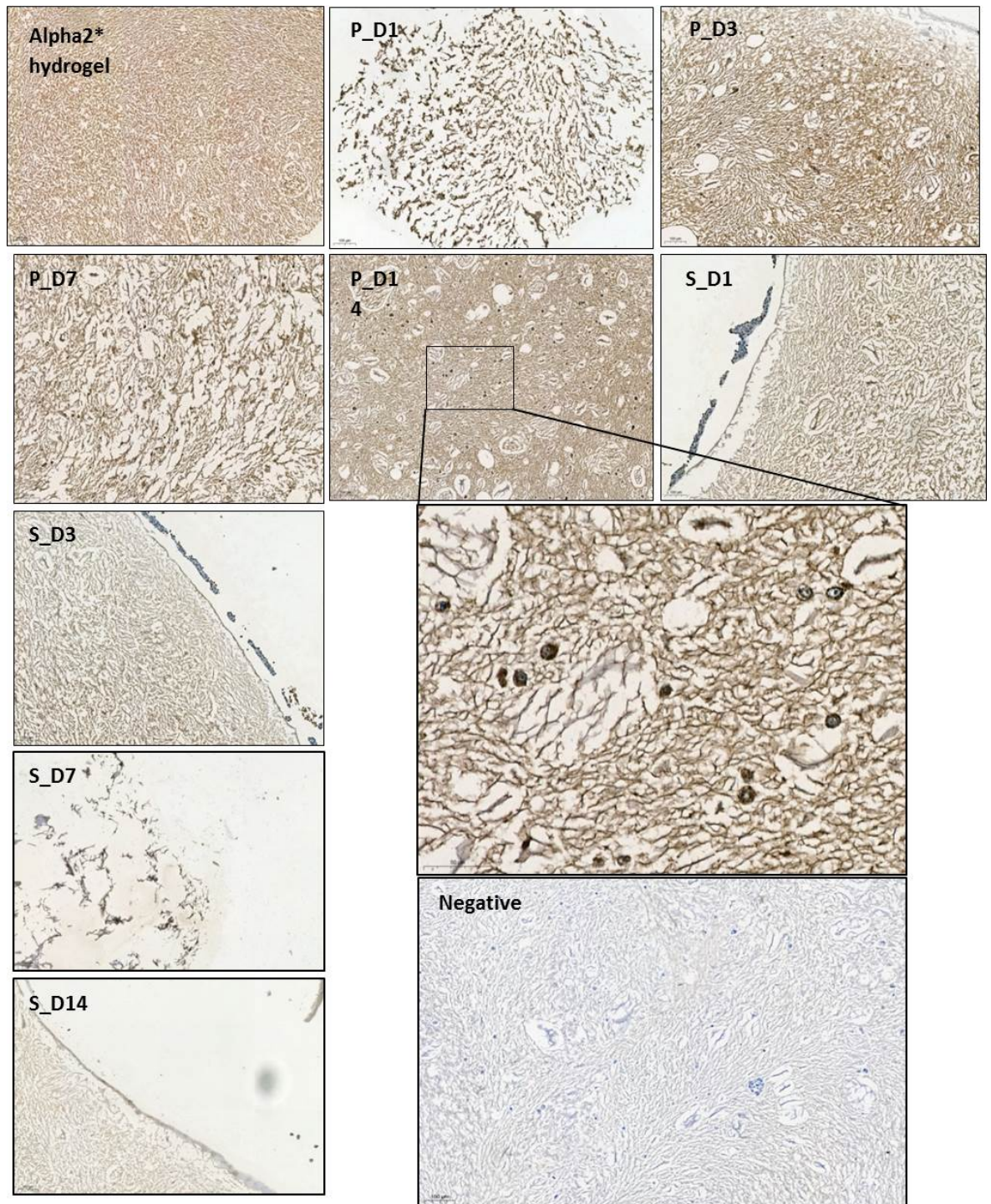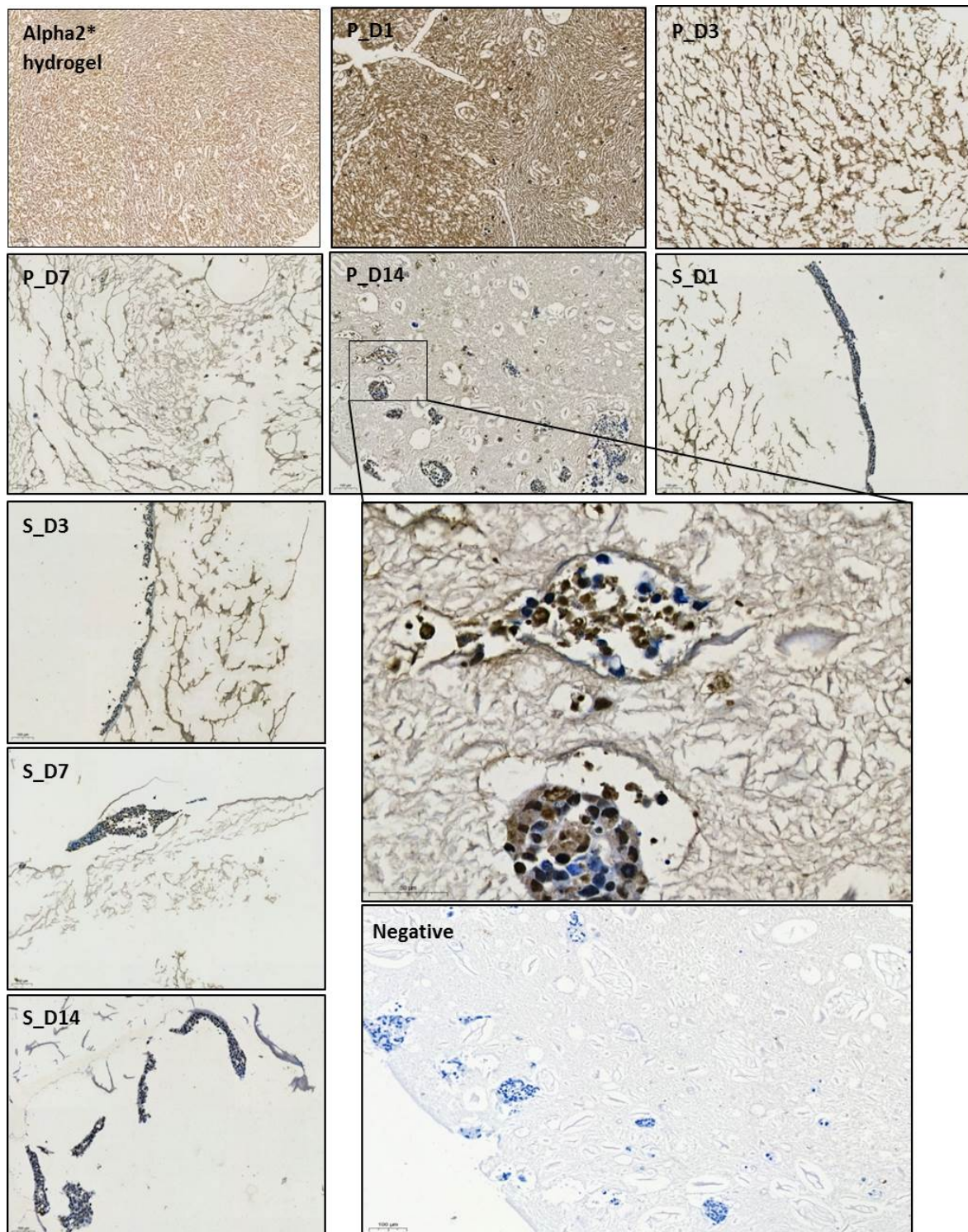
Figure 6.9: The images were taken for the hydrogel, PC3 printed and seeded constructs after staining with N and E cadherin, whereas P indicates printed constructs and S indicates seeded constructs. The dark brown stain surrounding the cells indicates the positive expression of the protein. In contrast, the only blue cells (with the absence of the dark brown surrounding them) indicates the negative expression of the protein. The stained hydrogel slide and the negatively stained slide of the printed construct are shown to compare the colour of the stain constructs.

Figure 6.10: The images were taken for the hydrogel, LNCaP printed and seeded constructs after staining with N and E cadherin, whereas P indicates printed constructs and S indicates seeded constructs. The dark brown stain surrounding the cells indicates the positive expression of the protein. In contrast, the only blue cells (with the absence of the dark brown surrounding them) indicates the negative expression of the protein. The stained hydrogel slide and the negatively stained slide of the printed construct are shown to compare the colour of the stain constructs.

Hydrogel N Cad	N Cad _S_D1	Hydrogel E Cad	E Cad _S_D1
N Cad _P_D1	N Cad _S_D3	E Cad _P_D1	E Cad _S_D3
N Cad _P_D3	N Cad _S_D7	E Cad _P_D3	E Cad _S_D7
N Cad _P_D7	N Cad _S_D14	E Cad _P_D7	E Cad _S_D14
N Cad _P_D14	N Cad _negative	E Cad _P_D14	E Cad _negative

Figure 6.11: The images were taken for the hydrogel, PNt2 printed and seeded constructs after staining with N and E cadherin, whereas P indicates printed constructs and S indicates seeded constructs. The dark brown stain surrounding the cells indicates the positive expression of the protein. In contrast, the only blue cells (with the absence of the dark brown surrounding them) indicates the negative expression of the protein. The stained hydrogel slide and the negatively stained slide of the printed construct are shown to compare the colour of the stain constructs.

It was expected that N cadherin to be positive and E cadherin is negative, since normal cells express E cadherin, while cancer cells express N cadherin. N cadherin is a sign of losing the cell-cell contact and being told to stop migrating away from a defined tissue structure. Although it was expected that N cadherin to be positive and E cadherin is negative for the cancerous cells, the different cell lines are expressing them differently. Only PC3 cells have the same as expected. LNCaP expresses them oppositely where E cadherin is expressed and N

cadherin is not expressed by them and PNT2 cells are expressing both. In literature, studies show that poorly differentiated cancer cells express N-cadherin. In invasive cancer, N cadherin is gained while E cadherin is lost (Tomita et al. (2000); Tran et al. (1999)). A study done by Bryden, Freemont, Clarke and George showed that the staining degree of N cadherin in bone metastasis was different from one site to another, which might give an indication that either E cadherin has not been lost from a particular site or it has been gained in a secondary site (Bryden et al., 1997). This gives an idea of the possible reasons for the positive expression of E cadherin in LNCaP and PNT2 cells. Moreover, the differentiated morphology of PNT2 cells might be the case of E cadherin expression.

Positive expression of **Pan cytokeratin** was also detected from the immunohistochemical images for all the three cell lines. The seeded constructs of PC3 were found not to have as much of the dark brown colour around the cells, but it was considered positive because of the small number of cells that do. The printed constructs were found to be highly positive for the expression of pan cytokeratin. Figure 6.12 presents the images for both printed and seeded cells of PC3. LNCaP and PNT2, on the other hand, show high expression of Pan cytokeratin for both seeded and printed constructs, as shown in Figures 6.13 and 6.14. Furthermore, the normalised stain intensities for the three cell lines are illustrated in Figure 6.8, and surprisingly the intensities of seeded and printed were almost the same for PC3 and LNCaP with a difference at a one-time point only. The intensities of seeded and printed constructs of PNT2 was exactly the same. Cytokeratins are holding the structure and the shape of the tissue where the pan cytokeratin antibody is a marker for all of them. It is expected to be seen in all different stages of cancer, as stated in literature (Moul et al. (1994); Weckermann et al. (2001)).
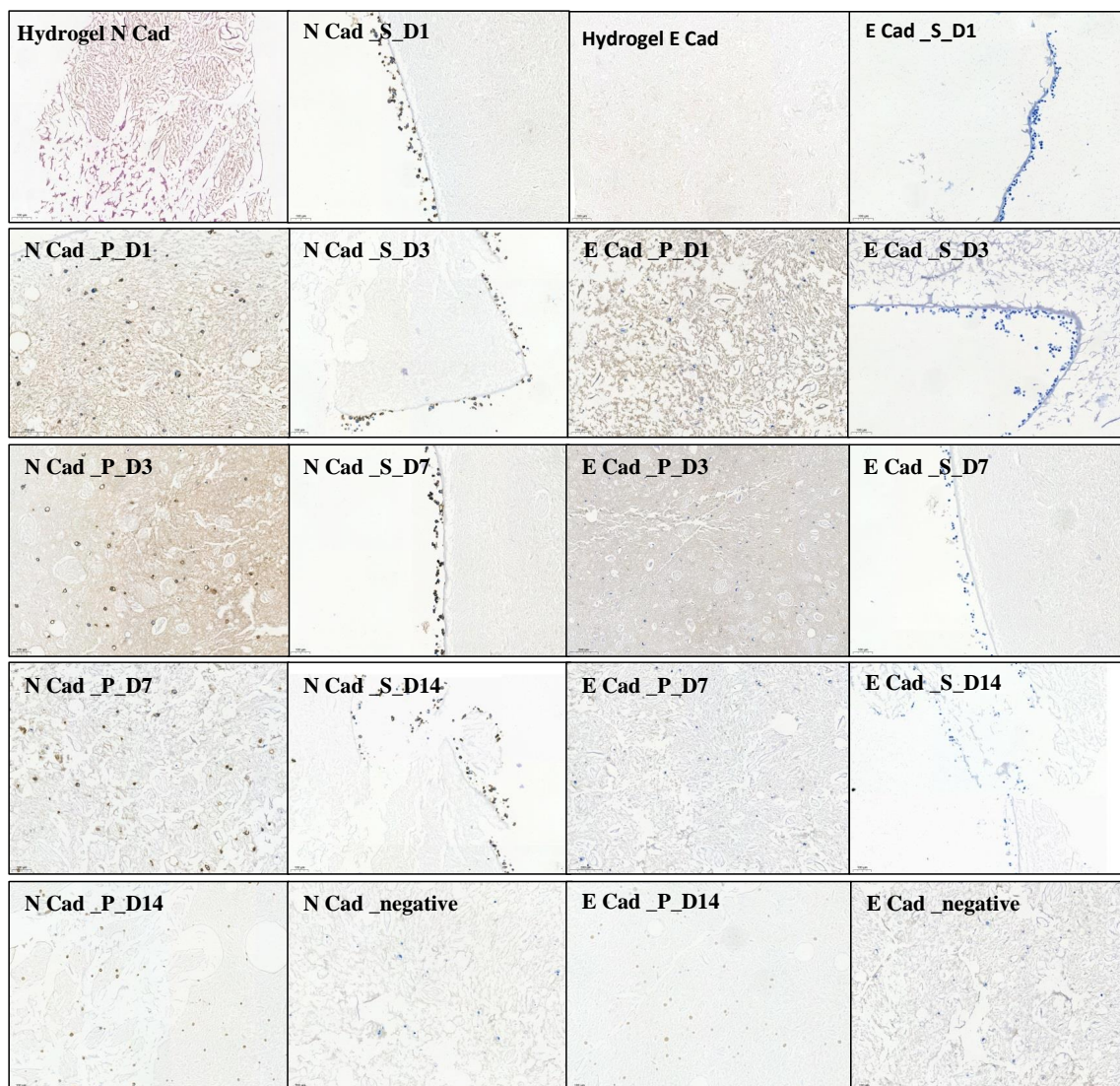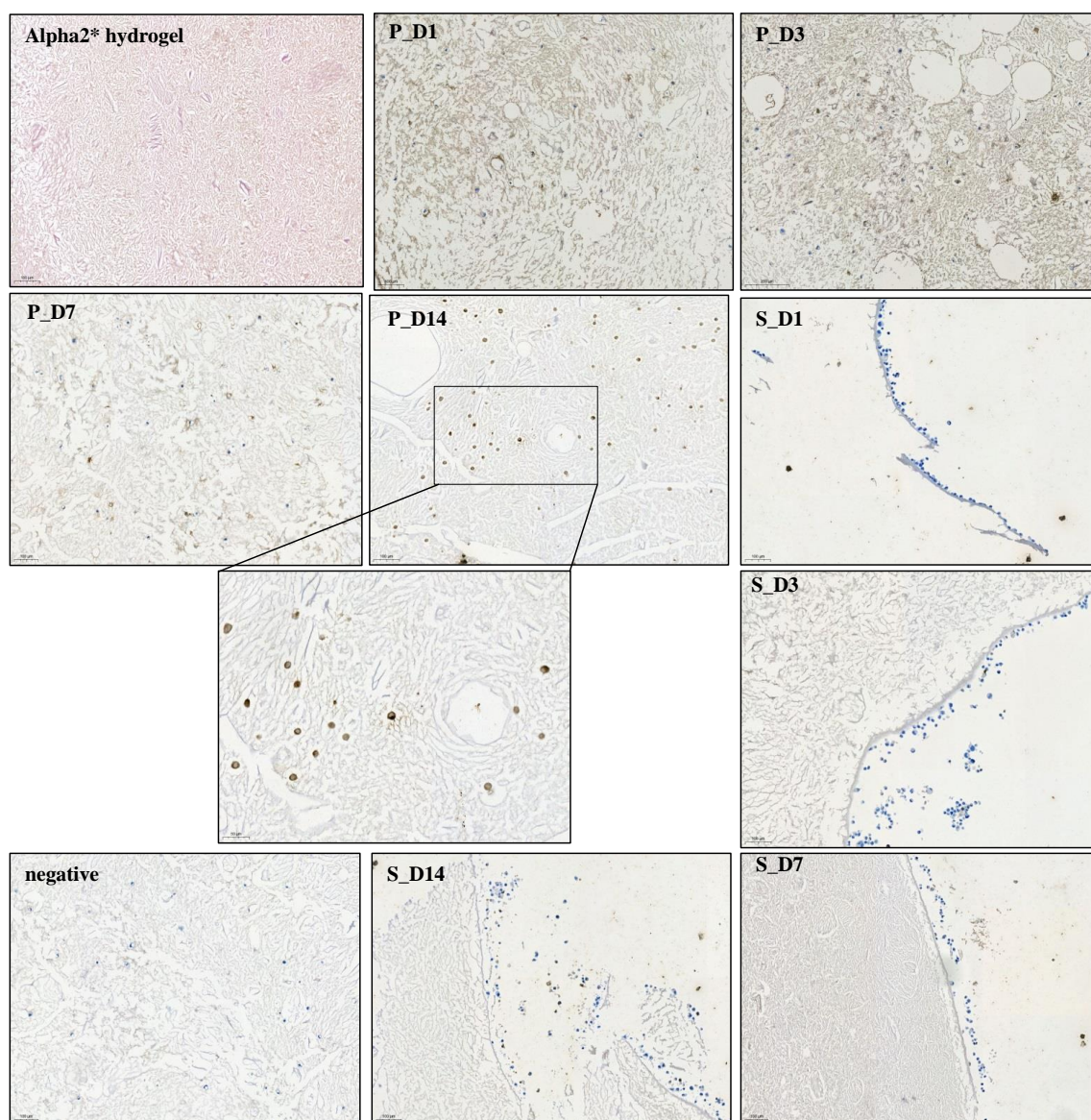
Figure 6.12: The images were taken for the hydrogel PC3 printed and seeded constructs after staining with Pan cytokeratin, whereas P indicates printed constructs and S indicates seeded constructs. The dark brown stain surrounding the cells indicates the positive expression of the protein. In contrast, the only blue cells (with the absence of the dark brown surrounding them) indicates the negative expression of the protein. The stained hydrogel slide and the negatively stained slide of the printed construct are shown to compare the colour of the stain constructs.
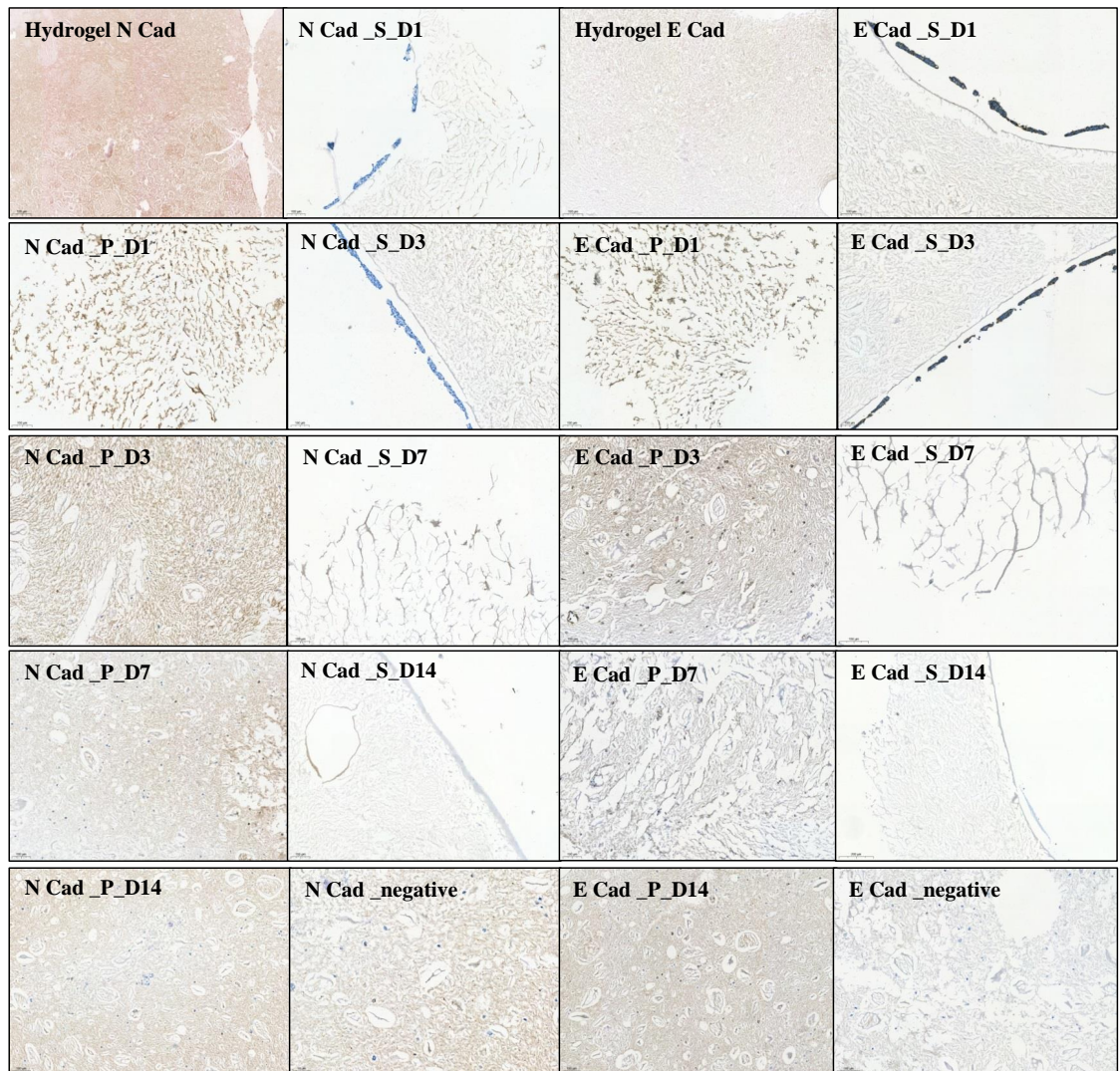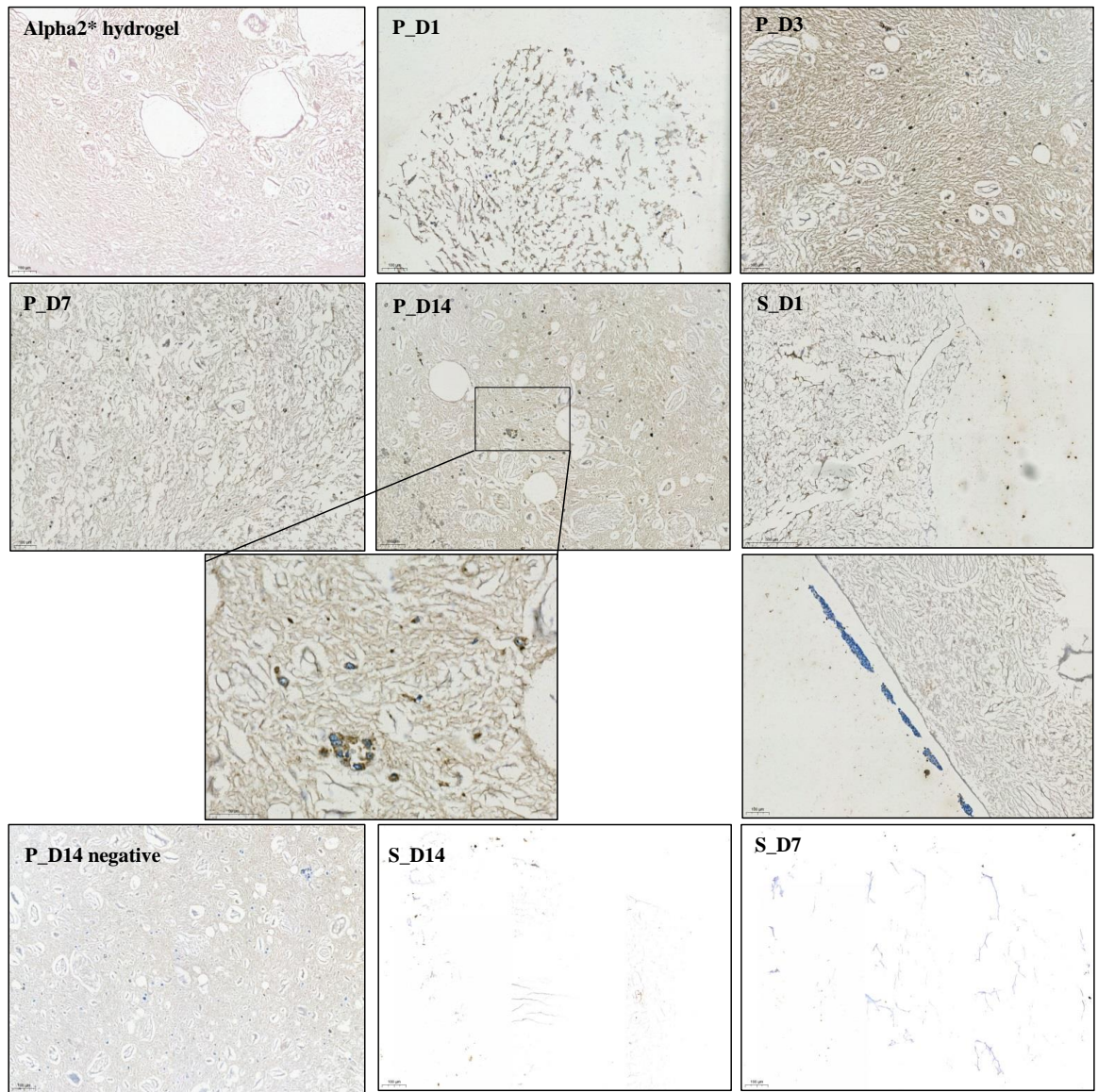
Figure 6.13: The images were taken for the hydrogel LNCaP printed and seeded constructs after staining with Pan cytokeratin, whereas P indicates printed constructs and S indicates seeded constructs. The dark brown stain surrounding the cells indicates the positive expression of the protein. In contrast, the only blue cells (with the absence of the dark brown surrounding them) indicates the negative expression of the protein. The stained hydrogel slide and the negatively stained slide of the printed construct are shown to compare the colour of the stain constructs.
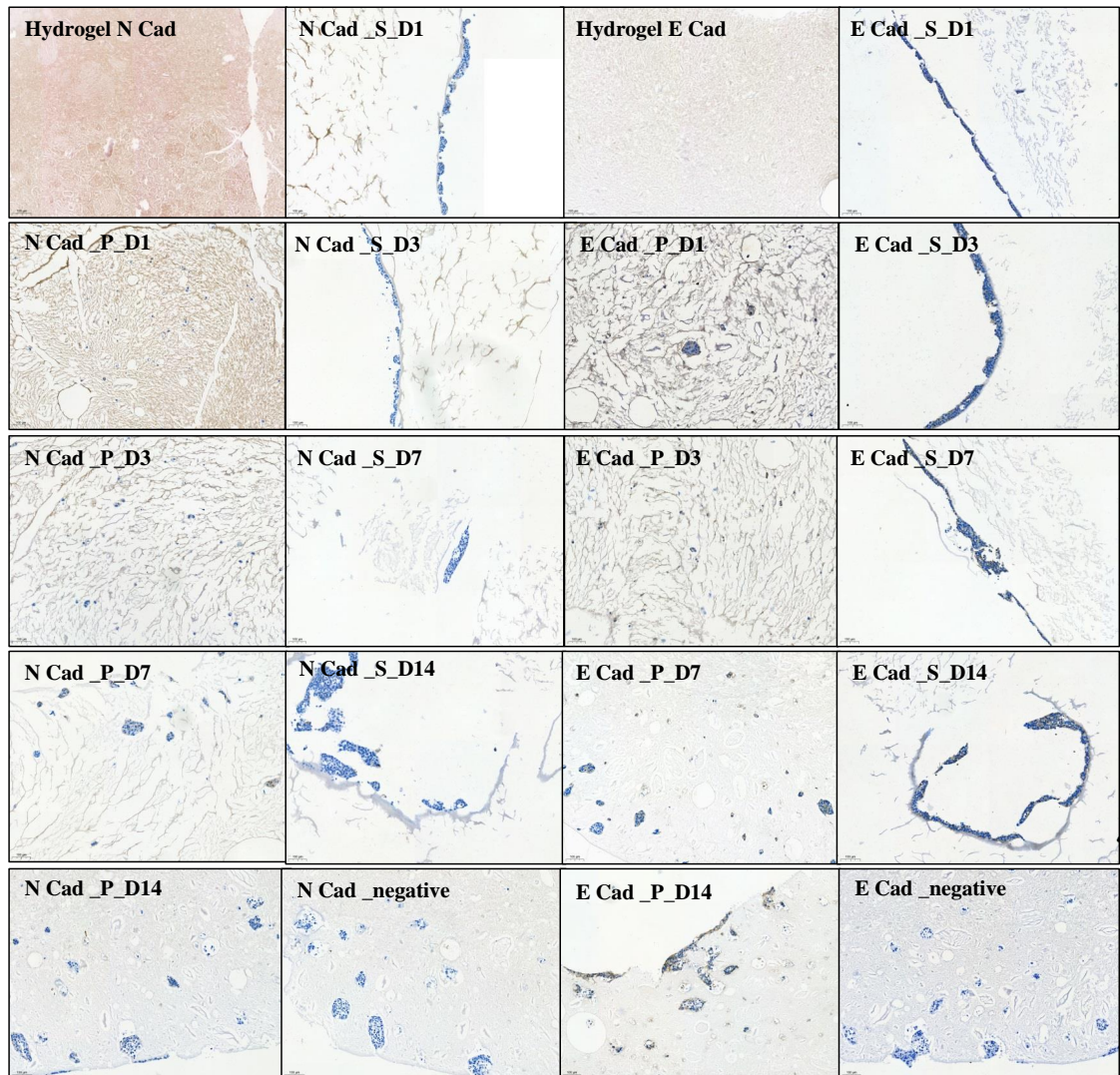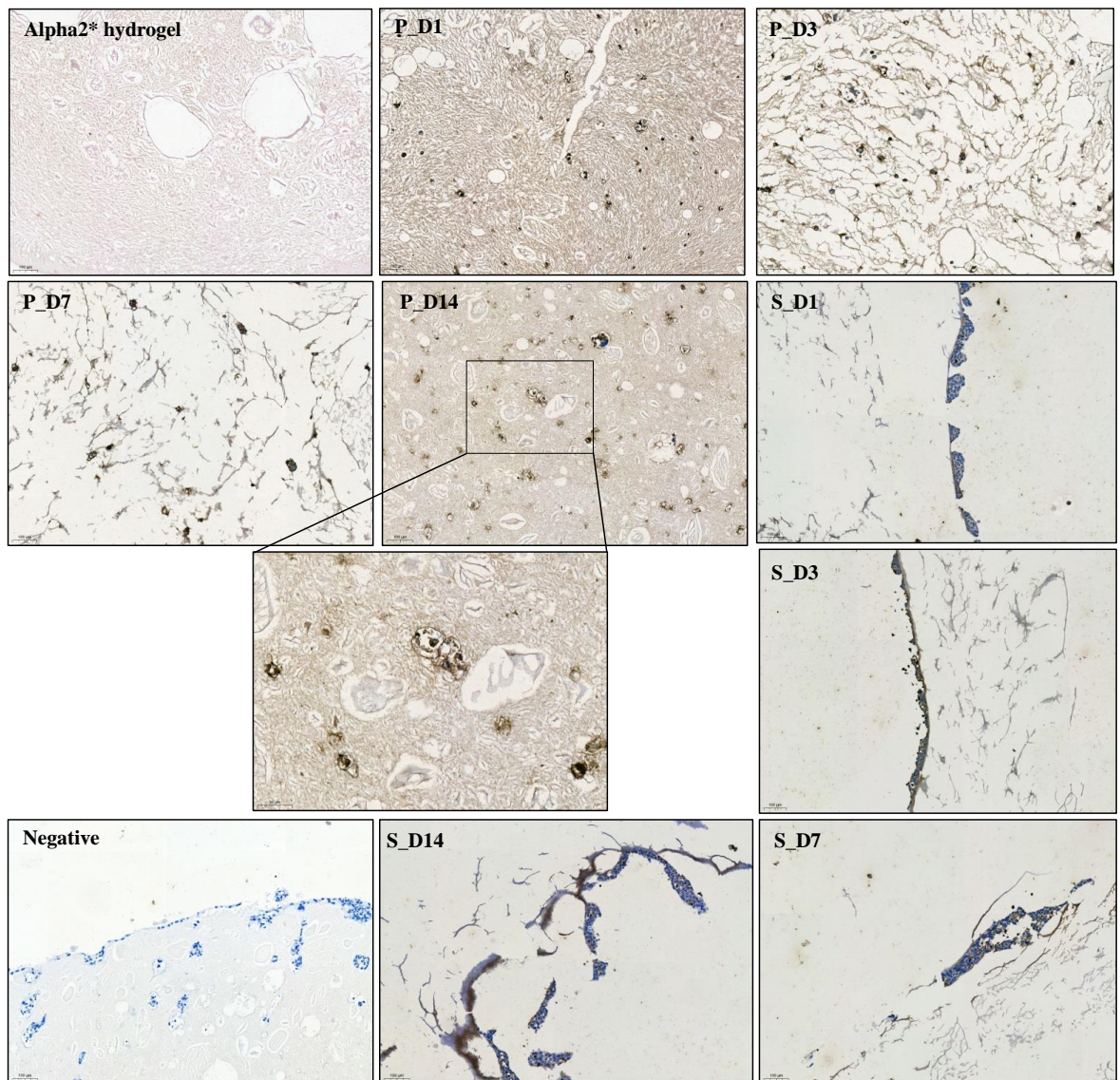
Figure 6.14: The images were taken for the hydrogel PNT2 printed and seeded constructs after staining with Pan cytokeratin, whereas P indicates printed constructs and S indicates seeded constructs. The dark brown stain surrounding the cells indicates the positive expression of the protein. In contrast, the only blue cells (with the absence of the dark brown surrounding them) indicates the negative expression of the protein. The stained hydrogel slide and the negatively stained slide of the printed construct are shown to compare the colour of the stain constructs.

The last protein checked was **HIF1**, which is an indication of hypoxia. This is expected to increase in cancer cells. The images show that the expression of it is positive, as can be seen in Figures 6.15, 6.16 and 6.17, respectively.
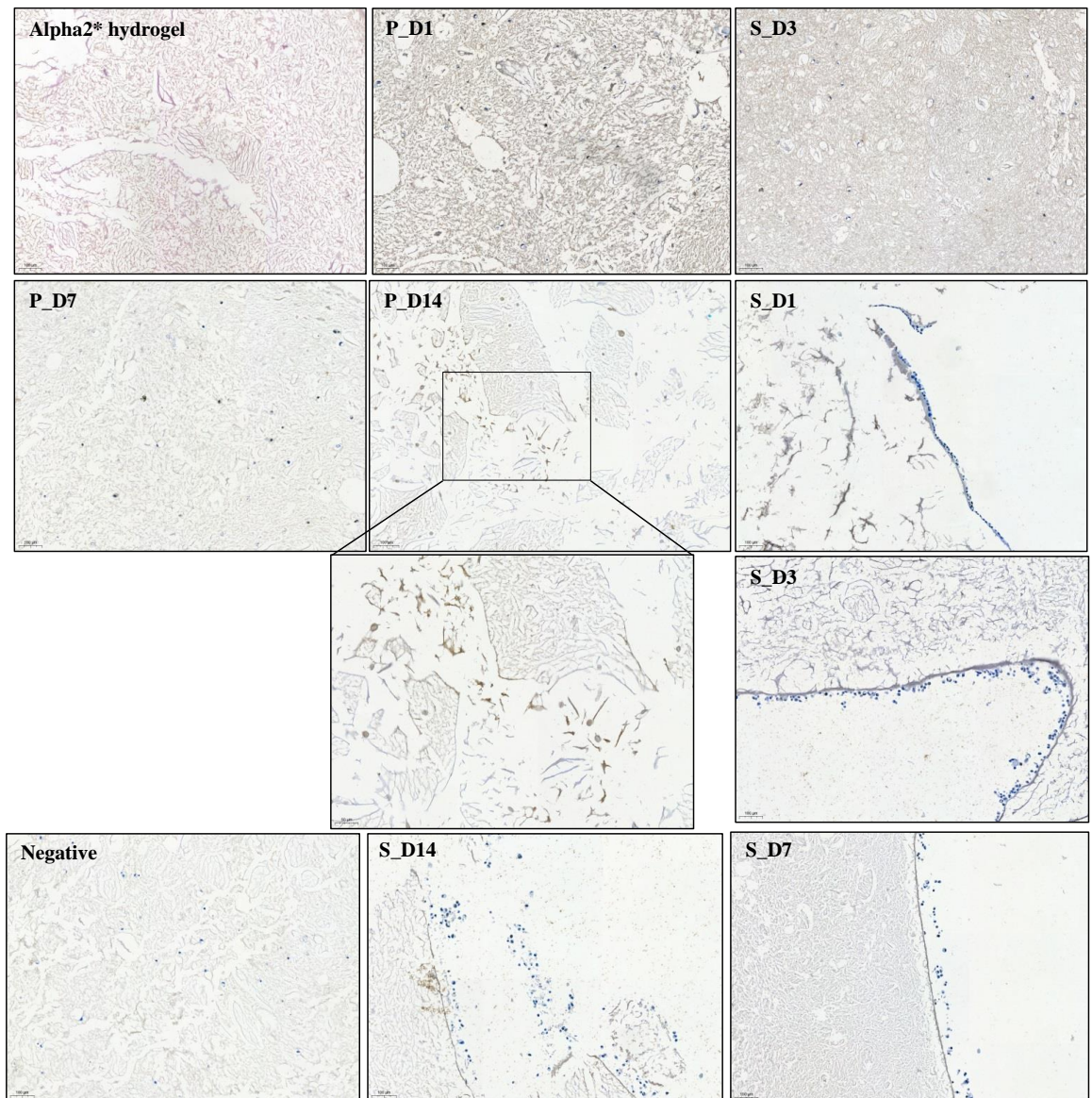
Figure 6.15: The images were taken for the hydrogel, PC3 printed and seeded constructs after staining with HIF1, whereas P indicates printed constructs and S indicates seeded constructs. The dark brown stain surrounding the cells indicates the positive expression of protein while the only blue cells (with the absence of the dark brown surrounding them) indicates the negative expression of the protein. The stained hydrogel slide and the negatively stained slide of the printed construct are shown to compare the colour of the stain constructs.
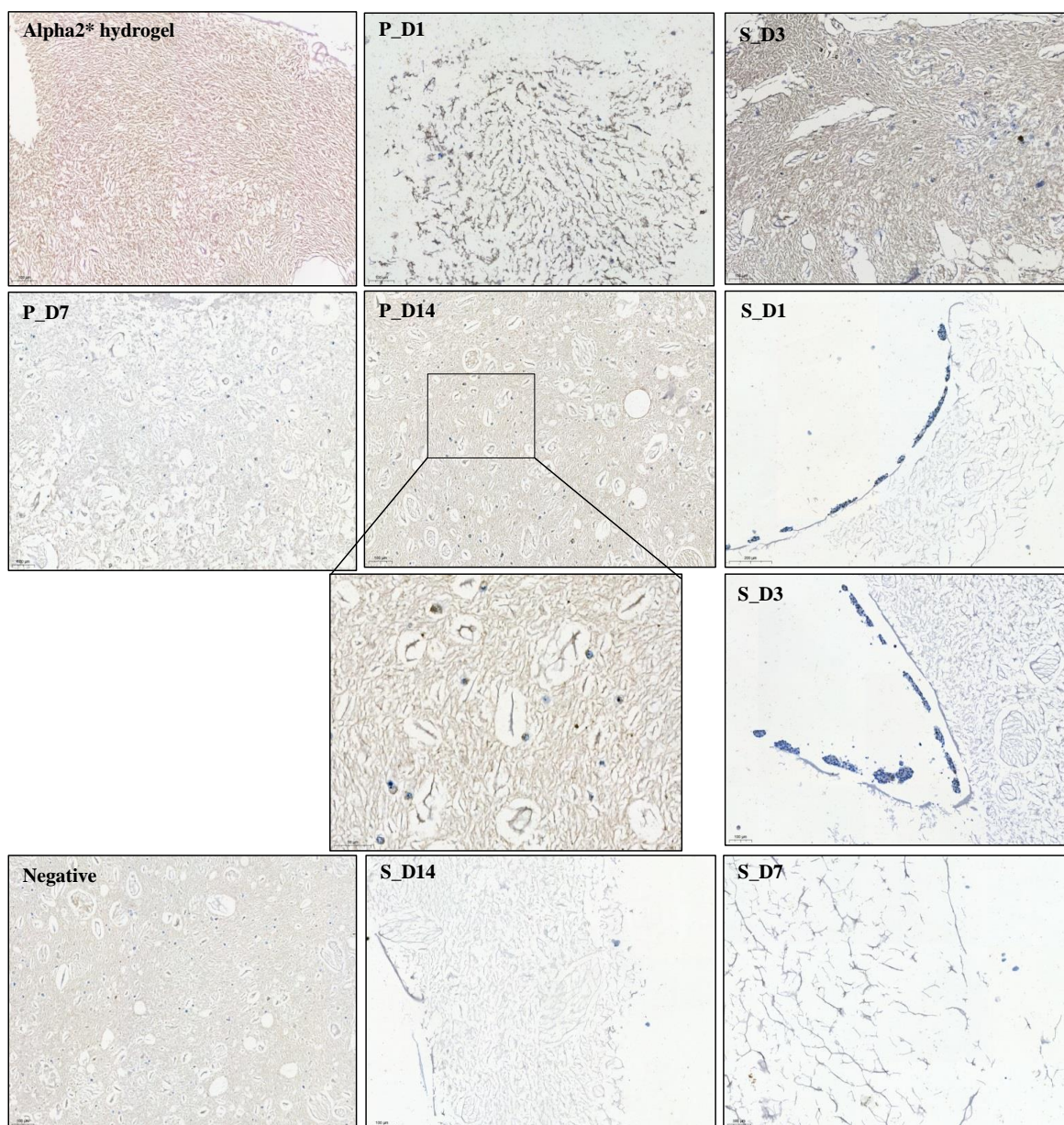
Figure 6.16: The images were taken for the hydrogel, LNCaP printed and seeded constructs after staining with HIF1, whereas P indicates printed constructs and S indicates seeded constructs. The dark brown stain surrounding the cells indicates the positive expression of the protein. In contrast, the only blue cells (with the absence of the dark brown surrounding them) indicates the negative expression of the protein. The stained hydrogel slide and the negatively stained slide of the printed construct are shown to compare the colour of the stain constructs.
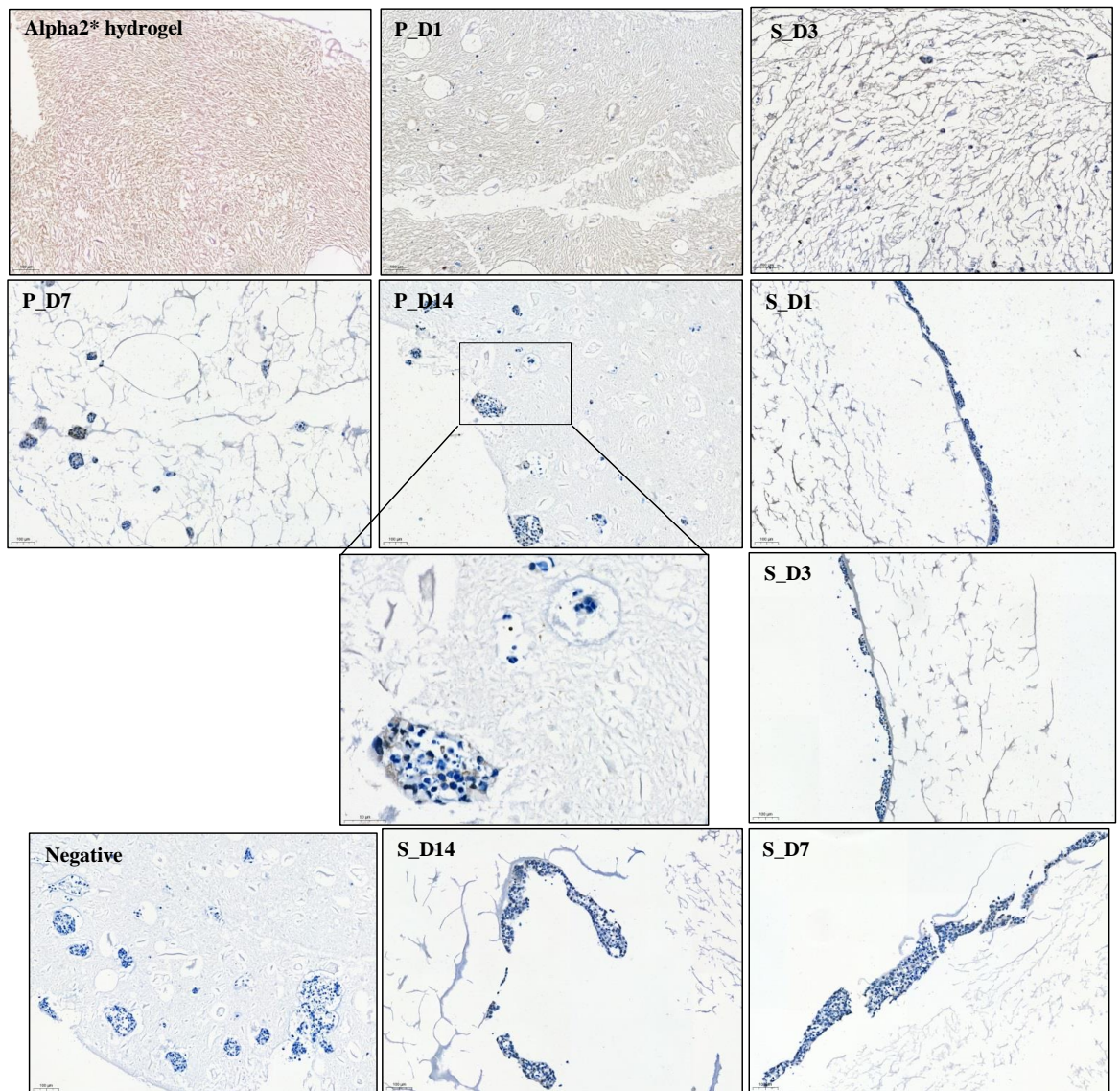
Figure 6.17: The images were taken for the hydrogel, PNT2 printed and seeded constructs after staining with HIF1, whereas P indicates printed constructs and S indicates seeded constructs. The dark brown stain surrounding the cells indicates the positive expression of the protein. In contrast, the only blue cells (with the absence of the dark brown surrounding them) indicates the negative expression of the protein. The stained hydrogel slide and the negatively stained slide of the printed construct are shown to compare the colour of the stain constructs.

The normalised intensity is shown in Figure 6.8 and it agreed with the other positively expressed proteins. Interestingly, the effect on the number of cells on the expression of HIF1 was found to be much higher than the other proteins as the intensity increase and decrease in a steeper trend for both seeded and printed cells. The expression of HIF1 protein that indicates

the hypoxia of the cancer was found to be associated with most of the prostate cancer cell lines and is considered to be one of the common derived condition in cancer development (Huang et al. (2018); Saramäki et al. (2001)).

6.4   Conclusion

The successful embedding and cutting of the printed and seeded construct of the three cell lines (PC3, PNT2 and LNCaP) increase the ability of the analysis and assessment of the build constructs. Also, it allowed the comparison of the seeded (as control) and printed constructs. The cut sections were stained with H&E, which proves the ability to analyse the constructs and the build model later in the same way as the clinical assessment. This is considered to be an important step enabling the comparison with the pathologists' work and it gives an idea of how the build model behaves biologically. The build model should behave in a similar way, biologically to the real clinical samples in order to be used in drug testing. To ensure the cells, after being embedded in the hydrogel, are still expressing the same proteins, the IHC test for five proteins was performed. The results show the differences in the expression of the proteins between the cell lines and prove that the proteins that were expressed in seeded cells are still expressed in printed cells. This a step forward in building a model that resembles a real cancerous prostate tissue. The use of single cells type can be expanded more than one cell type, probably gradually.

7

FTIR imaging

Introduction

With numerous applications of FTIR imaging in biomedical science, as can be seen in chapter 2, it has been chosen for the analysis of the built constructs. The aim of the use of FTIR imaging to analyse these constructs is to study the effect of the microenvironment (the adjacent cells) on tumour progression. Although the whole model has not been built during this study, the ability to analyse it will be a significant step towards the knowledge of what is going on with cancer and how it is progress.

7.1 Analysis of the seeded cells

The first part of the FTIR analysis is to check the seeded construct. The scans were of two different sites on the slide. The first site is where the hydrogel is seen with no cells and the second one is where the cells are. In this case, the aim was to try and to get the cells scan with no hydrogel. The slide chosen for this analysis test is the hydrogel seeded with PC3 cells on day 14. This was chosen since it contains a high number of cells compared to the other cell lines. In addition, one cell line will be tested, and it will be applied to the others if it found to work. Figure 7.1 (A) represents the spectra of the seeded construct, the hydrogel side and the cells side. The hydrogel side spectrum is obtained by getting the mean spectrum of all the 1638 spectra that make up one FPA tile and processed with denoise and CO_2 removal. The cell side spectrum is obtained with the same method as the hydrogel side with the addition to the use of cell finder code to ensure having cells only (as the exact place of them is known). The resulting spectra show that cells and hydrogel have the same peaks. The hydrogel consists of amino acids and it is expected to have a similar peaks position as the cells. The difference in the intensities is also expected since the amino acids in the hydrogel are in much more of a pure state than the proteins in cells, giving more intense sharp peaks. The cells, however,

143

consist of a large number of proteins causing the peaks to broaden. Figure 7.1 (B) shows the same spectra in the range of $1450 - 1000$ cm^{-1} to check the appearance of the phosphate antisymmetric and symmetric stretches 1230 and 1080 cm^{-1} (DNA). These peaks are found in the cells and not supposed to be seen in the hydrogel. A distinct peak was seen at 1230 cm^{-1} in the cell side spectrum. It looks like the same peak is present in the hydrogel side spectrum with low intensity.
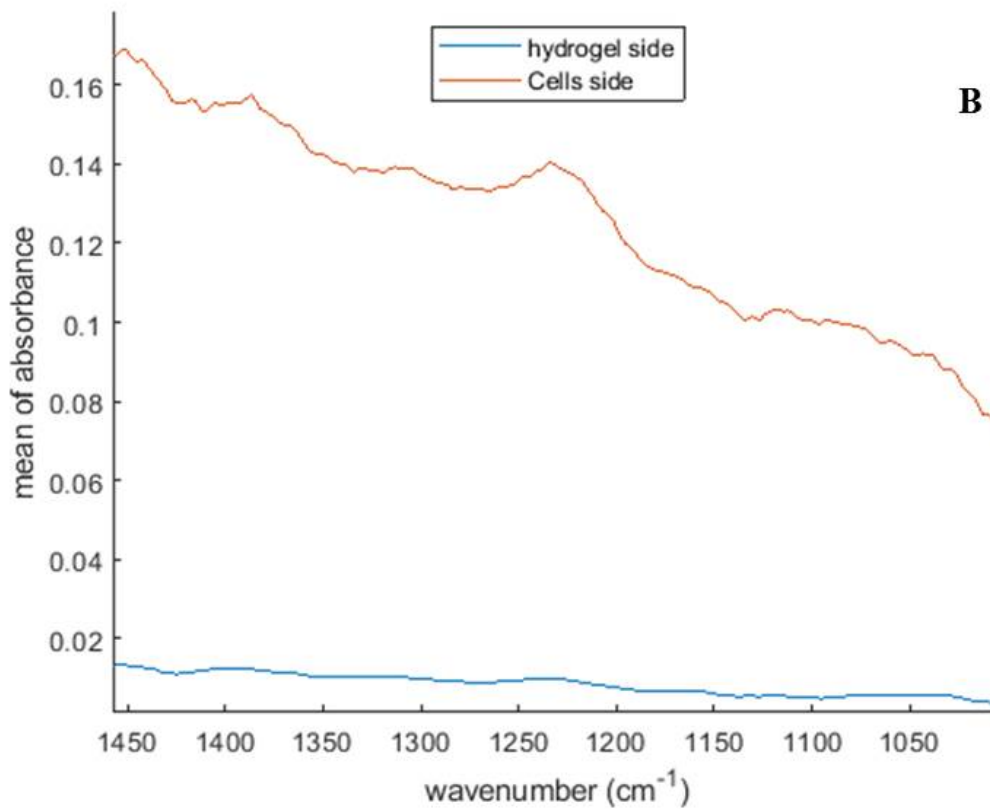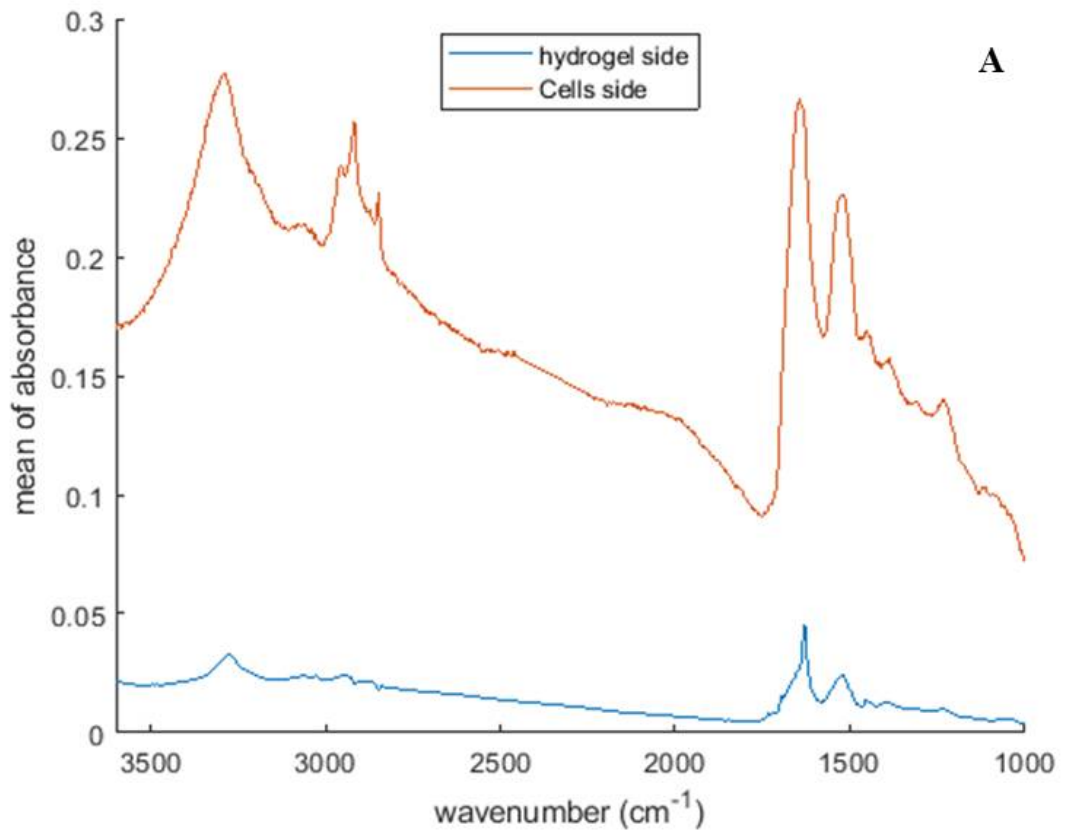
Figure 7.1: A) the spectra of the hydrogel side and the cells side from the same seeded construct. B) the range 1450 — 1000 cm^{-1} of the same spectra giving a closer look where the DNA peaks.

In order to have a better look at the differences between the two spectra, vector normalisation applied to them. Figure 7.2 shows the spectra after the normalisation in which A represents the full range spectra and B shows the spectra in the range $1450 — 1000$ cm^{-1}. The full range spectra show the two sides have almost the same peaks. The hydrogel side spectrum shows negative peaks, which means that the signal in the background is higher than the sample, and it is probably caused by fingerprints since the background slide is empty. The other thing that has been noticed is the appearance of the peak in 1230 cm^{-1}, which means neither this is a peak nor the other peaks in the same area cannot be relied on. They all appear in both spectra.
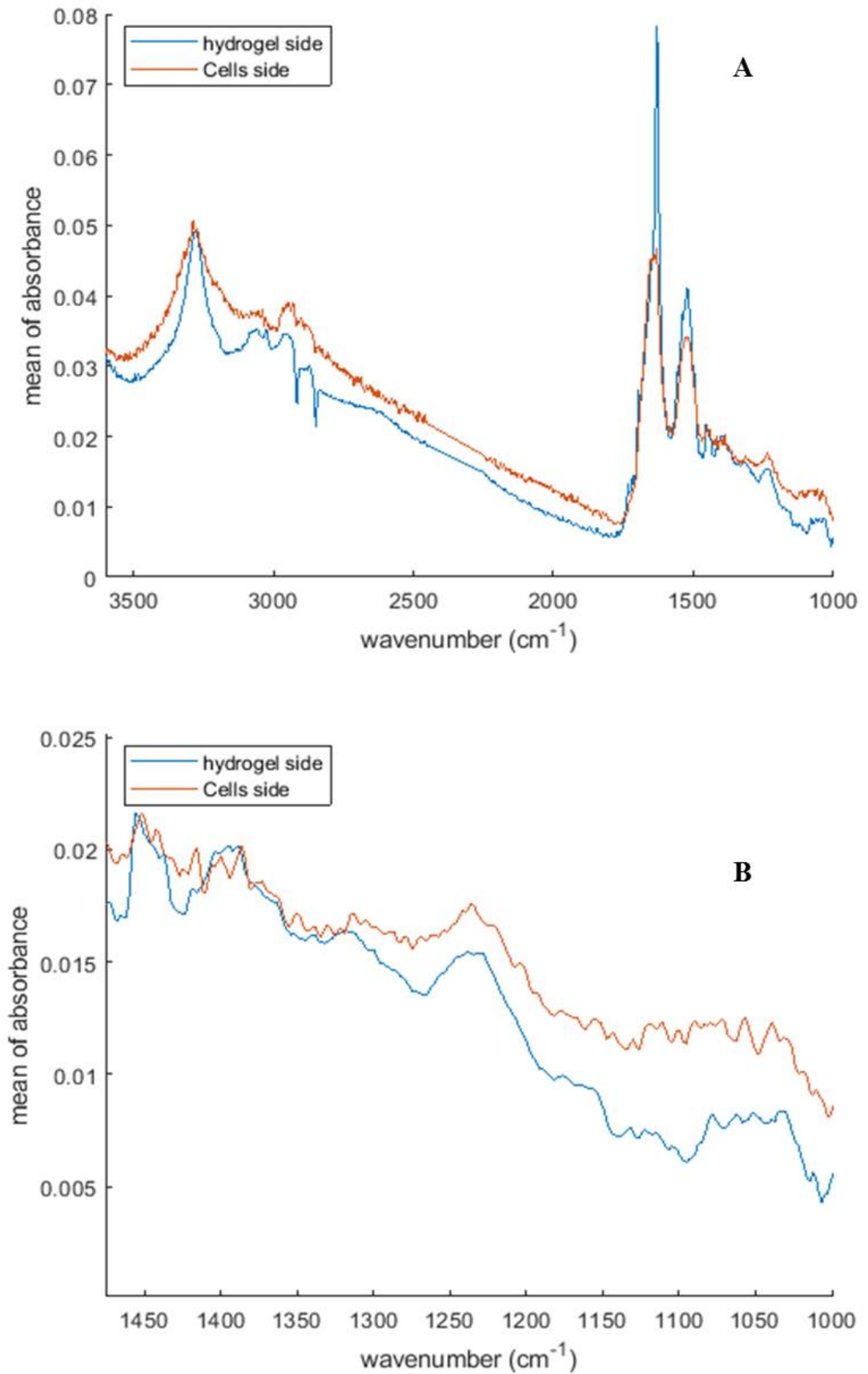
Figure 7.2: A) the spectra of the hydrogel side and the cells side from the same seeded construct after vector normalisation. B) the range 1450 — 1000 cm^{-1} of the same spectra giving a closer look where the DNA peaks after vector normalisation.

7.2   Analysis of the printed cells

After cutting the printed construct into 10 μm section and placed in a CaF$_2$ disc, they were scanned to obtain FTIR imaging spectra. The analysis of the spectra is carried out in the same way as the hydrogel side of the seeded slide discussed previously in section 7.1. The fact that the hydrogel and cells contain very similar peaks across the spectrum means that it is difficult to use the cell finder to find the cells in a mixture of the two. It always gives cells with hydrogel and there is no way we can separate them through it. The obtained mean spectrum is for both cells and hydrogel. Three different areas of the construct were scanned and compared to a hydrogel only mean spectrum as shown in Figure 7.3. The different areas of the printed construct show different intensities and that is probably due to the difference in the thickness of the different areas of the construct. It was also difficult to find a distinctive peak that can be used to separate the cells from the hydrogel. By having a closer look at the range of 1500 — 1000 cm^{-1} as shown in Figure 7.3 B, different peaks were seen and it found hard to decide which one is a real peak even if it goes through vector normalisation.
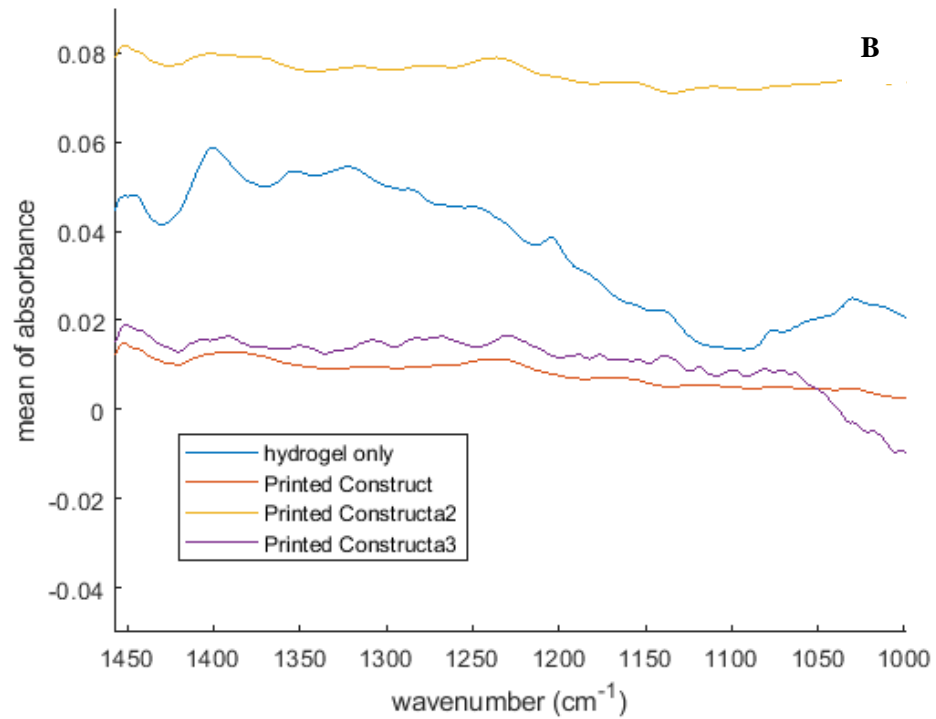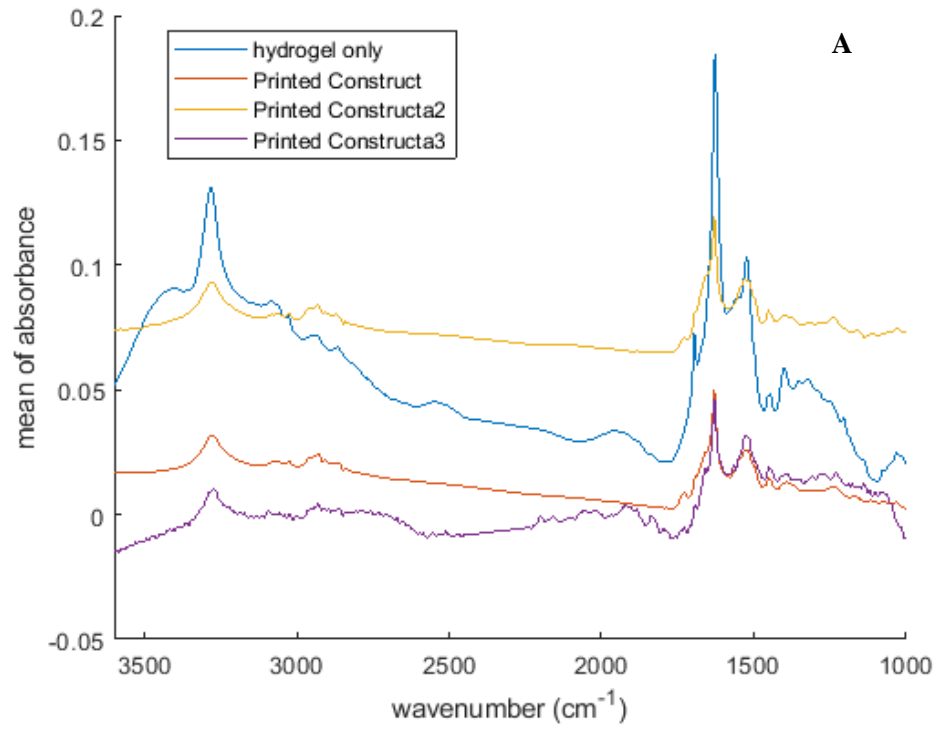
Figure 7.3: The spectra of the hydrogel and three different areas of the printed construct (hydrogel and cells). The differences between the areas of the printed construct are related to the differences in the thickness of these areas.

7.3 Multivariate curve resolution

Multivariate Curve Resolution (MCR) are analysis methods that solve the problems associated with the analysis of mixtures. MCR considered to be one of the analysis methods that suite spectroscopic measurements. The reason behind this is that MCR works with bilinear models that have pure contributions and spectroscopy data fits in this category since they follow Beer-Lambert Law. MCR helps to separate the components of the mixture with or without information about the mixture components. The development of the methods used in MCR moves the analysis from the basic bilinear models to multi-way methods (Haaland et al. (2016); Juan (2020)). In hyperspectral imaging, Multivariate Curve Resolution-Alternative Least Square (MCR-ALS) is the most common algorithms used. It is based on the use of alternating least squares to optimise the concentration and spectra that are related to the spatial and spectral characteristics of the image (Juan, 2020). Through this study, the data obtained by hyperspectral imaging were pre-processed before MCR used. The pre-processing methods differ from one experiment to another depending on the obtained data and what are the best ways that can be used to improve and increase the accuracy of the results obtained with MCR. The pre-processing used in this study starts with cropping the spectral data into the range of $1000 - 3800$ cm^{-1}. Then the minimum intensity is set to zero since some of the data were allocated under zero. The median of the hydrogel spectra was taken and shown in Figure 7.4.
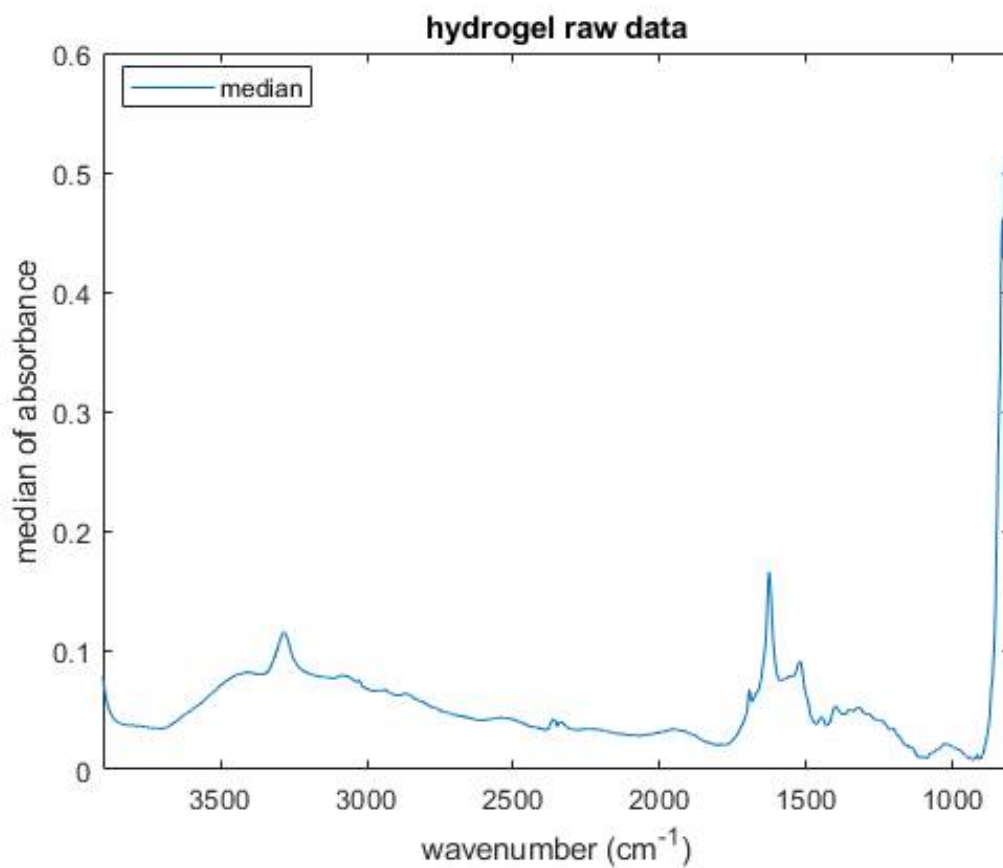
Figure 7.4: The median of the hydrogel spectra.

The printed constructs spectra, on the other hand, were processed with RMies algorithm (one iteration) to remove the scattering from the data. Figure 7.5 (A) shows the raw data and (B) show the data after scattering correction.
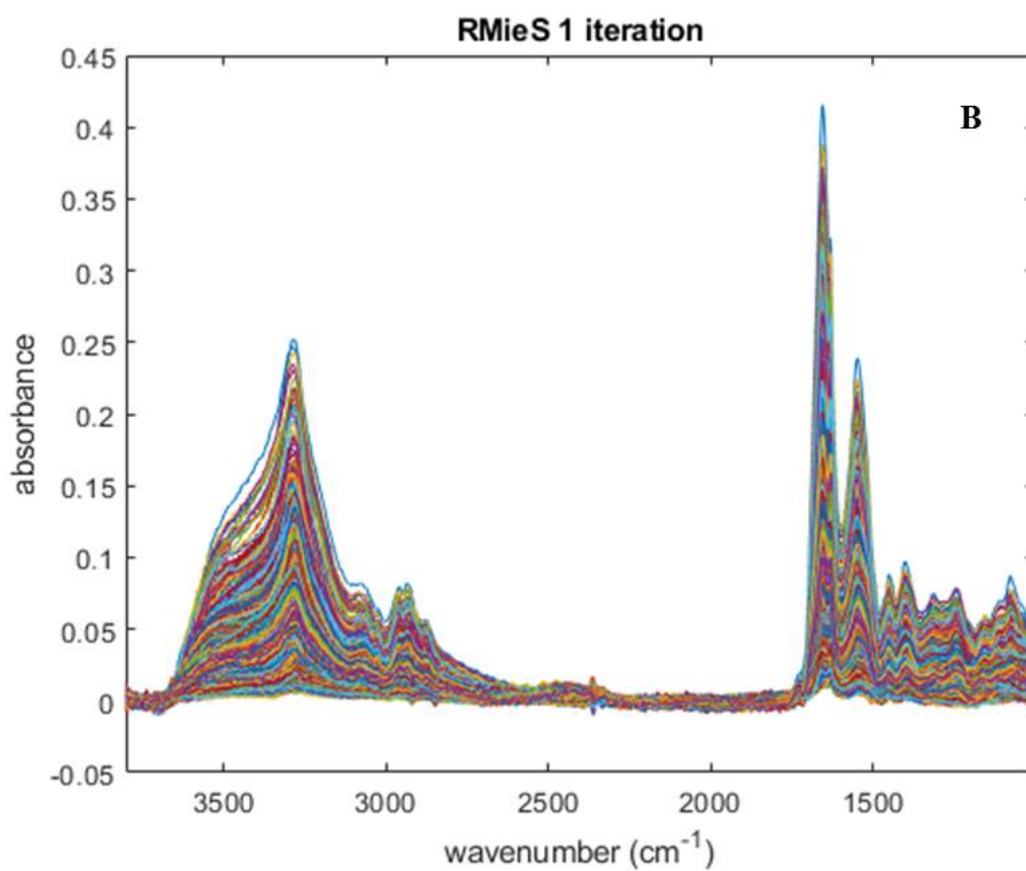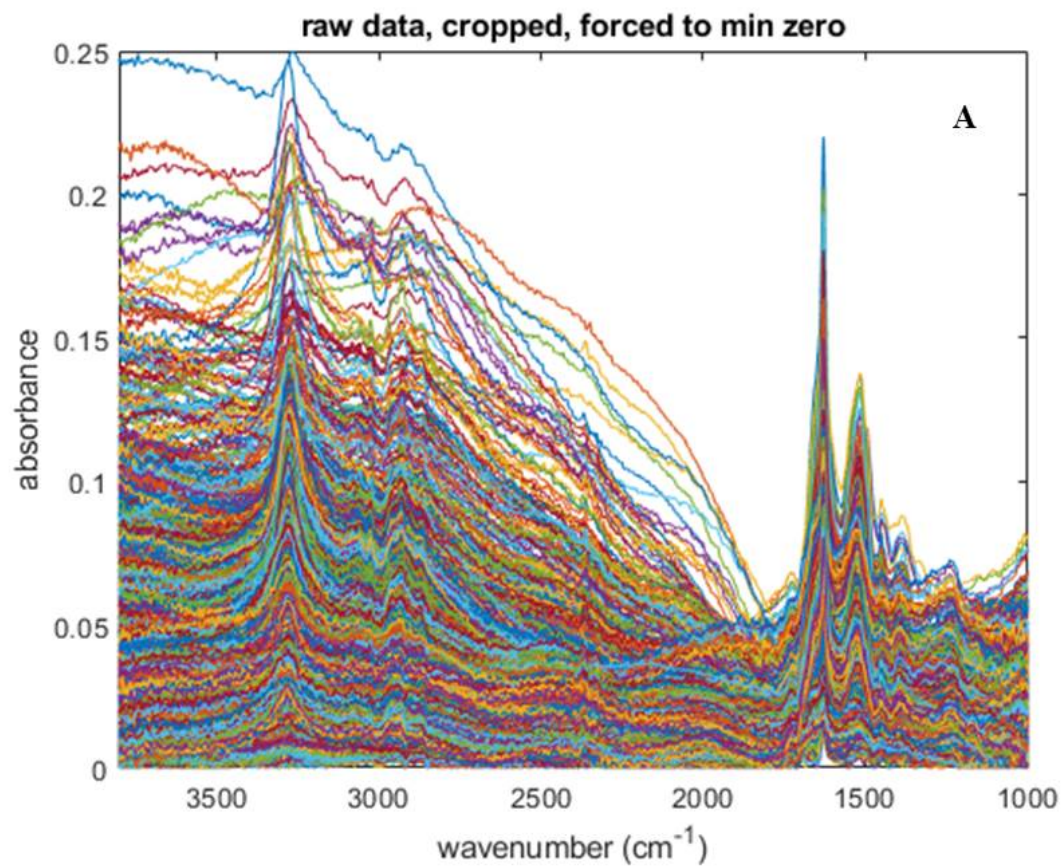
Figure 7.5: (A) the printed construct raw data and (B) data after scattering correction.

Putting the cells with the hydrogel into the RMies function might cause problems on the data since the hydrogel spectrum is fitted with a pure cells spectrum and this function will correct both. However, as it can be seen from Figure 7.5 (A), there is a high amount of scattering in the data and it worth trying the RMieS to get better spectra.

The main target of the data pre-processing is to separate the data using MCR; one of the issues found here is that some of the spectra have scattering and some are not, which will add extra proportion to the MCR function and there will be high chances of not getting good results. For the MCR process, the hydrogel median spectrum was appended to the spectra in the cells-in-hydrogel image data. The hydrogel spectrum will work as a reference on the separation that will be done. The data were reshaped into bilinear instead of having pixels of 3 dimensions before applying MCR. By setting the number of components to two; cells and hydrogel, the MCR was run with the default parameters.

The separation results are shown in Figure 7.6 and show the resultant spectra for the cells (component 1) and the hydrogel (component 2). The cell spectrum shows the general parts that usually seen in the cell spectrum (looks more like the spectrum of real cells). In addition, the image shows bright spots consistent with the location of the cells. The obtained result was compared with the biological spectrum of the cells shown in Figure 2.17 and the distinctive cells peaks can be seen clearly, especially amide I and amide II. However, gathering a real spectrum of the cells and adding it to the algorithm might give a better analysis. The hydrogel spectrum, though, does not look that much like a real spectrum, but the specific features of the hydrogel seem to have been preserved. The associated image is consistent with the hydrogel being present across the whole sample.
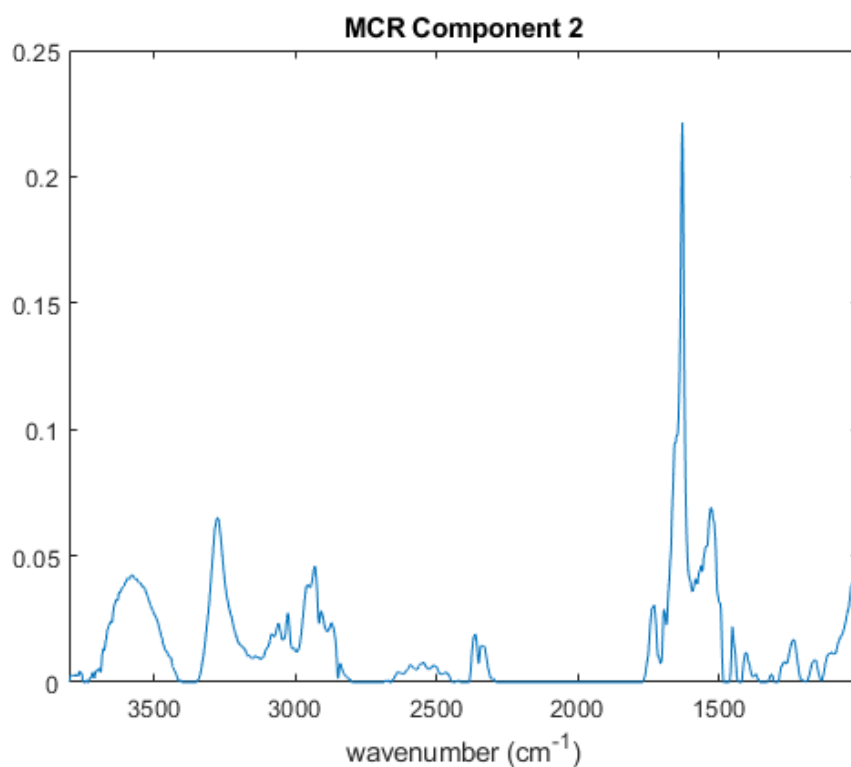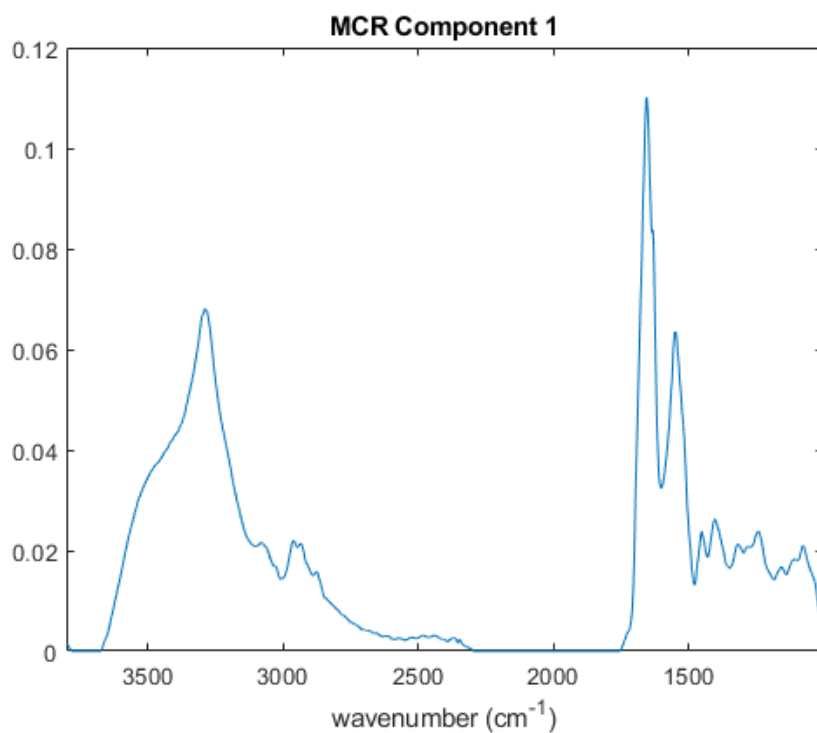
Figure 7.6: The MCR separation result showing the cells spectrum as component 1 and hydrogel spectrum as component 2.

The median hydrogel spectrum was combined with the hydrogel spectrum resulted from the MCR, as shown in Figure 7.7 . Although the features of the hydrogel can be seen in the

MCR results spectrum (orange), the probability of having a better result might increase when better hydrogel spectra obtained. One of the very distinctive peaks that can be seen in the hydrogel is the sharp amide I (at 1642 cm^{-1}) and it can be seen in both spectra.
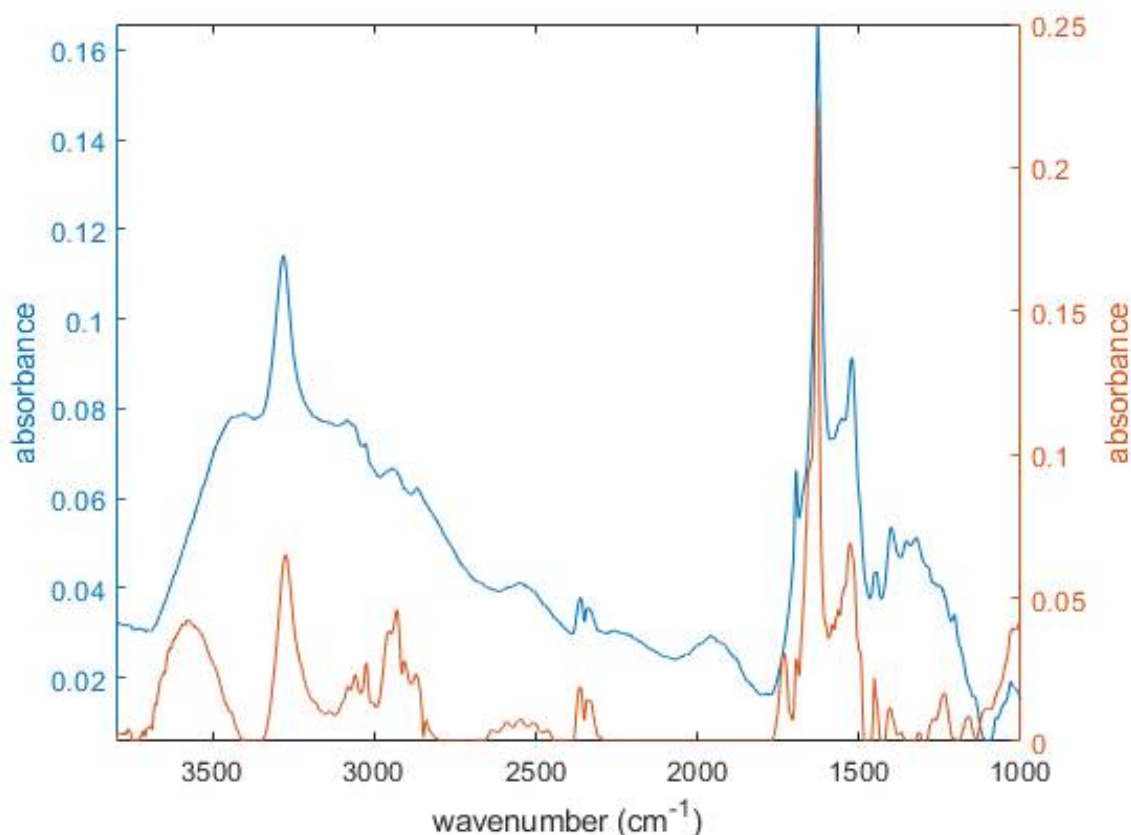
Figure 7.7: The hydrogel median spectrum (blue) combined with the hydrogel spectrum obtained using MCR (orange). The main hydrogel feature still can be seen after using MCR, although it does not look like a real spectrum.

The use of MCR for the separation seems to work, but it needs to go through a lot of improvement in order to get a better separation. One crucial part of the development is obtaining cells spectra and adding them to the MCR algorithm. In addition to obtaining better hydrogel spectra and the printed constructs spectra with the least amount of scattering. Also, the MCR can be done without the use of RMies for the cells with might works better when good spectra gathered with FTIR imaging machine. The other improvement is that using RMies for the background from this data and then three components; cells, hydrogel, and scattered background.

7.4   Conclusion

FTIR imaging has been used to scan the build constructs and the data was gathered and analysed. MATLAB software was used for the analysis of this data. The main goal of the analysis is to separate the cells peaks for the hydrogel one in order to be able to study the cells and the changing that they go through. The separation was found to be challenging since the hydrogel is consist of amino acids and it contains the same peaks as the cells. The first part of this analysis is to create an algorithm that works the same as an in house water correction algorithm water correction to remove the hydrogel bands. The inability to find a specific feature available in cells only that can be used to obtain an algorithm to separate them from the hydrogel causes the shift of the analysis towards MCR. Although MCR separates the two components, the results are still not satisfying and open the door to a lot of improvements that can be in future work. The main part of this improvement is gathering better FTIR imaging data for both hydrogel and the printed constructs.

8

Conclusions and Future Work

8.1 Conclusions

Prostate cancer is the most common cancer among men with a high death rate. The models that have been used to study this disease (i.e. animal models, 2D models and 3D models) present several limitations that undermine our ability to study important cellular mechanisms associated with prostate cancer initiation and progression. In this study, tissue engineering is used to design a 3D model that can be used to mimic the tumour environment.

Peptide hydrogels (alpha1, alpha2 and alpha2*) were used as ECM for prostate cancer cells (PC3, PNT2 and LNCaP). The study of the mechanical properties of the hydrogels shows that the media has a strong effect on the mechanical properties of the hydrogel but, interestingly, does not affect their viscosity. The study indicates that alpha 2 hydrogel has the lowest viscosity among the three and it was the most challenging when the optimal printing parameters are obtained.

3D bioprinted constructs were tested *in vitro* to evaluate the capacity of the alpha 1 hydrogel to support the viability and proliferation of encapsulated cells. Obtained results show that, despite being possible to print well-defined cell-laden hydrogels, the viability of encapsulated cells remains very limited. Alpha2 was found to work as a better ECM for all the cell lines. The issue that emerged for this hydrogel is the inability to print accurate constructs shape. Alpha2* shows a better printing shape and more accurate than alpha2. The viability of PC3 and PNT2 cells was high; however, LNCaP cells show a variation in their viability on this hydrogel which was confirmed by the metabolic activity test.

Cells encapsulated in alpha2* were successfully embedded in paraffin and cut. The cut sections were stained with H&E, which gives the ability to analyse the constructs and the future build model using the same method used in the clinics. Additionally, the IHC test for five proteins was performed to check the differences in their expression when the cells are

seeded on top of the hydrogel and encapsulated inside it for all the three cell lines. These proteins found to be expressed in the same way between the seeded cells and printed cells. The use if FTIR imaging to analyse the printed constructs was challenging since it was found to be hard to separate the signals of the cells from the hydrogel. The hydrogel consists of amino acids and contains the same peaks as the cells. The inability to finding a specific feature available in cells only that can be used to obtain an algorithm to separate them from the hydrogel was not possible and the analysis moved towards MCR. MCR was used to separate the cells and the hydrogel and the results obtained was not the best and needed to go through improvements.

8.2   Future Work

The research on building a model to study cancer has been going for a long time. Different studies have been looking forward to designing the best model that can mimic the cancer microenvironment and showing the heterogeneity needed to get closer to the real tissue. This study was done with the goal of building the theoretical model showed in Figure 1.1. Due to the high number of assessments and the long optimisation process, the time was just enough to go through the start-up model (Figure 1.2), leaving several unanswered questions that need to be further investigated and giving the ideas on the development of the constructs build into a model that can be used in different types of studies.

8.2.1   Research on the current build model

The printed constructs were analysed at different time-points going from day 1 to day 14. Since cancer needs much more than 14 days to progress, it will be worth trying to go for more time points. With the study of the degradation time of the hydrogel, the maximum time-point can be decided.

Also, further investigations for the LNCaP cell line can be done. It has been found that LNCaP shows a high variation between one-time-point to another. The number of cells fluctuated at the used time-points. One of the early experiments in this study indicates that LNCaP cells take a longer time to adapt to the hydrogel environment, but since it was a single experiment, it is not demonstrated in this thesis.

Another comparison point that can be studied and check whether it can make a difference or not is the use of the culture media without antibiotics. In this study, there was a high expectation of microbial contamination since the 3D bio-printer machine was not in a fume hood. The use of antibiotics was unquestionable to avoid this contamination. Although the printer was transferred at a certain point into a fume hood, it was not possible to move into a media without antibiotics since almost 80% of the study has been finished. The use

of antibiotics can cause changes in the cells' biochemistry and affect the cells differentiation potentials. Studying the use of the media without the antibiotics and compare it to the current results will allow to see if there are any differences between the two. Additionally, the culture media was found to have a high effect on the mechanical properties of the hydrogel. Two different culture media were used in this study; F-12 Ham used for PC3 cells and PRMI-1640 used for PNT2 and LNCaP. It would be worth trying culturing PC3 on RPMI-1640, and the differences between the current results and the newly obtained results can be studied. Moreover, this study used three different hydrogels, and one of them has been chosen to be continued with. alpha2* (hydrogel used for the model in this study) was found to have different mechanical properties after a certain time of the purchase. Different time points after purchase can be tested for the mechanical properties and check the best time point to build the model. In addition, the mechanical properties of the prostate can be considered and check the best time to build the model. The use of other techniques to help the analysis of FTIR imaging, such as the use of mass spectroscopy to find the content of the hydrogel and ease the separation of the cells' signals from the hydrogel signals as well as the use of different analysis techniques which in the separation process such as Independent Component Analysis (ICA). On the other hand, gathering better FTIR imaging data for the cells and the hydrogel can make the results of MCR better and probably more accurate. Also, separating the background and using it as a third component might improve the results even more.

8.2.2 Complexity of the model

The build constructs through this study contain only cancer cells. All the assessments were done for these cells to ensure the ability to culture them in a 3D environment. Due to time constraints, no other cells were added. One important future work is to add more cells to the model. All the added cells have to go through all the different biological tests that ensure the viability of these cells in the same environment. The various cells that can be added to the model are shown in the theoretical model in Figure 1.1. One of the assessments that can help with the model is the IHC and it can show whether the same proteins are still expressed in the build model. An example of it is the reactive stroma which found to increase vimentin expression. Another part of the work that can be done is the printing in different geometries that can get even closer to prostate shape with the different types of cells in similar places as the real tissue. Further development of the model is by developing a 3D printed tissue model for bone biopolymer (PCL), Calcium phosphate and bone marrow stem cells. Once it is completed, it will be combined with the prostate constructs and further analysis is done.

8.2.3 Micro-environment Study

One of the areas that need more studies is the knowledge of cancer initiation and progression. This knowledge can be gained by the study of the tumour microenvironment. The change in the morphology of the different types of cells used to build the model can be studied. Another part that can be studied in the tumour microenvironment studying the proteins that cells produced and the growth of the cancer cells is supported by these proteins. Also, looking at the tumour, studying the effect of cancer cells on the surrounding cells can show how these tumours grow. One of the influences of these cells on the microenvironment is the release of extracellular signals, such as paracrine signals. On the other side, the role of ECM is another area to be studied in this model. In this model, hydrogels are used as ECM and the interaction between the cells and this hydrogel can be studied. Moreover, the ability of cancer cells to alter their physical properties and topography can be checked. Also, the ability of these cancer cells to migrate within the model with the influence of the ECM and the speed of migration of these cells are part of studying the effect of the ECM on the tumour. Further analysis could be done to the changes in metabolic activity. The Warburg effect can be studied by checking the presence of nucleotides, amino acids, and lipids that are associated with it. The other part of cancer metabolism is the gain of MYC oncogene function, which can be studied by checking the express of the genes that support anabolic growth. This means checking the enzymes that are correlated to the synthesis of fatty acid, serine metabolism, and mitochondrial metabolism. Further research needs to be done on the background of cancer metabolism and the exact experiments can be decided then. This demonstration of possible future work gives a hint on what can be done.

8.2.4 Therapy testing

As the model gets complicated and more cells are added to it, the chances of having a better platform for therapy testing are increased. Avoiding the differences found either between animal (when therapies are tested in animals) and human or between the in-vitro models and human. The current therapies can be developed and test using the developed method.

References

Per-Anders Abrahamsson and Martina Tinzl. Do We Need PSA and Early Detection of Prostate Cancer? *European Urology Supplements*, 7(5):393–395, 2008. ISSN 15699056. doi: 10.1016/j.eursup.2008.01.018. URL `http://linkinghub.elsevier.com/retrieve/pii/S1569905608000225`.

Agilent Technologies. FTIR chemical imaging using focal plane array – based systems. 2011. URL `https://www.agilent.com/cs/library/technicaloverviews/public/si-2645.pdf`.

Wheeler TM Kinner BM Ohori M Scardino PT Aihara M, Lebovitz RM. prostate specific antigen and gleason grade : an immunohistochemical study of prostate cancer . *The Journal of Urology*, 151(6):1558–1564, 1994.

Reiner S Alzer and Heinz W. Siesler. *Infrared and Raman Spectroscopic Imaging.* Wiley-VCH, 2nd editio edition, 2009. ISBN 9783527321506.

M Amin and A Khalid. Zonal Anatomy of Prostate. *Annals of King Edward . . .*, 16(3):138–142, 2011. URL `http://www.annalskemu.org/journal/index.php/annals/article/viewArticle/212`.

Daniel Arcos and María Vallet-Regí. Bioceramics for drug delivery. *Acta Materialia*, 61(3): 890–911, 2013. ISSN 13596454. doi: 10.1016/j.actamat.2012.10.039.

ASTM International. *F2792-12a - Standard Terminology for Additive Manufacturing Technologies.* 2013. ISBN 9781493921126. doi: 10.1520/F2792-12A.2. URL `http://www.ciri.org.nz/nzrma/technologies.html`.

Christophe Avenel, Anna Tolf, Anca Dragomir, and Ingrid B Carlbom. Glandular Segmentation of Prostate Cancer : An Illustration of How the Choice of Histopathological Stain Is One Key to Success for Computational Pathology. 7:1–11, 2019. doi: 10.3389/fbioe.2019.00125.

Gustavo Ayala, Jennifer A. Tuxhorn, Thomas M. Wheeler, Anna Frolov, Peter T. Scardino, Makoto Ohori, Marcus Wheeler, Jeffrey Spitler, and David R. Rowley. Reactive Stroma as a Predictor of Biochemical-Free Recurrence in Prostate Cancer. *Clinical Cancer Research*, 9(13):4792–4801, 2003. ISSN 10780432.

Waqas Azeem, Yaping Hua, Karl-henning Kalland, Xisong Ke, Jan Roger Olsen, Anne Margrete Øyan, and Yi Qu. Biomarkers of the Tumor Microenvironment. pages 449–464, 2017. doi: 10.1007/978-3-319-39147-2. URL `http://link.springer.com/10.1007/978-3-319-39147-2`.

Thaína A. Azevedo Tosta, Paulo Rogério de Faria, Leandro Alves Neves, and Marcelo Zanchetta do Nascimento. Computational normalization of H&E-stained histological images: Progress, challenges and future potential. *Artificial Intelligence in Medicine*, 95(July 2018):118–132, 2019. ISSN 18732860. doi: 10.1016/j.artmed.2018.10.004.

M. J. Baker, E. Gazi, M. D. Brown, J. H. Shanks, P. Gardner, and N. W. Clarke. FTIR-based spectroscopic analysis in the identification of clinically aggressive prostate cancer. *British Journal of Cancer*, 99(11):1859–1866, 2008. ISSN 00070920. doi: 10.1038/sj.bjc.6604753.

Matthew J. Baker, Ehsan Gazi, Michael D. Brown, Jonathan H. Shanks, Noel W. Clarke, and Peter Gardner. Investigating FTIR based histopathology for the diagnosis of prostate cancer. *Journal of Biophotonics*, 2(1-2):104–113, 2009. ISSN 1864063X. doi: 10.1002/jbio. 200810062.

Matthew J Baker, Júlio Trevisan, Paul Bassan, Rohit Bhargava, Holly J Butler, Konrad M Dorling, Peter R Fielden, Simon W Fogarty, Nigel J Fullwood, Kelly A Heys, Caryn Hughes, Peter Lasch, Martin-Hirsch, Pierre L Obinaju, Blessing Ganesh D Sockalingum, Josep Sulé-Suso, Rebecca J Strong, Michael J Walsh, Bayden R Wood, Peter Gardner, and Francis L Martin. Using Fourier transform IR spectroscopy to analyze biological materials. Nature protocols. *Igarss 2014*, 9(8):1771–1791, 2014. ISSN 13514180. doi: 10.1007/s13398-014-0173-7.2.

Keith R Bambery, Bayden R Wood, and Don McNaughton. Resonant Mie scattering (RMieS) correction applied to FTIR images of biological tissue samples. *The Analyst*, 137(1):126–32, 2012. ISSN 1364-5528. doi: 10.1039/c1an15628d. URL http://www.ncbi.nlm.nih.gov/pubmed/22076587.

C. N. Banwell. The fundamental of molecular spectroscopy, 1983.

Wendy W. Barclay, Ralph D. Woodruff, M. Craig Hall, and Scott D. Cramer. A system for studying epithelial-stromal interactions reveals distinct inductive abilities of stromal cells from benign prostatic hyperplasia and prostate cancer. *Endocrinology*, 146(1):13–18, 2005. ISSN 00137227. doi: 10.1210/en.2004-1123.

David A. Barron and David R. Rowley. The reactive stroma microenvironment and prostate cancer progression. *Endocrine-Related Cancer*, 19(6):187–204, 2012. ISSN 13510088. doi: 10.1530/ERC-12-0085.

P. J. Bártolo, C. K. Chua, H. A. Almeida, S. M. Chou, and A. S. C. Lim. Biomanufacturing for tissue engineering: Present and future trends. *Virtual and Physical Prototyping*, 4(4): 203–216, 2009. ISSN 1745-2759. doi: 10.1080/17452750903476288. URL http://www.scopus.com/inward/record.url?eid=2-s2.0-71449126497&partnerID=tZOtx3y1.

Paul Bassan, Ashwin Sachdeva, Jonathan H. Shanks, Mick D. Brown, Noel W. Clarke, and Peter Gardner. Whole organ cross-section chemical imaging using label-free mega-mosaic FTIR microscopy. *Analyst*, 138(23):7066–7069, 2013. ISSN 13645528. doi: 10.1039/c3an01674a.

Paul Bassan, Ashwin Sachdeva, Jonathan H. Shanks, Mick D. Brown, Noel W. Clarke, and Peter Gardner. Automated high-throughput assessment of prostate biopsy tissue using infrared spectroscopic chemical imaging. *Medical Imaging 2014: Digital Pathology*, 9041 (March 2014):90410D, 2014. ISSN 16057422. doi: 10.1117/12.2043290.

Dorothy A. Beacham and Edna Cukierman. Stromagenesis: The changing face of fibroblastic microenvironments during tumor progression. *Seminars in Cancer Biology*, 15(5 SPEC. ISS.):329–341, 2005. ISSN 1044579X. doi: 10.1016/j.semcancer.2005.05.003.

Andreas P. Berger, Martina Deibl, Alexander Strasak, Jasmin Bektic, Alexandre E. Pelzer, Helmut Klocker, Hannes Steiner, Gernot Fritsche, Georg Bartsch, and Wolfgang Horninger. Large-Scale Study of Clinical Impact of PSA Velocity: Long-Term PSA Kinetics as Method of Differentiating Men with from Those without Prostate Cancer. *Urology*, 69(1):134–138, 2007. ISSN 00904295. doi: 10.1016/j.urology.2006.09.018.

J.S. Bergström and S. Brown. *Modeling and Mechanical Analysis of Fluoropolymer Components.* William Andrew Inc., 2005. doi: 10.1016/b978-081551502-9.50014-4. URL http://dx.doi.org/10.1016/B978-0-8155-1502-9.50014-4.

Thomas Billiet, Mieke Vandenhaute, Jorg Schelfhout, Sandra Van Vlierberghe, and Peter Dubruel. A review of trends and limitations in hydrogel-rapid prototyping for tissue engineering. *Biomaterials*, 33(26):6020–6041, 2012. ISSN 01429612. doi: 10.1016/j.biomaterials.2012.04.050. URL http://dx.doi.org/10.1016/j.biomaterials.2012.04.050.

Thomas Billiet, Elien Gevaert, Thomas De Schryver, Maria Cornelissen, and Peter Dubruel. The 3D printing of gelatin methacrylamide cell-laden tissue-engineered constructs with high cell viability. *Biomaterials*, 35(1):49–62, 2014. ISSN 01429612. doi: 10.1016/j.biomaterials.2013.09.078. URL http://dx.doi.org/10.1016/j.biomaterials.2013.09.078.

Richard Birnie, Steven D. Bryce, Claire Roome, Vincent Dussupt, Alastair Droop, Shona H. Lang, Paul A. Berry, Catherine F. Hyde, John L. Lewis, Michael J. Stower, Norman J. Maitland, and Anne T. Collins. Gene expression profiling of human prostate cancer stem cells reveals a pro-inflammatory phenotype and the importance of extracellular matrix interactions. *Genome Biology*, 9(5), 2008. ISSN 14747596. doi: 10.1186/gb-2008-9-5-r83.

Alberts Bruce, Bray Dennis, Hopkin Karen, Johnson Alexander, Lewis Julian, Raff Martin, Roberts Keith, and Walter Peter. *Essential Cell Biology*. Garland Science, 4th edition, 2013. ISBN 9780815344544.

Richard J. Bryant and Freddie C. Hamdy. Screening for Prostate Cancer: An Update. *European Urology*, 53(1):37–44, 2008. ISSN 03022838. doi: 10.1016/j.eururo.2007.08.034.

A. A.G. Bryden, A. Freemont, N. W. Clarke, and N. J.R. George. Positive expression of E-cadherin in prostatic bone metastases. *British Journal of Urology*, 79(SUPPL. 4):27, 1997. ISSN 00071331.

Lukas Bubendorf, Alain Schöpfer, Urs Wagner, Guido Sauter, Holger Moch, Niels Willi, Thomas C. Gasser, and Michael J. Mihatsch. Metastatic patterns of prostate cancer: An autopsy study of 1,589 patients. *Human Pathology*, 31(5):578–583, 2000. ISSN 00468177. doi: 10.1053/hp.2000.6698. URL http://www.sciencedirect.com/science/article/pii/S0046817700800350.

Sir Macfarlane Burnet. Cancer - A biological approach. *British Medical Journal*, 1:841–847, 1957. ISSN 0007-1447. doi: 10.1016/S0140-6736(57)91911-6.

Tong Cao, Kee-Hai Ho, and Swee-Hin Teoh. Scaffold design and in vitro study of osteochondral coculture in a three-dimensional porous polycaprolactone scaffold fabricated by fused deposition modeling. *Tissue engineering*, 9 Suppl 1:S103–S112, 2003. ISSN 1076-3279. doi: 10.1089/10763270360697012.

Roberta Censi, Wouter Schuurman, Jos Malda, Giorgio Di Dato, Petra E. Burgisser, Wouter J A Dhert, Cornelus F. Van Nostrum, Piera Di Martino, Tina Vermonden, and Wim E. Hennink. A printable photopolymerizable thermosensitive p(HPMAm-lactate)-PEG hydrogel for tissue engineering. *Advanced Functional Materials*, 21(10):1833–1842, 2011. ISSN 1616301X. doi: 10.1002/adfm.201002428.

L. Chang, P. H. Graham, J. Hao, J. Ni, J. Bucci, P. J. Cozzi, J. H. Kearsley, and Y. Li. Acquisition of epithelialmesenchymal transition and cancer stem cell phenotypes is associated with activation of the PI3K/Akt/mTOR pathway in prostate cancer radioresistance. *Cell Death and Disease*, 4(10), 2013. ISSN 20414889. doi: 10.1038/cddis.2013.407.

Fa-Ming Chen, Min Zhang, and Zhi-Fen Wu. Toward delivery of multiple growth factors in tissue engineering. *Biomaterials*, 31(24):6279–6308, 2010. doi: 10.1016/j.biomaterials.2010.04.053.

Helena N. Chia and Benjamin M. Wu. Recent advances in 3D printing of biomaterials. *Journal of Biological Engineering*, 9:4, 2015. ISSN 1754-1611. doi: 10.1186/

s13036-015-0001-4. URL `http://dx.doi.org/10.1186/s13036-015-0001-4%5Cnhttps://jbioleng.biomedcentral.com/articles/10.1186/s13036-015-0001-4%5Cnhttps://jbioleng.biomedcentral.com/track/pdf/10.1186/s13036-015-0001-4?site=jbioleng.biomedcentral.com`.

T.-M.Gabriel Chu, David G. Orton, Scott J. Hollister, Stephen E. Feinberg, and John W. Halloran. Mechanical and in vivo performance of hydroxyapatite implants with controlled architectures. *Biomaterials*, 23(5):1283–1293, 2002. doi: 10.1016/S0142-9612(01)00243-5.

Cindy Chung and Jason A. Burdick. Engineering cartilage tissue. *Advanced Drug Delivery Reviews*, 60(2):243–262, 2008. doi: 10.1016/j.addr.2007.08.027.

Ashlee K. Clark, Anna V. Taubenberger, Renea A. Taylor, Birunthi Niranjan, Zhen Y. Chea, Elena Zotenko, Shirly Sieh, John S. Pedersen, Sam Norden, Mark Frydenberg, Jeremy P. Grummet, David W. Pook, Clare Stirzaker, Susan J. Clark, Mitchell G. Lawrence, Stuart J. Ellem, Dietmar W. Hutmacher, and Gail P. Risbridger. A bioengineered microenvironment to quantitatively measure the tumorigenic properties of cancer-associated fibroblasts in human prostate cancer. *Biomaterials*, 34(20):4777–4785, 2013. ISSN 01429612. doi: 10.1016/j.biomaterials.2013.03.005.

K I M C O Connor, D Ph, and Richard M Enmon. Dimensional Cultures of DU 145 Human Prostate Carcinoma Cells Grown in Simulated Microgravity. 3(2):161–171, 1997.

E. David Crawford, Edward P. DeAntoni, Ruth Etzioni, Virginia C. Schaefer, Robert M. Olson, and Collen A. Ross. Serum prostate-specific antigen and digital rectal examination for early detection of prostate cancer in a national community-based program. *Urology*, 47(6):863–869, 1996. ISSN 00904295. doi: 10.1016/S0090-4295(96)00061-1. URL `http://www.sciencedirect.com/science/article/pii/S0090429596000611`.

Alexandra R Crowe and Wei Yue. Semi-quantitative Determination of Protein Expression using Immunohistochemistry Staining and Analysis: An Integrated Protocol. *Bio Protoc.*, 9(24), 2019. doi: 10.21769/BioProtoc.3465.

Mary Beth B. Culp, Isabelle Soerjomataram, Jason A. Efstathiou, Freddie Bray, and Ahmedin Jemal. Recent Global Patterns in Prostate Cancer Incidence and Mortality Rates. *European Urology*, 77(1):38–52, 2020. ISSN 18737560. doi: 10.1016/j.eururo.2019.08.005. URL `https://doi.org/10.1016/j.eururo.2019.08.005`.

Gerald R. Cunha, Simon W. Hayward, Y. Z. Wang, and William A. Ricke. Role of the stromal microenvironment in carcinogenesis of the prostate. *International Journal of Cancer*, 107(1):1–10, 2003. ISSN 00207136. doi: 10.1002/ijc.11335.

Allison Derenne, Alix Mignolet, and Erik Goormaghtigh. FTIR spectral signature of anticancer drug effects on PC-3 cancer cells: Is there any influence of the cell cycle? *Analyst*, 138(14):3998–4005, 2013. ISSN 13645528. doi: 10.1039/c3an00225j.

Jeanie L. Drury and David J. Mooney. Hydrogels for tissue engineering: Scaffold design variables and applications. *Biomaterials*, 24(24):4337–4351, 2003. ISSN 01429612. doi: 10.1016/S0142-9612(03)00340-5.

E. Eisenbarth. Biomaterials for tissue engineering. *Advanced Engineering Materials*, 9(12): 1051–1060, 2007. ISSN 14381656. doi: 10.1002/adem.200700287.

Stuart J. Ellem, Elena M. De-Juan-Pardo, and Gail P. Risbridger. In vitro modeling of the prostate cancer microenvironment. *Advanced Drug Delivery Reviews*, 79:214–221, 2014. ISSN 18728294. doi: 10.1016/j.addr.2014.04.008.

Gamal Elmasry, Da Wen Sun, and Paul Allen. Near-infrared hyperspectral imaging for predicting colour, pH and tenderness of fresh beef. *Journal of Food Engineering*, 110 (1):127–140, 2012. ISSN 02608774. doi: 10.1016/j.jfoodeng.2011.11.028. URL http://dx.doi.org/10.1016/j.jfoodeng.2011.11.028.

Laura Elomaa, Sandra Teixeira, Risto Hakala, Harri Korhonen, Dirk W. Grijpma, and Jukka V. Seppälä. Preparation of poly(ϵ-caprolactone)-based tissue engineering scaffolds by stereolithography. *Acta Biomaterialia*, 7(11):3850–3856, 2011. doi: 10.1016/j.actbio.2011.06.039.

Adam J. Engler, Shamik Sen, H. Lee Sweeney, and Dennis E. Discher. Matrix Elasticity Directs Stem Cell Lineage Specification. *Cell*, 126(4):677–689, 2006. ISSN 00928674. doi: 10.1016/j.cell.2006.06.044.

By Jonathan Epstein. Bad Grades for Gleason. (November), 2017.

Jonathan I Epstein, William C Jr Allsbrook, Mahul B Amin, and Lars L Egevad. The 2005 International Society of Urological Pathology (ISUP) Consensus Conference on Gleason Grading of Prostatic Carcinoma. *The American journal of surgical pathology*, 29(9):1228–1242, 2005. ISSN 0147-5185 (Print). doi: 10.1097/01.pas.0000173646.99337.b1. URL http://www.ncbi.nlm.nih.gov/pubmed/26492179.

Jonathan I. Epstein, Michael J. Zelefsky, Daniel D. Sjoberg, Joel B. Nelson, Lars Egevad, Cristina Magi-Galluzzi, Andrew J. Vickers, Anil V. Parwani, Victor E. Reuter, Samson W. Fine, James A. Eastham, Peter Wiklund, Misop Han, Chandana A. Reddy, Jay P. Ciezki, Tommy Nyberg, and Eric A. Klein. A Contemporary Prostate Cancer Grading System: A Validated Alternative to the Gleason Score. *European Urology*, 69(3):428–435, 2016.

ISSN 18737560. doi: 10.1016/j.eururo.2015.06.046. URL http://dx.doi.org/10.1016/j.eururo.2015.06.046.

Minna. Eriksson, Minna. Taskinen, and Sirpa. Leppä. Mitogen Activated Protein Kinase-Dependent Activation of c-Jun and c-Fos is required for Neuronal differentiation but not for Growth and Stress Reposne in PC12 cells. *Journal of cellular physiology*, 207(1):12–22, 2006. ISSN 0021-9541. doi: 10.1002/JCP.

Santiago Fajardo, García-Galvan, Federico R., Violeta Barranco, Juan C. Galvan, and Sebastian Feliu Batlle. We are IntechOpen , the world ' s leading publisher of Open Access books Built by scientists , for scientists TOP 1 %. *Intech*, i(tourism):13, 2016. doi: http://dx.doi.org/10.5772/57353. URL https://www.intechopen.com/books/advanced-biometric-technologies/liveness-detection-in-biometrics.

Alessandro Faroni, Victoria L. Workman, Alberto Saiani, and Adam J. Reid. Self-Assembling Peptide Hydrogel Matrices Improve the Neurotrophic Potential of Human Adipose-Derived Stem Cells. *Advanced Healthcare Materials*, 8(17), 2019. ISSN 21922659. doi: 10.1002/adhm.201900410.

Natalja E. Fedorovich, Joost R. De Wijn, Abraham J. Verbout, Jacqueline Alblas, and Wouter J.A. Dhert. Three-Dimensional Fiber Deposition of Cell-Laden, Viable, Patterned Constructs for Bone Tissue Printing. *Tissue Engineering Part A*, 14(1):127–133, 2 2008. doi: 10.1089/ten.a.2007.0158.

Stephen I. Fogarasi, Faisal M. Khan, Ho-Yuen H. Pang, Ricardo Mesa-Tejada, Michael J. Donovan, and Gerardo Fernandez. Glandular object based tumor morphometry in H&E biopsy samples for prostate cancer prognosis. *Medical Imaging 2011: Computer-Aided Diagnosis*, 7963(March 2011):79633F, 2011. ISSN 16057422. doi: 10.1117/12.878142.

Christian Frantz, Kathleen M. Stewart, and Valerie M. Weaver. The extracellular matrix at a glance. *Journal of Cell Science*, 123(24):4195–4200, 2010. ISSN 00219533. doi: 10.1242/jcs.023820.

T M Freyman, I V Yannas, and L J Gibson. Cellular materials as porous scaffolds for tissue engineering. *Progress in Materials Science*, 46(3-4):273–282, 2001. doi: 10.1016/S0079-6425(00)00018-9.

Dong Gao, Ian Vela, Andrea Sboner, Phillip J. Iaquinta, Wouter R. Karthaus, Anuradha Gopalan, Catherine Dowling, Jackline N. Wanjala, Eva A. Undvall, Vivek K. Arora, John Wongvipat, Myriam Kossai, Sinan Ramazanoglu, Luendreo P. Barboza, Wei Di, Zhen Cao, Qi Fan Zhang, Inna Sirota, Leili Ran, Theresa Y. Macdonald, Himisha Beltran, Juan Miguel Mosquera, Karim A. Touijer, Peter T. Scardino, Vincent P. Laudone, Kristen R. Curtis,

Dana E. Rathkopf, Michael J. Morris, Daniel C. Danila, Susan F. Slovin, Stephen B. Solomon, James A. Eastham, Ping Chi, Brett Carver, Mark A. Rubin, Howard I. Scher, Hans Clevers, Charles L. Sawyers, and Yu Chen. Organoid cultures derived from patients with advanced prostate cancer. *Cell*, 159(1):176–187, 2014. ISSN 10974172. doi: 10.1016/j.cell.2014.08.016. URL http://dx.doi.org/10.1016/j.cell.2014.08.016.

Régis Gasper, Tatjana Mijatovic, Audrey Bénard, Allison Derenne, Robert Kiss, and Erik Goormaghtigh. FTIR spectral signature of the effect of cardiotonic steroids with antitumoral properties on a prostate cancer cell line. *Biochimica et Biophysica Acta - Molecular Basis of Disease*, 1802(11):1087–1094, 2010. ISSN 09254439. doi: 10.1016/j.bbadis.2010.07.012. URL http://dx.doi.org/10.1016/j.bbadis.2010.07.012.

E. Gazi, J. Dwyer, P. Gardner, A. Ghanbari-Siahkali, A. P. Wade, J. Miyan, N. P. Lockyer, J. C. Vickerman, N. W. Clarke, J. H. Shanks, L. J. Scott, C. A. Hart, and M. Brown. Applications of Fourier transform infrared microspectroscopy in studies of benign prostate and prostate cancer. A pilot study. *Journal of Pathology*, 201(1):99–108, 2003. ISSN 00223417. doi: 10.1002/path.1421.

E. Gazi, N. P. Lockyer, J. C. Vickerman, P. Gardner, J. Dwyer, C. A. Hart, M. D. Brown, N. W. Clarke, and J. Miyan. Imaging ToF-SIMS and synchrotron-based FT-IR microspectroscopic studies of prostate cancer cell lines. *Applied Surface Science*, 231-232: 452–456, 2004. ISSN 01694332. doi: 10.1016/j.apsusc.2004.03.170.

E. Gazi, J. Dwyer, N. P. Lockyer, J. Miyan, P. Gardner, C. A. Hart, M. D. Brown, and N. W. Clarke. A study of cytokinetic and motile prostate cancer cells using synchrotron-based FTIR microspectroscopic imaging. *Vibrational Spectroscopy*, 38(1-2):193–201, 2005. ISSN 09242031. doi: 10.1016/j.vibspec.2005.02.026.

E. Gazi, T. J. Harvey, M. D. Brown, N. P. Lockyer, P. Gardner, and N. W. Clarke. A FTIR microspectroscopic study of the uptake and metabolism of isotopically labelled fatty acids by metastatic prostate cancer. *Vibrational Spectroscopy*, 50(1):99–105, 2009. ISSN 09242031. doi: 10.1016/j.vibspec.2008.09.006.

Ehsan Gazi, Matthew Baker, John Dwyer, Nicholas P. Lockyer, Peter Gardner, Jonathan H. Shanks, Roy S. Reeve, Claire A. Hart, Noel W. Clarke, and Michael D. Brown. A Correlation of FTIR Spectra Derived from Prostate Cancer Biopsies with Gleason Grade and Tumour Stage. *European Urology*, 50(4):750–761, 2006. ISSN 03022838. doi: 10.1016/j.eururo.2006.03.031.

Ehsan Gazi, Peter Gardner, Nicholas P Lockyer, Claire a Hart, Michael D Brown, and Noel W Clarke. Direct evidence of lipid translocation between adipocytes and prostate cancer cells

with imaging FTIR microspectroscopy. *Journal of lipid research*, 48(8):1846–1856, 2007. ISSN 0022-2275. doi: 10.1194/jlr.M700131-JLR200.

David MR Gibbs, Mohammad Vaezi, Shoufeng Yang, and Richard OC Oreffo. Hope versus hype: what can additive manufacturing realistically offer trauma and orthopedic surgery? *Regenerative Medicine*, 9(4):535–549, 2014. ISSN 1746-0751. doi: 10.2217/rme.14.20. URL `http://www.ncbi.nlm.nih.gov/entrez/query.fcgi?cmd=Retrieve&db=pubmed&dopt=Abstract&list_uids=25159068&query_hl=1%5Cnhttp://www.futuremedicine.com/doi/abs/10.2217/rme.14.20`.

Erik Goormaghtigh. Infrared imaging in histopathology: Is a unified approach possible? *Biomedical Spectroscopy and Imaging*, 5(4):325–346, 2017. ISSN 22128808. doi: 10.3233/BSI-160151. URL `http://www.medra.org/servlet/aliasResolver?alias=iospress&doi=10.3233/BSI-160151`.

Julie E. Gough, Alberto Saiani, and Aline F. Miller. Peptide hydrogels: mimicking the extracellular matrix. *Bioinspired, Biomimetic and Nanobiomaterials*, 1(1):4–12, 2012. ISSN 2045-9858. doi: 10.1680/bbn.11.00007.

A. A. Gowen, C. P. O'Donnell, P. J. Cullen, G. Downey, and J. M. Frias. Hyperspectral imaging - an emerging process analytical tool for food quality and safety control. *Trends in Food Science and Technology*, 18(12):590–598, 2007. ISSN 09242244. doi: 10.1016/j.tifs.2007.06.001.

C Gurchot. The trophoblast theory of cancer (John Beard, 1857-1924) revisited. *Oncology*, 31(5-6):310–333, 1975. ISSN 0030-2414 (Print). doi: 10.1159/000225037.

D. M. Haaland, H. D.T. Jones, and J. A. Timlin. *Experimental and Data Analytical Approaches to Automating Multivariate Curve Resolution in the Analysis of Hyperspectral Images*, volume 30. Elsevier B.V., 1 edition, 2016. ISBN 9780444636386. doi: 10.1016/B978-0-444-63638-6.00012-7. URL `http://dx.doi.org/10.1016/B978-0-444-63638-6.00012-7`.

Lisa Haines-Butterick, Karthikan Rajagopal, Monica Branco, Daphne Salick, Ronak Rughani, Matthew Pilarz, Matthew S. Lamm, Darrin J. Pochan, and Joel P. Schneider. Controlling hydrogelation kinetics by peptide design for three-dimensional encapsulation and injectable delivery of cells. *Proceedings of the National Academy of Sciences of the United States of America*, 104(19):7791–7796, 2007. ISSN 00278424. doi: 10.1073/pnas.0701980104.

Abigail S. Haka, Linda H. Kidder, and E. Neil Lewis. Biomarkers and Biological Spectral Imaging. *Biomarkers and Biological Spectral Imaging*, 4259(July 2001):47–55, 2002. ISSN 0277-786X. doi: 10.1117/12.432479.

Won Sik Ham, Heather J. Chalfin, Zhaoyong Feng, Bruce J. Trock, Jonathan I. Epstein, Carling Cheung, Elizabeth Humphreys, Alan W. Partin, and Misop Han. New Prostate Cancer Grading System Predicts Long-term Survival Following Surgery for Gleason Score 8–10 Prostate Cancer. *European Urology*, 71(6):907–912, 2017. ISSN 18737560. doi: 10.1016/j.eururo.2016.11.006. URL http://dx.doi.org/10.1016/j.eururo.2016.11.006.

Tim J. Harvey, Alex Henderson, Ehsan Gazi, Noel W. Clarke, Mick Brown, Elsa Correia Faria, Richard D. Snook, and Peter Gardner. Discrimination of prostate cancer cells by reflection mode FTIR photoacoustic spectroscopy. *Analyst*, 132(4):292–295, 2007. ISSN 00032654. doi: 10.1039/b618618a.

Setsuo Hirohashi and Yae Kanai. Cell adhesion system and human cancer morphogenesis. *Gann Monographs on Cancer Research*, 52(7):13–26, 2004. ISSN 00720151.

C P Sherman Hsu. Infrared Spectroscopy. *Handbook of Instrumental Techniques for Analytical Chemistry*, pages 247–284, 1997. ISSN 1936-086X. doi: 10.1021/nn203506n.

Meng Huang, Hexi Du, Li Zhang, Hong Che, and Chaozhao Liang. The association of HIF-1α expression with clinicopathological significance in prostate cancer: A meta-analysis. *Cancer Management and Research*, 10:2809–2816, 2018. ISSN 11791322. doi: 10.2147/CMAR.S161762.

Peter A. Humphrey. Gleason grading and prognostic factors in carcinoma of the prostate. *Modern Pathology*, 17(3):292–306, 2004. ISSN 0893-3952. doi: 10.1038/modpathol.3800054.

Peter A. Humphrey. Histopathology of prostate cancer. *Cold Spring Harbor Perspectives in Medicine*, 7(10):1–21, 2017. ISSN 21571422. doi: 10.1101/cshperspect.a030411.

D. W. Hutmacher and S. Cool. Concepts of scaffold-based tissue engineering - The rationale to use solid free-form fabrication techniques. *Journal of Cellular and Molecular Medicine*, 11(4):654–669, 2007. ISSN 15821838. doi: 10.1111/j.1582-4934.2007.00078.x.

Yoshito Ikada. Challenges in tissue engineering. *Journal of the Royal Society, Interface / the Royal Society*, 3(10):589–601, 2006. ISSN 1742-5689. doi: 10.1098/rsif.2006.0124.

Invitrogen Molecular Probes. LIVE/DEAD Viability/Cytotoxicity Kit for mammalian cells. *Product Information, Catalog number: MP 03224*, pages 1–7, 2005. URL https://tools.lifetechnologies.com/content/sfs/manuals/mp03224.pdf.

John T Isaacs. Commentary Aggressiveness of Prostate Cancer. 150(5):1511–1521, 1997.

Michael Ittmann, Jiaoti Huang, Enrico Radaelli, Philip Martin, Sabina Signoretti, Ruth Sullivan, Brian W. Simons, Jerrold M. Ward, Brian D. Robinson, Gerald C. Chu, Massimo

Loda, George Thomas, Alexander Borowsky, and Robert D. Cardiff. Animal models of human prostate cancer: The consensus report of the new york meeting of the mouse models of human cancers consortium prostate pathology committee. *Cancer Research*, 73(9):2718–2736, 2013. ISSN 00085472. doi: 10.1158/0008-5472.CAN-12-4213.

Anna De Juan. *Multivariate curve resolution for hyperspectral image analysis*. 2020. ISBN 9780444639776. doi: 10.1016/B978-0-444-63977-6.00007-9.

onathan C. Jun, Aman Rathore, Haris Younas, Daniele Gilkes, and Vsevolod Y. Polotsky. Hypoxia-Inducible Factors and Cancer. *Curr Sleep Med Rep*, 3(1):1–10, 2018. doi: 10.1007/s40675-017-0062-7.Hypoxia-Inducible.

Raghu Kalluri and Robert A Weinberg. Review series The basics of epithelial-mesenchymal transition. *The Journal of Clinical Investigation*, 119(6), 2009. doi: 10.1172/JCI39104.1420.

Raghu Kalluri and Michael Zeisberg. Fibroblasts in cancer. *Nature reviews. Cancer*, 6(5): 392–401, 2006. ISSN 1474-175X. doi: 10.1038/nrc1877.

Sergei G. Kazarian and K. L Andrew Chan. Sampling approaches in fourier transform infrared imaging applied to polymers. *Progress in Colloid and Polymer Science*, 132(March):1–6, 2006. ISSN 0340255X. doi: 10.1007/2882{_}034.

Jens M. Kelm and Martin Fussenegger. Microscale tissue engineering using gravity-enforced cell assembly. *Trends in Biotechnology*, 22(4):195–202, 2004. ISSN 01677799. doi: 10.1016/j.tibtech.2004.02.002.

Ali Khademhosseini and Robert Langer. Microengineered hydrogels for tissue engineering. *Biomaterials*, 28(34):5087–5092, 2007. ISSN 01429612. doi: 10.1016/j.biomaterials.2007.07.021.

Saif Khalil and Wei Sun. Biopolymer deposition for freeform fabrication of hydrogel tissue constructs. *Materials Science and Engineering C*, 27(3):469–478, 2007. ISSN 09284931. doi: 10.1016/j.msec.2006.05.023.

Amelia Ahmad Khalili and Mohd Ridzuan Ahmad. A Review of cell adhesion studies for biomedical and biological applications. *International Journal of Molecular Sciences*, 16(8): 18149–18184, 2015. ISSN 14220067. doi: 10.3390/ijms160818149.

Faisal M. Khan, Richard Scott, Michael Donovan, and Gerardo Fernandez. Predicting and replacing the pathological Gleason grade with automated gland ring morphometric features from immunofluorescent prostate cancer images Faisal M . Khan. *Journal of Medical Imaging*, 4(2), 2017. doi: 10.1117/1.JMI.4.2.021103.

Byung-Soo Kim and David J Mooney. Development of biocompatible synthetic extracellular matrices for tissue engineering. *Trends in Biotechnology*, 16(5):224–230, 1998. doi: 10. 1016/S0167-7799(98)01191-3.

Franziska Koch, Michael Müller, Finja König, Nina Meyer, Jasmin Gattlen, Uwe Pieles, Kirsten Peters, Bernd Kreikemeyer, Stephanie Mathes, and Sina Saxer. Mechanical characteristics of beta sheet-forming peptide hydrogels are dependent on peptide sequence, concentration and buffer composition. *Royal Society Open Science*, 5(3), 2018. ISSN 20545703. doi: 10.1098/rsos.171562.

J-P. Kruth, P. Mercelis, J. Vaerenbergh, L. Froyen, and M. Rombouts. Binding mechanisms in selective laser sintering and selective laser melting. *Rapid Prototyping Journal*, 11(1): 26–36, 2005. ISSN 1355-2546. doi: 10.1108/13552540510573365.

Subha K Kumpaty, Deborah Cottrill, Andrew Hollett, Jon Barrett, and Sheku Kamara. An Experimental Study of Heat Transfer in Selective Laser Sintering ^{TM} process. pages 5–9, 2006.

Jin Tae Kwak, Stephen M. Hewitt, Saurabh Sinha, and Rohit Bhargava. Multimodal microscopy for automated histologic analysis of prostate cancer. *BMC Cancer*, 11:1–16, 2011. ISSN 14712407. doi: 10.1186/1471-2407-11-62.

Jin Tae Kwak, André Kajdacsy-Balla, Virgilia Macias, Michael Walsh, Saurabh Sinha, and Rohit Bhargava. Improving prediction of prostate cancer recurrence using chemical imaging. *Scientific Reports*, 5:1–10, 2015. ISSN 20452322. doi: 10.1038/srep08758.

Shona H. Lang, Catherine Hyde, Ian N. Reid, Ian S. Hitchcock, Claire A. Hart, A. A.Gordon Bryden, Jean Marie Villette, Michael J. Stower, and Norman J. Maitland. Enhanced expression of vimentin in motile prostate cell lines and in poorly differentiated and metastatic prostate carcinoma. *Prostate*, 52(4):253–263, 2002. ISSN 02704137. doi: 10.1002/pros.10088.

Peter Lasch, Matthias Boese, and Max Diem. Diagnostic Optical Spectroscopy in Biomedicine. *Diagnostic Optical Spectroscopy in Biomedicine*, 4432(October 2001):10–16, 2001. ISSN 0277-786X. doi: 10.1117/12.447128.

Peter Lasch, Max Diem, and Dieter Naumann. FT-IR microspectroscopic imaging of prostate tissue sections. *Biomedical Vibrational Spectroscopy and Biohazard Detection Technologies*, 5321(July 2004):1, 2004. ISSN 0277786X. doi: 10.1117/12.529125.

C T Laurencin, A M Ambrosio, M D Borden, and J A Cooper. Tissue engineering: orthopedic applications. *Annual review of biomedical engineering*, 1:19–46, 1999. doi: 10.1146/annurev. bioeng.1.1.19.

Christine H. Lee, Oluyemi Akin-Olugbade, and Alexander Kirschenbaum. Overview of Prostate Anatomy, Histology, and Pathology. *Endocrinology and Metabolism Clinics of North America*, 40(3):565–575, 2011. ISSN 08898529. doi: 10.1016/j.ecl.2011.05.012.

Donghee Lee, Haipeng Zhang, and Sangjin Ryu. Elastic Modulus Measurement of Hydrogels. pages 865–884, 2019. doi: 10.1007/978-3-319-77830-3{_}60.

Kuen Yong Lee and David J Mooney. Hydrogels for Tissue Engineering Applications. *American Chemical Society*, 101(7):203–225, 2001a. ISSN 00092665. doi: 10.1007/978-1-4419-5919-5.

Kuen Yong Lee and David J. Mooney. Hydrogels for Tissue Engineering. *Chemical Reviews*, 101(7):1869–1880, 7 2001b. ISSN 0009-2665. doi: 10.1021/cr000108x.

Josef Leibold, Marcus Ruscetti, Zhen Cao, Yu Jui Ho, Timour Baslan, Min Zou, Wassim Abida, Judith Feucht, Teng Han, Francisco M. Barriga, Kaloyan M. Tsanov, Leah Zamechek, Amanda Kulick, Corina Amor, Sha Tian, Katarzyna Rybczyk, Nelson R. Salgado, Francisco J. Sánchez-Rivera, Philip A. Watson, Elisa de Stanchina, John E. Wilkinson, Lukas E. Dow, Cory Abate-Shen, Charles L. Sawyers, and Scott W. Lowe. *Somatic Tissue Engineering in Mouse Models Reveals an Actionable Role for WNT Pathway Alterations in Prostate Cancer Metastasis*, volume 10. 2020. ISBN 6468883342. doi: 10.1158/2159-8290.CD-19-1242.

Bruce E. LeRoy and Nicole Northrup. Prostate cancer in dogs: Comparative and clinical aspects. *Veterinary Journal*, 180(2):149–162, 2009. ISSN 10900233. doi: 10.1016/j.tvjl.2008.07.012. URL http://dx.doi.org/10.1016/j.tvjl.2008.07.012.

I.W. Levin and Rohit Bhargava. FOURIER TRANSFORM INFRARED VIBRATIONAL SPECTROSCOPIC IMAGING: Integrating Microscopy and Molecular Recognition. *Annu. Rev. Phys. Chem.*, 56(1):429–474, 2005. ISSN 0066-426X. doi: 10.1146/annurev.physchem.56.092503.141205. URL http://arjournals.annualreviews.org/doi/abs/10.1146/annurev.physchem.56.092503.141205.

C. C. Lin and K. S. Anseth. PEG hydrogels for the controlled release of biomolecules in regenerative medicine. *Pharmaceutical Research*, 26(3):631–643, 2009. ISSN 07248741. doi: 10.1007/s11095-008-9801-2.

Chang Liu, Qingguo Zhang, Song Zhu, Hong Liu, and Jie Chen. Preparation and applications of peptide-based injectable hydrogels. *RSC Advances*, 9(48):28299–28311, 2019. ISSN 20462069. doi: 10.1039/c9ra05934b.

Stacy Loeb and William J. Catalona. Prostate-specific antigen in clinical practice. *Cancer Letters*, 249(1):30–39, 2007. ISSN 03043835. doi: 10.1016/j.canlet.2006.12.022.

Chin-Yap Loh, Jian Yi Chai, Ting Fang Tang, Won Fen Wong, Gautam Sethi, Muthu Kumaraswamy Shanmugam, Pei Pei Chong, and Chung Yeng Looi. *The E-Cadherin and N-Cadherin Switch in Epithelial-to-Mesenchymal Transition: Signaling, Therapeutic Implications, and Challenges.* 2019. ISBN 6568737690.

Kristine S K.S. Louis and A.C. Andre C Siegel. Mammalian Cell Viability. *Methods in Molecular Biology*, 740(1):7–12, 2011. ISSN 1940-6029. doi: 10.1007/978-1-61779-108-6. URL http://link.springer.com/10.1007/978-1-61779-108-6.

Tingli Lu, Yuhui Li, and Tao Chen. Techniques for fabrication and construction of three-dimensional scaffolds for tissue engineering. *International journal of nanomedicine*, 8:337–50, 2013. ISSN 1178-2013. doi: 10.2147/IJN.S38635.

Cristina Magi-galluzzi, Andrew J Vickers, Anil V Parwani, and Victor E Reuter. Epstein 2016 A contemporary prostate cancer grading system.pdf. *Eur Urol*, 69(3):428–435, 2015. doi: 10.1016/j.eururo.2015.06.046.A. URL https://www.ncbi.nlm.nih.gov/pmc/articles/PMC5002992/.

Patrick W. McLaughlin, Sara Troyer, Sally Berri, Vrinda Narayana, Amichay Meirowitz, Peter L. Roberson, and James Montie. Functional anatomy of the prostate: Implications for treatment planning. *International Journal of Radiation Oncology Biology Physics*, 63 (2):479–491, 2005. ISSN 03603016. doi: 10.1016/j.ijrobp.2005.02.036.

Tineke W H Meijer, Johannes H A M Kaanders, Paul N Span, and Johan Bussink. Targeting Hypoxia , HIF-1 , and Tumor Glucose Metabolism to Improve Radiotherapy Ef fi cacy. *American Association for Cancer Research*, pages 5585–5595, 2012. doi: 10.1158/1078-0432. CCR-12-0858.

Ferry P W Melchels, Jan Feijen, and Dirk W Grijpma. Poly(D,L-lactide)/hydroxyapatite composite tissue engineering scaffolds prepared by stereolithography. In *2nd China-Europe Symposium on Biomaterials in Regenerative Medicine*, Barcelona, 2009.

Ferry P W Melchels, Marco A N Domingos, Travis J. Klein, Jos Malda, Paulo J. Bartolo, and Dietmar W. Hutmacher. Additive manufacturing of tissues and organs. *Progress in Polymer Science*, 37(8):1079–1104, 2012. ISSN 00796700. doi: 10.1016/j.progpolymsci.2011.11.007. URL http://dx.doi.org/10.1016/j.progpolymsci.2011.11.007.

Ulrich Meyer, Thomas Meyer, Jörg Handschel, and Hans Peter Wiesmann. *Fundamentals of Tissue Engineering and Regenerative Medicine.* Springer, New York, 2009. ISBN 9783540777540. doi: 10.1007/978-3-540-77755-7{_}20.

Jeff M. Michalski, Thomas M. Pisansky, Colleen A.F. Lawton, and Louis Potters. Prostate Cancer. Technical Report March, 2016. URL `http://linkinghub.elsevier.com/retrieve/pii/B9780323240987000538`.

Kurt Miller, Per-Anders Abrahamsson, Koichiro Akakura, Frans M.J. Debruyne, Christopher P. Evans, and Laurence Klotz. The Continuing Role of PSA in the Detection and Management of Prostate Cancer. *European Urology Supplements*, 6(3):327–333, 2007. ISSN 15699056. doi: 10.1016/j.eursup.2006.12.001. URL `http://linkinghub.elsevier.com/retrieve/pii/S1569905606003551`.

J J Minguell, A Erices, and P Conget. Mesenchymal stem cells. *Experimental biology and medicine*, 226(6):507–520, 2001.

Keith L. Moore, Arthur F. Dalley, and Anne M.R. Agur. *Clinically oriented anatomy*, volume 53. 2014. ISBN 9788578110796. doi: 10.1017/CBO9781107415324.004.

Colm Morrissey and Robert L. Vessella. The role of tumor microenvironment in prostate cancer bone metastasis. *Journal of Cellular Biochemistry*, 101(4):873–886, 2007. ISSN 07302312. doi: 10.1002/jcb.21214.

Judd W. Moul, Donald J. Lewis, Amy A. Ross, Douglas G. Kahn, Chi K. Ho, and David G. McLeod. Immunohistologic detection of prostate cancer pelvic lymph node micrometastases: Correlation to preoperative serum prostate-specific antigen. *Urology*, 43(1):68–73, 1994. ISSN 15279995. doi: 10.1016/S0090-4295(94)80267-X.

Kalyani Nair, Milind Gandhi, Saif Khalil, Karen Chang Yan, Michele Marcolongo, Kenneth Barbee, and Wei Sun. Characterization of cell viability during bioprinting processes. *Biotechnology Journal*, 4(8):1168–1177, 2009. ISSN 18606768. doi: 10.1002/biot.200900004.

Preetha R Nair, S.Ranjitha, and Suresh H N. An Infrared hyperspectral imaging technique for non-invasive canine cancer detection. *International Conference on Electrical, Electronics, and Optimization Techniques (ICEEOT)*, 2016. doi: 10.1109/ICEEOT.2016.7755374.

Raja Naren and Hui-suk Yun. A simultaneous 3D printing process for fabrication of bioceramic and cell-laden hydrogel core/shell scaffolds as potential application for bone tissue regeneration. *J. Mater. Chem. B*, 2016. ISSN 2050-750X. doi: 10.1039/C6TB00849F.

Nora M. Navone, Christopher J. Logothetis, Andrew C. Von Eschenbach, and Patricia Troncoso. Model systems of prostate cancer: Uses and limitations. *Cancer and Metastasis Reviews*, 17(4):361–371, 1999. ISSN 01677659. doi: 10.1023/A:1006165017279.

D. W. Neubauer. Cancer research. *Arizona medicine*, 13(12):535–541, 1956. ISSN 00041556.

Jason W Nichol and Ali Khademhosseini. Modular Tissue Engineering: Engineering Biological Tissues from the Bottom Up. *Soft matter*, 5(7):1312–1319, 2009. doi: 10.1039/b814285h.

R L Noble. The development of prostatic adenocarcinoma in Nb rats following prolonged sex hormone administration. *Cancer Res.*, 37(June):1929–1933, 1977.

Cyrille Norotte, Francois S. Marga, Laura E. Niklason, and Gabor Forgacs. Scaffold-free vascular tissue engineering using bioprinting. *Biomaterials*, 30(30):5910–5917, 2009. ISSN 01429612. doi: 10.1016/j.biomaterials.2009.06.034. URL http://dx.doi.org/10.1016/j.biomaterials.2009.06.034.

Fergal J O'Brien. Biomaterials & scaffolds for tissue engineering. *Materials Today*, 14(3): 88–95, 2011. doi: 10.1016/S1369-7021(11)70058-X.

Kim C. O'Connor. Three-dimensional cultures of prostatic cells: Tissue models for the development of novel anti-cancer therapies, 1999. ISSN 07248741.

Onisuru T. Okotie, Kimberly A. Roehl, Misop Han, Stacy Loeb, Sara N. Gashti, and William J. Catalona. Characteristics of Prostate Cancer Detected by Digital Rectal Examination Only. *Urology*, 70(6):1117–1120, 2007. ISSN 00904295. doi: 10.1016/j.urology.2007.07.019.

Sara M Oliveira, Rui L Reis, and João F Mano. Towards the design of 3D multiscale instructive tissue engineering constructs: Current approaches and trends. *Biotechnology Advances*, 33 (6):842–855, 2015. doi: 10.1016/j.biotechadv.2015.05.007.

Aria F Olumi, Gary D Grossfeld, Simon W Hayward, Prostatic Epithelium, Aria F Olumi, Gary D Grossfeld, Simon W Hayward, Peter R Carroll, Thea D Tlsty, and Gerald R Cunha. Carcinoma-associated Fibroblasts Direct Tumor Progression of Initiated Human Prostatic Epithelium Carcinoma-associated Fibroblasts Direct Tumor Progression of Initiated Human. pages 5002–5011, 1999.

Naoyoshi Onoda, Iwao Sugitani, Ken-ichi Ito, and Akifumi Suzuki. Evaluation of the 8th Edition TNM Classification for Anaplastic Thyroid Carcinoma. 4:1–12, 2020. doi: 10.3390/cancers12030552.

Arne Östman and Martin Augsten. Cancer-associated fibroblasts and tumor growth - bystanders turning into key players. *Current Opinion in Genetics and Development*, 19 (1):67–73, 2009. ISSN 0959437X. doi: 10.1016/j.gde.2009.01.003.

M. L. Oyen. Mechanical characterisation of hydrogel materials. *International Materials Reviews*, 59(1):44–59, 2014. ISSN 09506608. doi: 10.1179/1743280413Y.0000000022.

Ibrahim T. Ozbolat and Monika Hospodiuk. Current advances and future perspectives in extrusion-based bioprinting. *Biomaterials*, 76:321–343, 2016. ISSN 18785905. doi: 10.1016/j.biomaterials.2015.10.076. URL http://dx.doi.org/10.1016/j.biomaterials.2015.10.076.

Roman Paduch. Theories of cancer origin. *European Journal of Cancer Prevention*, 24(1): 57–67, 2015. ISSN 14735709. doi: 10.1097/CEJ.0000000000000024.

J. T. Painter, N. P. Clayton, and R. A. Herbert. Useful Immunohistochemical Markers of Tumor Differentiation J. *Toxicol Pathol*, 38(1):131–141, 2012. doi: 10.1177/0192623309356449.Useful.

Czesława Paluszkiewicz and Wojciech M Kwiatek. Analysis of human cancer prostate tissues using FTIR microspectroscopy and SRIXE techniques. *Journal of Molecular Structure*, 565-566:329–334, 2001. ISSN 00222860. doi: 10.1016/S0022-2860(01)00527-0. URL http://linkinghub.elsevier.com/retrieve/pii/S0022286001005270.

Maxime Parisotto and Daniel Metzger. Genetically engineered mouse models of prostate cancer. *Molecular Oncology*, 7(2):190–205, 2013. ISSN 18780261. doi: 10.1016/j.molonc.2013.02.005. URL http://dx.doi.org/10.1016/j.molonc.2013.02.005.

Ju Young Park, Yeong Jin Choi, Jin Hyung Shim, Jeong Hun Park, and Dong Woo Cho. Development of a 3D cell printed structure as an alternative to autologs cartilage for auricular reconstruction. *Journal of Biomedical Materials Research - Part B Applied Biomaterials*, pages 1–13, 2016. ISSN 15524981. doi: 10.1002/jbm.b.33639.

C Parker, S Gillessen, A Heidenreich, A Horwich, and Guidelines Committee. clinical practice guidelines Cancer of the prostate : ESMO Clinical Practice Guidelines for diagnosis , treatment and follow-up † clinical practice guidelines. *Annals of Oncology*, 26, 2015. doi: 10.1093/annonc/mdv222.

Donald L. Pavia, Gary M. Lampman, and George S. Kriz. Introduction to Spectroscopy third edition, 2001.

Barrias C. Granja P. & Bartolo P. Pereira, R. Advanced Biofabrication Strategies for Skin Regeneration and Repair. Nanomedicine. 8:603–621, 2013. ISSN 1748-6963. doi: 10.2217/nnm.13.50.

K. J. Pienta and P. S. Esper. Risk factors for prostate cancer. *Annals of Internal Medicine*, 118(10):793–803, 1993. ISSN 00034819. doi: 10.1038/ncpuro1290.

Phillip M. Pierorazio, Patrick C. Walsh, Alan W. Partin, and Jonathan I. Epstein. Prognostic Gleason grade grouping: Data based on the modified Gleason scoring system. *BJU*

International, 111(5):753–760, 2013. ISSN 14644096. doi: 10.1111/j.1464-410X.2012.11611. x.

Michael Pilling and Peter Gardner. Fundamental developments in infrared spectroscopic imaging for biomedical applications. *Chem. Soc. Rev.*, 45:1935–1957, 2016. ISSN 0306-0012. doi: 10.1039/C5CS00846H. URL http://xlink.rsc.org/?DOI=C5CS00846H.

Michael J Pilling, Paul Bassan, and Peter Gardner. Comparison of transmission and transflectance mode FTIR imaging of biological tissue. *The Analyst*, 140(7):2383–92, 2015. ISSN 1364-5528. doi: 10.1039/c4an01975j. URL http://pubs.rsc.org/en/content/articlehtml/2015/an/c4an01975j.

Morris Pollard. Spontaneous prostate adenocarcinomas in aged germfree wistar rats. *Journal of the National Cancer Institute*, 51(4):1235–1241, 1973. ISSN 14602105. doi: 10.1093/jnci/51.4.1235.

Morris Pollard and Phyllis H. Luckert. Production of autochthonous prostate cancer in lobund-wistar rats by treatments with n-nitroso-n-methylurea and testosterone. *Journal of the National Cancer Institute*, 77(2):583–587, 1986. ISSN 14602105. doi: 10.1093/jnci/77.2.583.

Bella Raphael, Tony Khalil, Victoria L. Workman, Andrew Smith, Cameron P. Brown, Charles Streuli, Alberto Saiani, and Marco Domingos. 3D cell bioprinting of self-assembling peptide-based hydrogels. *Materials Letters*, 190:103–106, 2017. ISSN 0167577X. doi: 10.1016/j.matlet.2016.12.127. URL http://dx.doi.org/10.1016/j.matlet.2016.12.127.

Prashanth Rawla. Epidemiology of Prostate Cancer. *World J Oncol.*, 10(2):63–89, 2019. doi: 10.14740/wjon1191.

K. Rezwan, Q.Z. Chen, J.J. Blaker, and Aldo Roberto Boccaccini. Biodegradable and bioactive porous polymer/inorganic composite scaffolds for bone tissue engineering. *Biomaterials*, 27(18):3413–3431, 2006. doi: 10.1016/j.biomaterials.2006.01.039.

Bernice Robinson-bennett and Aaron Han. *Role of Immunohistochemistry in Elucidating Lung Cancer Metastatic to the Ovary from Primary Ovarian Carcinoma*, volume 4. Elsevier Inc., 2006. doi: 10.1016/S1874-5784(05)80116-3. URL http://dx.doi.org/10.1016/S1874-5784(05)80116-3.

Joëlle Roche. The Epithelial-to-Mesenchymal Transition in Cancer. *cancers*, pages 10–13, 2018. doi: 10.3390/cancers10020052.

Maciej Roman, Tomasz P. Wrobel, Czeslawa Paluszkiewicz, and Wojciech M. Kwiatek. Comparison between high definition FT-IR, Raman and AFM-IR for subcellular chemical

imaging of cholesteryl esters in prostate cancer cells. *Journal of Biophotonics*, (August 2019):1–14, 2020. ISSN 18640648. doi: 10.1002/jbio.201960094.

Zhen Rong, Zikun Bai, Jianing Li, Hao Tang, Tianyi Shen, Qiong Wang, Chongwen Wang, Rui Xiao, and Shengqi Wang. Dual-color magnetic-quantum dot nanobeads as versatile fluorescent probes in test strip for simultaneous point-of-care detection of free and complexed prostate-specific antigen. *Biosensors and Bioelectronics*, 145(September): 111719, 2019. ISSN 18734235. doi: 10.1016/j.bios.2019.111719. URL https://doi.org/10.1016/j.bios.2019.111719.

David R. Rowley. What might a stromal response mean to prostate cancer progression? *Cancer and Metastasis Reviews*, 17(4):411–419, 1999. ISSN 01677659. doi: 10.1023/A: 1006129420005.

Ignacio F. San Francisco, William C. DeWolf, Donna M. Pefhl, and Aria F. Olumi. Expression of transforming growth factor-beta 1 and growth in soft agar differentiate prostate carcinoma-associated fibroblasts from normal prostate fibroblasts. *International Journal of Cancer*, 112(2):213–218, 2004. ISSN 00207136. doi: 10.1002/ijc.20388.

Nivedita Sangaj and Shyni Varghese. Biomaterials for Tissue Engineering Applications. *Material Matters*, 10(4):511–538, 2011. ISSN 1527-2648. doi: 10.1007/978-3-7091-0385-2.

Outi R Saramäki, Kimmo J Savinainen, Nina N Nupponen, Ola Bratt, and Tapio Visakorpi. Amplification of hypoxia-inducible factor 1α gene in prostate cancer. *Cancer Genetics and Cytogenetics*, 128(1):31–34, 7 2001. ISSN 0165-4608. doi: 10.1016/S0165-4608(01)00396-X. URL https://doi.org/10.1016/S0165-4608(01)00396-X.

P M Schlag, P Kleihues, B Groner, and P Rentchnik. *International Prostate Health Council VII*. 2013. ISBN 9783540408970.

Young Joon Seol, Hyun Wook Kang, Sang Jin Lee, Anthony Atala, and James J. Yoo. Bioprinting technology and its applications. *European Journal of Cardio-thoracic Surgery*, 46(3):342–348, 2014. ISSN 1873734X. doi: 10.1093/ejcts/ezu148.

S A Shain, B McCullough, and A Segaloff. Spontaneous adenocarcinomas of the ventral prostate of aged A X C rats. *Journal of the National Cancer Institute*, 55(1):177–180, 1975. ISSN 00278874.

Sadmeet Singh, Skanda Sadacharan, Scott Su, Arie Belldegrun, Sujata Persad, and Gurmit Singh. Overexpression of vimentin: Role in the invasive phenotype in an androgen-independent model of prostate cancer. *Cancer Research*, 63(9):2306–2311, 2003. ISSN 00085472.

Laurinda F. S. Siqueira and Kássio M. G. Lima. MIR-biospectroscopy coupled with chemometrics in cancer studies. *The Analyst*, pages 4833–4847, 2016. ISSN 0003-2654. doi: 10.1039/C6AN01247G. URL http://xlink.rsc.org/?DOI=C6AN01247G.

Laurinda F.S. Siqueira, Raimundo F. Araújo Júnior, Aurigena Antunes de Araújo, Camilo L.M. Morais, and Kássio M.G. Lima. LDA vs. QDA for FT-MIR prostate cancer tissue classification. *Chemometrics and Intelligent Laboratory Systems*, 162(December 2016):123–129, 2017. ISSN 18733239. doi: 10.1016/j.chemolab.2017.01.021.

Brian Smith. *Fundamentals of Fourier transform infrared spectroscopy*, volume 40. 2006. ISBN 9780387312347. doi: 10.1002/1521-3773(20010316)40:6<9823::AID-ANIE9823>3.3.CO; 2-C. URL http://medcontent.metapress.com/index/A65RM03P4874243N.pdf%5Cnhttp: //link.springer.com/content/pdf/10.1007/978-0-387-69008-7.pdf.

Cai L. Song, Meguya Ryu, Junko Morikawa, Archana Kothari, and Sergei G. Kazarian. Thermal effect on dispersive infrared spectroscopic imaging of prostate cancer tissue. *Journal of Biophotonics*, 11(12):1–12, 2018. ISSN 18640648. doi: 10.1002/jbio.201800187.

Cai Li Song and Sergei G. Kazarian. Three-dimensional depth profiling of prostate tissue by micro ATR-FTIR spectroscopic imaging with variable angles of incidence. *The Analyst*, 144(9):2954–2964, 2019. ISSN 13645528. doi: 10.1039/c8an01929k.

Carlos Sonnenschein and Ana M. Soto. Theories of carcinogenesis: An emerging perspective. *Seminars in Cancer Biology*, 18(5):372–377, 2008. ISSN 1044579X. doi: 10.1016/j. semcancer.2008.03.012.

Carlos Sonnenschein and Ana M Soto. Sonnenschein, Soto - 2000 - Somatic Mutation Theory of Carcinogenesis Why It Should Be Dropped and Replaced. 211(September):1–7, 2010. URL papers2://publication/uuid/FD299D0E-1839-475D-AFD0-5F9EBA33E56A.

Ana M. Soto and Carlos Sonnenschein. The somatic mutation theory of cancer: Growing problems with the paradigm? *BioEssays*, 26(10):1097–1107, 2004. ISSN 02659247. doi: 10.1002/bies.20087.

Ana M. Soto and Carlos Sonnenschein. The tissue organization field theory of cancer: A testable replacement for the somatic mutation theory. *BioEssays*, 33(5):332–340, 2011. ISSN 02659247. doi: 10.1002/bies.201100025.

Eosin Stain. MV10B Stain as a Broad Spectrum Stain in Histology - A Substitute for. 2 (November):80–84, 2012.

Barbara H Stuart. *Infrared Spectroscopy: Fundamentals and Applications*, volume 8. 2004.

ISBN 9780470011140. doi: 10.1002/0470011149. URL http://doi.wiley.com/10.1002/0470011149.

Wojciech Swieszkowski, Barnabas Ho Saey Tuan, Krzysztof J Kurzydlowski, and Dietmar W Hutmacher. Repair and regeneration of osteochondral defects in the articular joints. *Biomolecular Engineering*, 24(5):489–495, 2007. doi: 10.1016/j.bioeng.2007.07.014.

Akimitsu Takagi, Masatoshi Watanabe, Yasuhisa Ishii, Joji Morita, Yoshifumi Hirokawa, Takeshi Matsuzaki, and Taizo Shiraishi. Three-dimensional Cellular Spheroid Formation Provides Human Prostate Tumor Cells with Tissue-like Features. 54:45–53, 2007.

Mark Tester and Richard Jorgensen. *Ecology and the Environment.* 2014. ISBN 9781461475002.

Thermo Nicolet Corporation. FT-IR vs. Dispersive Infrared: Theory of Infrared Spectroscopy Instrumentation. *A Thermo Electron business*, page 2, 2002. URL http://www.thermo.com/eThermo/CMA/PDFs/Product/productPDF_21611.pdf.

Wei Seong Toh, Myron Spector, Eng Hin Lee, and Tong Cao. Biomaterial-Mediated Delivery of Microenvironmental Cues for Repair and Regeneration of Articular Cartilage. *Molecular Pharmaceutics*, 8(4):994–1001, 8 2011. ISSN 1543-8384. doi: 10.1021/mp100437a.

Davor Tomas and Božo Krušlin. The potential value of (myo)fibroblastic stromal reaction in the diagnosis of prostatic adenocarcinoma. *Prostate*, 61(4):324–331, 2004. ISSN 02704137. doi: 10.1002/pros.20109.

Kyoichi Tomita, Adrie Van Bokhoven, Geert J.L.H. Van Leenders, Emiel T.G. Ruijter, Cornelius F.J. Jansen, Marion J.G. Bussemakers, and Jack A. Schalken. Cadherin switching in human prostate cancer progression. *Cancer Research*, 60(13):3650–3654, 2000. ISSN 00085472. doi: 10.5980/jpnjurol.91.92.

Nhan L. Tran, Raymond B. Nagle, Anne E. Cress, and Ronald L. Heimark. N-Cadherin Expression in Human Prostate Carcinoma Cell Lines. *The American Journal of Pathology*, 155(3):787–798, 1999. ISSN 00029440. doi: 10.1016/s0002-9440(10)65177-2.

Jennifer a Tuxhorn, Gustavo E Ayala, Megan J Smith, Vincent C Smith, Truong D Dang, and David R Rowley. Reactive Stroma in Human Prostate Cancer : Induction of Myofibroblast Phenotype and Extracellular Matrix Remodeling Reactive Stroma in Human Prostate Cancer : Induction of Myofibroblast Phenotype and Extracellular. *Clinical Cancer Research*, 8(September):2912–2923, 2002. ISSN 10780432. doi: 10.1038/35077241.

UK National Screening Committee. Screening in the UK: Making Effective Recommendations

(2014 - 2015). (2015235), 2015. URL https://www.gov.uk/government/publications/uk-national-screening-committee-recommendations-annual-report.

David Varghese, Malay Deshpande, Tao Xu, Priya Kesari, Sunil Ohri, and Thomas Boland. Advances in tissue engineering: Cell printing. *The Journal of Thoracic and Cardiovascular Surgery*, 129(2):470–472, 2 2005. doi: 10.1016/j.jtcvs.2004.06.050.

Min Wang. Developing bioactive composite materials for tissue replacement. *Biomaterials*, 24(13):2133–2151, 2003. ISSN 01429612. doi: 10.1016/S0142-9612(03)00037-1.

Yulan Wang, Lili An, Yuanda Jiang, and Haiying Hang. Effects of simulated microgravity on embryonic stem cells. *PLoS ONE*, 6(12):587–597, 2011. ISSN 19326203. doi: 10.1371/journal.pone.0029214.

Siegfried Wartewig, Christian Schorn, and Peter Bigler. Spectroscopic Techniques : An Interactive Course. *Processing*, 2003.

Dorothea Weckermann, Peter Müller, Friedhelm Wawroschek, Rolf Harzmann, Gert Riethmüller, and Günter Schlimok. Disseminated cytokeratin positive tumor cells in the bone marrow of patients with prostate cancer: detection and prognostic value. *The Journal of urology*, 166(2):699–704, 2001.

Margaret J Wheelock, Yasushi Shintani, Masato Maeda, Yuri Fukumoto, and Keith R Johnson. Cadherin switching. *Journal of Cell Science*, (121):727–735, 2008. doi: 10.1242/jcs.000455.

WHO. Cancer, 2018. URL https://www.who.int/news-room/fact-sheets/detail/cancer.

Pernilla Wikström, Josip Marusic, Pär Stattin, and Anders Bergh. Low stroma androgen receptor level in normal and tumor prostate tissue is related to poor outcome in prostate cancer patients. *Prostate*, 69(8):799–809, 2009. ISSN 02704137. doi: 10.1002/pros.20927.

J. Wilson. *Metallic biomaterials*. Elsevier Ltd, 2018. ISBN 9780081022054. doi: 10.1016/B978-0-08-102205-4.00001-5. URL http://dx.doi.org/10.1016/B978-0-08-102205-4.00001-5.

Tomasz P. Wrobel, Jin Tae Kwak, Andre Kadjacsy-Balla, and Rohit Bhargava. High-definition Fourier transform infrared spectroscopic imaging of prostate tissue. *Medical Imaging 2016: Digital Pathology*, 9791(March 2016):97911D, 2016. ISSN 16057422. doi: 10.1117/12.2217341.

X. Wu, Y. Liu, X. Li, P. Wen, Y. Zhang, Y. Long, X. Wang, Y. Guo, F. Xing, and J. Gao. Preparation of aligned porous gelatin scaffolds by unidirectional freeze-drying method. *Acta Biomaterialia*, 6(3):1167–1177, 2010. ISSN 17427061. doi: 10.1016/j.actbio.2009.08.041.

Silke Wüst, Ralph Müller, and Sandra Hofmann. Controlled Positioning of Cells in Biomaterials—Approaches Towards 3D Tissue Printing. *Journal of Functional Biomaterials*, 2(3):119–154, 8 2011. doi: 10.3390/jfb2030119.

Xin Xu, Simon Meteyer, Nicolas Perry, and Yaoyao Fiona Zhao. Energy consumption model of Binder-jetting additive manufacturing processes. *International Journal of Production Research*, 53(23):7005–7015, 2015. ISSN 00207543. doi: 10.1080/00207543.2014.937013. URL http://10.0.4.56/00207543.2014.937013%5Cnhttp://search.ebscohost.com/login.aspx?direct=true&db=buh&AN=111968341&site=ehost-live.

Nitin Yadav, Meenakshi Kanwar Chauhan, and Virander Singh Chauhan. Short to ultrashort peptide-based hydrogels as platform for biomedical applications. *Biomaterials Science*, 43: 14–17, 2019. ISSN 2047-4830. doi: 10.1039/c9bm01304k.

Congqi Yan and Darrin J. Pochan. Rheological properties of peptide-based hydrogels for biomedical and other applications. *Chemical Society Reviews*, 39(9):3528–3540, 2010. ISSN 03060012. doi: 10.1039/b919449p.

Iwan Zein, Dietmar W. Hutmacher, Kim Cheng Tan, and Swee Hin Teoh. Fused deposition modeling of novel scaffold architectures for tissue engineering applications. *Biomaterials*, 23(4):1169–1185, 2002. doi: 10.1016/S0142-9612(01)00232-0.

Hongjuan Zhao and Donna M. Peehl. Tumor-promoting phenotype of CD90hi prostate cancer-associated fibroblasts. *Prostate*, 69(9):991–1000, 2009. ISSN 02704137. doi: 10.1002/pros.20946.